UNIVERSITY OF CALIFORNIA, SAN DIEGO

A Study of Magnetic Fields of Accreting X–Ray Pulsars With the Rossi X–ray Timing Explorer

A dissertation submitted in partial satisfaction of the requirements for the degree Doctor of Philosophy in Physics

by

Wayne Coburn

Committee in charge:

Laurence Peterson, Chair
Kim Griest, Co-Chair
James Branson
William Heindl
Kurt Marti
Barnaby Rickett

2001

The dissertation of Wayne Coburn is approved, and it is acceptable in quality and form for publication on microfilm:

Co-Chair

Chair

University of California, San Diego

2001

To

The Bird

TABLE OF CONTENTS

LIST OF FIGURES

LIST OF TABLES

ACKNOWLEDGEMENTS

I would like to start of by thanking the scientists at CASS and AIT whose help and guidance has made this work possible. William "Biff" Heindl, Duane Gruber, Rick Rothschild, Mike Pelling, Rüdiger Staubert, Jörn Wilms, and my faculty advisor Larry Peterson all helped create a relaxing, yet simulating environment in which I could grow intellectually. I would especially like to thank my thesis advisor Biff Heindl for his guidance, help, encouragement, and willingness to spare no red pen.

I especially thank my Mom and Dad, whose emotional and sometimes financial support kept me afloat. I love you both. I would like to thank my brother Joseph, his soon to be wife Michelle, and their zoo of cats, dogs, birds, spiders, and miscellaneous other creatures. I wish you health, happiness, and a long life together. I would like to thank my brother Jeff, his wife Annie, and their children Jacob, Samantha, and Jared. Having children around makes the holidays fun, not to mention giving me an excuse to visit Legoland. I would like to thank my oldest brother Louis, his wife Michelle, and their children Luke and Lauren. I would also like to thank my sister Marcy. Without the love, support, and help of my family I would have been lost.

Special thanks go out to my very good friends William Collins, Carolyn Thomas, and the enigmatically ubiquitous Mr. Sequoia B_____. You showed me that there was more to life than work. I would like to thank Danny Thomas, Matt Robinson, Alex Gobler, Alyson Collins, Rob & Mellisa Porter. You all helped keep me sane. Thanks also go out to Paul Yeatman for putting up with my nonsense, and Steve Shevlin, for begin a great guy. I would like to thank Lee Hinman and Christian Melander, who have been good friends since my undergraduate years. Remember Indio Hall or Deep Space 9? I didn't think so. And of course I cannot forget Mike Craig, who has been a friend since childhood. Thanks buddy, for everything.

I would like to thank the various graduate students I have worked with, hung out with, and even lived with over the years. The "The Monkeys," Lyle Ford, David Marsden, Emrah Kalemci, and Hugh Jorgan, made sharing an office enjoyable. Dave, it is good to have you back on the west coast. Just remember, there are no bananas (or power bars) on the comet. Emrah, I wish you and Funda the best of everything. I would like to thank Ingo Kreykenbohm, Katja Pottschmidt, and the other students at the Astronomy Institute in Tübingen for making my stays in their country enjoyable. I would like to thank my friends Dan Bliss, Chris Lund, John O'Meara, Scott Burles, Jason Kreisel & MiChelle Claphan, Jason & Gabriel Prochaska, Rick Shelby, James Danielson, and David Kirkman for making graduate school less miserable. I also thank Ian & Mary Pat Fisk, you are two wonderful people and I wish you both a long and happy life. Lastly, I owe a special thanks to Edward Potter, for although he did set me on fire he was also kind enough to put me out.

I would like to thank the crew of Porter's Pub. These include (but are not limited to) Matt, Todd, Ian, Brandy, Alaina, Jenni, Mike, Jennifer, Art, Melanie, Kat, Brian, and Dane. I would also like thank the friends I met over a pint at the Pub; Jon, Trevor, Jim, Mana, Dylan, Jessie, Sean, Jenni, Laurie, Tom, Tim, Moses, Sara, John, Emily, Dave, Jeff, and the list goes on.

I would like to thank the various people at CASS who have helped me over the years, especially Shirley Roy & Cheryl Matson in the directors office, and Susanna Pastell-Mendoza & Carolyn Danmier in the Business Office. I also thank Fred Duttweiler for being Fred, a pillar of calmness and sanity in the face of any absurdity, and Pete James, who had the job of keeping our computers running in the face of hardware failures, software bugs, and hacker attacks. I thank Tom Gasaway for tuna lunches and George Huszar for keeping the coffee coming.

I would like to thank the people from UC Berkeley who I shared a summer with on the Ice; Steve Boggs, Steve McBride, Henry Primbsch, Marsha Colby, and Said Slassi-Sennou. I would also like to thank Jack Kuttner and Jim Billups for keeping the HIREGS gondola going. I owe a special debit of gratitude to Steven Peterson of NSBF for getting me a ticket on the the Antarctic airplane ride of my life.

The text of Chapter 5, in part or in full, is a reprint of the material as it appears in the Astrophysical Journal. I was the primary researcher and author and the co-authors listed in this publication directed and supervised the research which forms the basis for this chapter.

The text of Chapter 6, in part or in full, is a reprint of the material that has been recommended for publication to the Astrophysical Journal. I was the primary researcher and the co-authors listed in this publication directed and supervised the research which forms the basis for this chapter.

VITA

1969 July 25	Born, Los Gatos, California
1993	B.S. with Honors, Physics University of California, Davis
1993	Teaching Assistant, Department of Physics University of California, San Diego
1994	M.S., Physics, University of California, San Diego
1994–2001	Graduate Student Researcher, University of California, San Diego
2001	Doctor of Philosophy University of California, San Diego

PUBLICATIONS

Angeli, M., Chessell, B., Isaacs, R., Routt, L., Coburn, W. 1995, *Serpent Moon*, (Berkeley: Chaosium)

Boggs, S. E., Lin, R. P., Coburn, W., Feffer, P., Pelling, R. M., Schroeder, P. & Slassi-Sennou, S. 1997, "HIREGS Observations of the Galactic Centre and Galactic Plane: Separation of the Diffuse Galactic Hard X–Ray Continuum from the Point Source Spectra", *Proc. Second INTEGRAL Workshop* (ESA:Noordwijk), 153

Boggs, S. E., Lin, R. P., Slassi-Sennou, S., Coburn, W., & Pelling, R. M. 2000, "Diffuse Galactic Soft Gamma–Ray Emission", *ApJ*, **544**, 320

Coburn, W., Gruber, D. E., Heindl, W. A., Pelling, M., Rothschild, R. E., Staubert, R., Wilms, J., Pottschmidt, K., Kretschmar, P., & Kreykenbohm, I. 2000, "Pulse Phase Resolved Spectroscopy of 4U 1626−67", *Rossi2000: Astrophysics with the Rossi X–ray Timing Explorer*, 49

Coburn, W., Gruber, D. E., Heindl, W. A., Pelling, M. R., Rothschild, R. E., Staubert, R., Kreykenbohm, I., Risse, P., Wilms, J. 1999, "The 1999 Her X−1 Anomalous Low State", *The Fifth Compton Symposium*, edited by M. L. McConnell and J. M. Ryan (AIP Press:New York), **366**, 158

Coburn, W., Heindl, W. A., Gruber, D. E., Rothschild, R. E., Staubert, R., Wilms, J., Kreykenbohm, I., 2000, "Discovery of a Cyclotron Resonant Scattering Feature in the RXTE Spectrum of 4U 0352+309 (X Per)", *ApJ*, **552**, 738

Coburn, W., Heindl, W. A., Gruber, D. E., Rothschild, R. E., Staubert, R., Wilms, J., & Kreykenbohm, I. 2000, "Discovery of a Cyclotron Line in the Spectrum of 4U 0352+309 (X Per)", *American Astronomical Society/High Energy Astrophysics Division*, **32**, 2208

Coburn, W., Heindl, W. A., Gruber, D. E., Rothschild, R. E., Staubert, R., Wilms, J., & Kreykenbohm, I. 2000, "Pulse Phase Resolved Spectroscopy of 4U 1626−67", *American Astronomical Society/High Energy Astrophysics Division*, **32**, 2202

Coburn, W., Heindl, W. A., Wilms, J., Gruber, D. E., Staubert, R., Rothschild, R. E., Postnov, K. A., Shakura, N., Risse, P., Kreykenbohm, I., & Pelling, M. R. 2000, "The 1999 Hercules X−1 Anomalous Low State", *Rossi2000: Astrophysics with the Rossi X–ray Timing Explorer*, 113

Coburn, W., Heindl, W. A., Wilms, J., Gruber, D. E., Staubert, R., Rothschild, R. E., Postnov, K. A., Shakura, N., Risse, P., Kreykenbohm, I., & Pelling, M. R. 2000, "The 1999 Hercules X−1 Anomalous Low State", *ApJ*, **543**, 351

Coburn, W., Rothschild, R., & Heindl, W. A. 2000, "4U 0115+63", *I.A.U. Circular*, **7487**, 1

Coburn, W. 2000, "A Study of the Magnetic Fields of Accreting X–Ray Pulsars with the RXTE", *American Astronomical Society Meeting*, **197**, 112602

Gruber, D. E., Heindl, W. A., Rothschild, R. E., Coburn, W., & Staubert, R. 2000, "RXTE Study of the Cyclotron Resonance Scattering Feature in Her X−1", *Rossi2000: Astrophysics with the Rossi X–ray Timing Explorer*, 52

Gruber, D. E., Heindl, W. A., Rothschild, R. E., Coburn, W., Staubert, R., Kreykenbohm, I., Wilms, J. 2001, "Stability of the Cyclotron Resonance Scattering Feature in Her X−1 with RXTE", submitted to *ApJ*

Gruber, D. E., Matteson, J., Coburn, W., Heindl, W., Pelling, M., Peterson, L. E., Rothschild, R. E., Skelton, T., & Hink, P. 1998, "An All-sky Survey for Tens of keV", *Astronomische Nachrichten*, **319**, 137

Heindl, W. A., Coburn, W., Gruber, D. E., Rothschild, R. E., Kreykenbohm, I., Wilms, J., & Staubert, R. 2001, "Discovery of a Cyclotron Resonance Scattering Feature in the X-ray Spectrum of XTE J1946+274", *ApJL* submitted

Heindl, W. A. & Coburn, W. 1999, "U 0115+63", *I.A.U. Circular*, **7126**, 2

Heindl, W. A., Coburn, W., Gruber, D. E., Pelling, M. R., Rothschild, R. E., Kretschmar, P., Kreykenbohm, I., Pottschmidt, K., Staubert, R., & Wilms, J. 2000, "Multiple Cyclotron Lines in the Spectrum of 4U 0115+63", *American Astronomical Society/High Energy Astrophysics Division*, **32**, 2906

Heindl, W. A., Coburn, W., Gruber, D. E., Pelling, M. R., Rothschild, R. E., Kretschmar, P., Kreykenbohm, I., Pottschmidt, K., Staubert, R., & Wilms, J. 2000, "Cyclotron Line Studies in the Accreting X–ray Pulsars Observed with RXTE", *American Astronomical Society/High Energy Astrophysics Division*, **32**, 2207

Heindl, W. A., Coburn, W., Gruber, D. E., Pelling, M. R., Rothschild, R. E., Wilms, J., Pottschmidt, K., & Staubert, R. 1999, "Discovery of a Third Harmonic Cyclotron Resonance Scattering Feature in the X–Ray Spectrum of 4U 0115+63", *ApJ*, **521**, L49

Heindl, W., Coburn, W., Gruber, D. E., Pelling, M., Rothschild, R. E., Staubert, R., Wilms, J., Pottschmidt, K., Kretschmar, P., & Kreykenbohm, I. 2000, "Cyclotron Lines from Magnetic Neutron Stars", *Rossi2000: Astrophysics with the Rossi X–ray Timing Explorer*, 43

Heindl, W. A., Coburn, W., Gruber, D. E., Pelling, M., Rothschild, R. E., Wilms, J., Pottschmidt, K., Staubert, R. 1999, "Multiple Cyclotron Lines in the Spectrum of 4U 0115+63", *The Fifth Compton Symposium*, edited by M. L. McConnell and J. M. Ryan (AIP Press:New York), **366**, 173

Heindl, W. A., Coburn, W., Gruber, D. E., Pelling, M., Rothschild, R. E., Kretschmar, P., Kreykenbohm, I., Wilms, J., Pottschmidt, K., Staubert, R. 1999, "RXTE Studies of Cyclotron Lines in Accreting Pulsars", *The Fifth Compton Symposium*, edited by M. L. McConnell and J. M. Ryan (AIP Press:New York), **366**, 178

Kreykenbohm, I., Coburn, W., Wilms, J., Kretschmar, P. Staubert, S., Heindl, W. A., Rothschild, R. E. 2001, "Phase-resolved Spectroscopy of Vela X-1", to be submitted to *A&A*

Kreykenbohm, I., Wilms, J., Kretschmar, P., Staubert, R., Heindl, W., Coburn, W., & Rothschild, R. 2000, "Cyclotron Lines in Accreting Pulsars", *Astronomische Gesellschaft Abstract Series*, **17**, 02

Matteson, J., Coburn, W., Heindl, W., MacDonald, D., Pelling, M., Peterson, L., Rothschild, R., Skelton, R., Hink, P., & Crabtree, C. 1996, "Cadmium Zinc Telluride (CZT) Detectors for High Energy X–Ray Astronomy", *American Astronomical Society Meeting*, **189**, 4311

Matteson, J., Coburn, W., Heindl, W., Pelling, M., Peterson, L., Rothschild, R., Hink, P., & Crabtree, C. 1997, "HEXIS High Energy X–Ray All-Sky Survey/Monitor", *American Astronomical Society Meeting*, **190**, 1603

Matteson, J., Coburn, W., Heindl, W., Peterson, L., Pelling, M., Rothschild, R., Skelton, R., Hink, P., & Slavis, K. 1998, "Position-Sensitive CZT Detectors for High Energy X–Ray Astronomy", *American Astronomical Society Meeting*, **192**, 4308

Matteson, J., Coburn, W., Heindl, W., Peterson, L., Pelling, M., Rothschild, R., Skelton, R., Hink, P., Slavis, K., & Crabtree, C. 1997, "Progress with CZT Detectors for High Energy X–Ray Astronomy", *American Astronomical Society Meeting*, **191**, 4816

Matteson, J. L., Coburn, W., Duttweiler, F., Heindl, W. A., Huszar, G. L., Leblanc, P. C., Pelling, M. R., Peterson, L. E., Rothschild, R. E., & Skelton, R. T. 1997, "CdZnTe arrays for astrophysics applications", *SPIE Proceedings*, **3115**, 160

Pelling, M., Matteson, J., Coburn, W., Hink, P., & Crabtree, C. 1997, "Position-Sensitive CZT Detectors for High Energy X–Ray Astronomy", *American Astronomical Society Meeting*, **190**, 1003

Rothschild, R. E., Coburn, W., Gruber, D. E., Heindl, W. A., & Pelling, M. R. 2000, "HEXTE Data Analysis with FTOOLS", *Rossi2000: Astrophysics with the Rossi X–ray Timing Explorer*, 141

FIELDS OF STUDY

Major Field: Physics

Studies in Classical Mechanics
Professor Herbert Levine

Studies in Statistical Mechanics
Professor Daniel Dubin

Studies in Mathematical Methods
Professor Roger Daschun

Studies in Quantum Mechanics and Quantum Field Theory
Professors George Fuller, Marvin Goldberger, and Anesh Manohar

Studies in Electromagnetism
Professor Thomas O'Neil

Studies in General Relativity and Cosmology
Professors George Fuller and Arthur Wolfe

Studies in Astrophysics
Professors George Fuller and Arthur Wolfe

Studies in Kung Fu
Si Fu Steven Shevlin and Shr Fu Michael Patterson

ABSTRACT OF THE DISSERTATION

A Study of Magnetic Fields of Accreting X–Ray Pulsars
With the Rossi X–ray Timing Explorer

by

Wayne Coburn
Doctor of Philosophy in Physics
University of California, San Diego, 2001
Professor Laurence Peterson, Chair

Pulsars are known to be rotating neutron stars that appear to emit regular flashes or radiation. For accretion powered pulsars, the emission is powered by the accretion of material from a normal stellar companion onto the magnetic poles of the neutron star. The conditions in these polar regions, which exhibit extremes in gravitation, temperature, and magnetic field strength, are impossible to recreate in terrestrial laboratories and are possibly unique in nature. Despite two decades of work, no compelling models exist explaining how the infalling material distributes itself across the polar caps, or how the observed X-ray continuum is formed. More fundamentally, these are unanswered questions of how matter acts and reacts in this extreme environment. By studying the X-ray spectra of these sources, we can hope to elucidate some of these questions. Some accreting pulsars exhibit absorption-like X-ray features, or cyclotron lines. The energies of these lines are the only direct measure of the magnetic field of a neutron star, and their detailed line profiles are sensitive to the physical parameters in the formation region.

In this work I have used data from NASA's *Rossi X-ray Timing Explorer* to study the geometry, physical conditions, and dynamical behavior of phenomena in the polar regions of these rotating neutron stars. I present two new cyclotron lines I discovered during the course of the research in the spectra of 4U 0352+309 and XTE J1946+274.

I outline a new method for using cyclotron line shapes as a function of neutron star rotation, along with the temporal structure of the X-ray pulses, to self consistently describe the geometry of the emission regions. This type of analysis is a powerful tool for studying the accretion structures that form at the pulsar magnetic poles. I apply the method qualitatively to three sources, and discuss prospects for future work. I find that the characteristic spectral break energy in X-ray continua is correlated with the magnetic field. This has important implications for theoretical work on the formation of the continuum. I also find two correlations among the line shape parameters, and discuss the possibility that this might imply that accretion seeks to align the dipole and spin axes. Finally, I detail a prescription for finding upper limits on cyclotron lines in accreting pulsar spectra, and apply it to twelve sources.

Chapter 1

Introduction

This dissertation is a study of the behavior of matter and its interactions in conditions of temperature density, gravity and magnetic field unobtainable in the terrestrial environment. The extremes studied here are obtained in the atmospheres at the magnetic polar caps of compact, rapidly rotating neutron stars ($R_{\rm ns} \sim 10\,{\rm km}$) with high ($B \gtrsim 10^{12}\,{\rm G}$) magnetic fields in a binary system accreting material from a stellar companion. The resulting pulsed X-ray emission has been observed with many spacecraft for nearly forty years. In this work I have used data from NASA's *Rossi X-ray Timing Explorer* to study the geometry, physical conditions, and dynamical behavior of phenomena in the polar regions of rotating neutron stars. In particular I have used cyclotron lines, observed in X-rays, to study the production and transport of radiation in these high-field regions.

The physical conditions inferred to exist in astrophysical sources are often far outside the realm of conditions achievable in terrestrial laboratories. The largest magnetic fields obtained in Earth bound experiments, generated using flux-compression techniques and existing for much less than a second, are of order MegaGauss (for a recent review see Bichenkov & Shvetsov 1997). The discovery of radio and X-ray pulsars, neutron stars that emit regular flashes of radiation at their stellar rotation period, revealed that these objects have fields that are a million times larger, of order a few TeraGauss ($\sim 10^{12}$ G). Magnetars (extremely highly magnetized neutron stars), have pushed inferred field strengths into the hundreds, even thousands, of TeraGauss (Duncan & Thompson 1992; Thompson & Duncan 1995, 1996). If magnetars exits, they may possess the strongest fields occurring in nature. These degenerate stars provide laboratories for the study of matter in conditions unobtainable on Earth.

One such laboratory is at the magnetic polar caps of accreting X-ray pulsars. These are neutron stars that exist in binary systems and accrete material from their companion. If the neutron star has a large enough magnetic field ($B \gtrsim 10^{11}$ G), then for realistic mass transfer rates ($\dot{M} \ll 0.2\,\mathrm{M}_{\odot}/\mathrm{yr}$) the energy density in the field will dominate the kinetic energy density of the accreting plasma. In these cases the accreting material is entrained on the neutron star B-field lines and channeled to the magnetic polar caps. As the plasma falls down the gravitational well to the surface of the neutron star, it gains a tremendous amount of kinetic energy; approximately 200 MeV/nucleon or nearly 30 times larger than what is released in 4H $\rightarrow$ He nuclear fusion. At the surface of the neutron star, "hot spots" form at the magnetic poles which emit primarily non-thermal X-rays. If the magnetic and spin axes are misaligned, then the observed X-ray emission will be modulated at the rotation period of the neutron star; hence the name "pulsar." This emission is in general beamed as well, thus enhancing the modulation (see §4.1). While radio and optical observations give insights to conditions out at many neutron star radii, the polar regions of accreting X-ray pulsars, and therefore the behavior of matter under extremes of temperature, gravity, and magnetism, can be investigated directly by observing the emitted X-rays. To date (2001 April) approximately 76 accreting X-ray pulsars have been discovered (see Tables 1.1 and 1.2, compiled from Liu, van Paradijs & van den Heuvel 2000; Bildsten et al. 1997).

Some of these accreting X-ray pulsars exhibit X-ray absorption lines, or "cyclotron lines," due to the magnetic field in the neutron star polar regions. These lines are similar to the absorption lines seen in optical spectra. Cyclotron lines, however, arise due to scattering and absorption by electrons with energies quantized by the magnetic

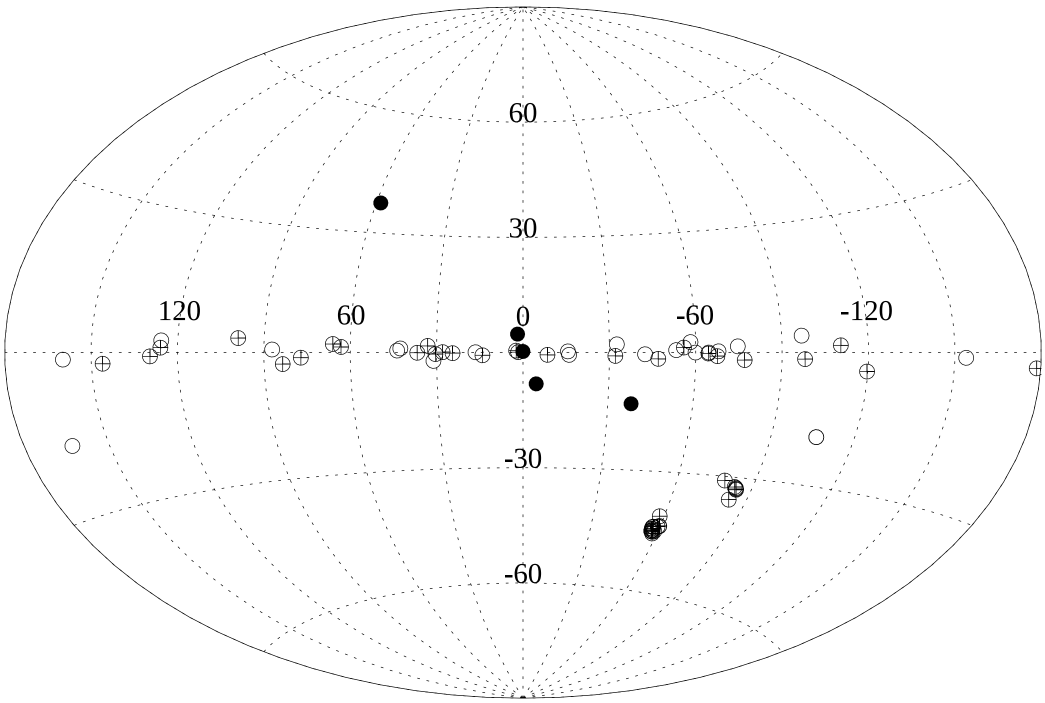

Figure 1.1: The distribution of accreting X-ray pulsars, plotted in Galactic coordinates. Most of the known X-ray pulsars are concentrated in the Galactic plane or the Magellanic clouds (the two clusters of sources south-west of the Galactic center). Low-mass systems are shown as solid circles, while persistent high-mass systems are open circles. Transient sources are indicated with a cross inside a circle.

field of the pulsar. Cyclotron lines, named after the cyclotron resonances that are the source of the quantization, are the only direct way to measure the B-field of a neutron star.

One of the fundamental questions concerning accreting neutron stars is how does matter act in, and distribute itself across, the polar region of the pulsar. More fundamentally this is a question of how matter acts and reacts under extremes of gravitation, temperature, and magnetic field. This question is a difficult one to solve, involving parameters for which there are few direct observational hooks. Cyclotron lines and their profiles, however, do contain information about the physical parameters in the emission region. The bulk of this work is devoted to the study of these spectral features, and what they can tell us about the polar emission regions of neutron stars.

Accreting X-ray pulsars are categorized in several ways. First they are split into low-mass and high-mass systems based upon the mass of the companion. This distinction has implications on how much and how efficiently material is transferred from the companion to the neutron star. All but 6 accreting X-ray pulsars are categorized as high-mass systems. A second distinction, and one that has important implications for when these sources can be studied, is between those pulsars which exhibit persistent X-ray emission and those which spend most of their time in quiescence and emit X-rays only in transient outbursts. These are classified as persistent and transient pulsars respectively. The list of known accreting X-ray pulsars (as of 2001 April, compiled from Bildsten et al. 1997, Liu, van Paradijs & van den Heuvel 2000, and Haberl & Sasaki 2000) is given in Tables 1.1 and 1.2. These sources are concentrated primarily in the plane of our Galaxy and in the Magellanic Clouds, their Galactic distribution is shown in Fig 1.1.

In this chapter I review accreting X-ray pulsars, and their context within the larger zoo of Galactic compact objects. After a brief litany of X-ray satellites, I introduce some of the general properties of neutron stars. I then briefly describe the low-mass and high-mass classifications of X-ray binaries, along with some properties of the two classes. I follow this with a discussion of the various types of pulsars, along with a detailed description of accreting X-ray pulsars. I end the chapter with the theoretical framework for two methods by which the magnetic fields of accreting pulsars can be measured; directly using cyclotron lines and indirectly via accretion torque theory. I also discuss how the profiles of cyclotron lines can be used to infer more about the conditions at the neutron star poles than just the strength of the B-field.

In Chapter 2 I discuss how the data for this work was obtained and analyzed, including details of the *RXTE*. Chapter 3 details a class study of the pulse average spectral properties of 10 sources where cyclotron lines have been observed with the *RXTE*. In Chapter 4 I refine this analysis by resolving the spectra of 3 sources as a function of rotation phase, and infer information about the geometric properties of these pulsars. I also further test the results of the class study in Chapter 3. I report on the discovery of cyclotron lines spectra of 4U 0352+309 (X Per, Chapter 5) and XTE J1946+274 (Chapter 6). Chapter 5 has appeared in the Astrophysical Journal (Coburn et al. 2001), and Chapter 6 has been submitted to ApJ Letters. In Chapter 7 I detail a prescription for determining upper limits on the presence of cyclotron lines in X-ray spectra, and the results of this analysis for 12 sources. Chapter 8 concludes this work and outlines some prospects for the future.

Table 1.1: Low-Mass and Persistent High-Mass Accreting Pulsars (as of 2001 April)

System	$l(^\circ)$	$b(^\circ)$	$P_{\rm spin}$ (s)	$P_{\rm orb}$ (d)	System	$l(^\circ)$	$b(^\circ)$	$P_{\rm spin}$ (s)	$P_{\rm orb}$ (d)
				Low-Mass Systems					
SAX J1808.4−3658[a]	355.39	−8.15	0.0025	0.837	Her X−1	58.20	37.50	1.238	1.70
GRO J1744−28[a]	0.04	0.28	0.467	11.76	4U 1626−67	321.80	−13.10	7.66	0.029
2A 1822−371	356.85	−11.29	0.593	0.23	GX 1+4	1.90	4.80	120.	–
				Persistent High-Mass Giant and Supergiant Systems					
SAX J0635.2+0533	206.1	−1.0	0.0338	–	1E 1145.1−6141	295.50	−0.00	297.	–
SMC X−1	300.40	−43.60	0.717	3.89	AX J0051−73.3	303.00	−43.86	323.2	–
Cen X−3	292.10	0.30	4.82	2.09	RX J0103.2−7209	301.6	−44.9	345.2	–
AX J0049−732	303.1	−43.9	9.13	–	SAX J2103.5+4545	87.1	0.71	358.61	12.68
RX J0648.1−4419	253.7	−19.1	13.18	1.55	XTE J1855−026	31.1	−2.15	361.	6.1
LMC X−4	276.30	−32.50	13.5	1.41	SAX J1452.8−5949	317.6	−0.44	437.4	–
OAO 1657−415	344.40	0.30	37.7	10.4	4U 1907+09	43.70	0.50	440.4	8.38
XTE J1906+09	42.6	1.04	89.17	–	4U 1538−52	327.40	2.10	528.8	3.73
AX J1820.5−1434	16.5	0.07	152.26	–	GX 301−2	300.10	0.00	681	41.5
SAX J1324.4−6200	306.8	0.61	170.84	–	AX J1700.1−4157	344.0	−0.6	714.5	–
1H 1238−599	301.8	2.6	191.	–	4U 0352+309	163.10	−17.10	837.7	250.3
RX J0440.9+4431	159.8	−1.3	202.5	–	RX J1037.5−5647	285.4	1.5	862.	–
AX J0058−72.0	302.22	−45.07	280.4	–	A0114+650	125.71	2.56	10008.	11.6
Vela X−1	263.10	3.90	283.2	8.96					

a Transient System

Table 1.2: Transient High-Mass Accreting Pulsars (as of 2001 April)

System	$l(^\circ)$	$b(^\circ)$	$P_{\rm spin}$ (s)	$P_{\rm orb}$ (d)
A0535−668	276.88	−32.30	0.069	16.7
RX J0059.2−7138	302.1	−45.5	2.76	–
RX J0105.1−7211	301.90	−41.10	3.34	–
4U 0115+63	125.92	1.03	3.61	24.3
RX J0502.9−6626	277.00	−35.40	4.06	–
V0332+53	146.05	−2.19	4.37	34.25
GRO J1750−27	2.37	0.50	4.45	29.8
2E 0050.1−7247	302.62	−44.37	8.9	–
2S 1553−542	327.94	−0.86	9.26	30.6
GS 0834−430	262.02	−1.51	12.3	111.64
EXO 053109−6609.2	276.06	−32.71	13.7	25.4
RX J0052.1−7319	302.80	−43.80	15.3	–
XTE J1946+274	63.20	1.38	15.8	80
4U 1417−624	313.02	−1.60	17.6	42.12
KS 1947+300	66.09	2.10	18.76	–
RX J0117.6−7330	300.40	−43.50	22.07	–
GS 1843+009	33.10	1.70	29.5	–
XTE J0111.2−7317	301.00	−43.70	31.03	–
RX J0812.4−3114	249.60	1.60	31.89	80
EXO 2030+375	77.15	−1.24	41.8	46
1WGA J0053.8−7226	302.67	−44.68	46.63	139
XTE J0055−724	302.56	−44.68	58.97	65
Cep X−4	99.01	3.31	66.2	–
RX J0529.8−6556	275.90	−32.90	69.5	–
AX J0049−729	303.18	−44.28	74.675	–
GS 1839−04	27.90	0.10	81.1	–
AX J0051−722	302.99	−44.90	91.12	120
GRO J1008−57	283.00	−1.82	93.4	135
GS 1843−024	30.40	−0.40	94.8	241
SAX J0544.1−710	281.63	−31.00	96.079	–
SAX J1818.6−1703	14.08	−0.71	100.	–
3A 0726−260	240.30	−4.10	103.2	34.5
A0535+26	181.45	−2.64	110.	110.58
Sct X−1	24.46	−0.16	111.	–
XTE J0054−720	302.59	−45.06	169.3	–
GRO J2058+42	83.50	−2.75	198.	110
AX J1749.2−2725	1.7	0.1	220.38	–
XTE J1958+034	36.73	−0.06	221.	–
GX 304−1	304.10	1.25	272.	133
4U 1145−619	295.61	−0.24	292.	187.5
A1118−615	292.50	−0.89	405.	–
EXO 1722−363	351.5	−0.6	413.	–
RX J0146.9+6121	129.54	−0.80	1455.	–

1.1 X-ray Observatories

Unlike the study of the heavens at optical wavelengths, X-ray astronomy is still a very young discipline. It was on 1962 June 18 that the second ASE-MIT experiment was launched on a USAF Aerobee 150 rocket and became the first experiment to detect cosmic X-rays. Initially intended to look for X-rays from the moon, it instead discovered both the first discrete extra-solar X-ray source Sco X$-$1, as well as the diffuse cosmic X-ray background. Since then there have been thousands of X-ray sources discovered by numerous balloon and satellite instruments. For example, the *UHURU* satellite, launched on 1970 December 12, cataloged 339 sources (known as the 4U catalog, Forman et al. 1978). The *High Energy Astrophysical Observatory*–1 (*HEAO*–1) satellite, launched on 1977 August 12, surveyed the X-ray sky almost three times in the $0.2 - 10^4$ keV energy band (Wood et al. 1984; Nugent et al. 1983; Levine et al. 1984). The *Röntgen Satellite* (*ROSAT*) satellite, launched on 1990 June 1, conducted a soft X-ray survey (0.1–2.4 keV) and cataloged over 120 thousand sources (Voges et al. 1999, 2000).

These, however, are just a few. Other X-ray observatories include the Japanese *Tenma*, *Ginga*, and *Advanced Satellite for Cosmology and Astrophysics* (*ASCA*), the *European X-ray Observatory Satellite* (*EXOSAT*), the Russian *Granat* satellite, and the American *Einstein Observatory* and *Compton Gamma-Ray Observatory* (*CGRO*), and the list goes on. Current, or soon to be launched, missions include the *Chandra X-ray Observatory* (*CXO*), the *X-ray Multi-Mirror Mission* (*XMM-Newton*), *Beppo*SAX (the *Satellite per Astronomia X*, named for Giuseppe "Beppo" Occhialini), the *International Gamma-Ray Astrophysics Laboratory* (*INTEGRAL*), and the *Rossi X-ray Timing Explorer* (*RXTE*) which is the source of data for this dissertation.

1.2 Neutron Stars

The possibility of a neutron star was first suggested by Baade & Zwicky (1934), shortly after the discovery of the neutron by Chadwick (1932). However, it was not until the 1960's and the discovery of radio (Hewish et al. 1968) and X-ray pulsars (Giacconi et al. 1971a) that their existence was observationally confirmed. Now it is thought, based upon extrapolating pulsar birthrates (Narayan & Ostriker 1990) and from the number of supernovae required to account for the abundances of heavy elements (Arnett, Schramm & Truran 1989), that the Galaxy is populated by about $10^8 - 10^9$ neutron stars.

A neutron star is formed during a type II (core collapse) supernova of a massive star. During normal stellar evolution, stars burn the nuclear fuel at their cores, releasing energy and heating the interior. The pressure generated by this heat balances the gravitational collapse of the star, keeping the star stable. As hydrogen in the interior is burned into heavier and heavier elements, less and less energy is released and more and more non-burning nuclei ("ashes") accumulate in the stellar core. These ashes inhibit burning, and as the core grows it is eventually supported against collapse not by pressure generated through nuclear fusion, but instead by electron degeneracy pressure. If the star is of a low enough mass ($M_* \lesssim (3-6)\,\mathrm{M}_\odot$, Arnett 1979) then eventually all that will be left is the degenerate core, which is observed as a white dwarf. Although white dwarfs are compact objects, for the remainder of this chapter I will only consider neutron stars and black holes, and in the rest of this work only neutron stars.

If the star is massive enough ($M_* \gtrsim (5-8)\,\mathrm{M}_\odot$, Arnett 1979) the white dwarf core will continue to grow until it reaches the $1.4\,\mathrm{M}_\odot$ Chandrasekhar mass limit. At this point electron degeneracy pressure is no longer adequate to support the star, and the core will experience a sudden and catastrophic collapse. As the density increases, protons will capture electrons through reverse β-decays and be converted into neutrons. When the density in the core reaches $10^{14} - 10^{15}\,\mathrm{gm\,cm^{-3}}$, neutron degeneracy pressure is enough support the interior against further gravitational collapse. The infall suddenly stops and a neutron star forms. The sudden formation of a solid surface, along with the release of $\sim 10^{53}$ ergs of energy (primarily as neutrinos) during the collapse, is the trigger for the supernova explosion. This explosion violently removes the outer star, leaving behind a $\sim 1.4\,\mathrm{M}_\odot$ neutron star. If the star is too massive, however, then neutron degeneracy pressure will be insufficient to stop the gravitational collapse. In these instances gravity will dominate, and as the core of the star shrinks inside its Schwartzschild radius a black hole is formed.

This $1.4\,\mathrm{M}_\odot$ mass for neutron stars is not just theoretical, however. Giacconi et al. (1971a), with observations obtained with the *UHURU* satellite, reported the detection of regular 4.8 s X-ray pulsations from the source Cen X−3, making it the first X-ray pulsar ever discovered. The pulsations were eventually interpreted as due to the the rotation of a mass-accreting magnetized neutron star. Additionally, X-rays from Cen X−3 disappeared every 2.1 d, and the pulse period showed a regular 2.1 d Doppler modulation. These were interpreted as due to the orbital motion of an eclipsing binary system. The binary nature of Cen X−3 was later confirmed with the optical identification of an O-type companion star (Krzemiński 1974). Using the derived orbital ephemeris and an estimate of the companion mass, the mass of the neutron star estimated to be $1.4\,M_\odot$ (Avni & Bahcall 1974, 1975). Timing observations of ~12 X-ray pulsars have indicated neutron star masses in the $1–2\,M_\odot$ range, with a typical value being the $1.4\,M_\odot$ Chandrasekhar mass (Joss & Rappaport 1976; Rappaport & Joss 1983).

In addition to these constraints on neutron star masses, the discovery of Type-I X-ray bursts helped constrain neutron star sizes (There are also Type-II bursts, which are thought to be caused by spasmodic accretion onto the neutron star; however, I will not discuss them here). Type-I X-ray bursts are due to thermonuclear flashes on the surface of a neutron star without a strong magnetic field ($< 10^{12}$ G, Lamb & Lamb 1978). The nearly black-body shape of the observed burst spectra, along with the assumption that the luminosity is near the Eddington limit ($\sim 10^{38}\,\mathrm{ergs\,s^{-1}}$), allows the estimation of the neutron star surface area. These observations indicate that typical neutron star radii are ~10 km. For comparison, the Schwartzschild radius of a $1.4\,M_\odot$black hole is only 4.2 km. Throughout this work I will assume a canonical neutron star mass and radius of $1.4\,M_\odot$ and 10 km respectively.

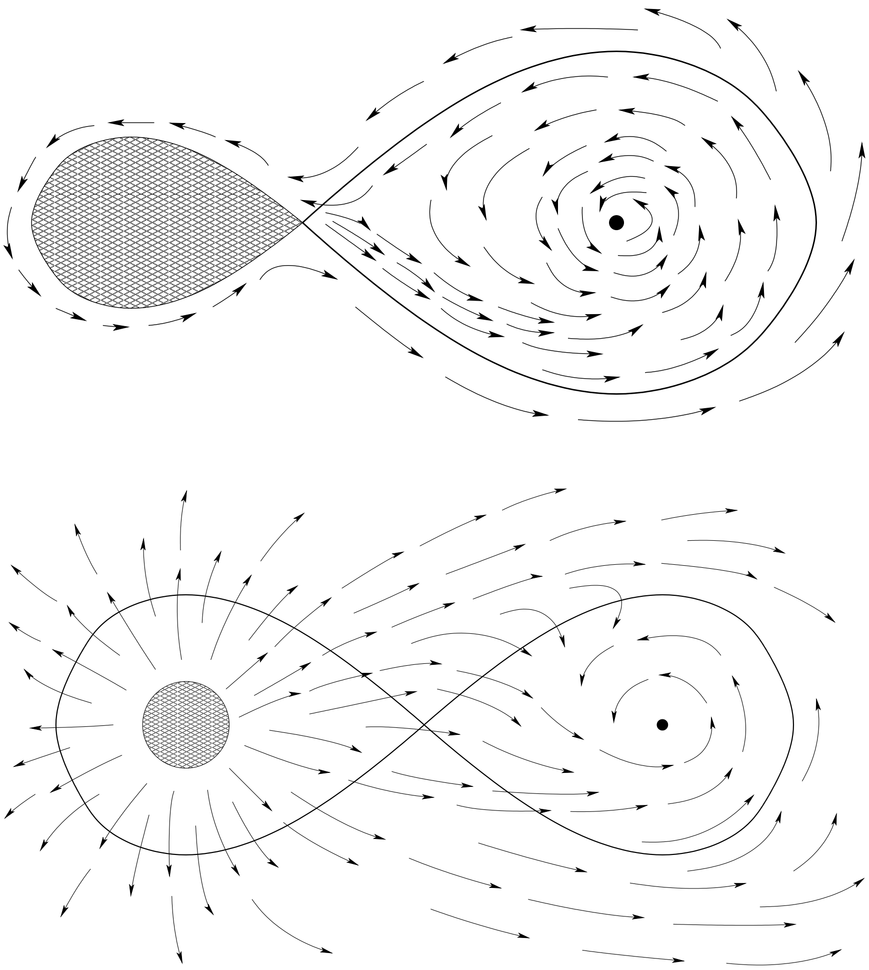

Figure 1.2: Two scenarios for accretion of material onto a compact object. In both cases the companion star is shown on the left, while the compact object is on the right. Top: A normal companion fills its Roche-Lobe, and the outflow proceeds mainly thorough the first Lagrangian point. Bottom: Material is transferred to the compact object through the strong stellar wind of the companion. After Shakura & Sunyaev (1973), Figure 1.

1.3 X-ray Binaries

Although for some accreting X-ray pulsars the exact companion star remains unidentified, all (with the possible exception of AXPs, see §1.4.2) belong to binary systems. As their name implies, X-ray binaries (XRBs) are stellar binary systems that exhibit X-ray emission. They contain a compact object (either a white dwarf, neutron star, or black hole) along with a "normal" (non-compact) companion star. Known companions range from low-mass dwarfs to high-mass supergiants. XRBs constitute the brightest class of X-ray sources in the sky, and have been a major focus of X-ray astronomy since its inception. For neutron stars, the X-ray luminosity is derived from the accretion of material from the companion star onto the surface of the compact object. This accretion proceeds either through Roche-lobe overflow or via a strong stellar wind. As mentioned above, XRBs are broken into two main subcategories based on the mass of their companion star; Low-Mass X-ray Binaries (LMXBs) and High-Mass X-ray Binaries (HMXBs). These sources exhibit a wide variety of phenomena, from quasi-periodic oscillations to X-ray outbursts.

There are several main factors that determine the emission properties of the accreting compact object. First is the nature of the object itself. In the case of a black hole, with its lack of a solid surface, the X-ray emission region is a hot plasma that surrounds the black hole (either as a corona or one of several types of accretion disks). For a neutron star X-ray emission is seen from near the star's solid surface. The second factor in the character of the X-ray emission is, if the compact object is a neutron star, the strength and geometry of its magnetic field. The magnetic field affects where accretion onto the surface occurs and how material spreads across the surface of the star. The third factor is the geometry of the accretion flow around the compact object, and whether it is spherical, forms a disk, or is some hybrid of the two.

If the compact object is in a close binary with the companion star, then accretion can occur via Roche-lobe overflow (see Fig. 1.2, top panel). This occurs when the envelope of the companion extends beyond the inner Lagrangian point of the system, and so material literally falls from the companion to the compact object. As the material spirals inward angular momentum is conserved, preventing the material from being directly accreted. Instead, the material goes into quasi-Keplerian orbits around the compact object and an accretion disk is formed. In the accretion disk viscous forces transfer angular momentum outward in the disk as material moves inward and eventually onto the compact object (Shakura & Sunyaev 1973). This is the common form of accretion for low-mass systems, where the envelope of the companion has expanded as it evolved away from the the main sequence.

In high-mass systems, those with OB or OBe stars, the winds of the companion can be quite dense, removing between $10^{-10} - 10^{-6}\,\mathrm{M}_{\odot}\,\mathrm{yr}^{-1}$ and reaching terminal velocities up to $\sim 1000\,\mathrm{km\,s^{-1}}$. A compact object in a close orbit will capture a significant fraction of the wind, both through quasi-spherical and disk accretion (see Fig 1.2, bottom panel). Roche-lobe overflow can also supplement the mass transfer rate, although it will become unstable $\sim 10^5\,\mathrm{yr}$ after it starts (Savonije 1983, and references therein). Quasi-Roche-lobe overflow may also occur as the envelope of the supergiant approaches the inner Lagrangian point. There the reduced gravity can cause focusing of the wind towards the compact object (Friend & Castor 1982).

Whether or not a neutron star has a disk has important implications for its spin history as well. Assuming that all of the angular momentum of the accreted material is transferred to the neutron star, then the star will experience a "spin-up" torque (Pringle & Rees 1972; Rappaport & Joss 1977) which results in the decrease of the neutron star spin period P_{spin}. Even if the angular momentum axes of the neutron star and accretion disk are initially misaligned, the torque exerted on the star by the disk will quickly cause such an alignment (Ghosh & Lamb 1979). For a detailed discussion of spin-up (and spin-down) torques, see §1.5.2.

1.3.1 Low-Mass X-ray Binaries

By far the most common of X-ray binaries, LMXBs consist of either a neutron star or a black hole with a low-mass ($\lesssim 2.5\,\mathrm{M_\odot}$) star. The lower luminosity systems ($10^{36} - 10^{37}\,\mathrm{ergs\,s^{-1}}$) typically have orbital periods of $\lesssim 15\,\mathrm{hr}$ and are primarily Type-I X-ray burst sources. The orbital period distribution of the high luminosity systems ($\sim 10^{38}\,\mathrm{ergs\,s^{-1}}$) is still largely unknown as many are located in the optically obscured Galactic bulge region. The X-ray emission is due to accretion onto the compact object via Roche-lobe overflow from an evolved giant companion. Because of this the systems are thought to be, in general, much older than their high-mass counterparts. Examples of this class are Sco X$-$1, 4U 1626$-$67, and GRO J1944$-$28.

Most neutron star LMXBs do not exhibit coherent pulsations. As mentioned above, the magnetic fields of accreting X-ray pulsars disrupt the normal accretion flow, channeling the material to the stellar polar regions. In nearly all known LMXBs the magnetic fields of the compact object are too weak ($\lesssim 10^9\,\mathrm{G}$) for this to occur. Instead the disk extends down to nearly the star's surface and material is accreted equatorially.

Despite the lack of coherent pulsations, many LMXBs do exhibit irregular intensity variations on time scales from fractions of a second to hours. These variations are almost, but not quite, periodic in nature and therefore are called Quasi-Periodic Oscillations (QPOs). The study of these timing signatures, especially kHz QPOs since they arise from very near the compact object and are therefore sensitive to general relativistic effects, is an active field of research.

1.3.2 High-Mass X-ray Binaries

High-Mass X-ray Binaries (HMXBs) are systems consisting of a compact object and a massive ($\gtrsim 6\,\mathrm{M}_\odot$), early type companion star. Most known accreting X-ray pulsars belong to this class of objects (see Tables 1.1 and 1.2).

Since the companion star tends to be in one of two categories, the convention is to further divide this class into two subgroups. Supergiant X-ray binaries (SG/X-ray binaries) are those in which the companion is either an O or B type giant or supergiant star, and in general these are sources of persistent X-ray emission. Systems where the companion is an Oe or Be star (O or B stars with strong emission lines) are termed Be/X-ray binaries. Since these systems exhibit outbursts between long periods of quiescence, they are are also referred to as Be-Transients. The primary source of mass accretion in both these subgroups, and therefore the observed X-ray emission, is from the companion's strong stellar wind. Accretion onto the compact object itself can occur either through a disk or directly from the wind. Due to the relatively short lifespan of the supergiant companions, these are younger systems.

The persistent HMXBs (SG/X-ray binaries) are systems where the compact object is embedded deep inside the companion's highly supersonic wind. The orbital periods of these systems typically range from a few hours to days. Given the large masses of the companion stars, this translates to orbital radii that are few times that of the companion. Given the close proximity of the two stars, the orbital eccentricity of these systems is typically quite low ($e \lesssim 0.1$) and many show evidence for eclipses in their light curves. The mass accretion rates onto the compact object are typically in the $10^{-10} - 10^{-8}\,\mathrm{M}_\odot\,\mathrm{yr}^{-1}$. Their X-ray spectra often exhibit low-energy absorption and strong fluorescent Fe-K lines, which indicate that the entire binary system is immersed in relatively dense, cool matter (i.e. a stellar wind or common stellar envelope). Examples of these systems are LMC X−4, Cen X−3, and Vela X−1.

The majority of known HMXBs (and also accreting X-ray pulsars) are the Be-Transient systems. Be stars are a rapidly rotating and exhibit variable excretion disks in their rotational equatorial planes that are the source of the bright optical emission lines. Most of these binaries have wide orbits ($P_{\rm orb} \gtrsim 20\,{\rm d}$) with moderate to large eccentricities ($e \gtrsim 0.3$). Because of this the compact object spends most if the time far away from their companion, and X-ray eclipses are almost never seen. Outbursts from these sources are generally associated with periastron passage and passage of the neutron star through the Be-star excretion disk. Although outbursts are not necessarily seen during every orbit, and can also occur at other orbital phases as well. Examples of Be-Transient systems are A 0535+26 and 4U 0115+63.

Some Be/X-ray binaries are not transient, but instead emit persistent low-level (10^{33}−10^{35} ergs s^{-1}) X-ray emission. The prototypical source in this class 4U 0352+309 (X Per, see Chapter 5).

1.4 Pulsars

Today there are two broad categories of pulsars, those that are powered by the rotational energy of the neutron star, and those that emit because of accretion from a nearby companion. While the results of my dissertation are based upon studies of accretion powered pulsars (see §1.4.3), I also discuss very briefly their rotation powered cousins (see §1.4.1) as well as the new class of anomalous X-ray pulsars (see §1.4.2), whose exact nature is still of some debate.

The first pulsar was discovered at in 1967 (Hewish et al. 1968) by a Cambridge University graduate student Jocelyn Bell (now Jocelyn Bell Burnell) working with her advisor Anthony Hewish. The group, lead by Hewish, had designed and built a telescope to study the scintillation of radio signals from quasars as they propagated through the solar wind. Studying the thousands of feet of chart recorder paper produced by their receivers, Bell noticed an unusual periodic signal that recurred on several nights. Follow-up observations showed that the signal was a series of short pulses with a 1.337 s period. The extreme regularity of the pulsations was puzzling, and while the name "pulsar" was ultimately applied, the signal was initially (and only half jokingly) termed LGM for "little green men." It was quickly realized, however, that the pulsations were the result of a naturally occurring, rapidly spinning object. The significance of the discovery was highlighted by the award of the Nobel Prize to Hewish in 1974.

The existence of neutron stars was first predicted decades before by Baade & Zwicky (1934) and Oppenheimer & Volkoff (1939). Baade & Zwicky (1934), Colgate & White (1966), and others had already suggested that such objects could be produced in supernova explosions. It was even predicted that they would be rapidly rotating (Hoyle, Narlikar & Wheeler 1964; Tsuruta & Cameron 1965) with strong magnetic fields (Woltjer 1964; Hoyle, Narlikar & Wheeler 1964), and that the Crab nebular might be powered by such a rotating star (Wheeler 1966). Indeed, even a simple model for the conversion of rotational energy into electromagnetic radiation through the acceleration of particles in a dipolar field was in print before the discovery (Pacini 1967). So the discovery of Hewish et al. (1968) was certainly not in a theoretical vacuum.

Still, the identification of pulsars with neutron stars rather than white dwarfs was not immediately obvious. The first argument that these new pulsars were neutron stars with 10^{12} G magnetic fields was put forward by Gold (1968). It was not until the discovery of the Crab and Vela pulsars (Large, Vaughan & Wielebinski 1968; Staelin & Reifenstei 1968; Comella et al. 1969), whose spin periods were too rapid to be a stable white dwarf, that the neutron star hypothesis became widely accepted.

1.4.1 Rotation Powered Pulsars

There are over 700 known rotation powered pulsars (Taylor, Manchester & Lyne 1993)[1]. They are also often referred to as "radio pulsars" since the bulk of these sources emit principally in the radio. They are distributed primarily within the Galactic bulge and along the Galactic plane, and most are isolated rather than in binary systems. These pulsars are powered through the loss of rotational energy into electromagnetic radiation through Magnetic Dipole Radiation (MDR, see Manchester

1 also http://pulsar.princeton.edu/

& Taylor 1977; Shapiro & Teukolsky 1983; Mészáros 1992, and references therein). The combination of rapid rotation and a high magnetic field induces a strong electric field near the surface of the neutron star. This accelerates charged particles, primarily from the magnetic poles, away from the star and along the magnetic field lines. As the neutron star rotates, the magnetic field accelerates these charged particles, creating non-thermal beamed radiation. If the magnetic and spin axes are misaligned, then pulses are seen at the neutron star spin period.

This conversion of rotational energy into electromagnetic radiation creates a persistent spin-down torque on the star. Since the MDR luminosity scales as $L_{\rm MDR} \propto B^2 P^{-4}$, as the pulsar ages the spin-down causes the rotation period to increase and therefore the luminosity to decrease. The observed spin-down rate can be converted into a rotational energy loss rate $L_{\rm rot} = -I\dot{P}_{\rm spin}P_{\rm spin}^{-3}$, where $I \sim 10^{45}\,{\rm g\,cm^3}$ is the neutron star moment of inertia. Equating $L_{\rm rot}$ with $L_{\rm MDR}$ one finds (Manchester & Taylor 1977):

$$B = \left(\frac{3Ic^3 P_{\rm spin}\dot{P}_{\rm spin}}{8\pi^2 R_{\rm ns}^6}\right)^{1/2} \approx 3.2 \times 10^{19}\sqrt{P_{\rm spin}\dot{P}_{\rm spin}}\,{\rm G} \tag{1.1}$$

which estimates radio pulsar magnetic fields to be in the $10^{11} - 10^{13}\,{\rm G}$ range. Figure 1.3 shows the distribution of radio pulsar magnetic fields, along with the cyclotron energies (see §1.5.1) implied by those fields.

Millisecond Pulsars

There is a subclass of radio pulsars, all with rotation periods of $< 0.1\,{\rm s}$, known as millisecond radio pulsars. These sources have very low spin-down rates, indicating that their magnetic fields are quite small; in the $10^8 - 10^{10}\,{\rm G}$ range. They are also preferentially found in the Galactic bulge region and in globular clusters, among the oldest populations of stars in our Galaxy. Another characteristic of these objects is that about a third of them are found in binary systems, whereas ordinary radio pulsars are largely isolated objects. For a review of these objects and their connection to LMXBs see Bhattacharya (1995).

The popular interpretation of this data is that millisecond pulsars are "recycled" LMXB systems (van den Heuvel 1991; van den Heuvel & Rappaport 1992). In this

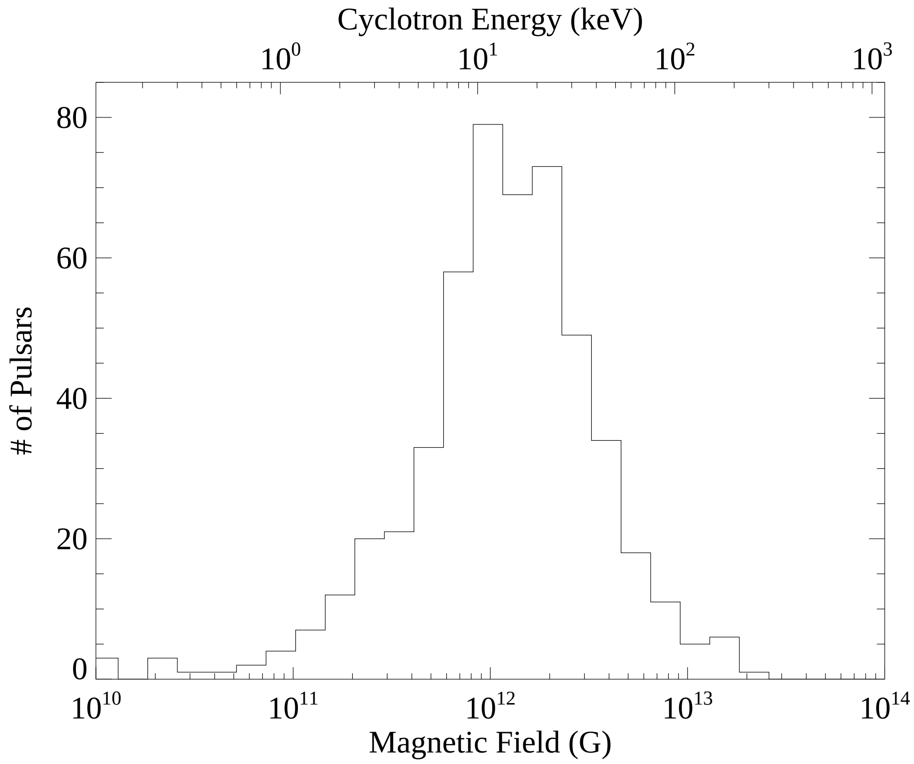

Figure 1.3: Distribution of the 706 objects in the Princeton Radio Pulsar Catalog (Taylor, Manchester & Lyne 1993, also http://pulsar.princeton.edu/). Along the bottom axis is the inferred magnetic field, assuming $B = 3.2 \times 10^{19} (P_{\rm spin} \dot{P}_{\rm spin})^{1/2}$ Gauss. Plotted across the top is the cyclotron resonance energy at that magnetic field (before correcting for the gravitational redshift of the neutron star). If accreting pulsars have a magnetic field distribution similar to that of the radio pulsars, then most cyclotron-lines would observed in the *RXTE* 2–250 keV range.

scenario, these are very old objects (age $> 10^9$ yr) where the neutron star underwent an extended period of mass accretion. As mentioned briefly in §1.3, steady mass transfer from a disk will result in a decrease of the neutron star spin period. For a star with a 10^8 G magnetic field accreting at the Eddington limit, the period will reach a few milliseconds in $\sim 10^7$ yr. Eventually the mass transfer stops (causing the X-ray emission to cease), and the neutron star begins to emit millisecond pulsations in the radio. The recent discovery of the millisecond X-ray pulsar SAX J1808.4$-$3658 (Wijnands & van der Klis 1998) in a 2 h orbit with a low-mass companion (Chakrabarty & Morgan 1998) seems to confirm this scenario, providing a "missing link" between LMXBs and millisecond radio pulsars.

1.4.2 Anomalous X-ray Pulsars

Recently a new class of X-ray pulsars with clearly different properties has been recognized (Mereghetti & Stella 1995; van Paradijs, Taam & van den Heuvel 1995). Anomalous X-ray Pulsars (AXPs) are named such because their rotational energy loss (implied by their $P_{\rm spin}$ and $\dot{P}_{\rm spin}$) is insufficient to power their observed luminosities, and at the same time they do not seem to have a companion. They have been linked to the Soft γ−ray Repeater (SGR) phenomenon, as AXPs and SGRs in quiescence is very similar. The main difference is the recurrent detection of soft γ−ray bursts from SGRs.

As a class, both AXPs and SGRs have a number of very perplexing similarities. Their periods tend to cluster in the 6–8 s range, and are monotonically increasing with timescales in the $t \sim 10^4 - 4 \times 10^5$ yr. Yet the rotational energy loss implied by $P_{\rm spin}$ and $\dot{P}_{\rm spin}$ is not sufficient to power their observed $L_{\rm x} \sim 10^{34} - 10^{36}\,{\rm ergs\,s^{-1}}$ luminosities. The X-ray spectra of AXPs and SGRs in quiescence are quite different than accreting pulsars, being much softer in comparison. For a recent review of their properties see (Mereghetti 1999).

This has lead to the hypothesis that AXPs are actually extremely highly magnetized ($B \sim 10^{14} - 10^{16}$ G) neutron stars, or "magnetars" (Duncan & Thompson 1992; Thompson & Duncan 1995, 1996). Indeed, assuming that the emission is purely magnetic dipole radiation implies magnetic fields in the $B \sim 10^{14} - 10^{15}$ G range. Not all observed SGR phenomena can be explained with invoking super-high magnetic fields, however (see Marsden 1999, and references therein). An alternative model is that AXPs are powered by a relic, or residual accretion disk (Corbet et al. 1995; van Paradijs, Taam & van den Heuvel 1995; Ghosh, Angelini & White 1997; Chatterjee & Hernquist 2000). This disk might have formed from material that fell back after the supernovae explosion, or possibly has been swept up from the interstellar medium.

1.4.3 Accreting X-ray Pulsars

Discovery of orbitally modulated, periodic X-ray pulsations from Centaurus X−3 (Giacconi et al. 1971a; Schreier et al. 1972) and Hercules X−1 (Tananbaum et al. 1972) with *UHURU* quickly lead to the understanding of X-ray pulsars as rotating, highly magnetized ($B \sim 10^{12}\,$G) neutron stars accreting material from a binary companion (Pringle & Rees 1972; Davidson & Ostriker 1973; Lamb, Pethick & Pines 1973). For reviews of their properties see White, Swank & Holt (1983), Nagase (1989), and Bildsten et al. (1997). For the remainder of this work, unless otherwise specified the term pulsar will apply to an accreting X-ray pulsar.

Of the known X-ray pulsars (see Tables 1.1 & 1.2), all but 6 are classified as HMXBs, with a significant fraction being transient sources associated with Be star companions. Like other X-ray binaries (see §1.3), X-ray pulsars capture material from their companion star, either from its stellar wind or through Roche-lobe overflow (see Fig. 1.2). As mentioned above, the accreting plasma gains approximately 200 MeV/nucleon of kinetic energy while falling down the gravitational well of the neutron star. Since a neutron star (unlike a black hole) has a solid surface, this energy is radiated away and the resulting accretion luminosity is:

$$L_{\rm acc} = \frac{G M_{\rm ns} \dot{M}}{R_{\rm ns}} \tag{1.2}$$

where $M_{\rm ns}$ and $R_{\rm ns}$ are the neutron star mass and radius respectively, and $\dot{M}$ the instantaneous mass accretion rate. The luminosities of these sources can vary over many orders of magnitude, especially during transient outbursts, and fall in the $L_{\rm x} \sim 10^{34} - 10^{39}\,{\rm ergs\,s^{-1}}$ range. The observed range of pulsation periods spans 7 orders of magnitude, from 2.5 ms in SAX J1808.4−3658 to 2.8 h for A0114+650.

In the simplest picture, as material approaches the neutron star, either in the accretion disk or captured from a stellar wind, it becomes entrained on the strong magnetic field. This occurs at the magnetospheric radius $r_{\rm m}$, which is a scaled Alfvén radius $r_{\rm m} = (0.52 - 1) \times r_{\rm A}$. The Alfvén radius is found by equating the fluid stresses of the material in the disk with the magnetic stresses:

$$r_{\rm A} \simeq 6.8 \times 10^8\,{\rm cm} \left(\frac{\mu}{10^{30}\,{\rm G\,cm^3}}\right)^{4/7} \left(\frac{\dot{M}}{10^{-10}\,{\rm M_\odot\,yr^{-1}}}\right)^{-2/7} \left(\frac{M_{\rm ns}}{1.4\,{\rm M_\odot}}\right)^{-1/7} \tag{1.3}$$

where μ is the neutron star magnetic moment and $\dot{M}$ is the mass accretion rate. For more details on accretion onto highly magnetized neutron stars see §1.5.2. Inside the magnetospheric radius the magnetic stresses dominate, and the ionized plasma entrained on the field lines is channeled onto the magnetic poles. As mentioned above,

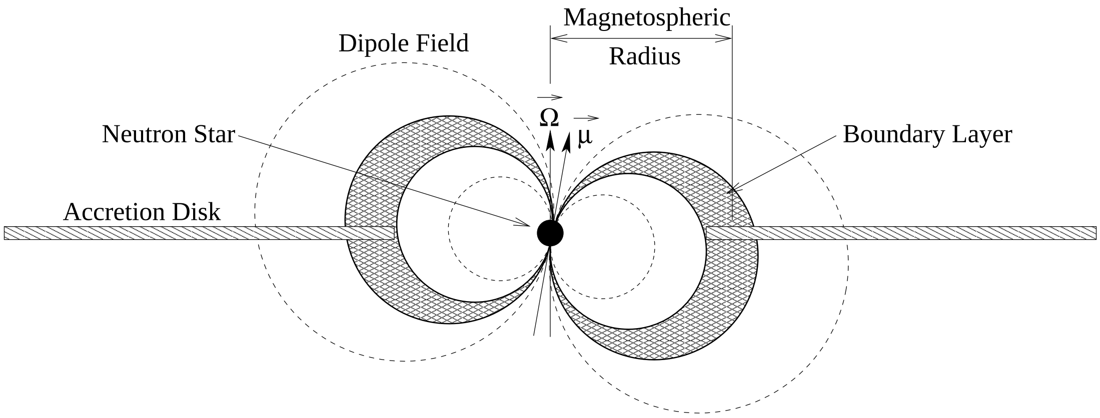

Figure 1.4: Side view of the accretion flow around a neutron star with an accretion disk. The magnetic field of the pulsar disrupts the disk at the magnetospheric radius, channeling plasma through the boundary layer to the neutron star magnetic poles (see text for a full discussion, after Ghosh & Lamb (1979), Fig. 1). Although not shown, the magnetic field is expected to be deformed away from a purely dipolar configuration by plasma in the disk at radii larger than the magnetospheric radius.

this creates two hot spots on the neutron star surface which are the primary source of X-ray emission. If the magnetic and spin axes are offset, then as the star rotates the X-ray emission will be modulated at the spin period and pulsations seen by a distant observer. In general the X-ray emission is also beamed, enhancing the modulation (see §4.1). Simple blackbody estimates of the emission region give polar cap areas that are typically $A_{\rm cap} \sim 1 \mathrm{km}^2$.

What happens at the magnetospheric radius depends on how the material is accreted. In the case of pure wind accretion, the flow is quasi-spherical Bondi-Hoyle accretion (Bondi & Hoyle 1944; Davidson & Ostriker 1973) beyond the magnetospheric radius while inside the behavior of matter is governed by the magnetic field. For accretion from a disk, which can form from either a stellar wind or Roche-lobe overflow, the picture is much more complex (Ghosh & Lamb 1979). The magnetic field is strong enough to disrupt the inner edge of the accretion disk, sweeping up material and funneling it to the poles. A diagram of this is given in Fig. 1.4. The detailed physics by which the material at the magnetosphere loses its orbital angular momentum, becomes entrained on the field lines, and makes its way to the polar caps is thought to involve magnetohydrodynamic (MHD) versions of Rayleigh-Taylor and Kelvin-Helmholtzs instabilities (Lamb, Pethick & Pines 1973; Arons & Lea 1976,

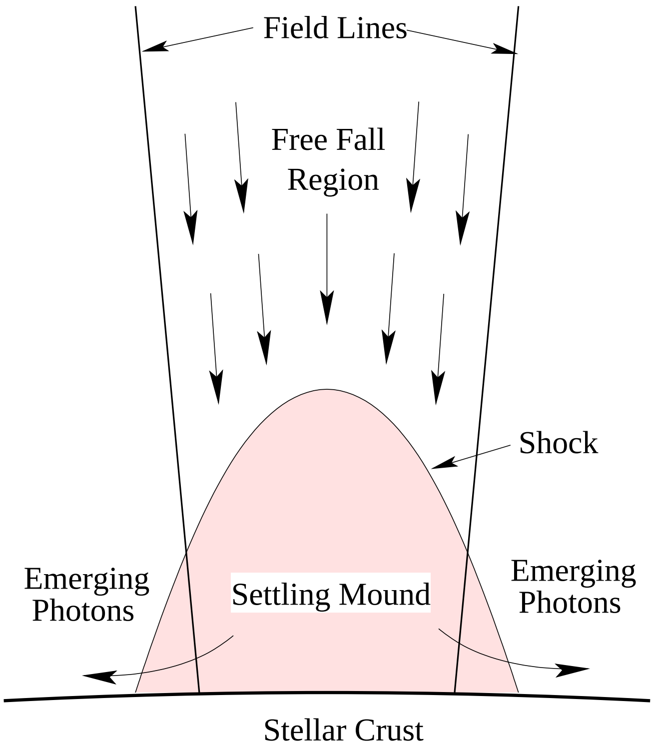

Figure 1.5: Diagram of the accretion flow near the surface of the neutron star, showing the infalling material, standing shock, settling mound, and emergent radiation. From Burnard, Arons & Klein (1991).

1980; Elsner & Lamb 1977).

The free-fall velocities for material approaching the neutron star surface are not only highly supersonic, but of order $v_{\rm ff} \gtrsim 0.1c$. At high accretion rates ($L_{\rm x} \gtrsim 10^{36}\,{\rm ergs\,s^{-1}}$) the infalling material is halted *above* the surface, in a standing shock maintained by radiation pressure from below (Davidson 1973; Burnard, Arons & Klein 1991). In the simplest case, where the accretion is uniform across the polar cap, the postshock emission region assumes a simple mound structure (see Fig. 1.5). This accretion structure, which is dynamic in nature as material both accumulates from above and spreads out at the base, is expected to be inhomogeneous in both temperature and density. The steady state shape of the emission region will depend on the details of the accretion into the polar cap as well as the magnetic field configuration. The temporal structure of pulses seen at the Earth will depend not only on how the emission from the accretion mound is beamed, but also on the relative locations of the hot spots on the surface and the viewing geometry as well. These effects are discussed in detail in §4.1.

In the low luminosity case ($L_x \lesssim 10^{36}\,\mathrm{ergs\,s^{-1}}$) a radiative shock will be unable to form. It is unclear, however, whether the infalling material will be decelerated by multiple Coulomb collisions inside the atmosphere or whether collective effects may give rise to a collisionless shock above the surface (Lamb, Pethick & Pines 1973; Zel'dovich & Shakura 1969). The low-luminosity source 4U 0352+309 is discussed in detail in Chapter 5.

The hard X-ray spectra of X-ray pulsars are typically non-thermal, and are known to vary considerably with rotation phase (White, Swank & Holt 1983). Below a characteristic cutoff energy ($E_{\mathrm{cut}} \sim 20\,\mathrm{keV}$) the sources exhibit a fairly hard power law, with a photon index in the $\Gamma \sim 0.8 - 1.5$ range. Above the cutoff the spectrum rolls over exponentially (see §2.2.4). Despite over two decades of work on the subject, there still exists no compelling theoretical model for the X-ray spectral shape of accreting X-ray pulsars, and therefore observers are forced to use phenomenological spectra in the fitting process.

1.5 Magnetic Fields of Neutron Stars

Neutron stars have long been argued to possess surface magnetic fields of order $10^{12}\,\mathrm{G}$ on grounds of magnetic flux conservation during the gravitational collapse of supernovae cores (Woltjer 1964; Hoyle, Narlikar & Wheeler 1964; Pacini 1967). At these field strengths, which are a million times larger than what can be produced here on Earth (Bichenkov & Shvetsov 1997), the characteristic electron cyclotron resonance energy of the field is of order 10% of the electron rest mass, implying that relativistic effects are becoming important. Also, under these conditions electron motion transverse to the magnetic filed is quantized. The surface of a neutron star itself is at the bottom of a deep gravitational well, with a gravitational acceleration 2×10^{11} that felt at the surface of the Earth. The combination of relativistic particle energies and quantizing magnetic fields requires a quantum electrodynamic (QED) description of the physical processes, and provides a physical laboratory unlike any other.

One of the first steps to probing these laboratories is to accurately measure the average magnetic field, and eventually the magnetic field distribution, in the neutron star polar regions. Depending on the source, there are several methods for obtaining measurements of the B-field. For rotation powered pulsars, which are assumed to be emitting due to MDR, the magnetic fields are *inferred* from observations of the period $P_{\rm spin}$ and period-derivative $\dot{P}_{\rm spin}$. These estimates give dipole fields in the $10^{11} - 10^{13}$ G range ($10^{8} - 10^{10}$ G for millisecond pulsars). See §1.4.1 for more information on rotation powered pulsars.

For systems powered by accretion there are currently two methods for determining the magnetic field strength. First, it can be estimated using accretion torque theory from the observed spin period $P_{\rm spin}$ and the mass accretion rate inferred from the measured flux (Ghosh & Lamb 1979). For a detailed description of accretion torques see §1.5.2. The second method is through the measurement of hard X-ray spectral lines, or cyclotron lines, which are discussed next.

1.5.1 Cyclotron Resonance Scattering Features

The only direct evidence for neutron star magnetic field strengths is provided by X-ray cyclotron "absorption lines." Although these quasi-harmonic lines appear in absorption, they are not absorption lines in the true sense. Instead, photons with energies near the cyclotron energy are scattered by electrons in the emission region (see Fig. 1.5) out of the observer's line of sight. This gives rise to absorption line features in the X-ray spectrum, with the centroid of the line at the cyclotron energy. The cyclotron energy is set by the magnetic field strength, and for most neutron star surface fields is in the hard X-ray band (see Fig. 1.3).

Classically, electrons moving in a uniform magnetic field are free to move along the fields lines, while motion transverse to the field is constrained to circular motion. The net result is a helical motion, with the radius of the circular component (the gyration radius) given by

$$r_{\rm gy} = \frac{cp_\perp}{eB} \tag{1.4}$$

where $p_\perp$ is the electron momentum perpendicular to the field and B the magnetic field strength. The radius $r_{\rm gy}$ decreases with increasing B, until eventually it is of order the de Broglie wavelength ($\lambda = \hbar/p$) of the electron and quantum mechanical effects dominate. Once this is the case, the transverse motion of the electron is quantized into Landau levels. In the non-relativistic limit the n^{th} Landau level is given by

$$E_n = (n' + \frac{1}{2} + s)E_{\rm c}, \quad n' = 0, 1, 2, \ldots \tag{1.5}$$

where $s = \pm 1/2$ is the electron spin and $E_{\rm c}$ the cyclotron energy. The non-relativistic cyclotron resonance energy, in terms of the magnetic field B and for $n' = 0$ and $s = -1/2$ is:

$$E_{\rm c} = \frac{\hbar e}{m_{\rm e} c} B \tag{1.6}$$

Or equivalently, scaled by a 10^{12} G field and given in units of keV, is

$$E_{\rm c} \simeq 11.6 \frac{B}{10^{12}{\rm G}} \,{\rm keV} \tag{1.7}$$

In Eq. 1.5, the $(n' + 1/2 + s)$ term will always result in an integer, allowing the equation to be simplified. Therefore the harmonically spaced Landau levels are given by:

$$E_n = nE_{\rm c}, \quad n = 0, 1, 2, \ldots \tag{1.8}$$

The scattering process proceeds when a resonant photon is absorbed by an electron in the $n = 0$ ground state which is then excited to an $n \geq 1$ Landau level (depending on whether the photon is at a single or higher multiple of the cyclotron energy). In plasmas that are cool compared to the cyclotron energy, the lifetime of electrons above the $n = 0$ ground state is very short. The radiative cyclotron de-excitation rate is given by (Latal 1986):

$$\nu_{\rm r} = \left(\frac{\alpha m_{\rm e} c^2}{\hbar}\right) \left(\frac{B}{B_{\rm QED}}\right)^{\beta} \tag{1.9}$$

where $\alpha = e^2/(4\pi\hbar c)$ is the fine structure constant, $B_{\rm QED} = (m_{\rm e}^2 c^3)/(\hbar e) \simeq 4.4 \times 10^{13}$ G the QED quantum field scale, and $\beta = 2$ for $B < B_{\rm QED}$ (or $\beta = 0.5$ if $B < B_{\rm QED}$). For the pulsars discussed in this work $\nu_{\rm r} \sim 2 \times 10^{15} (B/10^{12}\,{\rm G})^2\,{\rm s}^{-1}$, so an excited electron immediately returns to the ground state by emitting a resonant photon. This prompt return to the ground state is why, at least for the $n = 1$ to $n = 0$

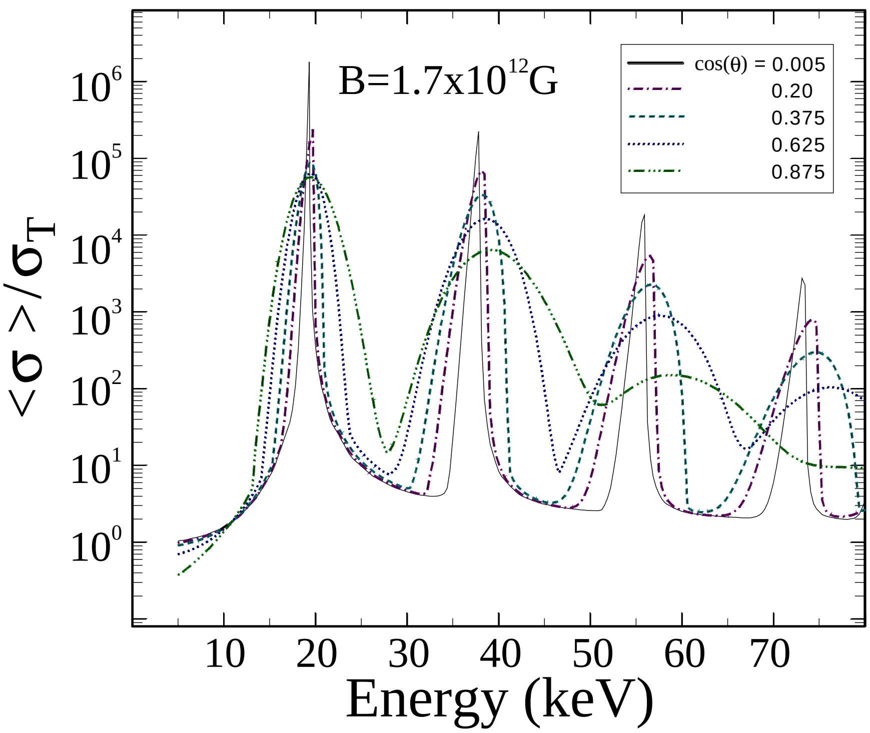

Figure 1.6: Cyclotron scattering cross sections (in terms of the Thomson cross section σ_{T}) for a $B = 1.7 \times 10^{12}$ G field. The angle θ is defined as the angle between the magnetic field and photon propagation direction. The tallest, narrowest profile corresponds to $\cos(\theta) = 0.005$, where the photons travel nearly perpendicular to the field. As the propagation angle decreases, the cross sections become broader and shallower due to thermal motions ($kT_{\mathrm{e}} = E_{\mathrm{c}}/4$) of the electrons along the field lines. (after Araya & Harding 1999, Fig. 2)

transition, the process is scattering rather than true absorption. Because of this, and the fact that few cyclotron line sources exhibit any features beyond the fundamental, these lines are known as Cyclotron Resonance Scattering Features (CRSFs). This is the nomenclature I will use in the rest of this work.

For higher ($n > 1$) harmonics the decay process is slightly more complex. While the electron still may decay directly back down the the ground state, it can also cascade down through the Landau levels, producing n photons each with energy E_{c} keV. This is process is known as "photon spawning," and is the decay channel preferred in $B < B_{\mathrm{QED}}$ fields. So while higher harmonics are both absorption and scattering features, I will (as is customary in the literature) refer to them as CRSFs as well. Due to the prompt decay from all Landau levels, most of the electrons in the scattering region are in the $n = 0$ ground state with aligned spin ($s = -1/2$).

Since the radius of the neutron star is only a few (2–3) Schwartzschild radii, general relativistic effects are also important in the emission region. In particular, the CRSF feature will be redshifted by the neutron star gravitational field such that the *observed* energy, as indicated by a scattering feature in an X-ray spectrum, is less than the true energy. The correction term is given by:

$$E_{\mathrm{c}}^{obs} = E_{\mathrm{c}}(1+z)^{-1} \tag{1.10}$$

where,

$$(1+z)^{-1} = \left(1 - \frac{2GM_{\mathrm{ns}}}{R_{\mathrm{ns}}c^2}\right)^{\frac{1}{2}} \tag{1.11}$$

and z is the gravitational redshift. Assuming a canonical neutron star, then $(1+z)^{-1} \simeq 0.76$.

As the cyclotron energy becomes comparable to the electron rest mass, or alternatively as the B-field approaches B_{QED}, relativistic affects start to become important. In this regime the cyclotron resonance energy is given by (Harding & Daugherty 1991):

$$E_{\mathrm{c}} = m_{\mathrm{e}}c^2 \frac{[1 + 2n(B/B_{\mathrm{QED}})\sin^2(\theta)]^{1/2} - 1}{\sin^2(\theta)} \tag{1.12}$$

where θ is the angle of the incident photon to the magnetic field. This equation reduces to Eq. 1.6 in the $B \ll B_{\mathrm{QED}}$ limit. The dependence on θ, however, leads to slightly non-harmonic line spacing in the relativistic case which is unlike the classical limit. Since these energies depend nontrivially on the photon's propagation angle with respect to the field, the emergent spectral features are influenced heavily by the spatial distribution of electrons (the plasma "geometry") and the orientation of the magnetic field inside the scattering region. Araya & Harding (1999) calculated the relativistic, magnetic Compton-scattering cross sections as a function of angle, the results of which for a $B = 1.7 \times 10^{12}$ G field are plotted in Fig. 1.6. The general behavior, regardless of magnetic field strength, is that the cross sections become narrower and peak higher with increasing θ. This is primarily due to thermal broadening of the lines by the electrons ($kT_{\mathrm{e}} = E_{\mathrm{c}}/4$ in the simulations), which are free to move along the B-field lines.

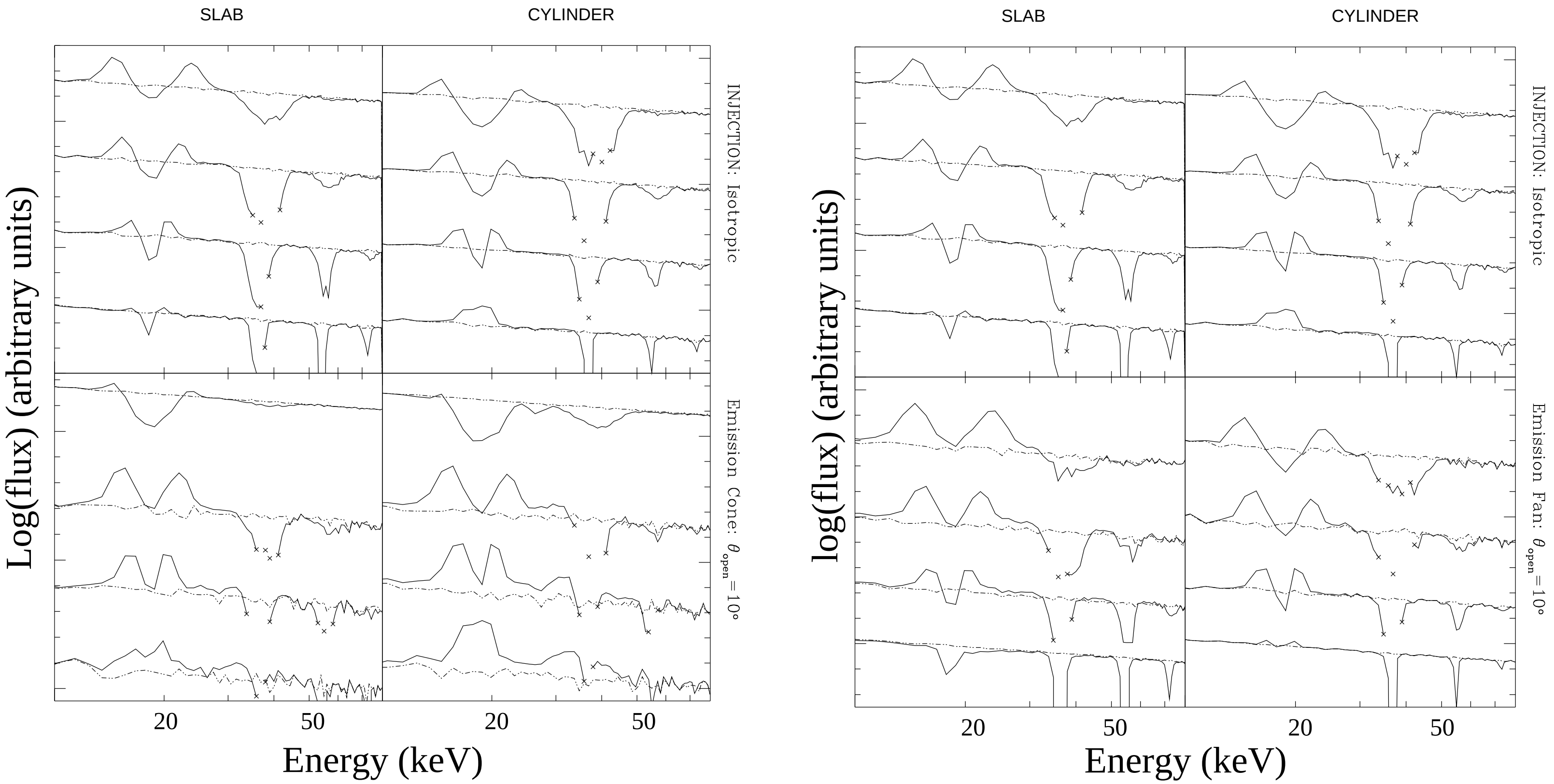

Figure 1.7: Monte Carlo simulations of CRSF formation with the field strength of B=1.7×10^{12} G, (after Araya-Góchez & Harding (2000), Figures 1 and 3). The injected, $\Gamma = 1$ continuum is shown as dotted lines, while the resulting scattered output as a solid line. Each panel shows angle-dependent model photon spectra assuming isotropic (top) and non-isotropic (bottom) injection into slab (left) and cylindrical (right) geometries. The left pane, bottom panel, has the spectrum injected along the B-field in a cone pattern. The right pane, bottom panel is for a fan-beam injection perpendicular to the field. In each quadrant, the top curve is for $\cos(\theta) > 0.75$ where θ is defined as the viewing angle to the magnetic field, followed by $0.5 < \cos(\theta) < 0.75$, $0.25 < \cos(\theta) < 0.5$, and $\cos(\theta) < 0.25$ on the bottom.

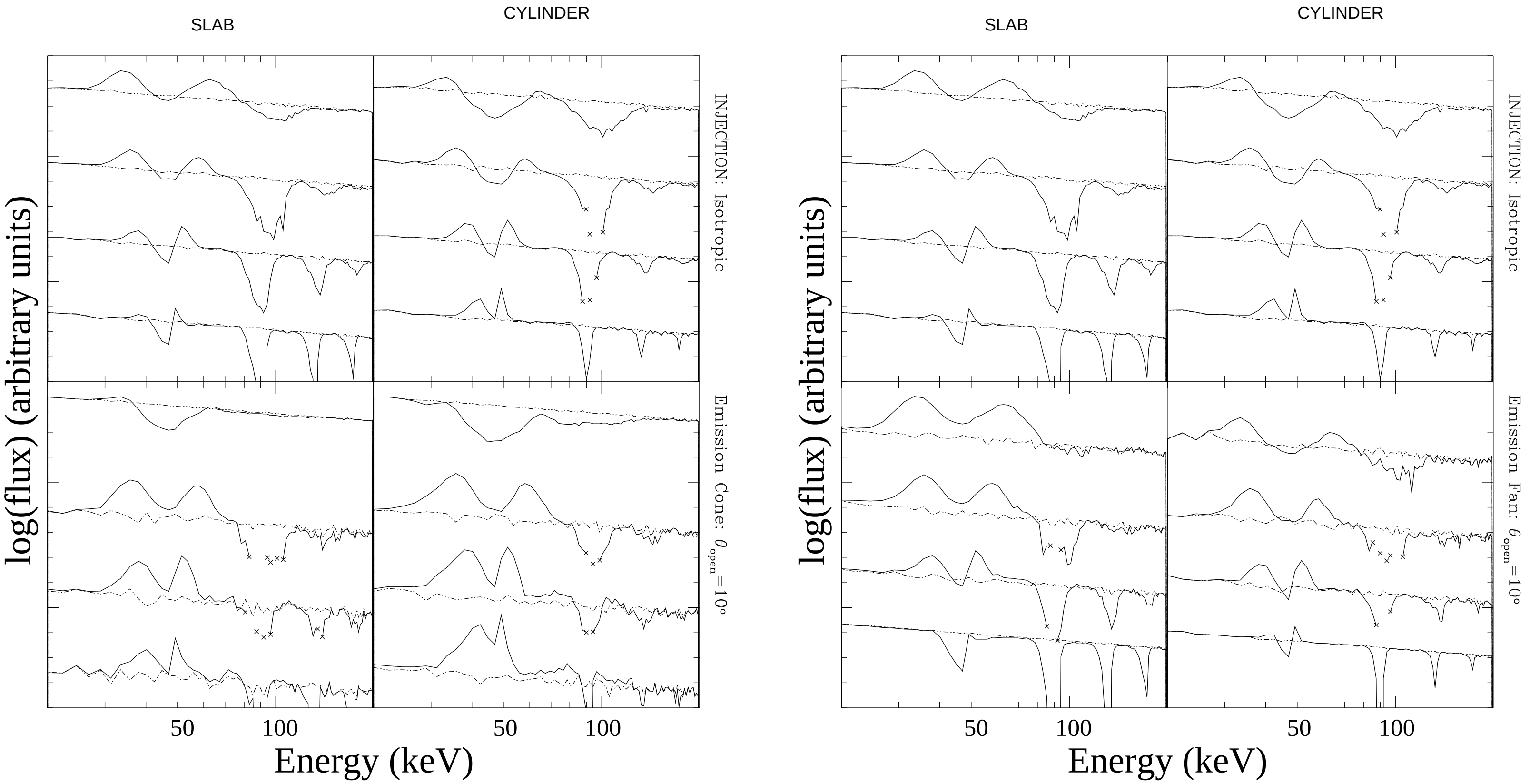

Figure 1.8: These curves plotted here are the same as in Fig. 1.7, only for a B-field strength of B$=4.4\times10^{12}$ G. (after Araya-Góchez & Harding (2000), Figures 5 and 7)

These cross sections have been used in Monte Carlo simulations to predict CRSF line shapes (Araya & Harding 1999; Araya-Góchez & Harding 2000, e.g. Figs. 1.7 and 1.8). These simulations also include a detailed consideration of Landau-Raman scattering (including photon spawning), and with various injection and scattering geometries. The authors found that the fundamental feature can have a very complex shape, with red and/or blue emission "wings," and in some cases can even appear completely in emission. These complex shapes are primarily due to two effects. The first is photon spawning, as discussed above. These new photons will enhance the wings of the fundamental feature, and can even fill it in entirely. Therefore, under some conditions it is expected that the fundamental feature will be shallow and difficult to detect with the first harmonic is very prominent in the spectrum. Second, due to the angular dependence of the cross sections illustrated in Fig. 1.6, scattered photons are not redistributed isotropically with respect to angle and energy.

The Monte Carlo simulations illustrated in Figs. 1.7 and 1.8 (Araya & Harding 1999; Araya-Góchez & Harding 2000) were done assuming a very hard continuum spectrum ($\Gamma = 1$ and no spectral break) and are better suited to γ−ray bursts (e.g. GB 880205, Fenimore et al. 1988) than accreting pulsars. This shape is quite different than the standard pulsar continuum (see §2.2.4), and is an especially poor assumption for pulsars since observed CRSFs lie in the exponentially falling region of the spectrum. This continuum was chosen by the authors, however, because it does offer a distinct advantage over a softer spectral shape. Since there are more photons at higher energies, the effects of photon spawning, geometry, and relativistic angular redistribution on the fundamental cyclotron feature are greatly enhanced. It is therefore easier to identify and study these effects in the theoretically produced spectra. This means that the line profiles observed in accreting X-ray pulsars will be less exaggerated than those illustrated in Figs. 1.7 and 1.8.

Still, CRSF line profiles, with their strong dependence on viewing geometry and physical parameters such as density and electron temperature, provide a powerful diagnostic tool for the conditions in the emission region. By comparing observed CRSFs with the results of Monte Carlo simulations, some of the physical conditions in the emission regions of accreting X-ray pulsars can be inferred. This is a valuable first step to fully understanding the dominant physical processes in these magnetic polar regions. A qualitative analysis illustrating this technique is given in Chapter 4.

1.5.2 Theory of Accretion Torques

In addition to measurements of CRSFs, magnetic fields of accreting X-ray pulsars can be estimated using accretion torque theory (Ghosh & Lamb 1979). As mentioned previously, in systems with accretion disks the inner edge of the disk is truncated by the magnetic field at the magnetospheric radius $r_{\mathrm{m}} = \xi r_{\mathrm{A}}$. The Alfvén radius r_{A} is given by:

$$r_{\mathrm{A}} = \left(\frac{\mu^4}{2GM_{\mathrm{ns}}\dot{M}^2}\right)^{1/7} \tag{1.13}$$

(see also Eq. 1.3) and is a characteristic length found by equating the fluid stresses of the material in the disk at a mass transfer rate $\dot{M}$, with the magnetic stresses for a neutron star with magnetic moment μ. For the pulsars under consideration here, the Alfvén radius is typically $10^8 - 10^9$ cm. Estimates of the model-dependent dimensionless parameter ξ, which essentially represents the ability of the accreting material to "pinch" in the magnetic field in the plane of the disk, range from $\xi = 0.52$ (Ghosh & Lamb 1979) to $\xi \approx 1$ (Arons 1993; Ostriker & Shu 1995; Wang 1996). Therefore there is an uncertainty in these calculations of at least a factor of 2 to the appropriate power, and agreement between CRSF and accretion torque measurements within a factor of a few can be considered relatively good.

Assuming that the magnetic field lines at the magnetospheric boundary transfer all of the angular momentum to the star (Pringle & Rees 1972; Rappaport & Joss 1977), then the pulsar will experience the spin-up torque

$$N \approx \dot{M}\sqrt{GM_{\mathrm{ns}}r_{\mathrm{m}}} \tag{1.14}$$

For accretion directly from a stellar wind, Eq. 1.14 gives an upper limit on the torque. Accretion will be inhibited by a centrifugal barrier if the magnetosphere rotates faster than the Kepler frequency at the inner edge of the disk, so for accretion to occur the magnetospheric radius must therefore lie inside the corotation radius. The corotation radius, where the Keplerian orbital period equals the neutron star rotation period, is given by:

$$r_{\mathrm{co}} = \left(\frac{GM_{\mathrm{ns}}P_{\mathrm{spin}}^2}{4\pi^2}\right)^{1/3} \tag{1.15}$$

with $P_{\rm spin}$ being the spin period of the neutron star. If this is true then there is a characteristic torque:

$$N_0 \equiv \dot{M}\sqrt{GM_{\rm ns}r_{\rm co}} \tag{1.16}$$

which is a convenient scale as it depends only on the observable spin period of the pulsar and the inferred mass accretion rate. A pulsar experiencing the torque given in Eq. 1.16 will spin-up at a rate $\dot{\nu} = N/(2\pi I)$, where $I \simeq 0.4 M_{\rm ns} R_{\rm ns}^2$ is the neutron star moment of inertia (Ravenhall & Pethick 1994). For typical pulsar spins and mass accretion rates, this gives a spin-up timescale $t_{\rm spin-up} \equiv \nu/\dot{\nu}$ of order 2×10^5 yr, much shorter than the observed ages of most X-ray binaries (Elsner, Ghosh & Lamb 1980). Therefore, in this picture neutron stars with accretion disks will spin-up until the spin frequency matches the Kepler frequency at the magnetosphere ($r_{\rm m} \approx r_{\rm co}$).

Conversely, in systems where $r_{\rm m} > r_{\rm co}$, a strong spin-down torque will be exerted as the field lines at the magnetosphere fling material out of the accretion disk. This "propeller effect" (Illarionov & Sunyaev 1975) acts to spin the neutron star down to the equilibrium period. However, for material to transfer angular momentum out of the system it cannot be accreted by the neutron star. Even if small amounts of material does "leak" in and get accreted, neutron stars undergoing the propeller effect will not be luminous X-ray sources. Therefore, since spin-down is observed in systems with accretion disks, other mechanisms have been proposed (see below).

The combination of spin-up through accretion and spin-down via the propeller effect leads to $p_{\rm spin,eq}$ being a stable equilibrium spin period. Indeed, some of the observed persistent disc accreting pulsars seem to be spinning near this period (for an example see §4.4.2).

Assuming that the star is spinning in equilibrium, the magnetic moment of the neutron star can be estimated simply based upon the mass accretion rate $\dot{M}$ inferred from the luminosity, and the directly observable spin period. The proportionally goes as

$$\mu \propto \xi^{-7/4} M_{\rm ns}^{5/6} P_{\rm spin}^{7/6} \langle \dot{M} \rangle^{1/2} \tag{1.17}$$

where $\langle \dot{M} \rangle$ is the long term time averaged mass accretion rate. This can be quite different than the observed instantaneous rate, or even the average rate over the past few decades. Just as with the parameter ξ, this uncertainty means that agreement within a factor of a few in magnetic field measurements between CRSFs and accretion torque theory can be considered good.

Conversion of the dipole moment μ to a surface magnetic field B is simple. For a purely dipolar field, the dipole moment is given by $\mu = 0.5\,B\,R^3$, where B and R are the neutron star polar magnetic field and radius respectively (Shapiro & Teukolsky 1983; Jackson 1975).

This picture of accretion torques provides a good explanation of spin-up. A number of X-ray pulsars, however, are seen to be either spinning down or experiencing erratic episodes of both spin-up and spin-down. In these cases, Ghosh & Lamb (1979) argue that for stars spinning very near equilibrium, additional *negative* torques can act if magnetic field lines thread the disk beyond the corotation radius (where the disk is spinning slower than the neutron star). Then, in the rest frame of the neutron star, the magnetic field lines are swept backward, transporting angular momentum from the star to the disk and allowing for both accretion and spin-down. Other models to explain pulsar spin-down involve MHD outflows (Anzer & Boerner 1980; Arons et al. 1984; Lovelace, Romanova & Bisnovatyi-Kogan 1995), where a pulsar wind moves outward along field lines like beads on a wire, gaining angular momentum and spinning the star down.

With the launch of the Burst And Transient Source Experiment (BATSE) experiment on the *CGRO*, detailed spin histories of many accreting pulsars became available, revealing several problems with the standard model of accretion torques (see Bildsten et al. 1997, and references therein). First, after decades of steady spin-up the pulsars 4U 1626$-$67 and GX 1+4 were observed to change to steady spin-down (Chakrabarty et al. 1997; Makishima et al. 1988). It was surprising that the new torque was nearly equal in magnitude to the initial torque, but opposite in sign. Additionally, Cen X$-$3 and OAO 1657$-$415 show similar torque reversals, only on time scales of weeks instead of decades (Chakrabarty et al. 1993). The change in sign without a significant change in magnitude is difficult to explain within the standard framework of accretion torque theory, although it may be an indication that the disk itself oscillates between prograde and retrograde rotation (Nelson et al. 1997).

While the equilibrium period derived from accretion torque theory depends on the average accretion rate, instantaneous torques during transient outbursts should result in spin period changes. Since the magnetospheric radius $r_{\rm m} \propto \dot{M}^{-2/7}$ for $r_{\rm m} < r_{\rm co}$, this implies that the pulsar should spin up at a rate $\dot{\nu} \propto \dot{M}^{6/7}$. This gives a predicted correlation between the torque and the bolometric luminosity. Fortunately, outbursts in GRO J1744−28 and A0535+262 showed enough dynamic range that the relation between torque and observed luminosity could be tested directly (Finger, Wilson & Chakrabarty 1996; Finger et al. 1996). The observed data using $\dot{\nu} \propto F^{\gamma}_{obs}$, however, are not well fit with a $\gamma = 6/7$ power law. Instead the values of γ are near unity, with $\gamma = 0.951 \pm 0.026$ for A0535+26 and $\gamma = 0.957 \pm 0.026$ for GRO J1744−28. It is important to note that the BATSE only measured pulsed flux in the 20–50 keV range, not total flux. Changes in the pulsed fraction could be related nonlinearly to the mass accretion rate, and therefore could have contaminated the measurement of γ.

While accretion torque theory goes a long way in explaining the gross behavior of accreting pulsars and is overall a triumph in explaining the observations, the uncertainties in the theory make it difficult to extract precise measurements of neutron star magnetic moments. Moreover, since it measured the strength of the dipolar field at a radius $\sim 10^3 R_{\rm ns}$, the distribution of the B-field across the $1\,{\rm km}^2$ polar cap is completely unknown. So X-ray spectral measurements of CRSFs are still the best and only way to directly measure neutron star magnetic fields. These measurements also provide an independent verification of accretion torque theory, as well as provide observations that can be used to further refine the theory.

Now that the basic foundation has been laid, in the next chapter I will discuss the satellite used to obtain the observations discussed in this work, along with the methods, tools, and techniques used to analyze them. The chapters following contain the bulk of my work on accreting pulsar spectra in general and CRSFs in particular, and what these features can tell us so far about the polar emission regions of accreting pulsars.

Chapter 2

Instrumentation and Analysis

This chapter consists of two main sections. The first, entitled The *Rossi X-ray Timing Explorer*, outlines the instrument used to accumulate the spectral and timing information from the X-ray pulsars of interest. One of the 2 pointed instruments on the *RXTE*, the High Energy X-ray Timing Experiment (HEXTE) was designed and built at the Center for Astrophysics and Space Sciences at UC San Diego. For this research I worked closely with the HEXTE instrument team, which was an invaluable asset since many of the observed CRSFs are well observed with the HEXTE. The second section focuses on X-ray spectral analysis, along with a brief overview of *RXTE* data selection, spectral accumulation, and instrumental calibration issues germane to this work. The chapter ends with a discussion of the techniques and caveats when identifying and analyzing CRSFs in the X-ray spectra of accreting X-ray pulsars.

2.1 The *Rossi X-ray Timing Explorer*

The *Rossi X-ray Timing Explorer* (*RXTE*) was launched on 1995 December 30 from Cape Canaveral, Florida. A Delta II rocket inserted the satellite into low-Earth circular orbit with an altitude of 580 km and a 23°inclination. One of the major advantages of the *RXTE* is its maneuverability. The spacecraft can slew onto a source at 6°/minute, allowing it to respond quickly to transient sources. Named after the pioneering Italian astrophysicist Bruno B. Rossi, the nominal lifetime of the mission was two years, with the goal of five years. The satellite is currently in its 6th year of operation.

A detailed technical description of the instruments is given in the *RXTE* Technical Appendix F (http://rxte.gsfc.nasa.gov/docs/xte/appendix_f.html), and unless otherwise noted the rest of this section is based on this publication. Unlike the current generation of soft X-ray telescopes, such as *Chandra X-ray Observatory* and *XMM-Newton*, the *RXTE* does not have focussing capabilities. Instead the spacecraft acquires a single spectrum of everything in the 1° Full Width Half Maximum (FHWM) field of view. The source density is very low at these energies and sensitivities, however, and so source contamination other than the X-ray background is rarely a problem.

A diagram of the *RXTE* is shown in Figure 2.1, with the 3 scientific instruments (the PCA, HEXTE, and ASM, see Table 2.1 and §§2.1.1, 2.1.2, 2.1.3 respectively) highlighted. Compared to previous missions, such as the Japanese *Ginga* satellite (Turner et al. 1989), the *RXTE* offers a much larger degree of flexibility. Due to its rotating solar panels the spacecraft is able to observe almost any region of the sky, although because of thermal considerations the spacecraft is not pointed within 30° of the sun. Also, the onboard software of the *RXTE* is more intelligent than what has been flown in previous missions. For example, changing the pointing position requires only a source position (right ascension and declination) and a slewing-rate, the rest is done autonomously by the spacecraft.

The instruments on board *RXTE* were designed to study the temporal properties of strong X-ray sources, with moderate spectral resolution over ~2 decades of energy. Simply having μs time resolution is not adequate, however, since large numbers of

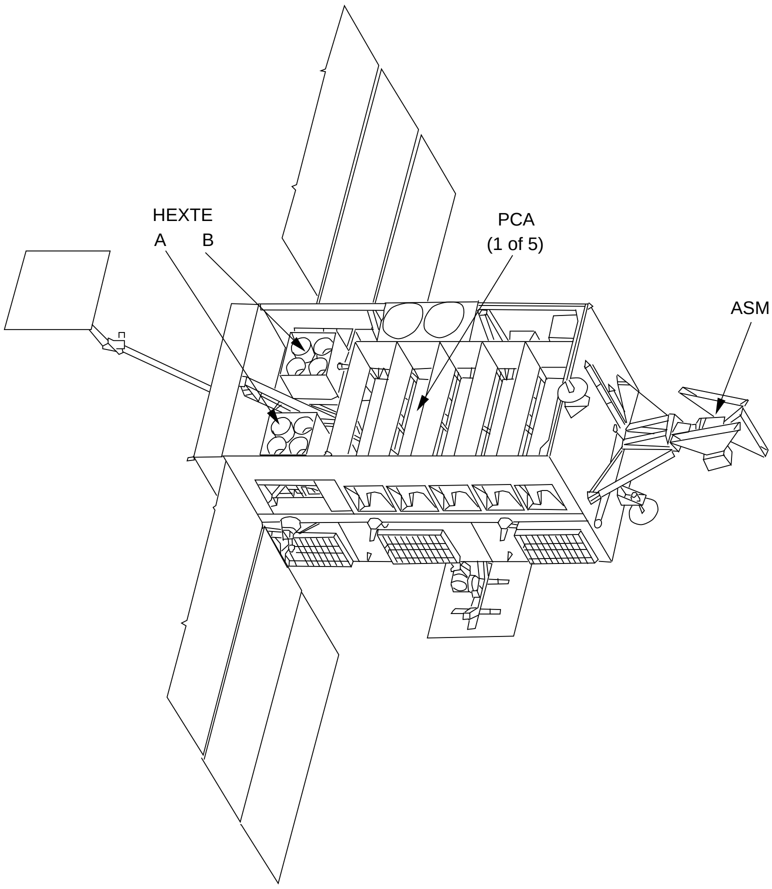

Figure 2.1: Schematic of the *RXTE* spacecraft. Observations from predominantly the two pointed instruments, the PCA and the HEXTE, were used in the thesis.

photons need to be collected to give adequate signal to noise in these thin time bins. Therefore the goal of high time resolution studies, especially below 1 ms, requires large areas with a high throughput as well.

To achieve this high degree of timing accuracy the *RXTE* mission operations center performs 10 calibration observations for the spacecraft clock per day. The calibration relies on a round trip signal, tagged by the spacecraft clock's time stamp, to determine the spacecraft clock offset. Parabolic fits to the datasets show deviations of no more than 1 μs. The dominant uncertainty in this calibration is the clock at the ground station in White Sands, New Mexico, which is typically only kept within 2–5 μs of UTC. Other sources of timing error are the 3–σ uncertainties in the solar system ephemeris and *RXTE* orbital ephemeris, which are 0.1 μs and 0.25 μs respectively. Still, the *RXTE* time stamps can be corrected to within 5 μs of absolute time (Rots

Table 2.1: *RXTE* at a Glance

Instrument	Area	Energy Range	Reference	§
PCA	$6500\,\mathrm{cm}^2$	2–60 keV	Jahoda et al. (1996)	2.1.1
HEXTE	$800\,\mathrm{cm}^2$/Cluster	15–250 keV	Rothschild et al. (1998)	2.1.2
ASM	$30\,\mathrm{cm}^2$/Camera	1.5–12 keV	Levine et al. (1996)	2.1.3

et al. 1998). This level of timing accuracy is much more than adequate for the analysis presented here.

In addition to the timing properties, the spectral capabilities of the *RXTE* cover the range 2–250 keV. This is over two decades of continuous coverage, or equivalent to coverage in the optical from the mid-infrared to near ultraviolet. This broad band spectral capability makes the *RXTE* an ideal instrument for the detection of CRSFs in the hard X-ray spectra of binary pulsars, and thus the study of their magnetic fields.

2.1.1 The Proportional Counter Array

The Proportional Counter Array (PCA, see Fig. 2.2) onboard the *RXTE* spacecraft was built by NASA's Goddard Space Flight Center (GSFC). It is a direct descendant of the *HEAO*–1 A–2 instrument (Rothschild et al. 1979, and references therein), only with a much larger area and much higher temporal resolution. The PCA consists of 5 nearly identical proportional counter units (PCUs) sensitive in the range 2–60 keV. In this work they will be referred to sequentially as PCUs 0–4. A diagram of a single PCU is shown in Fig. 2.3.

Proportional counters rely on the principle phenomenon of gas multiplication to measure the energy of an incident X-ray photon (Knoll 1979). When a photon interacts with the gas, primarily through photoelectric absorption, it creates a cloud of electron-ion pairs. If there is a voltage applied to the gas, then the electrons and ions drift to their respective electrodes. During this migration collisions occur with neutral gas molecules, but because of their low mobility the ions achieve very little average energy between collision. Free electrons, on the other hand, are easily accelerated by the applied field and may have a significant kinetic energy when colliding. If this energy is greater than the ionization energy of the gas, it is possible for additional

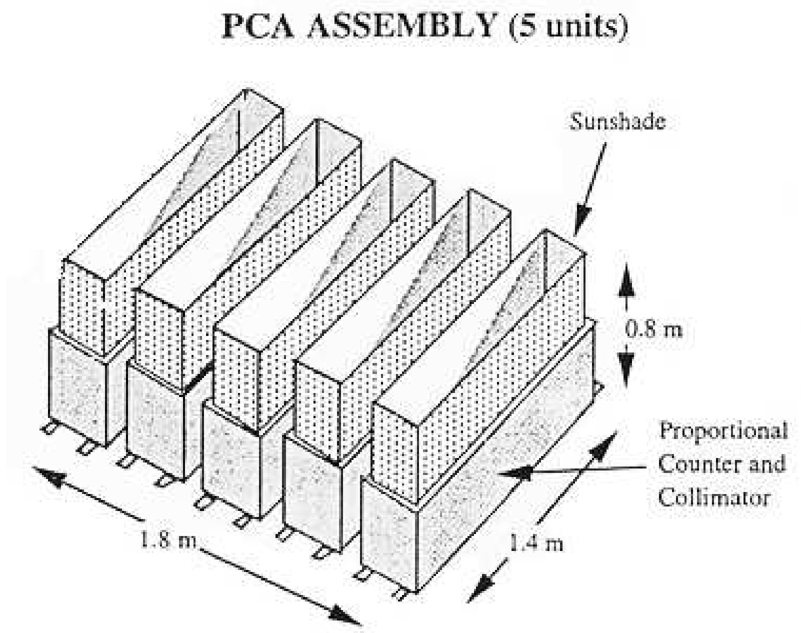

Figure 2.2: Arrangement of the 5 Proportional Counter Array Proportional Counter Units onboard the *RXTE*. For the location of the PCA relative to the other instruments on the *RXTE* spacecraft, see Fig. 2.1.

electron-ion pairs to be created in these collision. These secondary electrons are then accelerated, undergo collisions, and create further ionizations. The gas multiplication process therefore takes the form of a cascade, known as a Townsend avalanche. Within a specific voltage range (which is a property of the material) the size of this avalanche, and therefore the amount of charge collected at the electrodes, is nearly linearly proportional to the incident photon energy. This is the region that the PCA operates in, hence the name proportional counter array.

The response of these detectors is made slightly more complex by the atomic physics of the gases used. In particular, the cross section for photoelectric absorption in Xenon increases sharply at the K-edge with increasing energy. This can be seen in Fig. 2.4 as a significant increase in the PCA effective area (the product of the efficiency for the detection of a photon with the physical area of the detector) above 34.6 keV. Another complication are the L-escape photons due to the L-edges near $\sim$5keV. Again, the photoelectric cross section of Xenon drops below each of these L-edges. Photons with energies just above an edge will be photoelectrically absorbed near the surface of the detector and eject an L-shell electron. As higher-shell electrons

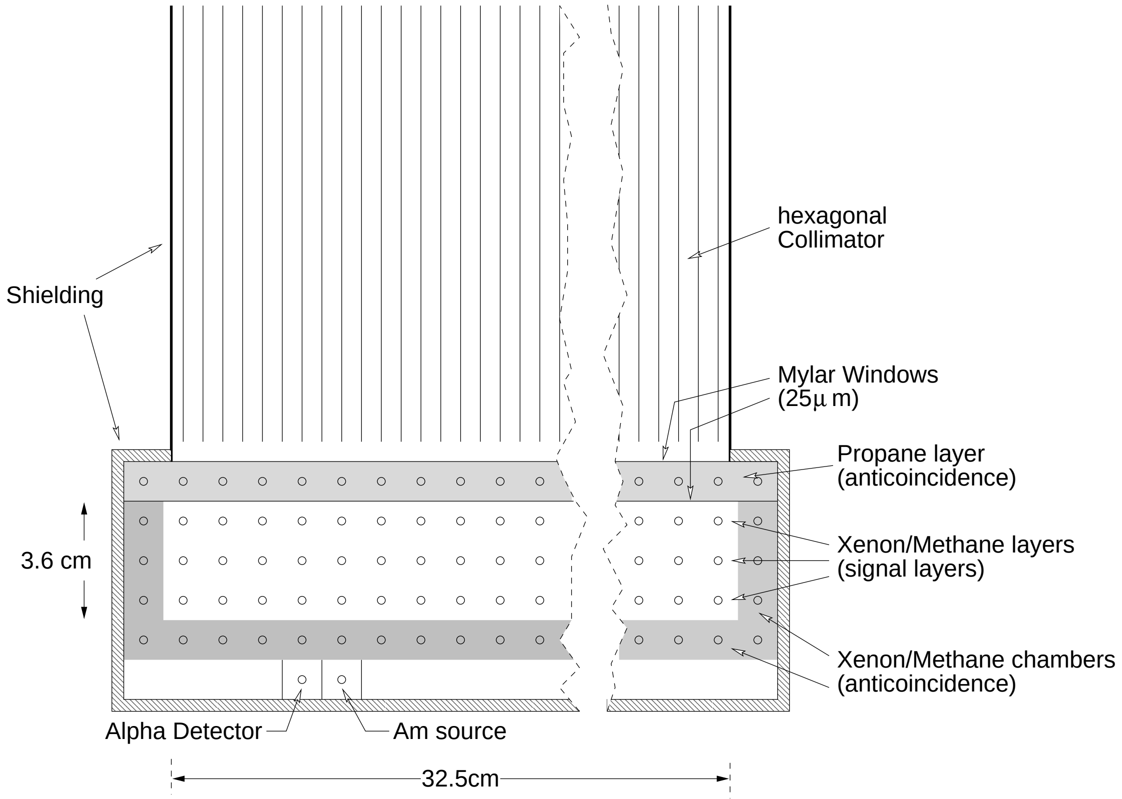

Figure 2.3: Diagram of a single proportional counter unit of the PCA. A charge pulse event is classified as a valid X-ray photon event ("good event") if none of the anti-coincidence anodes, located at the sides and bottom of the chamber, or the propane layer, are simultaneously triggered.

cascade into lower levels, photons with energies below the L shell will be emitted. In particular, the M to L shell transition will have a much larger mean free path than the incident photon, and so there is a probability these photons will escape out the front of the detector. The effects of these edges can be seen in both the instrument effective area (see Fig. 2.4) and fits to the Crab (see Fig. 2.12).

Each PCU is collimated to a 1° FHWM field of view by a hexagonal collimator of BeCu. Behind the collimator are two mylar windows, each 1 mil thick and coated on both sides with a thin layer of aluminum. These windows are separated by 1.3 cm and contain a layer of propane used to screen out low-energy electrons ($E_e < 2\,\mathrm{keV}$). Behind the second mylar window is the main detector volume, filled with a 90/10 Xenon/Methane mixture held at 840 torr. Inside the Xenon/Methane chamber are three layers of signal anodes which collect the charge deposited by incident X-rays,

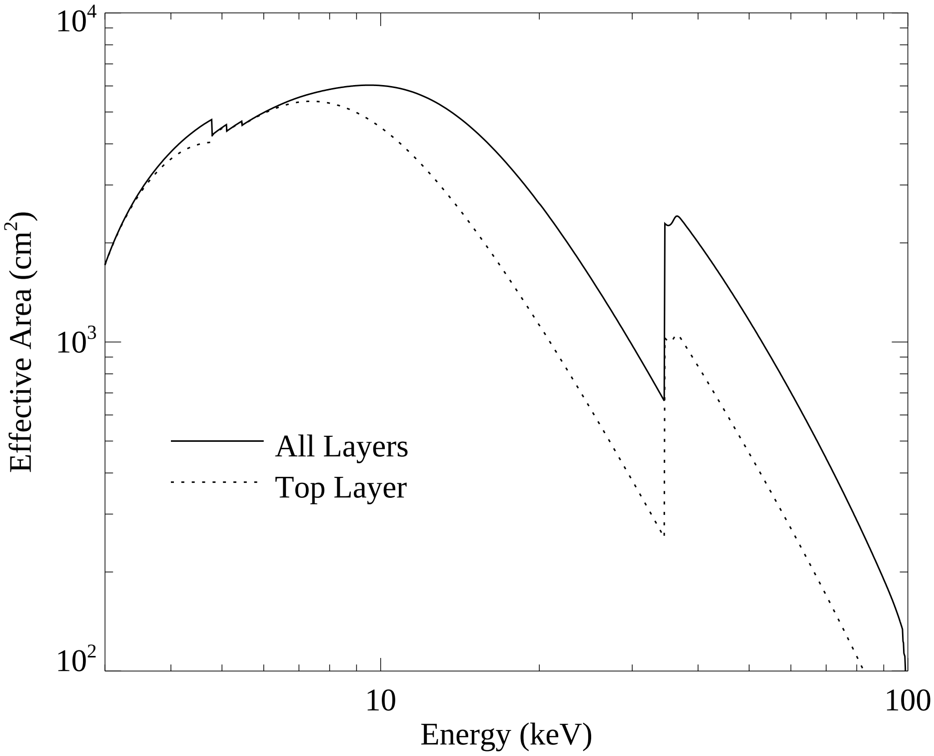

Figure 2.4: The effective area (the product of the detection efficiency with the physical collecting area) of the PCA as a function of energy with all 5 PCUs operating. The dotted line is the effective area for the top layer only. Although the area of the top layer alone is less when compared to all layers, the instrumental calibration is superior, resulting in a reduction of the systematic uncertainties in PCA spectra. The top layer alone was predominantly used for this analysis.

followed by a single anticoincidence anode layer at the bottom of the chamber. Side anodes provide further anticoincidence, and the detectors are passively shielded (Tl and Zn) to provide additional background reduction. The total collecting area of the 5 detectors is $\sim$6500 cm^2. The energy resolution $\Delta E/E$ of proportional counters depends mainly on the counting statistics of the number of electrons received at the anode for an X-ray photon of a given energy E, and therefore varies as $\sqrt{E}$ (Serlemitsos et al. 1976). The nominal energy resolution of the PCA is 18% at 6 keV.

Gain control and calibration are done using a tagged ^{241}Am source in each of the detectors. One of the decay channels of the ^{241}Am source, the one used for calibration, is the simultaneous emission of an α-particle with a 59.6 keV photon. The ^{241}Am source sits inside the gas chamber, along with an α particle detector, and photons that register simultaneously with an α particle are assumed to be at 59.6 keV and are used for gain correction.

Due to the large area of the instrument the count rates can be large enough to saturate the telemetry capabilities of the satellite. In these cases the raw data has to be compressed, selecting only the information desired by the observer. This is the task of the Experiment Data System (EDS), built at the Massachusetts Institute of Technology along with the All Sky Monitor(see §2.1.3). The EDS consists of 8 parallel, independent computers known as Event Analyzers (EAs). Six of these are dedicated to the PCA, while the remaining 2 process data from the ASM.

For the PCA, each EA can process a different observing "datamode", or prescription for compressing the data based upon time and energy information. At launch the EDS had a set of ~650 available datamodes, along with the ability to accept new modes uploaded while in orbit. The available PCA datamodes span nearly continuously the phase space between temporal and spectral resolution. It is up the the observer to choose which combination is best for the science topic under consideration, given the constraint of maximum telemetry rate allowed. There are two main classes of modes (and therefore data). The first set are the "event" modes, where each photon collected is registered as an event. For example, the event mode designated as `E_250us_128M_18_1s` has events tagged with 250 μs time resolution, the full energy range has been compressed from the original 256 channels into 128 using the "M" rebinning scheme and starting at channel 18, and the events are read out every second.

As counting rates increase, the ability to preserve each photon individually is lost. For these sources "binned" modes are available, where histograms instead of events are telemetered to the ground. These are designated in a fashion similar to the event mode data. For example, the binned mode `B_125us_4B_0_17_Q` produces a histogram every 125 μs with 4 spectral channels rebinned from the original channels 0–17 using the "B" scheme. The final "Q" denotes how many bits each histogram contains.

If the source counting rate is low enough, then there is no need for any onboard data compression. For these sources the `GoodXenon` datamode is available, which preserves all information. Unlike the rest of the datamodes which require a single EA, `GoodXenon` mode data requires 2. Much of the analysis for this work was done using archival *RXTE* data, and as such I was at times limited by the principal investigator's

Table 2.2: PCA Gain Epoch History

Epoch	1	2	3	4
Start Date	–	1996 Mar 21	1996 Apr 15	1999 Mar 22
End Date	1996 Mar 21	1996 Apr 15	3/22/99	–
Stop Time (UTC)	18:33	23:05	17:37	–

choice of datamode.

While the EDS can accumulate 6 different modes simultaneously, 2of these are reserved for the PCA "standard mode" data. These cannot be changed by the observer, and available for every observation. The PCA Standard 1 data has a temporal resolution of 0.125 s, but is without any spectral information. The PCA Standard 2 data has a temporal resolution of 16 s, with 129 pulse height analyzer (PHA) channels for each layer of each PCU. The Standard 2 data is the basis of most of the phase average work presented here (see Chapter 3). The 16 s time resolution is, however, inadequate for timing even the slowest pulsars. So for the phase resolved analysis given in Chapters 4 and 5 the specific datamodes are given.

The high voltage of the PCA has been changed several times during the mission, resulting in 4 "Gain Epochs" (see Table 2.2). After launch the PCA high voltage was set to the designed value of 2000 V, and reduced to 1000 V during South Atlantic Anomaly (SAA) passages. In the SAA the Earth's magnetic field dips, allowing trapped radiation to reach much lower altitudes and affect the spacecraft). In mid 1996 March PCUs 3 and 4 exhibited signs of occasional breakdowns that were most probably caused by sparks within the Xenon/Methane chamber followed by polymerization of the quenching gas around the anodes (Jahoda et al. 1996). On 1996 March 21 the high voltage was reduced, marking the end of PCA gain epoch 1, and the detectors began being switched off during SAA passages. Epoch 2 was short lived, however, since the high voltage was reduced again on 1996 April 15. Since the end of gain epoch 1, PCUs 3 and 4 have been switched off regularly to help extend their useful lifetime. In 1999 March PCU 1 began failing as well, and on 1999 March 22 the PCA high voltage was again reduced. As of this writing (2001 April) the PCA is still in gain epoch 4. Due to the relatively short durations of PCA Epochs 1 and 2, there has been less emphasis on understanding the calibration and producing background models during these periods (see below). Therefore observations taken in PCA Epochs 1 and 2 will have larger systematic uncertainties associated with them when compared to epochs 3 and 4.

On 2000 May 12, the propane layer of PCU 0 started leaking, reaching 0 torr within a day. Luckily this leak did not affect the Xenon chamber and that detector is still functioning, albeit with a slightly higher background rate. This does not affect any of the results presented here, however, since the observations I have analyzed were made before the problem; I indicate it here merely for completeness.

The PCA background consists to two main components. The first is internal to the instrument, caused by interactions of cosmic rays and their secondaries with the detector material and by short-term radioactivity produced during passages through the SAA. The second is contamination of the source spectrum due to the diffuse cosmic X-ray background, radiation thought to be produced by the superposition of many weak active galactic nuclei (Fabian & Barcons 1992, and references therein). For the PCA these background components cannot be observed directly, and therefore have to be modeled.

I have done all of the PCA background estimation using one of 2 background models released by the PCA instrument team. The choice of which depends on the source counting rate. The FAINT model is for source count rates below $40\,\mathrm{cts\,s^{-1}\,PCU^{-1}}$. It is based partly upon the "L7" rate, a background rate made up of a combination of 7 rates in pairs of adjacent signal anodes read from standard 2 data. The FAINT model is also derived from the integrated recent particle doses during SAA passages as measured by the HEXTE particle monitor. For brighter sources the SkyVLE was used. This model was created by using blank sky pointings to correlate the Very Large Event (VLE) count rate with the simultaneous particle background. Comparisons of the simulated and measured background spectra and light curves show that these models work quite well, especially below $\sim$20 keV where my analysis is concentrated (Jahoda et al. 1996).

2.1.2 The High Energy X-ray Timing Experiment

The High Energy X-ray Timing Experiment (HEXTE) instrument on the *RXTE* was designed and built at UC San Diego by the High Energy Astrophysics (HEA) group at the Center for Astrophysics and Space Sciences (CASS). and is a direct descendent of the *HEAO*–A4 detector (Matteson 1978). The HEXTE consists of two assemblies of four NaI(Tl)/CsI(Na) phoswich scintillation counters, named clusters "A" and "B" respectively. A diagram of the entire HEXTE assembly is given in Fig. 2.5, while a cutaway illustration of 1 detector assembly is shown in Fig. 2.6. The HEXTE instrument is described in detail in Rothschild et al. (1998).

The detectors are collimated to 1° FHWM using a lead honeycomb and are co-aligned to the same source pointing field of view as the PCA. The nominal area of each cluster is $800\,\mathrm{cm}^2$, and the HEXTE has a maximum time resolution of $8\,\mu$s. On 1996 March 21 one of the pulse height analyzers in cluster B failed, effectively reducing the area of that cluster by 25%. Unless noted otherwise, the observations analyzed here were made after the loss of that detector. The current effective area of each cluster as a function of energy is plotted in Fig. 2.7.

The HEXTE detectors are based upon the process of scintillation by energetic particles. The incident photons are photoelectrically absorbed by the crystals. Through interactions with the crystal lattice of the detector material, the energy of these photoelectrons is converted to a shower of UV/optical photons. The intensity of this "scintillation" of light is nearly proportional to the energy deposited in the the crystal. Behind the NaI(Tl) crystal is a window of quartz glass which optically couples the detector crystals to a photomultiplier tube (PMT). The PMT in turn converts the scintillation pulse into an electronic signal whose magnitude is approximately proportional to the energy of the incident X-ray photon. The energy resolution is nearly proportional to $E^{-1/2}$, and is 16% at 60 keV.

In each phoswich, the light emitted by the NaI(Tl) crystals has a characteristic decay time of $0.25\,\mu$s, while the decay times of the sodium doped CsI(Na) crystals is much slower ($0.63\,\mu$s). This allows for the rejection of CsI(Na) events via a measurement of the decay time, or pulse shape. An event is accepted by the HEXTE electronics is the decay time is indicative of a NaI(Tl) event, and there is no anti-

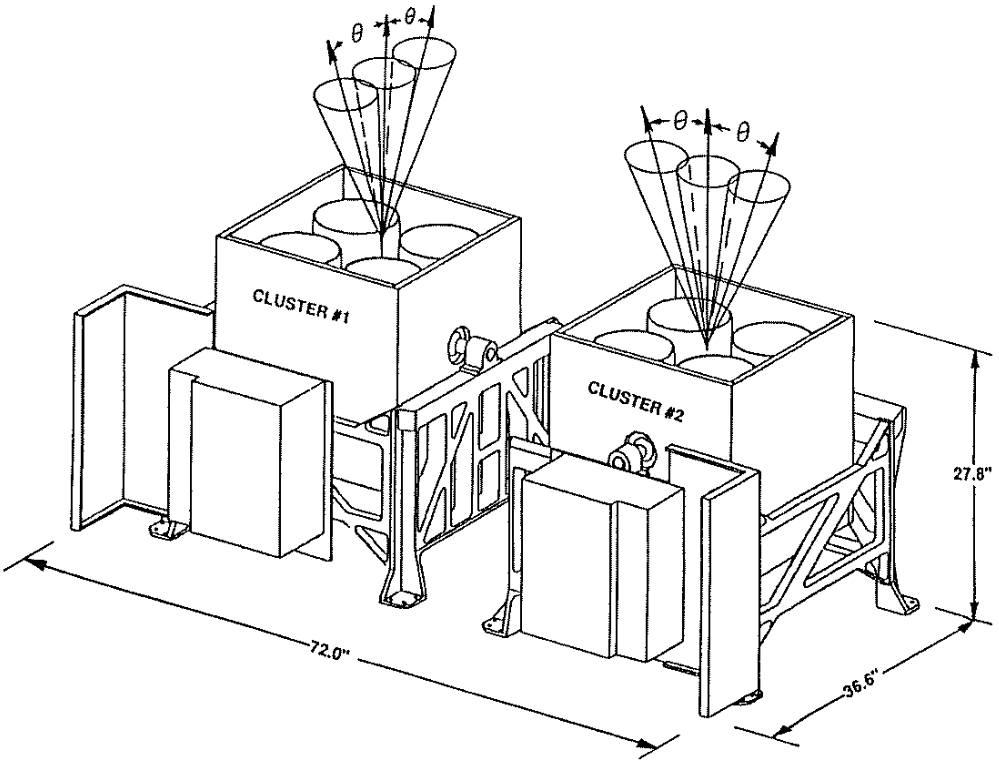

Figure 2.5: Arrangement of the two HEXTE clusters onboard the *RXTE*. For the location of the PCA relative to the other instruments on the *RXTE* spacecraft, see Fig. 2.1.

coincidence signal from the shields. The CsI(Na) crystals are used to suppress the instrumental background in the detectors (see below).

Much like at the PCA L edges, the HEXTE detectors suffer from a loss of response due to the K-edge of Iodine at 33.17 keV. Photons with energies just above the K-edge will be photoelectrically absorbed relatively near the surface of the detector, ejecting a K-shell photoelectron in the process. As higher-shell electrons cascade into the lower levels, photons with energies below the K-shell will be emitted. In particular, the L to K-shell transition will produce a photon with an energy below K edge, where the cross section is lower and the mean free path in the crystal larger than for the incident photon. Because of this there is a probability these photons will escape out the front of the detector, effectively reducing the ability to detect photons just above the K-edge. This can be seen as a "dip" in the effective area of the instrument above 33 keV (see Fig. 2.7). In the HEXTE detectors this feature is well understood and

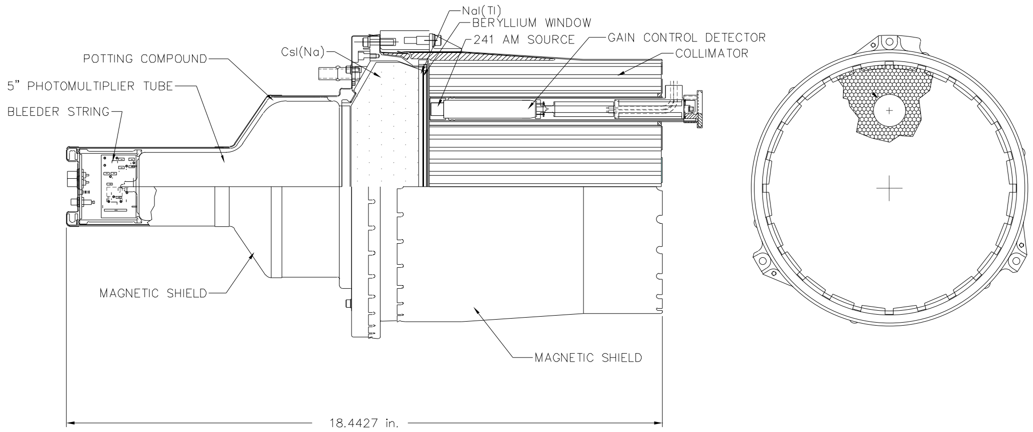

Figure 2.6: Cutaway schematic of a single HEXTE phoswich detector unit, consisting of a photomultiplier tube, scintillation crystals, and collimator assembly. The front view on the right shows the placement of the automatic gain control ^{241}Am source in the collimator and shows a portion of the collimator honeycomb.

calibrated, as can be seen in fits to the Crab nebula/pulsar (see Fig. 2.13).

Gain control and calibration in the HEXTE is done in a similar fashion as for the PCA. A radioactive ^{241}Am source mounted into the collimator of each phoswich (see Fig. 2.6) emits an α particle coincident with a 59.6 keV photon. Photons that register simultaneously with the detection of an α particle are used to perform continuous automatic gain control (Pelling et al. 1991).

Compared with the PCA, the HEXTE has far fewer data modes available. But due the the smaller area of the instrument, coupled with the fact that most sources have a lower luminosity in the HEXTE energy range, there is less of a requirement on the telemetry. Therefore nearly all observation made with the HEXTE are able to preserve full time and spectral information without the need for compression on the spacecraft.

After launch, it was found that the HEXTE electronics experienced a deadtime which was much larger than the prelaunch expectations. This increase is believed to be due to the presence of additional “noise” in the scintillation light signal due to the presence of long-lived decay states that are excited by large cosmic-ray energy loss

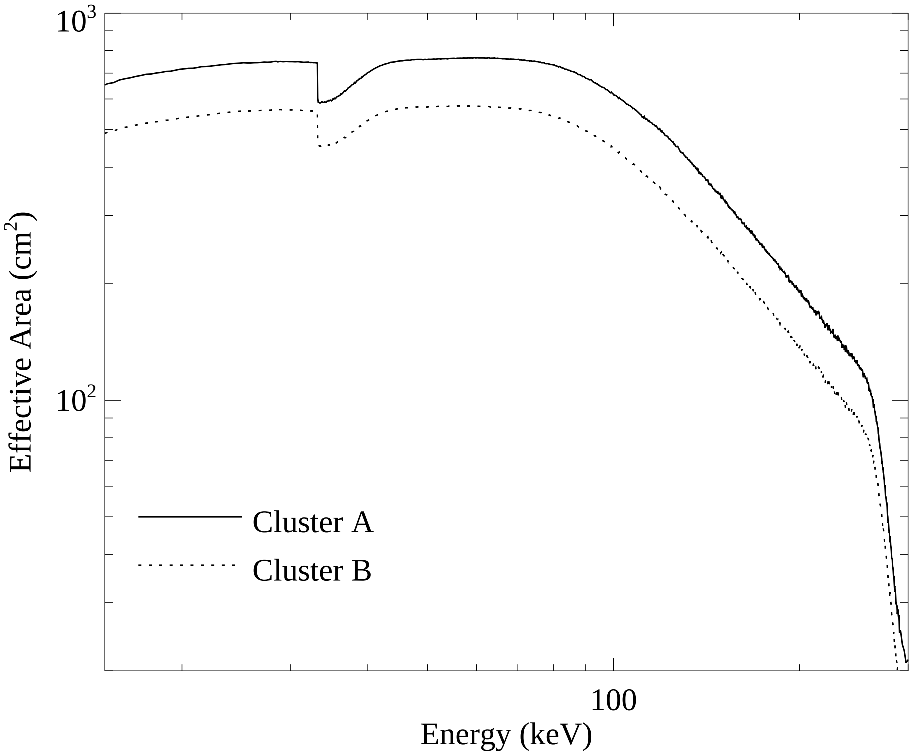

Figure 2.7: The effective area of the two HEXTE clusters. Cluster B has a slightly lower effective area due to the loss of the phoswich early in the mission. Before 1996 March 6 the area of the two clusters was nearly identical. The reduction at lower energies is due to the housing of the detector, while the reduction at higher energies is doe the the finite thickness of the detector. The sharp drop 30 keV is due to the change in the photoelectric cross section at the K-edge of Iodine and the onset of K-escape photons.

events in the NaI(Tl) crystals. This reduced the livetime accumulated during each observation by an appreciable fraction, on average ~40%, and is why the HEXTE livetimes quoted in this work are less than the PCA exposure. A detailed description of this effect is given by Rothschild et al. (1998). The correct livetime for each observation has to be modeled on the ground as part of the HEXTE data analysis procedure, using software released by the HEXTE instrument team.

The HEXTE background consists of both internal background and that from the cosmic diffuse X-ray background, much like the PCA. As mentioned previously, the internal background in the detectors is reduced by using pulse shape discrimination to select only events from the NaI(Tl) crystal (Rothschild et al. 1998). The benefit of the CsI(Na) crystal is to provide active anticoincidence shielding from both X-rays from outside the filed of view, and from events that result in only a partial energy loss

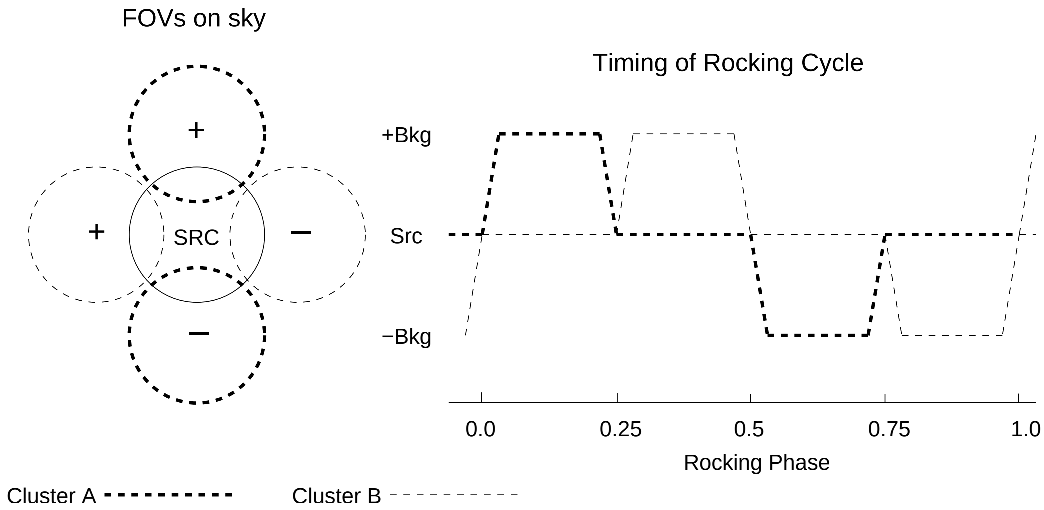

Figure 2.8: Left: The various background pointing positions on the sky with respect to to the source position. The 2° full width zero maximum (FWZM) fields are shown. Right: The timing diagram for the rocking cycle. The duration of each single on-source pointing (with 4/cycle) is a multiple of 16 s. Notice that one of the clusters is always pointing in the source direction, while the background pointings are shorter by 4 seconds irrespective of rocking period.

in the NaI(Tl) crystal. Plastic anticoincidence detectors around each crystal perform additional background rejection. The resulting instrumental background is reduced to $\sim$100 cts s^{-1} by these procedures.

To remove the remaining background, the HEXTE clusters "rock" on and off source, where each of the clusters can be displaced by 1°.5 or 3° from the central pointing position. When the HEXTE is in rocking mode (as opposed to "staring," where no background is measured) one cluster observes the source while the other observes a background field. Source and background swapping is done every 16 s (or multiple of 16 s), with one and only one cluster always pointing in the source direction. The HEXTE source and background fields of view, as wells as the rocking scheme, can be seen in Fig. 2.8. Because of the near simultaneous measurement of source and background for each cluster, the background subtraction in HEXTE is painless and functions flawlessly.

2.1.3 The All Sky Monitor

The third instrument on the *RXTE* is the All Sky Monitor (ASM), built by the Center for Space Research at the Massachusetts Institute of Technology. The ASM was designed to monitor the fluxes of many discrete sources simultaneously (Levine et al. 1996). Although data from the ASM was not analyzed extensively for this research, it is very useful for monitoring the flux of sources between pointed observations and so will be mentioned briefly here. In this work I have used it to determine the 1.5–12 keV source behavior between pointed observations (see Fig. 5.1). Also, the ASM has been vital in identifying (e.g. Coburn, Rothschild & Heindl 2000) and monitoring (REFERENCE 1946 ASM FIGURE) outbursts from transient accreting X-ray pulsars.

The ASM consists of 3 Scanning Shadow Cameras (SSCs), each operating in the 1.5–13 keV energy range. The field of view of each SSC is collimated to a $6^\circ \times 90^\circ$ FHWM, the detectors have a spatial resolution of $3' \times 15'$ (see Fig. 2.9). The shadow mask on each of the SSCs is a thin aluminum sheet subdivided into 6×2 subsections. Each of the 12 subsections contains $\sim$15 open and $\sim$16 closed slit elements arranged in 1 of 6 carefully chosen pseudo-random patterns. The SSC detector plane contains a Position-Sensitive Proportional Counter (PSPC) with an effective area of $\sim$30 cm^2. The PSPCs are used to measure the displacements and strengths of the shadow patterns cast by X-ray sources within the field of view, and thereby allowing source intensities and directions to be measured.

The cameras are mounted platform at the "rear" of the spacecraft (see Fig. 2.1), and operates independently of the other two instruments while the spacecraft conducts pointed observations. The platform is rotated about its axis, dwelling at each sky position for 90 s. In this way $\sim$80% of the sky passes through the ASM field of view during each spacecraft orbit. This allows the ASM to monitor the 1.5–12 keV intensity of the $\sim$150 brightest X-ray sources in the sky. This data is made available to the public via the World Wide Web, usually within 24 hours, allowing for near realtime monitoring of source intensities. Due to the variability of the X-ray sky, the ASM a powerful tool for identifying when transient sources, both known and previously undiscovered, have gone into outburst.

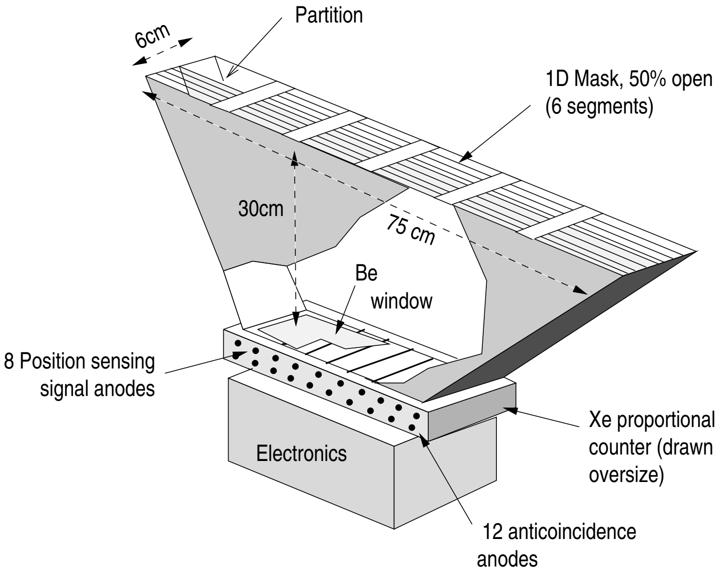

Figure 2.9: Diagram of a single ASM shadow camera. Note that this is *not* drawn to scale; each segment of the shadow mask is the size of the detector window, allowing for a full reconstruction of the shadow pattern.

2.2 Data Accumulation and Analysis

Along with timing, one of the primary uses of the *RXTE* is to measure the spectra of bright X-ray sources. The distribution of emitted photon energies from a source is called the source *photon spectrum*, or often simply just the source spectrum. Unfortunately this cannot be measured directly with instruments such as proportional counters or scintillation detectors. In general, the measured spectral shape is influenced by the effects of the instrumental response, such as the effective area (see Figs. 2.4 and 2.7) and energy resolution, as well as photon counting statistics. Therefore what is actually measured is the referred to the *counts spectrum.* Since this is what is measured by the *RXTE* instruments, unless otherwise noted when I refer to a spectrum , it will be a counts spectrum.

The observed counts spectrum $C(I)$ is represented by (Arnaud 1996):

$$C(I) = \int_0^\infty F(E)R(I,E)dE + N(I) \tag{2.1}$$

where I represents the detector channel number and E photon energy, $F(I)$ is the incident photon spectrum, $N(I)$ the additive noise component, and $R(I,E)$ the detector *response matrix.* The response matrix is the mathematical function that relates the observed counts spectrum to the "true" incident photon spectrum. Along with the determination of the noise component $N(I)$, the response matrix can be a major source of systematic uncertainties in the inference of the source spectrum. In practice, the response matrix is determined through a combination of Monte Carlo simulations, observations of calibration sources with known spectra, and observations of the "standard" X-ray source the Crab Nebula/Pulsar. The understanding the response matrix, along with its limitations and features, is vital the the interpretation of X-ray spectra. A discussion of the instrumental response, along with the method I used for estimating the size of the systematic errors, is given in §2.2.3.

The fitting of data from astronomical X-ray observatories is fundamentally different than what is done in much of the rest of astronomy. Although a direct inversion of Eq. 2.1 would be ideal, it is unfortunately not practical. The response matrices of real detectors are often non-linear and have off-diagonal elements, making the inversion non-unique and often simply impossible. Since the measured counts spectrum $C(I)$ cannot be converted into the incident photon spectrum $F(E)$ directly, an indirect fitting method must be used. Starting with an *a priori* model, it is folded forward through the response matrix to get the predicted counts. These are then compared to what was measured using the χ^2 statistic. By doing a number of iterations of the model fit parameters, a minimum in χ^2 can be found, thus giving the best fit for that model.

2.2.1 Data Accumulation

The first step in the analysis procedure, however, is the conversion of PCA and HEXTE raw data files provided by the *RXTE* Guest Observer Facility (GOF) into meaningful X-ray counts spectra and light curves. This is done in a straightforward manor using the NASA released `HEASoft` analysis tools[1]. The `HEASoft` consists of two main packages, the `FTOOLs` data accumulation software and the `XANADU` spectral, timing, and image analysis software. The entire process of accumulating data using the `FTOOLs` is outlined in "The RXTE Cook Book: Recipes for Data Analysis and Reduction," provided by the High Energy Astrophysics Science Archive Research

1 see `http://heasarc.gsfc.nasa.gov/` on the world wide web

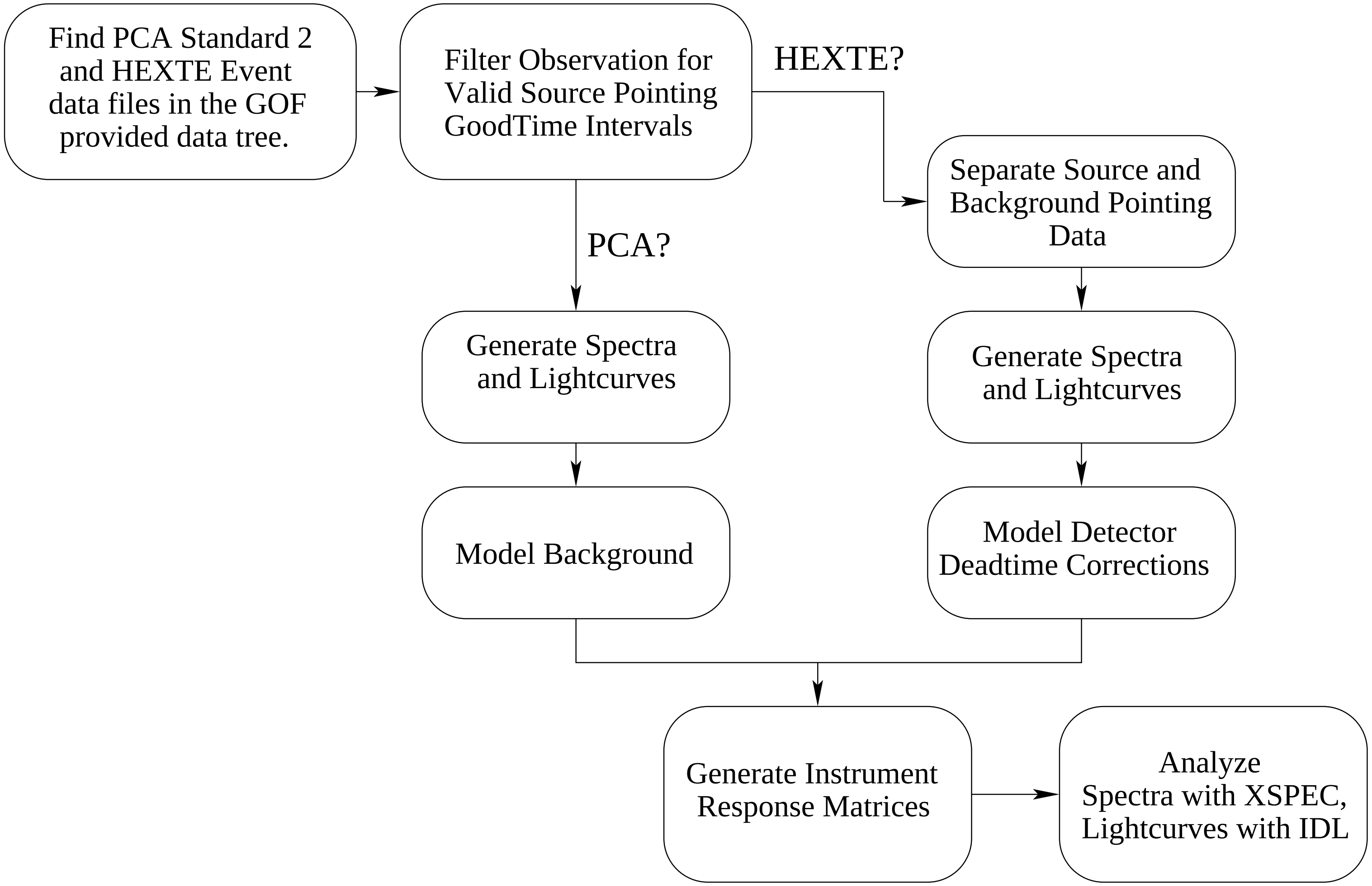

Figure 2.10: Flow diagram of the steps taken to properly accumulate *RXTE* spectra and lightcurves. The entire process is detailed at the *RXTE* Guest Observer Facility website, `http://heasarc.gsfc.nasa.gov/docs/xte/xtegof.html`

Center (HEASARC) and is available via the world wide web at the *RXTE* GOF. Further information is available in "The ABC of XTE" guide, also available at the *RXTE* Guest Observer web site. A flow diagram of the basic procedure is given in Fig 2.10.

When determining source "goodtime" intervals, times from which to allow the extraction of source (or background) counts, I used the following data selection criteria. To avoid possible contamination from X-rays from the Earth's limb, data was accumulated only when the satellite was pointing more than 10° above the horizon. To avoid possible contamination from activation in the detectors due to the high particle rates associated with SAA passages, I rejected data from a 30 minute interval beginning with the satellite entering the SAA. I also required that the satellite be pointing to within 0°.01 of the source position. Lastly, for faint sources and with the PCA instrument only, the electron ratio in each of the accumulated PCUs was required to be less than 0.10.

All other data accumulation steps, such as the modeling of the PCA background, modeling HEXTE deadtime corrections, and generating response matrices, was done using the released `HEASoft FTOOL` appropriate for the task. Since the procedure to generate spectra and light curves has many discrete steps and uses a variety of different `FTOOLs`, I wrote and developed several shell scripts to automate the process. As a user I have also been active in identifying and reporting problems with the software to the *RXTE* GOF. For spectral analysis I used the `XSPEC` fitting package, released as part of `XANADU` in the `HEASoft` tools. I initially used version 10.00, and later when it was released version 11.0.1 (Arnaud 1996).

2.2.2 Pulse Phase Resolved Analysis

As mentioned in section §1.4, it is the rotation of the neutron star that gives rise to the observed pulsations (and hence the name "pulsar"). It is also well known that the emission of accreting X-ray pulsars can vary considerably with pulse phase (White, Swank & Holt 1983). This gives rise to a very power diagnostic of the emission region, whereby resolving the source flux as a function of pulsation phase gives spectral "snapshots" of the emission region at different rotation phases. Used in succession this type of analysis can be used to infer many of the geometric properties of the emission region, along with the relative locations of the emitting poles on the neutron star surface.

Pulse phase resolved spectral analysis is especially useful in the study of CRSFs. Since CRSFs can change with pulse phase (e.g. Soong et al. 1990), this means that as the emission geometry is changing, so is the observed magnetic field strength. Therefore pulse phase resolved spectroscopy both aids in the search for and study of these magnetic features. Ultimately, the two dimensional nature of accreting pulsar spectra can make interpreting spectra averaged over the pulsation period difficult. I discuss the results of a pulse phase resolved analysis of the sources 4U 1538−52, 4U 1626−67, and 4U 1907+09 in Chapter 4.

Another method used to study the emission as a function of pulsation phase are Folded Light Curves (FLCs). An FLC is generated by first converting photon arrival times into rotation phase φ $(0 \leq \varphi < 1)$ using the pulsation period of the star, and then accumulating a light curve binned on phase instead of time. In this way the source intensity (counts) in a given energy range is plotted as a function of pulsation phase. An example of an FLCfor the source Hercules X−1 is given in Fig. 2.11. In accreting X-ray pulsars, the general trend seen in FLCs is toward more complicated pulse shapes at lower energies, and larger pulsed fractions at higher energies.

Pulsar Timing

In order to accumulate the pulse phase resolved spectra of an observation, I first had to determine a pulsation period of the source. I did this using folding techniques on either source light curves or event times. For light curves the technique works by folding the data on a test period, and calculating χ^2 against the assumption that the resulting folded light curve (FLC) is a constant. At the pulsation period the folded light curve will exhibit the largest deviation and therefore the largest χ^2. When I used light curves the time resolution was better than 0.1% of the pulsation period.

A similar approach is taken using event data, the difference being that the Z^2 statistic (with 2 harmonics) is calculated instead of χ^2. The Z^2 test (Buccheri et al. 1983) is based on a Fourier analysis of the photon arrival phases assuming no periodic signal, and for n harmonics has a probability distribution function equal to that of

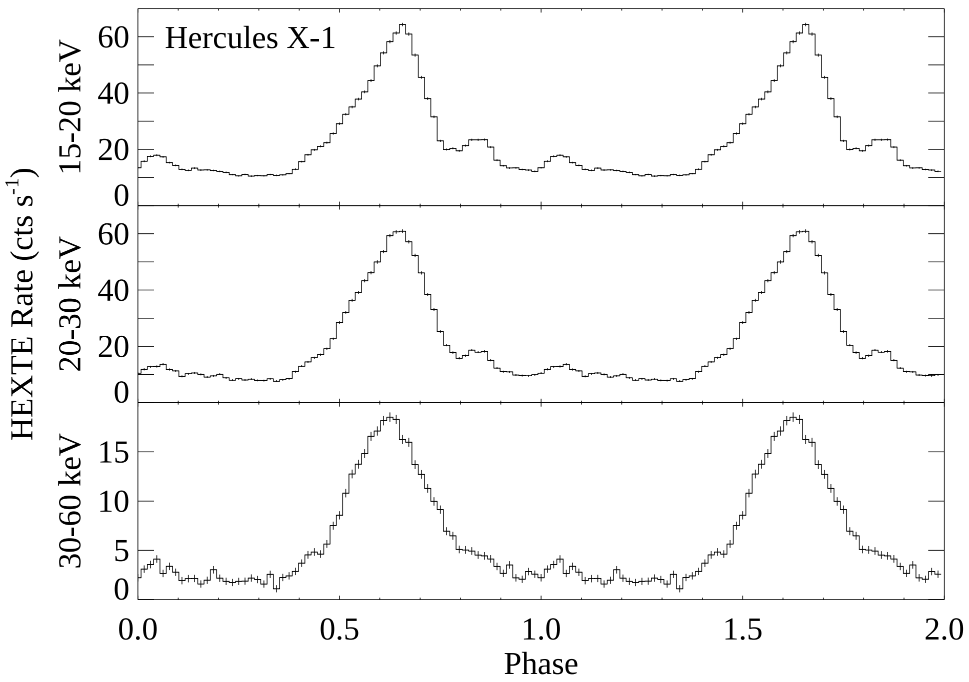

Figure 2.11: A sample folded light curve (FLC), this one for the source Hecules X−1 (during the peak of the main-on, see §3.1.1) in the HEXTE energy range. Following the normal convention, the same pulse plotted twice for clarity.

χ^2 with $2n$ degrees of freedom (Bendat & Piersol 2000). Like the χ^2 test, the Z^2 statistic reaches a maximum at the pulsation period.

I first corrected the light curve or event times to the solar system barycenter, using the satellite orbital history files released with the data and the `fxbary` FTOOL. This was done to remove Doppler motions of the satellite around the Earth and Earth around the sun which would smear out the signal. Then, if the system in question had a known orbital ephemeris, I corrected for Doppler shifts due the binary orbital motion using an Interactive Data Language (IDL) routine provided by Dr. D. Chakrabarty (Chakrabarty 1996). To remove the absolute phase as a parameter I centered the photon arrival times around zero. Once these corrections were made I was able to use IDL routines I authored along with several provided by Dr. D. Marsden (Marsden 1999) to perform the epoch folding searches around known rotation periods. I determined the error by folding the data on nearby periods, calculating the χ^2 statistic with respect to the FLC of my best period, and noting where χ^2 increased by 2.7 for 1 interesting parameter (the period) (Lampton, Margon & Bowyer 1976).

`fasebin`

I have done all of the pulse phase resolved spectral accumulations using a locally modified version of the `fasebin` `FTOOL`. The changes were made by both myself and Ingo Kreykenbohm at the Eberhard Karls Universität Tübingen, Germany. The released version of `fasebin` accepts most PCA datamodes, and folds the in a fashion similar to generating FLCs folds the spectrum at a specified period. The output of the program is a two dimensional counts histogram, versus both phase and energy. This allows for easy analysis of spectra as a function of pulsation phase, or folded light curves as a function of energy.

The released version, however, had three main drawbacks. First, it required the maintenance of a pulsar database containing pulsar spin histories and orbital ephemerides. This proved to be an inconvenient method for accreting pulsars, especially transient sources in outburst and wind driven systems, which can exhibit very erratic spin histories (Bildsten et al. 1997) and therefore necessitated database entries for each individual observation. Now, the `fasebin` tool allows the spin period $P_{\rm spin}$ to be designated at runtime. My primary contribution to the code, apart from testing and debugging, was to modify the software such that it accepted both parameters at runtime (e.g. the spin period) as well as entries from the database (e.g. the pulsar's right ascension and declination).

Second, the released version of `fasebin` did not properly process HEXTE data files, resulting in spectra with incorrect exposure times. This was fixed. Third, `fasebin` was unable to phase resolve background files in addition to source looking data. For long period pulsars ($P_{\rm spin} \gtrsim 100\,{\rm s}$) this can potentially be important, although for the $\sim$835 s pulsar 4U 0352+309 (Chap. 5) the 4 phase resolved backgrounds are consistent within errors of being identical. As of 2001 April, however, only the HEXTE background files can be pulse phase resolved.

2.2.3 Response Matrices

As mentioned above in §2.2, the understanding instrumental response features is vital to understanding and interpretation astrophysical X-ray spectra. This is particularly important for the study to CRSFs. Since these features are in general

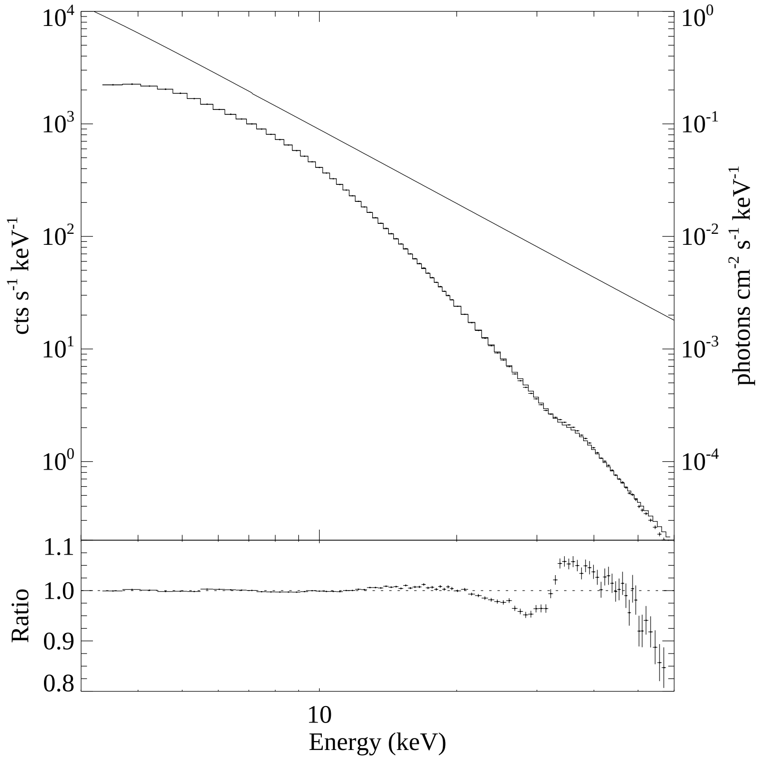

Figure 2.12: Top: A dual power-law fit of to the PCA spectrum of the Crab pulsar/nebula (see text). The measured counts are shown as crosses, the inferred model a continuous line, and the model folded through the PCA response matrix as histograms. The observation was made on 1996 August 23, with 10.0 ks of exposure in the PCA. Here I have accumulated the top layer only of all 5 PCUs. Bottom: Ratio of the data to the best fit power-law model. Due to the large line-like residual above 20 keV in the response matrix, for the analysis presented here I have truncated my analysis of PCA data above 20–25 keV.

both broad and shallow, they can easily blend into the continuum. Instrumental features in the spectral response of the instruments, especially around the L and K-edges of Xenon for the PCA and the K-edge of Iodine for HEXTE, can mimic, hide, and distort these features. Therefore anyone doing this type of research needs to take great care to understand the calibration of their instruments.

The standard way to investigate the systematic effects in an instrumental response matrix is to make observations of the Crab nebula and pulsar. The Crab is a relatively nearby, bright source whose spectrum is considered to be well understood. What makes it particularly useful as a standard is the stability of both its spectrum and luminosity. In the *RXTE* energy range the spectrum of the Crab nebula is known to be a simple power-law with an index of $\Gamma \sim 2.1$ (Jung 1989). The Crab pulsar is about ~10% of the total flux, and a slightly harder power-law index (Γ~1.8Knight 1982). The stability of the luminosity from the Crab has led to the use of a "mCrab" as a unit of flux density (the intensity of the source relative to $1/1000^{\rm th}$ of the Crab nebula/pulsar in the same energy range).

The dominant source of uncertainties in spectra obtained with the PCA, with its large collecting area and thus excellent counting statistics, are the systematic errors associated with the response matrix and background modeling (Wilms et al. 1999). This is not surprising since the PCA is the largest proportional counter ever flown on an X-ray astronomy satellite, with an effective area 50% more than the second largest (which was on *Ginga*, Turner et al. 1989). The PCA effective area, which is the product of the PCA detection efficiency at a given energy with the physical collecting area, is given in Fig. 2.4.

Estimates of the PCA systematic errors are left for the observers to optimize for the period of time when the observation of interest took place. For the results presented here, I have analyzed pulse phase averaged spectra of the Crab nebula and pulsar taken as contemporaneous as possible, as recommended by the PCA instrument team (K. Jahoda, private communication). When fitting the Crab, I used a combination of two power-laws. The first power-law was to account for flux from the Crab nebula. The second power-law, which was harder and modeled emission from the Crab pulsar, had a normalization that was fixed to be 10% of the first (Jahoda 2000a; Knight 1982). I then examined the best fit, and increased the size of the systematic errors as a function of energy until I achieved a reduced χ^2 near unity. The second power-law is important in this type of analysis since ignoring the contribution of the pulsar would have led us to estimate larger systematic errors.

Figure 2.12 shows the results of such a fit with no systematic errors applied. Of particular note is the large line-like residual starting at ~20 keV. This is a typically seen in all PCA spectra, and there are two methods for dealing with it. The first is to use much larger systematic errors in this region, of order 5%. This is necessary because of the size of the residual. However, since I was particularly interested in searching for and analyzing CRSF lines in this region, to avoid contamination I opted to ignore this part of the PCA spectra completely.

Below 20 keV, the systematic errors used depend upon the gain epoch of the PCA

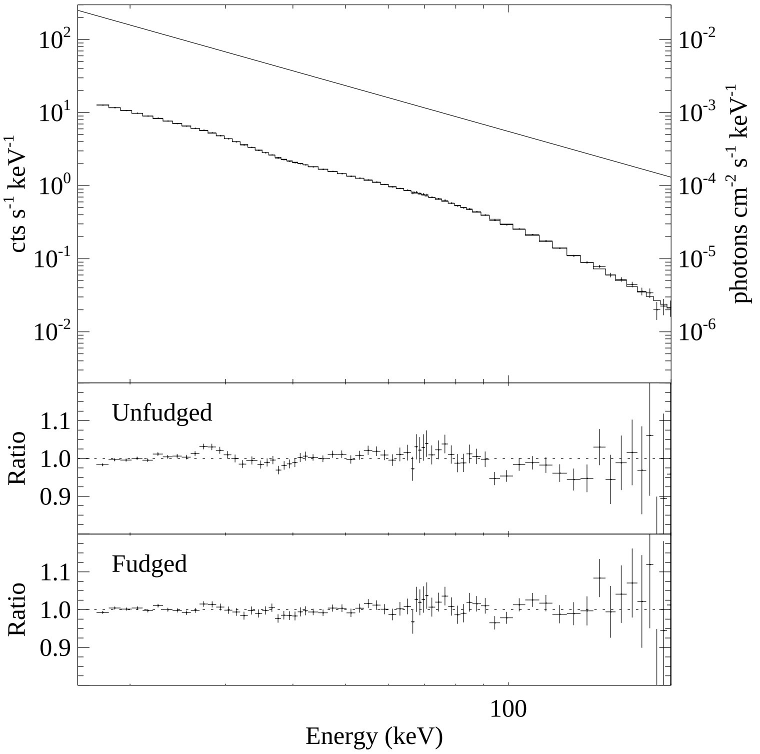

Figure 2.13: Top: Fit of a single power-law to the HEXTE spectrum of the Crab pulsar/nebula. The observation was made on 1996 August 23, with 6.6 ks of accumulated livetime for both clusters. Middle: Ratio of the data to the best fit power-law model using the unreleased, non-Crab-fudged matrices. The break around 30 keV is caused due to K escape photons from the K-edge of Iodine. Bottom: Ratio of the data to the best fit using the released matrices. These have had empirical corrections made to account for the systematic errors.

during the observation (see §2.1.1). For gain epochs 3 and 4, where the calibration of the PCA is well understood, the typical systematic error at a given energy is 0.4%. For gain epoch 1, which was shorter and earlier in mission, I found that the systematic errors required below 20 keV were 0.8%. Since PCA gain epoch 2 lasted only 25 days, little work has been done on the calibration for this period. Therefore I have not used any observations taken during PCA gain epoch 2.

The application of systematic errors to the data, although necessary, does mean that the use of the χ^2 statistic in fitting (see above) is no longer completely valid. This is because instrumental statistic errors are not χ^2 distributed. Still, quoting the χ^2 statistic when doing spectral fitting is a good, if not strictly correct, indication of how well a model fits the data.

Unlike the PCA, the dominant source of errors in spectra obtained with the HEXTE are associated with photon counting statistics. This is due partly because the collecting area of the HEXTE is much less than that of the PCA(see Table 2.1), and partly because of the lower intrinsic source fluxes in the HEXTE energy range. To this statistical limit the HEXTE calibration and is reasonably well understood and the released response matrices work quite well.

The systematic uncertainties in the raw (unreleased) response matrix when fit to a spectrum of the Crab are of order 2% near the K-edge of Iodine. This can be seen as a "wiggle" in the middle panel of Fig. 2.13. The released matrices, the same ones I have used in the analysis presented here, have had empirical corrections made ("Crab-fudges") to remove these uncertainties. The resulting fit to the Crab can be seen in the top and bottom panels of Fig. 2.13. It should be noted, however, that while these fudges do reduce the residuals in fits to the Crab, they are not strictly appropriate for sources with other spectral shapes. Therefore one has to be very careful before claiming the detection of any spectral features, including CRSFs (see §5.3.2), found near the K-edge of Iodine.

2.2.4 Continuum Models

When searching for CRSFs, having a good model of the underlying continua that the lines modify is very important. Unfortunately, after two decades of work there still exists no convincing theoretical model for the shape of the continuum X-ray spectrum in accreting X-ray pulsars (Harding 1994, and references therein). Therefore observers are forced to use phenomenological spectra in the fitting process.

In the *RXTE* band (2–250 keV) these models take the general form of a power law that breaks into a power-law times an exponential above a characteristic cutoff energy. Throughout this work I will refer to this shape as the standard X-ray continuum shape for accreting pulsars, or simply the standard pulsar spectrum. There are 3 primary analytic realizations of this shape; the power-law with a high-energy cutoff (PLCUT), a power-law with a Fermi-Dirac form of the cutoff (FDCO), and dual power-laws with opposite signs along with an exponential cutoff (NPEX). All three are described below.

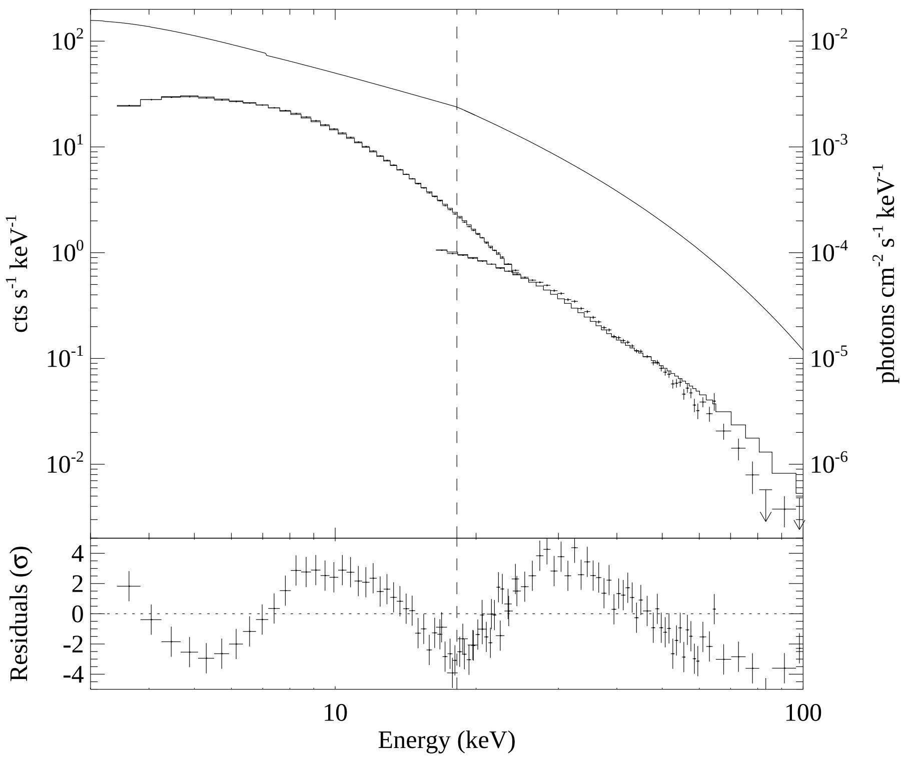

Figure 2.14: A smoothly varying continuum spectrum fit with the PLCUT continuum. The simulated spectrum was generated using the FDCO model without a CRSF(Γ=1.0, $E_{\rm cut}$=20 keV, 3–100 keV source flux of 2.61×10^{-9}). The discontinuity in the model has resulted in a large, broad residual centered at the cutoff energy ($E_{\rm cut}$=18.2 keV, indicated by the vertical dashed line).

PLCUT

The historical version of the standard pulsar continuum is the power-law with a high-energy cutoff (PLCUT). This model is of the form (White, Swank & Holt 1983):

$$\mathrm{PLCUT}(E) = A\ E^{-\Gamma} \times \begin{cases} 1 & (E \leq E_{\rm cut}) \\ \mathrm{e}^{-(E-E_{\rm cut})/E_{\rm fold}} & (E > E_{\rm cut}) \end{cases} \tag{2.2}$$

where Γ, $E_{\rm cut}$, and $E_{\rm fold}$ are the photon index, cutoff energy, and folding energies respectively.

The PLCUT has the problem of having a discontinuous derivative at the cutoff energy $E_{\rm cut}$, while the source spectrum probably does not have such a sudden change. This "kink" in the model can cause line-like residual errors at the cutoff energy, and thus can mimic the appearance of a CRSF. For CRSF searches one has to be very careful of features that appear near or at this break energy. This is clearly illustrated in Fig. 2.14, where a simulated smoothly varying *RXTE* spectrum (simulated using the FDCO model) has been fit with the PLCUT model.

Even so, the PLCUT model can be used successfully if the statistics of the observation are small enough (thus hiding the discontinuity). Any claims, however, of a spectral feature near the cutoff energy are not only highly suspect, but also almost certainly artifactual. For observations with a significant detection of the source, like the one simulated in Fig. 2.14, the effect on the fitting procedure can be substantial.

To successfully apply the PLCUT model in cases with excellent counting statistics, a smoothing function must be used to continuously join the power-law with the cutoff power-law. For example, Burderi et al. (2000) used a third order polynomial (with the requirement that the derivatives be continuous) in a region $\pm\Delta E$ around the cutoff energy. Another technique, the one I have adopted for this work, is to add a narrow, shallow Gaussian shaped absorption feature (see GABS, defined in §2.2.5)at the cutoff energy. This significantly reduces out the effects of the discontinuity, although again any spectral feature found near the break is suspect.

FDCO

Another analytic version of the standard pulsar continuum, proposed by Tanaka (1986), is the Fermi-Dirac cutoff power-law (FDCO). This is of the form:

$$\mathrm{FDCO}(E) = A\ E^{-\Gamma}\ \frac{1}{1 + \mathrm{e}^{(E - E_{\mathrm{cut}})/E_{\mathrm{fold}}}} \tag{2.3}$$

where E_{cut} and E_{fold} are the cutoff and folding energies of this model. The chief advantage of this form is that it has a smooth and continuous turnover. I have successfully used this model to fit a large number of accreting pulsar spectra.

Historically, the names for E_{cut} and E_{fold} are the same for both the PLCUT and FDCO models. These are, however, very different forms of an exponential cutoff and the fit parameters from these two models cannot be compared directly. Also, although the FDCO cutoff is the same as the Fermi-Dirac distribution from statistical mechanics, it is being used here solely for its analytic shape and not because of some underlying fundamental physics.

NPEX

Another spectral shape that approximates the standard pulsar continuum while also avoiding a discontinuity is the Negative and Positive power-law Exponential (NPEX), first suggested by Mihara (1995). It is realized in the form

$$\mathrm{NPEX}(E) = A(E^{-\Gamma_1} + BE^{+\Gamma_2})\mathrm{e}^{-E/E_{\mathrm{fold}}} \tag{2.4}$$

where Γ_1 and Γ_2 are both positive power-law indices, and E_{fold} is a characteristic folding energy. This model can fit a wide variety of continuum shapes, including dips, bumps, and nearly flat areas, depending on the relative normalization B of the two power-laws. If the positive photon index is fixed at a value $\Gamma_2 = 2.0$, this model is a simple analytical approximation of the Comptonization spectrum by Sunyaev & Titarchuk (1980). Mihara (1995) found that this model fit a wide variety of accreting X-ray pulsar spectra observed with the *Ginga* satellite in the range 1.5–37 keV. I have found, however, that when fitting the full *RXTE* energy range this form cannot always be applied successfully.

2.2.5 CRSF Models

Monte Carlo simulations of the cyclotron resonant scattering process have shown that the line profiles and harmonic content are strong functions of source geometry, temperature, magnetic field strength, and viewing angle (for example see Araya-Góchez & Harding 2000; Araya & Harding 1999; Isenberg, Lamb & Wang 1998a,b). In particular the shape of the fundamental can be quite complex, exhibiting large wings on one or both sides of the line, and in certain cases can even appear as an *emission* feature.

Most of the studies of CRSFs so far, include those presented here with the *RXTE*, have been without the spectral resolution or counting statistics to see these deviations from simple line shapes. Instead CRSFs have been successfully modeled with the simple analytical models GABS and CYCLABS, described below. It should be noted, however, that the fundamental CRSF in 4U 0115+36, which is at $\sim$12 keV, is not well fit with any of these simple analytic forms (Heindl et al. 1999). In the future, as the spectral resolution of hard X-ray satellites increases, so will the need to fit the observed spectra using more realistic models based upon both theory and Monte Carlo simulations.

The analytic CRSF model that I have used extensively in this research is a simple Gaussian shaped absorption line (GABS) of the following form:

$$\mathrm{GABS}(E) = \tau_{\mathrm{c}}\ \mathrm{e}^{-(E-E_{\mathrm{c}})^2/(2\sigma_{\mathrm{c}}^2)} \tag{2.5}$$

where E_{c} is the CRSF resonance energy (also called line energy), σ_{c} is the CRSF width, and τ_{c} is the optical depth at the resonance. This line modifies the continuum spectrum $I_0(E)$ in the following way:

$$I_0(E) \rightarrow I_0(E)e^{-\mathrm{GABS}(E)} \tag{2.6}$$

There are two principle drawbacks of this line shape. First, since the line modifies the incident spectrum as an exponential of an exponential, the FHWM of the feature is a complex function of not only the width σ_{c}, but also the optical depth τ_{c}. The functional form of the full-width at half max Γ is:

$$\Gamma_{\mathrm{GABS}} = 2\sigma_{\mathrm{c}}\sqrt{2\ln\left[\frac{\tau_{\mathrm{c}}}{\ln\left(\frac{2}{1+\mathrm{e}^{-\tau_{\mathrm{c}}}}\right)}\right]} \tag{2.7}$$

with the resulting Γ_{GABS} slightly larger than $2\sqrt{2\ln 2}\sigma_{\mathrm{c}}$ for a given width σ_{c}, but asymptotically approaching the standard value as τ_{c} goes to zero. This fact needs to be remembered when comparing to theoretical predictions for the line width.

The second disadvantage is that the line modifies the continuum at all energies. While the effect of the wings of the line become small away from the resonance energy, it is non-zero. For lines with a depth $\tau_{\mathrm{c}}{\sim}$few this is not a problem. However, as the line becomes narrow with respect to the energy resolution and channel binning, the wings of a deep line will still influence the fitting while the core of the line has all but disappeared. It is important when fitting to monitor and control this type of pathological behavior.

Another analytic form used historically is the Cyclotron Absorption or CYCLABS. This is realized analytically as

$$\mathrm{CYCLABS}(E) = D_{\mathrm{c}}\frac{(W_{\mathrm{c}}\,E/E_{\mathrm{c}})^2}{(E-E_{\mathrm{c}})^2+W_{\mathrm{c}}^2} \tag{2.8}$$

where E_c, D_c, and W_c are the CRSF energy, depth, and width respectively. This function is multiplied to the incident spectrum as exp($-$CYCLABS), just as in the case of the GABS. This pseudo-Lorentzian form is based on the shape of the Thomson/Compton cross sections of photons on electrons in a cold plasma (Ventura 1979). These cross sections depend on the incoming and outgoing photon polarization, with E||B the ordinary mode and E⊥B the extraordinary mode. Of the 4 combinations, only the extraordinary-extraordinary mode scattering has a resonance. The current simulations of photon scattering in more realistic conditions, however, show that the calculations for a cold plasma are not directly applicable to the regions of interest here. Also, like the GABS form, the CYCLABS model has a complex FWHM behavior and modifies the entire continuum.

When fitting CRSFs observed in astrophysical sources, in general both the CYCLABS and GABS models provide reasonable fits to the data. This is due largely because both of the models produce a similar shape around the CRSF centroid energy. Also, since the measured CRSF widths are comparable to the energy resolutions of the of satellite instruments used to detect them, the true line shapes are almost always only weakly resolved. As mentioned above, the one counter-example is 4U 0115+63.

The CYCLABS model, however, does have one distinct disadvantage when compared to the GABS form. The non-symmetric nature of the function around the CRSF energy E_c means that the blue-wing of the line remains significant out to higher energies. Also, as the width of the line increases the shape itself changes from a line-like feature into something mimicking an exponential cutoff in the spectrum. Because of this I have opted to use the slightly simpler analytical form of the GABS for this research.

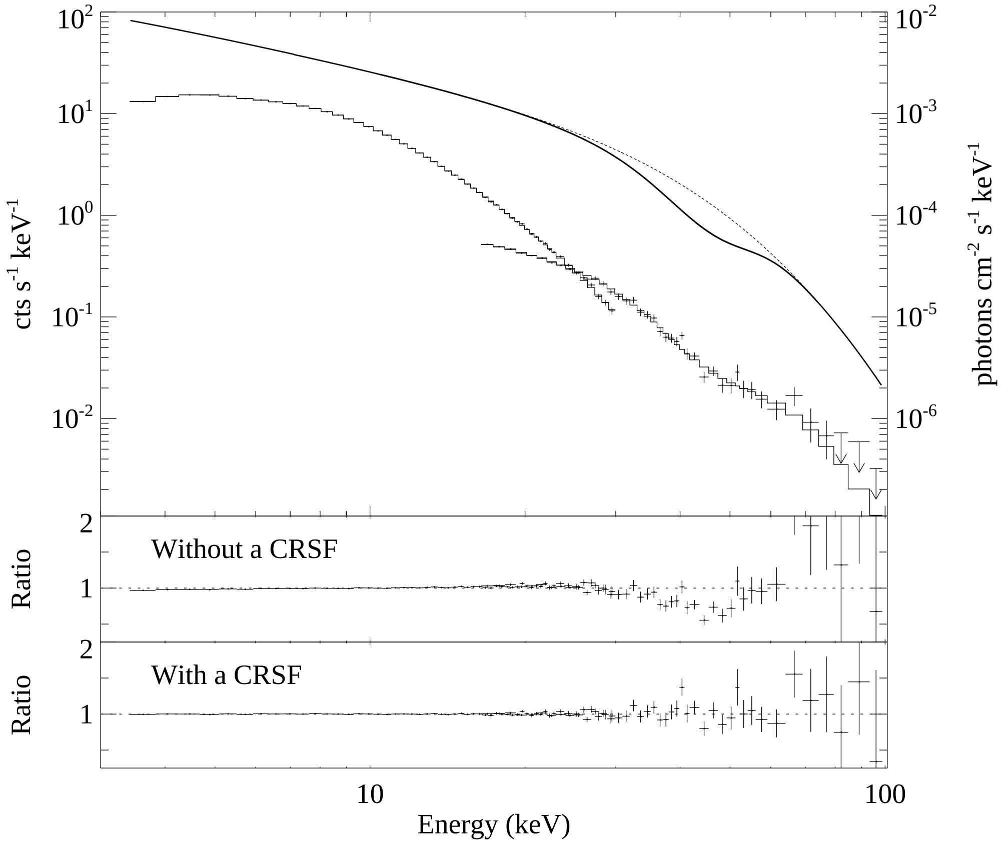

Figure 2.15: Top: A 30 ks simulated *RXTE* spectrum with a CRSF, with a 3–100 keV flux of 1.19×10^{-9}. The PCA and HEXTE counts are shown as crosses, the input model as a solid line, and the model folded forward through the appropriate response matrices as histograms. The line is at 45 keV, with $\sigma_c = 9$ keV and $\tau_c = 0.67$, and can be seen as an inflection in the counts spectrum at ~50 keV. To illustrate how the CRSF modifies the photon spectrum, the input model with the CRSF depth set to zero is given as a dotted line. Middle: Ratio of the data to the model without a CRSF in the fit model. The rising pattern at energies above 40 keV is a classic signature of a CRSF(see §2.2.6). Bottom: Ratio of the simulated data fit with a CRSF. Note that the vertical scale has been compressed when compared to the pane above.

2.2.6 CRSF Identification

Unlike the lines seen in the UV-IR (3150 Å~1 μm) wavelengths which are generally very prominent, CRSFs are often very difficult to detect in hard X-ray spectra. This is largely due to two main reasons. First, the lines themselves tend to be broad ($\sigma_c \sim 0.2 E_c$) and quite shallow ($\tau_c \sim 0.5$–1). Because of this CRSFs can easily hide in the continuum, a fact which is further exacerbated by the phenomenological nature of the continuum models themselves. Great care has to be taken to ensure that the feature is truly present, and not just an artifact of the fitted model or procedure. In the literature one of the main criterion for the existence of a CRSF is that it persists no matter which continuum model is used.

Another problem in line detection is that CRSFs lie in the exponentially cutoff part of the spectrum (see §3.2.3). The one counter example, where whether or not a cutoff is present is still unknown, is 4U 0352+309 (see §5.4). So not only are the lines shallow and broad, they modify a steeply falling continuum in a region where the counting statistics are becoming poor. This conspiracy of shallow features in steeply falling continua make the detection and secure identification of CRSFs difficult.

The usual way of identifying CRSF is to fit a number of continuum models (see §2.2.5 above), and then search for line-like residuals in plots of ratios of data to the model. Since there are more counts at energies below the resonance energy, the errors are smaller and thus have a greater effect on the fitting process. When fitting without a CRSF in the model, these smaller errors drive the continuum to hug the red wing of the line, miss the resonance energy, and under predict the continuum at higher energies. This gives rise to a dip followed by a rise in a ratio plot - the classic signature of a CRSF. This is illustrated in the simulated *RXTE* spectrum in Fig. 2.15. If there is a CRSF exhibited in the spectrum, then adding one to the model will cause this pattern to disappear and the fit should improve significantly.

Chapter 3

Spectra and Magnetic Fields

As mentioned in Chapter 2, despite more than two decades of research there is still no compelling model for the hard X-ray spectrum of accretion powered pulsars. This stands as a monument to the difficulties and complexities of radiative transport and MHD in extremes of temperature, gravitation, and magnetic field found at the neutron star magnetic polar caps.

In this chapter I present an investigation into the effects of the strong pulsar magnetic fields ($\gtrsim 10^{12}$ G) on the resulting hard X-ray spectra for the sources where there is a measurement of the pulsar B-field. I have accomplished this by parameterizing the pulse phase averaged spectral shapes of these sources, and then searching for correlations among the shape parameters. In particular, I searched for how the CRSF energy (or neutron star B-field strength) influenced the standard accreting pulsar spectrum, and therefore how the magnetic field might be influencing the overall X-ray emission from the pulsar polar caps. This analysis is important for the understanding of what is happening in the polar emission regions, and can possibly be extrapolated to accreting X-ray pulsars where the magnetic field strength is unknown.

Another motivation is to provide observations that can help theoretical investigations into which physical mechanisms are important, and help constrain future calculations and simulations of pulsar spectra.

To this end I have done a uniform pulse phase averaged spectral analysis of all the pulsars in the *RXTE* database that exhibit cyclotron resonance scattering features. A list of these sources, along with some of their properties, is given in Table 3.1. By working with sources where the magnetic field is known, one variable is removed from the parameter space and the gross effects of the field can be inferred. These sources are also useful because the line-shape parameters, width and depth, can be used to further infer information about the temperature and possibly the emission and viewing geometries (see §1.5.1).

I have parameterized the spectral shape of these 10 sources (see Table 3.1) using a smoothed PLCUT model (see §2.2.4) for each source. The functional form of the smoothing that I chose was a relatively narrow ($\sigma \sim 10\%$), shallow ($\tau \sim 0.1\,\mathrm{keV}$) Gaussian absorption feature (see Eq. 2.5). While this did not analytically smooth the PLCUT, it did reduce the pattern of residuals near the cutoff energy. The centroid energy of the Gaussian was allowed to vary in the fits, but fell within 0.3% (usually less) of the cutoff energy.

Since the ultimate goal of this analysis was to search for correlations in fit parameters, I first analyzed the various models themselves for any systematic effects which would create spurious or false results. Of the three analytic forms normally used (the PLCUT, FDCO, and NPEX, see §2.2.4), I have chosen to use the PLCUT because it offers 3 distinct advantages. First, this is the form that has been most used historically to fit pulsar spectra (White, Swank & Holt 1983). It therefore allows for the direct comparison of fit parameters of earlier observations. Even though the PLCUT, FDCO, and NPEX models produce similar shapes, the details of the various functional forms make a meaningful comparison of results across models impossible.

Second, the analytic complexities of the other forms meant that, in general, the χ^2 valleys for the fits were relatively broad and flat. Therefore it was difficult for the fitting routines to find sets of parameters that represented a true minimum in χ^2, resulting in fits that were slow to converge. These flat error basins also often implied larger uncertainties in the fit themselves. Comparisons of these error valleys

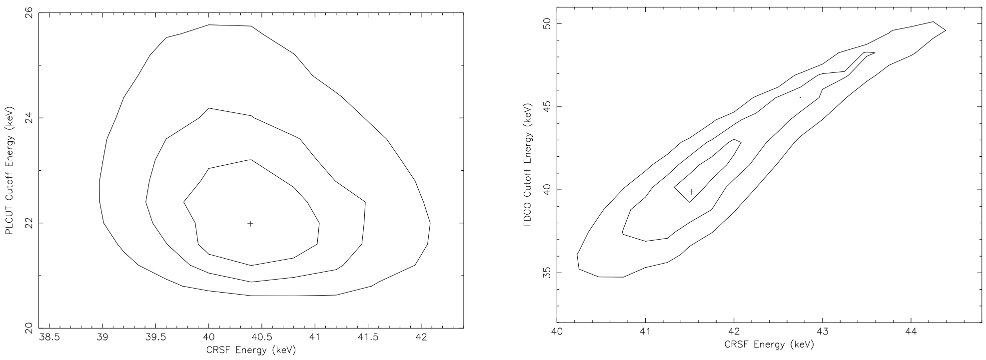

Figure 3.1: Left: Contour plot of CRSF energy E_c versus PLCUT cutoff energy E_{cut}(all plots on this page were obtained using spectral fits of Hercules X−1). Right: A similar plot using the FDCO continuum model. See §2.2.4 for a description of the model forms. It is readily apparent the the two parameters are highly correlated with each other in the FDCO model, while for the PLCUT model they are relatively independent. This aspect of the FDCO makes attempts to correlate the values obtained in spectral fitting suspect, hence my use of a smoothed PLCUT in the analysis presented here.

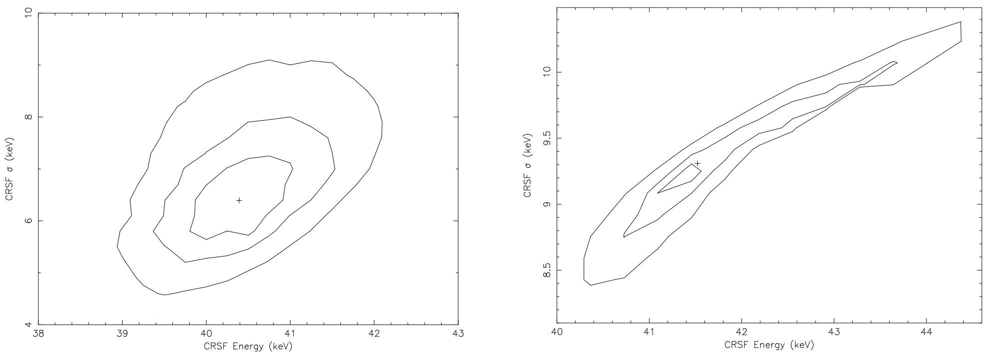

Figure 3.2: Left: Contour plot of CRSF energy E_c versus CRSF width σ_c with a PLCUT continuum model. Right: A similar plot using the FDCO continuum model. Again, the parameters of the FDCO model exhibit a high degree of interdependence.

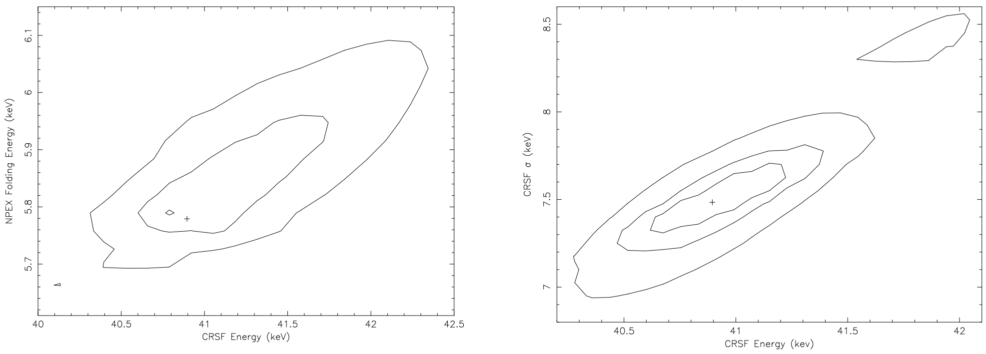

Figure 3.3: Similar contours to those above using the NPEX model. While the contours are not as pronounced as in the FDCO model, they are still quite elongated.

Table 3.1: *RXTE* CRSF Sources

System	Type	$P_{\rm spin}$ (s)	$P_{\rm orb}$ (days)	Companion (MK Type)	Eclipsing
Hercules X−1	LMXB	1.2377	1.70	HZ Her (A/F)	**Yes**
4U 0115+63	Be-Transient	3.61	24.3	V635 Cas (Be)	No
Centaurus X−3	HMXB	4.82	2.09	V779 Cen (O6-8f)	**Yes**
4U 1626−67	LMXB	7.67	0.0289	KZ TrA	No
XTE J1946+274	Transient	15.83	–	–	No
Vela X−1	HMXB	283.2	8.96	HD 77581 (B0.5 Ib)	**Yes**
4U 1907+09	HMXB	440.4	8.38	(Be?)	**Nearly**
4U 1538−52	HMXB	528.8	3.73	QV Nor (B0 Iab)	**Yes**
GX 301−2	HMXB	681	41.5	Wray 977 (B1.5 Ia)	**Nearly**
4U 0352+309	Be-Persistent	837.7	250.3	X Per (09 III-Ve)	No

are shown in Figures 3.1, 3.2, and 3.3.

The third, and by far the most important, consideration was that the PLCUT model parameters themselves are relatively orthogonal to one another. This can be readily seen in Fig. 3.1, which shows error contours for spectral fits to the X-ray pulsar Hercules X−1. In the case of the PLCUT the contours are rounder, implying a lower degree of correlation between the model parameters. In contrast, the contours when fitting with the FDCO model (see Fig. 3.2) are quite elongated. The NPEX model is slightly better than the FDCO, but it is still not ideal for this type of analysis (see Fig 3.3). The problem arises when analyzing an ensemble of fits using models that exhibit such systematic correlations. Even if the underling physical parameters are initially random, convolving them though such contours will result in correlated data. These correlations, however, are merely artifacts of the modeling procedure and *not* intrinsic to the data set. This also means that any real signal in the data will be suspect because of the potential for spurious results.

So by using a smoothed PLCUT continuum, I have removed much of the systematic effects from the fitting process. In this way the work presented here hopefully reflects the underlying nature and physics of the pulsar polar emission region, and not artifacts of the fitting process itself. The results of the fits themselves are given at the beginning of §3.2 in Table 3.4.

Table 3.2: PCA Configurations During Observations (see §2.1.1)

Source	Gain Epoch	Background Model	PCUs	Layers
Hercules X−1	3	SkyVLE	0,1,2	Top
4U 0115+63	3	SkyVLE	0,1,2,3	Top
Centaurus X−3	3	SkyVLE	All	Top
4U 1626−67	1	Faint	All	Top
XTE J1946+274	3	SkyVLE	0,1,2	Top
Vela X−1	3	SkyVLE	0,1,2,4	Top
4U 1907+09	1	Faint	All	All
4U 1538−52	3	SkyVLE/Faint	0,1,2	Top
GX 301−2	3	SkyVLE	All	Top
4U 0352+309	3	SkyVLE	0,1,2	Top

Note, however, that since a uniform model was applied to all sources instead of finding an analytic form of the continuum that best described each dataset individually, the fits presented here are not necessarily the best fit to the data. In fact, the fits to, for example, 4U 1538−52 (§3.12) and 4U 19007+09 (§3.11) are somewhat poor. Having a best fit, however, was secondary to obtaining a consistent set of parameterizations with which to compare the spectral shapes. Because of this these fits should not be considered the definitive *RXTE* measurements of these source spectra.

3.1 Sources and Observations

The various pulsars discussed in this work, both in this and later chapters, have received varying amounts of coverage by the *RXTE* in the first 5 years of operation. In fact (as of April 2001) there is over 8.7 Ms of accumulated time in the *RXTE* archive. That is over 100 d of observations, and with cuts in efficiency due to Earth occultation and SAA passages the total observing times is much higher. The subset of time spent on sources that exhibit CRSFs is 3.6 Ms and is spread out over nearly 600 observations.

Given the size and richness of this database, it is unfeasible to present here the results of all of these many observations. So instead I discuss a representative subset (see Table 3.3), chosen to be as long and continuous as possible, and with the source as bright as possible. The spectra presented in this chapter were accumulated and analyzed using the methods and techniques outlined in Chapter 2, with specifics of the PCA data accumulation given in Table 3.2. Anything else germane for particular sources is mentioned during the discussion of that source. The rest of this section is devoted to descriptions of the 10 *RXTE* CRSF pulsars and their pulsation phase averaged spectra.

Table 3.3: Summary of Observations

Source	Date	PCA: Exposure (ks)	PCA: Rate (cts s^{-1} PCU^{-1})[a]	HEXTE: Livetime (ks)	HEXTE: Rate (cts s^{-1})[b]
Hercules X−1	1997 September 14	19.4	254.2 ± 0.2	11.9	56.2 ± 0.1
4U 0115+63	1999 March 3	16.7	927 ± 1	15.4	112.6 ± 0.1
Centaurus X−3	1997 Feb 28/Mar 2	157.3	560.4 ± 0.4	129.4	51.83 ± 0.04
4U 1626−67	1996 February 11–14	121.5	26.78 ± 0.02	81.8	6.49 ± 0.05
XTE J1946+274	see Table 6.1	30.6	237.1 ± 0.1	19.7	43.0 ± 0.1
Vela X−1	1998 January 22	19.1	208.0 ± 0.3	11.5	120.4 ± 0.2
4U 1907+09	1996 February 21	18.3	18.29 ± 0.04	12.2	1.9 ± 0.2
4U 1538−52	1997 January 3–5	100.8	46.83 ± 0.04	62.1	5.10 ± 0.06
GX 301−2	1996 September 12	27.0	114.6 ± 0.08	20.6	50.1 ± 0.1
4U 0352+309	see Table 5.1	161.4	20.55 ± 0.03	109.3	1.60 ± 0.04

a In the range 3–20 keV
b In the range 15–100 keV

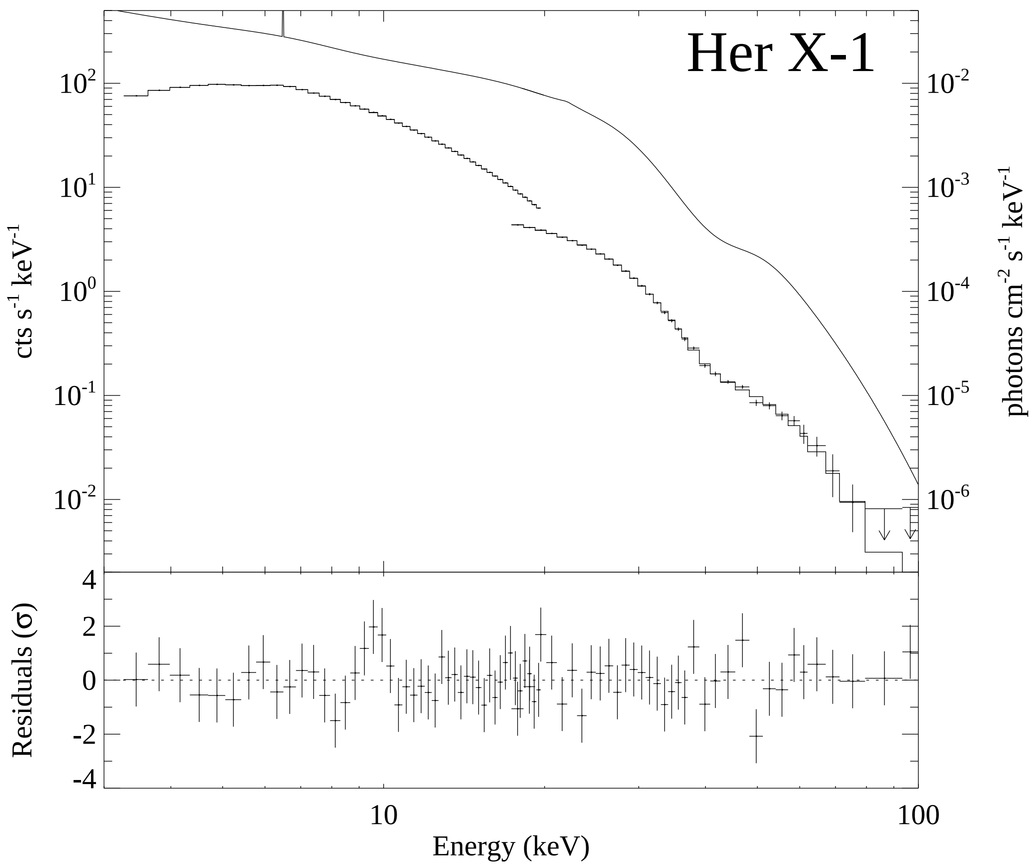

Figure 3.4: Top: Spectrum of Her X−1, fit with a smoothed PLCUT continuum, both broad and narrow Fe-K lines, and a CRSF. Shown are the counts spectrum (crosses), inferred photon spectrum (smooth curve) and model folded through the instrumental responses (histogram). The CRSF is readily apparent in both the models and the counts as the feature at ∼40 keV. Bottom: Residuals to the fit, plotted in units of σ.

3.1.1 Hercules X−1

Her X−1 is a well known persistent accreting X-ray pulsar and one of the most extensively studied sources in all of X-ray astronomy. It is the second X-ray pulsar discovered (Tananbaum et al. 1972), following Cen X−3. Her X−1 is characterized by a 1.24 s pulse period (Tananbaum et al. 1972) and a 1.7 d orbit (Deeter, Boynton & Pravdo 1981) around the A/F star HZ Her (Doxsey et al. 1973; Gottwald et al. 1991). Her X−1 also exhibits a 35 d intensity cycle that is generally believed to be due to the precession of a tilted, warped accretion disk viewed nearly edge on and which periodically obscures X-rays from the central neutron star. Detailed models of the physical cause of the warping have been suggested by Shakura et al. (1999),

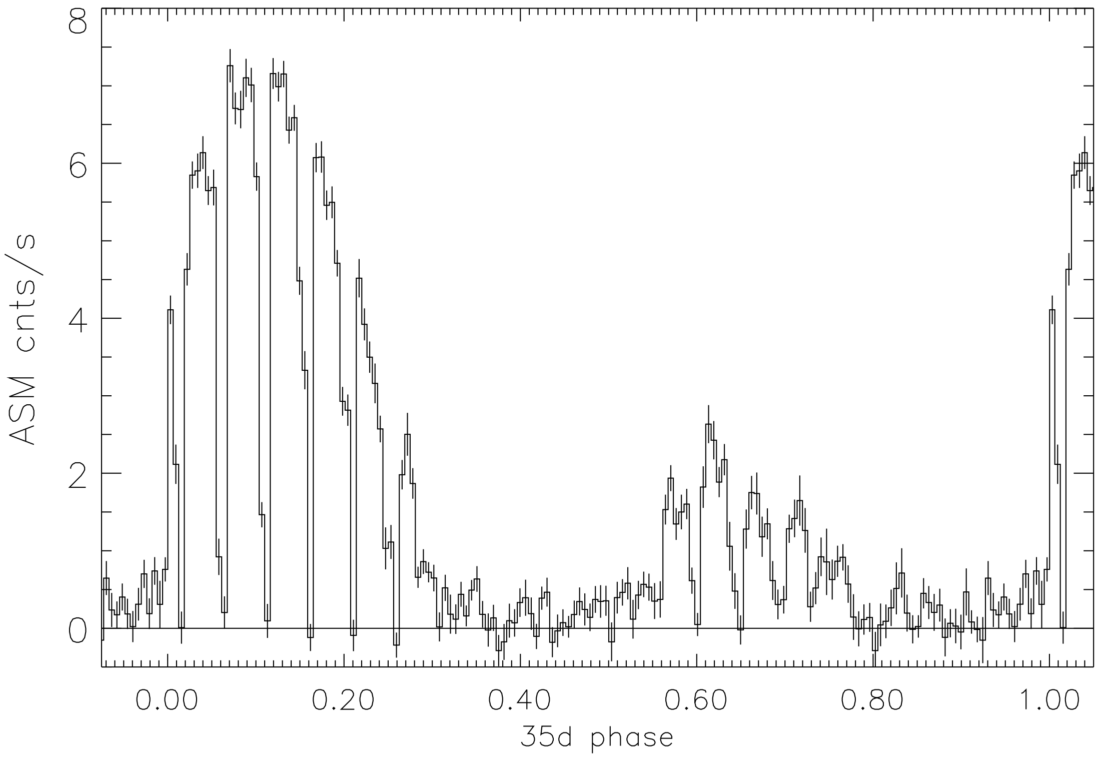

Figure 3.5: ASM light curve of Hercules X−1, folded on the 35 d intensity period. The primary peak in the light curve is the 10 d main-on state, followed by a 10 d off-state and then a ∼5 d short-on. The sharp dips every 1.70 d in the FLC are caused by the neutron star being eclipsed by its companion. (after Scott & Leahy (1999), Figure 1, bottom panel)

Maloney & Begelman (1997), Pringle (1996), and Schandl & Meyer (1994).

During the 35 d cycle, Her X−1 normally has a ∼10 d main-on state and a ∼5 d short-on state, each separated by ∼10 d low states. This is illustrated in the folded ASM light curved show in Fig 3.5. The peak count rate in the ASM for the short-on is usually ∼35% that of the main-on while the low state is ∼3% (Scott & Leahy 1999). Eclipses are seen at the 1.7 d orbital period, as are regular pre-eclipse absorption dips every 1.62 days (the 1.7 d and 35 d beat period, Giacconi et al. 1973; Crosa & Boynton 1980), and anomalous dips shortly after the main-on turn-on. The X-ray absorption dips are discussed in more detail by Stelzer et al. (1999), Shakura et al. (1998), Leahy (1997), and Reynolds & Parmar (1995). Additionally, Her X−1 undergoes periods of continuous X-ray occultation known as anomalous low states (Coburn et al. 2000, and references therein).

Her X−1 is also notable as the first X-ray pulsar where a CRSF was discovered.

Trümper et al. (1978), in a spectrum obtained during a balloon observation using NaI scintillators, found evidence for a feature which they interpreted as an *emission* line at $\sim$58 keV. This feature, as either cyclotron emission or absorption, was confirmed by Voges et al. (1982) using a detailed pulse phase resolved spectral analysis. Later satellite observations, with finer spectral resolution and better statistics, found that the feature was best modeled as an absorption rather than emission line (Soong et al. 1990; Mihara et al. 1990). Recent analysis by Gruber et al. (2001), comparing *HEAO–1* and *RXTE* observations, has shown that the cyclotron resonance energy changed from $\sim$34 keV to $\sim$42 keV sometime between 1991 and 1993.

The Her X$-$1 observation analyzed here is a subset of a larger group of pointings which have been analyzed by Kuster et al. (1999) for other purposes, and covers a complete turn-on of the source, including low-state data, eclipse, and an anomalous X-ray dip. For the analysis here only data from the peak of the main-on, after the X-ray eclipse, was used. This was done to ensure that the resulting spectrum represented the intrinsic neutron star polar cap emission, minimizing the effect of the accretion disk.

The resulting spectrum, along with the parameterizing fit, is shown in Fig. 3.4. In addition to a PLCUT continuum and CRSF, the fit contains two Fe-K lines (both near the iron fluorescence energy 6.5 keV). The first line was narrow, with a 78 eV Equivalent Width (EW), and the second one much broader, 370 eV EW. Overall the fit is quite good, with (unfortunately) no indication of a second CRSF harmonic near 80 keV. The broad Fe-K line is similar to the single 240 eV Fe-K line seen with *Ginga* (Mihara et al. 1991) during the main-on, although I find that a second, narrow line (which is at the detection limit for an Fe-K line in the PCA) is required by the *RXTE* data.

There is also a small pattern in the residuals near 10 keV. This feature is only a $\pm$0.8% deviation so does not affect the fit significantly. It does, however, appear systematically through $\sim$10 PHA channels. This unexplained feature near 10 keV is exhibited in the spectra of many accreting X-ray pulsars, and is discussed in §3.2.4.

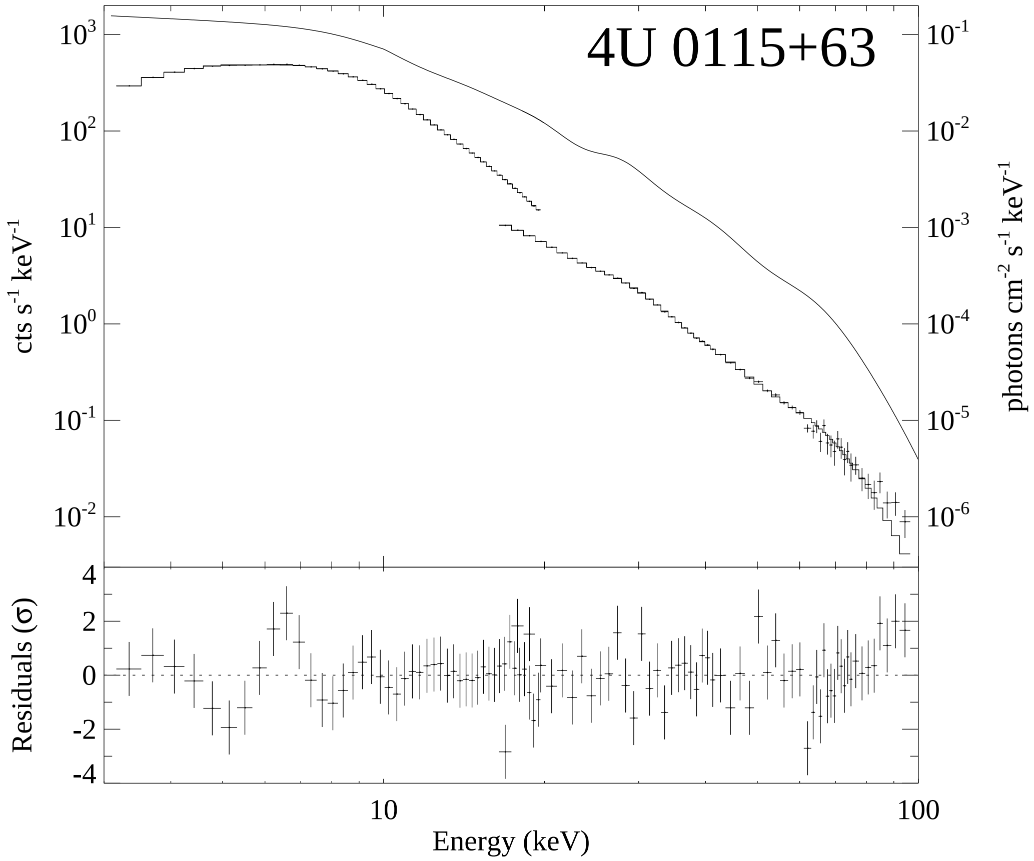

Figure 3.6: Top: Spectrum of 4U 0115+63 taken during outburst, fit with a smoothed PLCUT continuum, and 4 CRSFs. Shown are the counts spectrum (crosses), inferred photon spectrum (smooth curve) and model folded through the instrumental responses (histogram). The CRSFs can be seen as the wiggles in the inferred photon spectrum. Bottom: Residuals to the fit, plotted in units of σ.

3.1.2 4U 0115+63

The transient X-ray source 4U 0115+63 is an accreting X-ray pulsar in an eccentric 24 d orbit (Bildsten et al. 1997) with the O9e star, V635 Cassiopeiae (Unger et al. 1998). X-ray outbursts have been observed from 4U 0115+63 with *UHURU* (Forman, Tananbaum & Jones 1976), *HEAO*–1 (Wheaton et al. 1979; Rose et al. 1979), *Ginga* (e.g. Tamura et al. 1992), and *CGRO*/BATSE (Bildsten et al. 1997), with a separation times of 1–few years. The *RXTE* has observed two flares of 4U 0115+63. The first was in 1999 March (Wilson, Harmon & Finger 1999; Heindl & Coburn 1999), and the second in 2000 September (Coburn, Rothschild & Heindl 2000).

A CRSF in 4U 0115+63 was discovered near 20 keV by Wheaton et al. (1979)

with the UCSD/MIT hard X-ray (10–100 keV) experiment aboard *HEAO*–1. White, Swank & Holt (1983) analyzed concurrent data from the lower energy (2–50 keV) *HEAO*–1/A2 experiment and found an additional feature at ~12 keV, making this the first pulsar to exhibit more than a single harmonic.

Two outbursts of 4U 0115+63 were observed with *Ginga*, in 1990 February and again in 1991 April (Nagase et al. 1991; Tamura et al. 1992; Mihara 1995). In 1990 a pair of features similar to the *HEAO*–1 results were seen. In the 1991 observation, however, the CRSF pair gave way to a single feature near 16 keV (Mihara, Makishima & Nagase 1998; Makishima et al. 1999). It is possible, however, that this single 16 keV CRSF is simply due to a pulse phase averaged analysis. Both the continuum and the fundamental CRSF energy of 4U 0115+63 vary considerably with pulse phase, and the shape of the fundamental itself is quite complex (Heindl et al. 1999b). In the *RXTE* observations, a pulse phase resolved analysis puts the fundamental CRSF at ~12 keV. In fits to the phase average spectrum, however, the fit CRSF centroid energy is 16 keV, similar to what was observed with *Ginga*. Therefore it is unsafe to conclude the the magnetic field in the emission region of 4U 0115+63 was different for the 1990 and 1991 outbursts.

I discuss here observations of the 1999 March outburst (Wilson, Harmon & Finger 1999; Heindl & Coburn 1999) obtained with the *RXTE*. It was during this outburst that 4U 0115+63 became the first X-ray pulsar found to exhibit more than just a fundamental and single overtone CRSF (Heindl et al. 1999; Santangelo et al. 1999), with 5 features observed before the spectrum runs out of statistics (Heindl et al. 1999b).

The fit shown in Fig. 3.6 consists of a PLCUT continuum along with 4 CRSFs. Although I allowed for low-energy interstellar absorption, none was required by the fits. Due to the non-Gaussian shape of the fundamental feature (Heindl et al. 1999), fitting with a GABS model results in a CRSF energy of 16.4 keV. This is slightly higher than what is obtained from pulse phase resolved fitting. Using an energy that is half that of the second harmonic, a CRSF fundamental energy of $E_{\mathrm{c}} = 11.6^{+0.2}_{-0.4}$ is obtained. Another caveat is that the line energy is a strong function of pulse phase (Heindl et al. 1999b). So while the 16 keV value is a better parameterization of the line shape, the cyclotron energy of the magnetic field is closer to 12 keV. In the fit there is also a pattern in the residuals near 7 keV that resembles an Fe-K line. These are very small deviations however, only $\pm 0.8\%$, and therefore an Fe-K line is not formally required by the fit.

This *RXTE* observation was unusual because it consisted of a single, $\sim$20 ks pointing with continuous coverage (no Earth occultations or SAA passages). Due to the length and continuous nature of the pointing we discovered a 2 mHz quasi-periodic (QPO) oscillation in 4U 0115+63 (Heindl et al. 1999). This QPO is slower by two orders magnitude than predicted by the magnetic beat frequency model for QPOs, where the oscillation is explained as a beating between the neutron star spin period and the Keplerian period at the inner edge of the accretion disk (Alpar & Shaham 1985; Lamb et al. 1985). The QPO in 4U 0115+63 is also one of the slowest QPOs seen in any accreting X-ray pulsar.

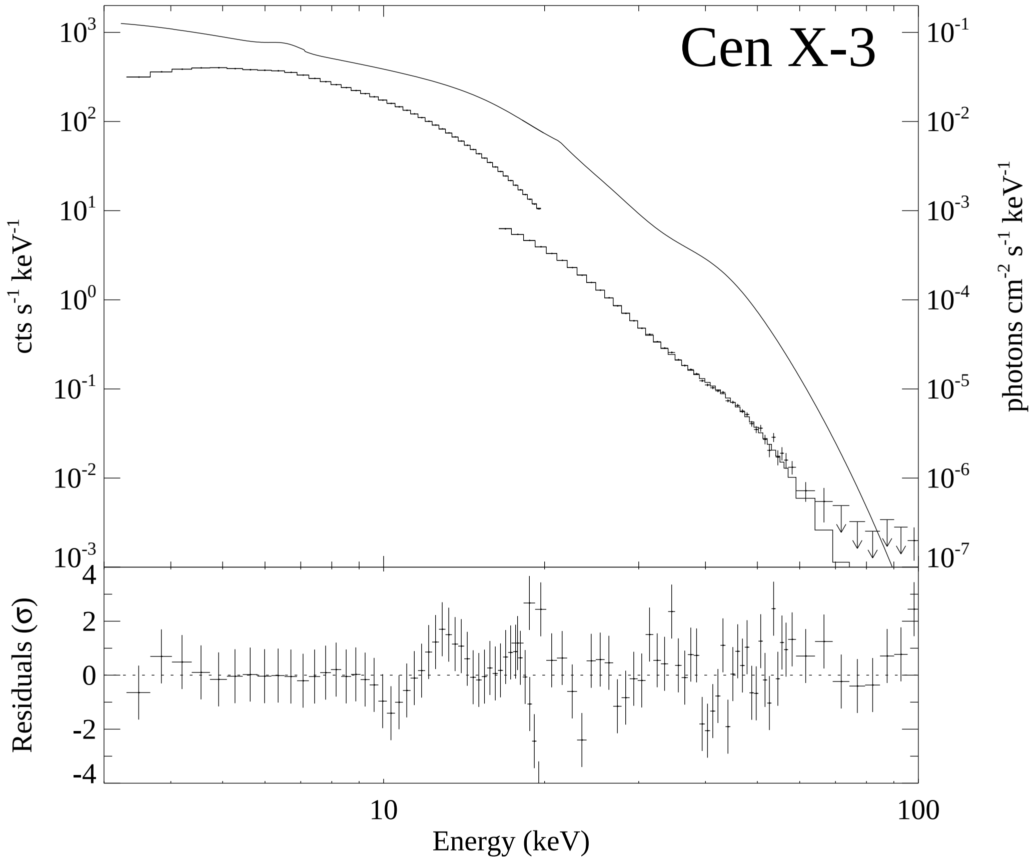

Figure 3.7: Top: Spectrum of Cen X−3, fit with a smoothed PLCUT continuum, an Fe-K line, and a CRSF. Shown are the counts spectrum (crosses), inferred photon spectrum (smooth curve) and model folded through the instrumental responses (histogram). The CRSF is apparent as the dip in both the counts and photon spectrum at ~30 keV. Bottom: Residuals to the fit, plotted in units of σ.

3.1.3 Cen X−3

The eclipsing HMXB source Cen X−3 has the distinction of being the first X-ray pulsar discovered (Giacconi et al. 1971a). The source has a spin period of 4.8 s and has a 2.1 d orbital period (Kelley et al. 1983) around the O6-8 supergiant V779 Cen (Krzemiński 1974; Rickard 1974; Hutchings et al. 1979). An accretion disk is apparent from the optical light curve of the system (Tjemkes, van Paradijs & Zuiderwijk 1986). The distance of the system is estimated to be 8 kpc (Krzemiński 1974).

Continuous monitoring with the *CGRO*/BATSE found that the long term (~years) spin-up trend actually consists of alternating spin-up and spin-down on 10–100 d intervals (Finger, Wilson & Fishman 1994). The curious thing is that the spin-up and spin-down rates are nearly equal in magnitude. Similar behavior has been observed in OAO 1657-414, and is difficult, if not impossible, to understand in terms of the accretion torque theory discussed in §1.5.2. Observations of the orbital period over the last 20 years has revealed that it is decreasing (Kelley et al. 1983; Nagase et al. 1992; Finger et al. 1993). This is thought to be due to the tidal interaction of the neutron star with its companion.

Historically the 1–40 keV spectrum has been fitted with a PLCUT, Fe-K line, and soft X-ray absorption (White, Swank & Holt 1983). The analysis of *Ginga* data by Nagase et al. (1992) showed that the high-energy cutoff is better modeled by a broad, quasi-Lorentzian CYCLABS turnover rather than by the usual e-folding energy cutoff. Their fit, however, does not provide a firm detection of the feature since the energy of the resonance ($\gtrsim$ 30 keV) is near the 37 keV limit of the *Ginga* LAC detectors. The presence of a cyclotron line at 30 keV has since been unquestionably detected by Heindl & Chakrabarty (1999) and Santangelo et al. (1998).

In addition to a PLCUT continuum and CRSF, I allowed for an Fe-K line and low-energy absorption in my fit of Cen X$-$3 (Fig. 3.7). The equivalent width of the Fe-K line was 141 eV, which is similar to the value obtained by Burderi et al. (2000) using observations obtained with *Beppo*SAX. The amount of low-energy absorption my fit required, $N_{\rm H} = (2.2 \pm 0.2) \times 10^{22}\,{\rm cm}^{-2}$, is consistent with the *Beppo*SAX value of $(1.95 \pm 0.03) \times 10^{22}\,{\rm cm}^{-2}$. As with Her X$-$1 I find a small yet systematic pattern in the residuals near 10 keV, although for Cen X$-$3 the "peak" is at a slightly higher energy.

The CRSF energy ($E_{\rm c} = 30.4^{+0.3}_{-0.4}$) presented here is the pulse phase averaged value, and is also consistent with that found with *Beppo*SAX. *RXTE* and *Beppo*SAX pulse phase resolved analysis have both revealed that the energy moves through the pulse; from $29.0^{+0.4}_{-0.3}$ keV during the pulse fall to 37.1 ± 1.7 keV during pulse rise (Heindl & Chakrabarty 1999). This implies that the magnetic field in the scattering region is changing by $\sim$20% as the neutron star rotates, and this may be evidence for the dipole moment being significantly offset from the center of the neutron star (Burderi et al. 2000). It might also be expected that this variation in the CRSF energy could also artificially broaden a phase average measurement of CRSF line width. The average emission is, however, dominated by flux from the peak of the pulse. A comparison of my fits with those of Heindl & Chakrabarty (1999); Burderi et al. (2000) indicate that this movement did not significantly contaminate my parameterization of the CRSF width σ_c.

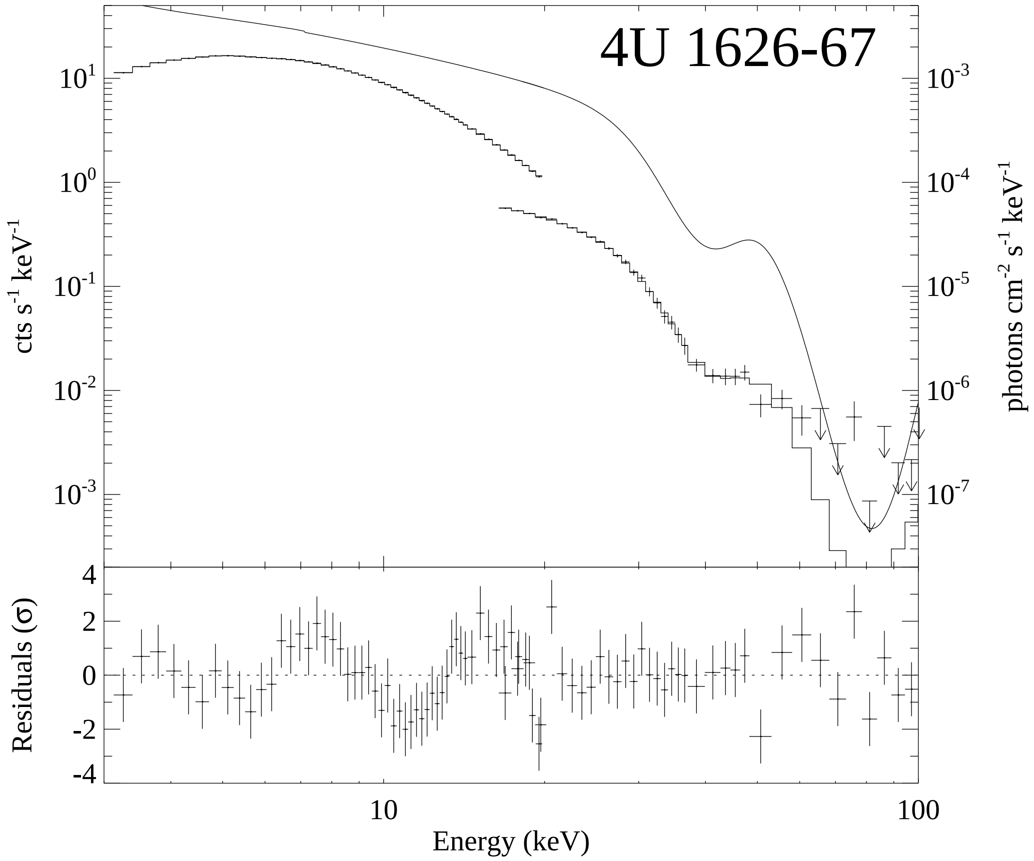

Figure 3.8: Top: Spectrum of 4U 1626−67, fit with a smoothed PLCUT continuum, blackbody, and 2 CRSFs. Shown are the counts spectrum (crosses), inferred photon spectrum (smooth curve) and model folded through the instrumental responses (histogram). The fundamental CRSF is readily apparent as the dip in both the counts and photon spectrum at ~40 keV. Since the centroid and blue wing of a possible second harmonic are completely unresolved, the existence of such a line is questionable and could be due to inadequate modeling of the underlying continuum. Bottom: Residuals to the fit, plotted in units of σ.

3.1.4 4U 1626−67

The 7.66 s pulsar 4U 1626−67 is one of five known X-ray pulsars in LMXB systems. Its companion is the low-mass dwarf star KZ TrA, and although a complete orbital ephemeris is unknown there is evidence for a 42 min orbital period (Middleditch et al. 1981). The system has one of the lowest known mass functions for a pulsar (Levine et al. 1988), with a limit of $a_x \sin(i) < 8$ lt-ms on the size of a 42 min orbit (Shinoda et al. 1990). Optical limits on the companion's luminosity rule out the possibility of accretion by a normal stellar wind (Chakrabarty 1998), so mass flow is most probably due to Roche lobe overflow of the companion in a very close binary system.

The timing history of 4U 1626−67 is characterized by a sudden change from steady spin-up to spin-down in 1990 (Chakrabarty et al. 1997). Similar apparent torque reversals have been seen in GX 1+4 (Makishima et al. 1988) and 4U 0352+309 (Di Salvo et al. 1998, and references therein). This is similar to the reversals seen in Cen X−3 and OAO 1657−415 (see §3.1.3), although on much longer timescales. In addition to the source pulsations, the power spectrum also shows a strong QPO in both the X-rays (Kommers, Chakrabarty & Lewin 1998; Shinoda et al. 1990) and the optical (Chakrabarty 1998) at $\sim$40 mHz.

Historically the hard X-ray spectrum of 4U 1626−67 has been modeled with an absorbed $\sim$0.6 keV blackbody in addition to the standard pulsar continuum, so when when fitting I have allowed for these components as well. In addition to the fundamental CRSF, I found that the addition of a *second* harmonic significantly improves the fit as well. As can be seen in Fig. 3.8, however, this feature is only evidenced only by the effects of its red wing on the continuum and so its existence is questionable. A detailed pulse phase resolved analysis of the source, including a discussion of this second harmonic, is given in §4.4.

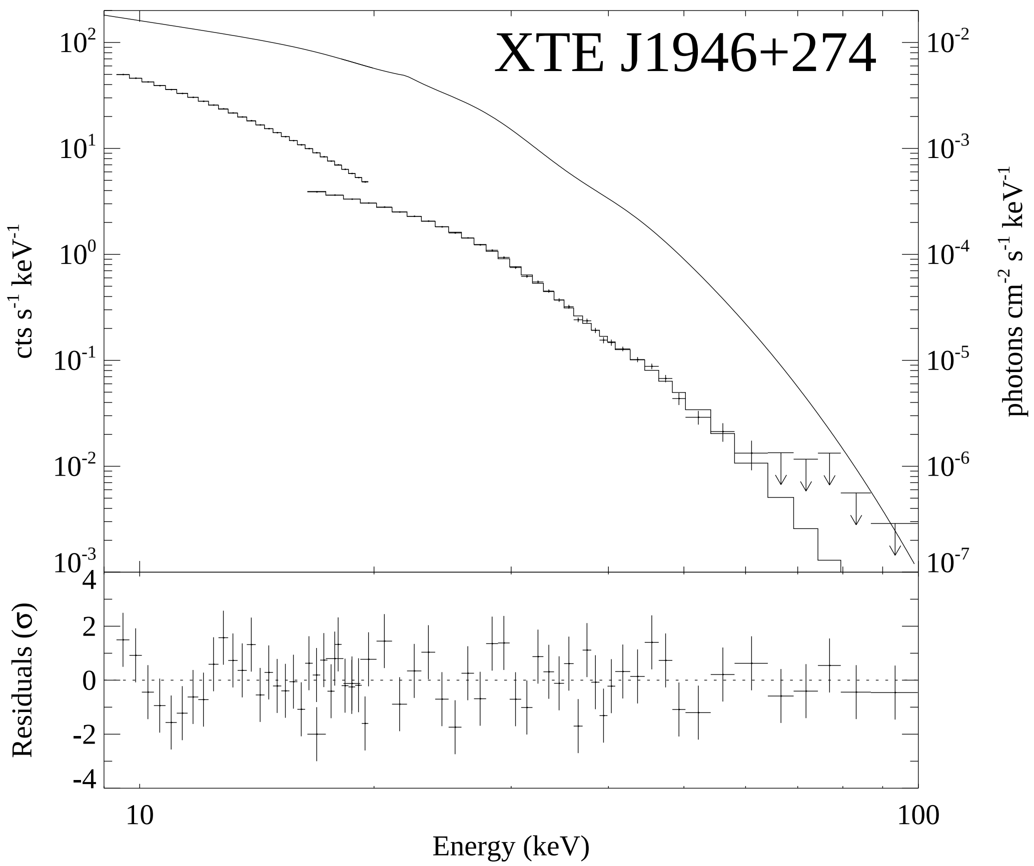

Figure 3.9: Top: Spectrum of XTE J1946+274, fit with a smoothed PLCUT continuum and a CRSF. Shown are the counts spectrum (crosses), inferred photon spectrum (smooth curve) and model folded through the instrumental responses (histogram). The fundamental CRSF is evidenced in the photon spectrum at ~30 keV. Bottom: Residuals to the fit, plotted in units of σ.

3.1.5 XTE J1946+274

Not much is known about the transient pulsar XTE J1946+274. The source was discovered with the *RXTE*/ASM during a scan of the Vul-Cyg region on 1998 September 5. It was detected at a 2–12 keV flux level of ~13 mCrab (Smith & Takeshima 1998), reaching a peak of ~110 mCrab around 17 September 1998 (Takeshima & Chakrabarty 1998). Pulsations at 15.8 s were discovered by the *CGRO*/BATSE (Wilson et al. 1998) and were later confirmed through pointed *RXTE* observations (Smith & Takeshima 1998). There is also evidence for a ~80 d periodicity in the ASM lightcurve, which is most likely due to the orbital motion of the binary system (Campana, Israel & Stella 1999). XTE J1946+274 lies in the error box of the

1976 *Ariel V* transient 3A 1942+274 (Warwick et al. 1981), suggesting that the two sources are identical (Takeshima & Chakrabarty 1998). The source has also been designated 1SAX J1945.6+2721 and GRO J1944+26. I use the ASM designation XTE J1946+274 throughout this work.

As part of my analysis of *RXTE* archival data I discovered a CRSF in this source. This discovery, along with a detailed analysis of this spectrum, is presented in Chapter 6, and has been submitted to the *Astrophysical Journal Letters*.

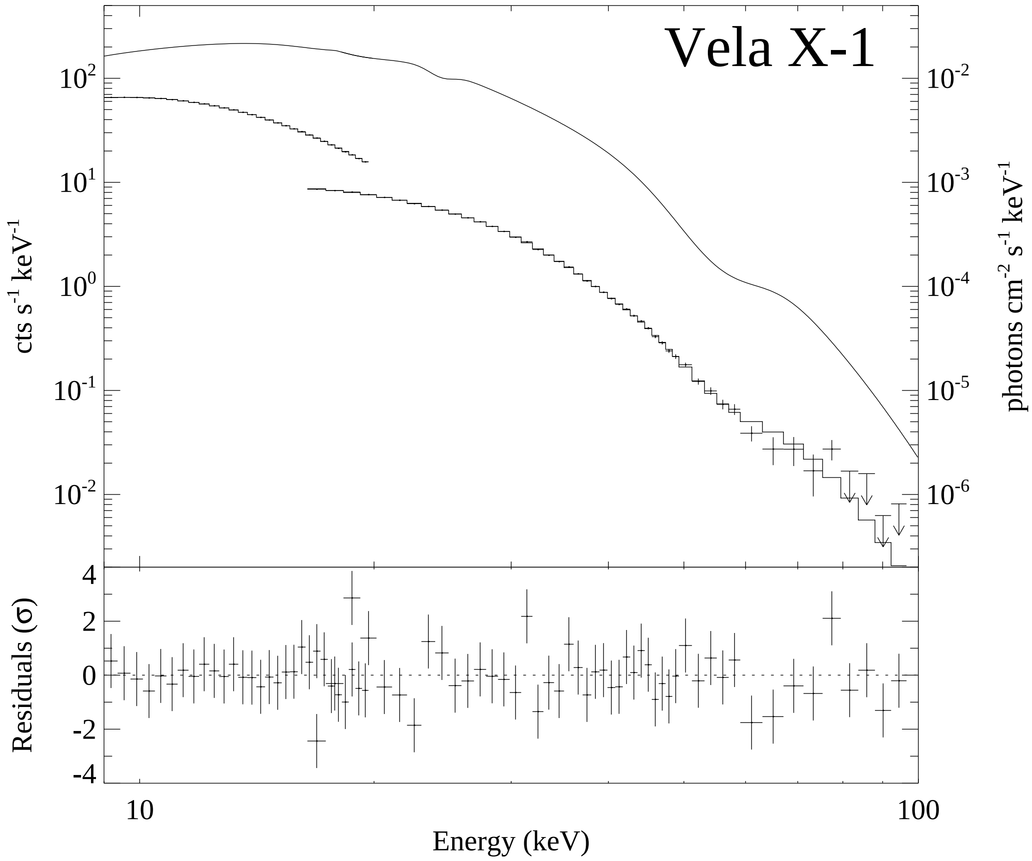

Figure 3.10: Top: Spectrum of Vela X−1, fit with a smoothed PLCUT continuum and two CRSFs. Shown are the 3counts spectrum (crosses), inferred photon spectrum (smooth curve) and model folded through the instrumental responses (histogram). The second harmonic CRSF is readily apparent in both the counts and photon spectra at ~55 keV. Bottom: Residuals to the fit, plotted in units of σ.

3.1.6 Vela X−1

Vela X−1 (4U 0900−40) is an eclipsing HMXB with an orbital period of 8.964 d (van Kerkwijk et al. 1995). The companion star is the B0.5Ib supergiant HD 77581, and the system is at a distance of 2.0 kpc (Sadakane et al. 1985). Due to the closeness of the neutron star and its companion, the neutron star is deeply embedded in the strong stellar wind of HD 77581 ($\dot{M} \sim 4 \times 10^{-6}\,\mathrm{M}_{\odot}\,\mathrm{yr}^{-1}$, Nagase et al. 1986) and X-rays are produced due to accretion of this wind onto the neutron star surface. The X-ray luminosity is typically $L_{\mathrm{x}} \sim 4 \times 10^{36}\,\mathrm{ergs\,s}^{-1}$, but can also suddenly change to less than 10% of its normal value (Inoue et al. 1984). The cause of this variability is still unknown, although it could be due to changes in the accretion rate due to variations in the stellar wind, or possibly associated with the formation of a temporary accretion disk (Inoue et al. 1984). For a detailed discussion of the system parameters, see van Kerkwijk et al. (1995).

The X-ray spectrum of Vela X$-$1 is usually described by the standard accreting pulsar continuum, plus an Fe-K line (Nagase et al. 1986; White, Swank & Holt 1983; Ohashi et al. 1984). The spectrum is further modified by photoelectric absorption due to a gas stream trailing the neutron star and due to circumstellar matter (Kaper, Hammerschlag-Hensberge & Zuiderwijk 1994). This results in significantly increased absorption near periastron passage. In addition, erratic increases in N_{H} by a factor of 10 are seen at all orbital phases (Haberl & White 1990). Evidence for CRSF at $\sim$54 keV has been reported from the *High Energy X-ray Experiment* (HEXE) on the Mir space station (Kendziorra et al. 1992), from *Ginga* (Mihara 1995), from the *RXTE* (Kreykenbohm et al. 1999, 2002), and from *Beppo*SAX observations (Orlandini et al. 1998). There is further evidence that the fundamental CRSF lies at $\sim$24 keV (e.g. Kendziorra et al. 1992; Mihara 1995; Kreykenbohm et al. 2002).

In the first half of the *RXTE* observation an anomalous X-ray dip was observed from the source, lasting $\sim$17 ks. During this time no pulsations from the source were seen. The spectrum I present here (see Fig. 3.10) was accumulated in spacecraft orbits after the dip, where the average counting rate was steady and pulsations were observed. I have parameterized the phase average spectrum of Vela X$-$1 with a PLCUT continuum and two CRSFs. To minimize the effects on the fit continuum spectrum due to the highly variable absorption column and Fe-K line in this source I have ignored PCA data below 9 keV. However, I find that some X-ray absorption is still required by the data, with $N_{\mathrm{H}} = (2.9^{+0.3}_{-0.2}) \times 10^{23}\,\mathrm{cm}^{-2}$. The width and depth of the fundamental CRSF are poorly constrained. However the addition of an absorption line near 24 keV gives an FTEST probability of 1.14×10^{-7} for a chance improvement.

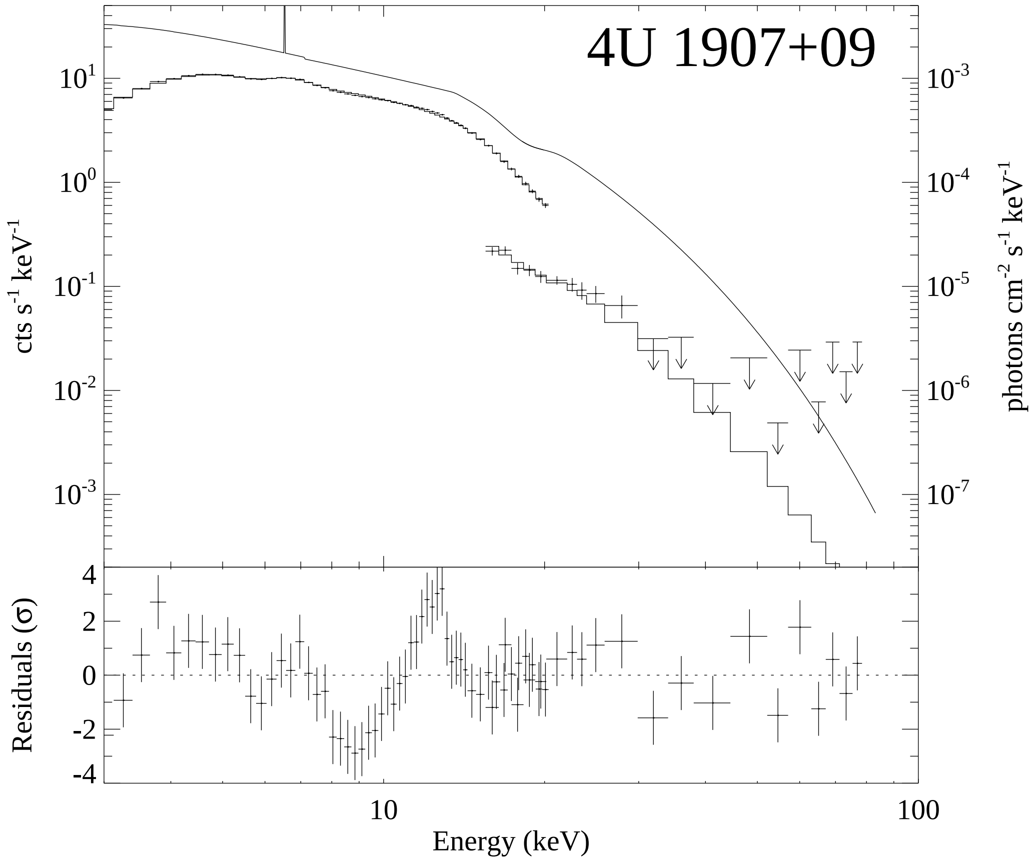

Figure 3.11: Top: Spectrum of 4U 1907+09, fit with a smoothed PLCUT continuum, Fe-K line, and a CRSF. Shown are the counts spectrum (crosses), inferred photon spectrum (smooth curve) and model folded through the instrumental responses (histogram). The CRSF is apparent in the photon spectrum at ~20 keV. Bottom: Residuals to the fit, plotted in units of σ. The large deviation at ~10 keV is seen an most accreting X-ray pulsar spectra, and is not thought to be due to a CRSF (see §3.2.4)

3.1.7 4U 1907+09

The X-ray source 4U 1907+09 was discovered with the *UHURU* X-ray satellite (Giacconi et al. 1971b). Using data taken over a period of 5 years from the *Ariel V* satellite, Marshall & Ricketts (1980) determined the 8.38 d orbital period from a folded light curve of the data which showed a pronounced primary flare and a dimmer, irregular secondary flare. Later observations with *Tenma* revealed the source to be a pulsar with a 437.5 s period (Makishima et al. 1984), as well as confirmed the existence of two orbital phase-locked flares and the measurement of the orbital eccentricity. Recent work with *RXTE* observations has produced an improved binary orbital ephemeris (in't Zand, Baykal & Strohmayer 1998), along with the discovery of X-ray dips in the source (in't Zand, Strohmayer & Baykal 1997). The neutron star, which is a reasonably persistent source of X-ray flux, is powered by wind accretion from either a close OB supergiant (Schwartz et al. 1980) or possibly a Be (Iye 1986; Roberts et al. 2001) companion star.

The hard X-ray spectrum of 4U 1907+09 has been observed by a number of satellites, including *Ariel V*, *Tenma*, *EXOSAT*, *Ginga*, *Beppo*SAX, and the *RXTE*. In addition to the standard pulsar continuum, there is evidence for soft X-ray absorption in the range $N_{\rm H} = (1.5 - 1.7) \times 10^{22}\,{\rm cm}^{-2}$ (Schwartz et al. 1980; Marshall & Ricketts 1980; Makishima et al. 1984; Cook & Page 1987; Chitnis et al. 1993, see) and an Fe-K emission line. A CRSF at $\sim$21 keV was discovered in this source by Makishima & Mihara (1992) using *Ginga* observations. Cusumano et al. (1998), using a 70 ks *Beppo*SAX observation, detected a second harmonic at $\sim$39 keV.

The spectrum presented here (see Fig. 3.11) was obtained before the failure of a pulse height analyzer in one of the HEXTE detectors (see §2.1.2), so spectral information from all 8 phoswich detectors is present. The light curve for this dataset is free from X-ray flares or dips, so the spectrum presented here is not contaminated by possible spectral variability during these intervals.

In addition to the phase averaged parameterization here, I have also conducted a pulse phase resolved analysis of 4U 1907+09. The results of this detailed spectral analysis are given in §4.5.1. I would like to point out here, however, the large ($\pm$3%) pattern in the residuals that "peaks" slightly above 10 keV. As mentioned previously, this deviation from the standard pulsar continuum is common among accreting pulsars, yet its origin is unknown. This feature is discussed briefly in §3.2.4.

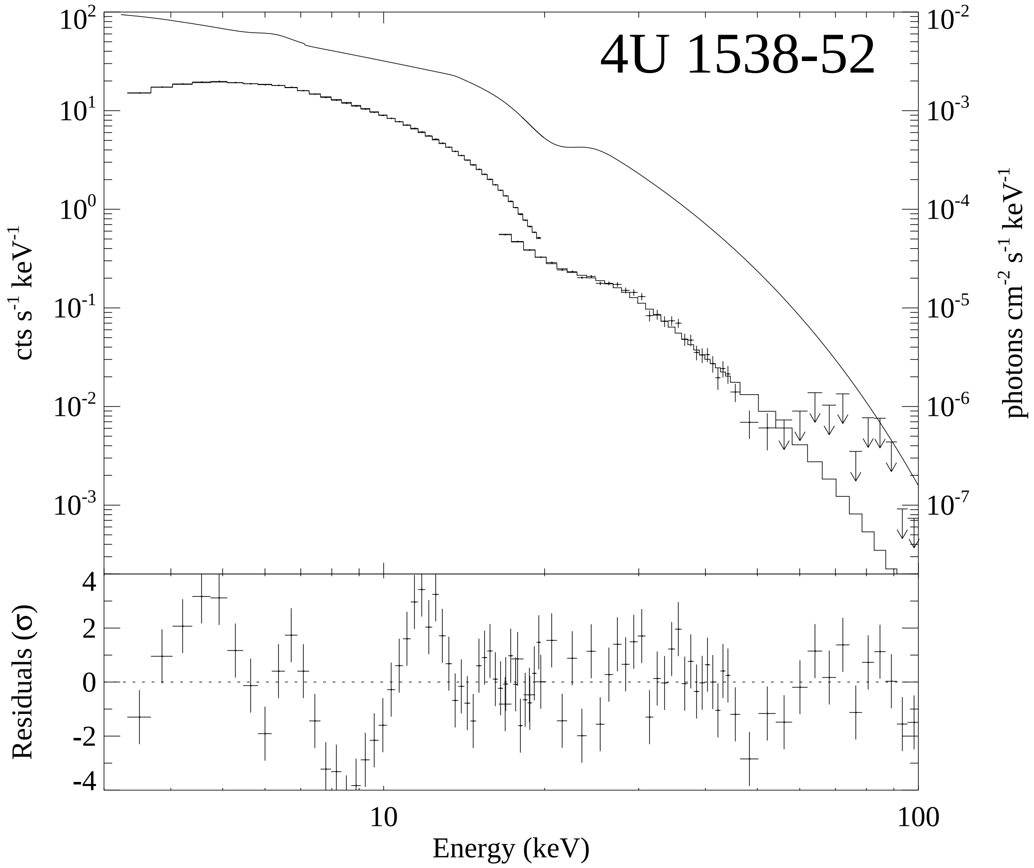

Figure 3.12: Top: Spectrum of 4U 1538−52, fit with a smoothed PLCUT continuum, Fe-K line, and a CRSF. Shown are the counts spectrum (crosses), inferred photon spectrum (smooth curve) and model folded through the instrumental responses (histogram). The CRSF is apparent in both the counts and photon spectra at ∼20 keV. Bottom: Residuals to the fit, plotted in units of σ. The large deviation at ∼10 keV is seen an most accreting X-ray pulsar spectra, and is not thought to be due to a CRSF (see §3.2.4)

3.1.8 4U 1538−52

The HMXB pulsar 4U 1538−52 is in an eclipsing system with the B0 Iab star QV Nor (Rubin et al. 1994; Corbet, Woo & Nagase 1993), with accretion proceeding through the companion's wind rather than Roche-lobe overflow (Crampton, Hutchings & Cowley 1978). The source was first detected with the *UHURU* satellite (Giacconi et al. 1974), with coherent ∼530 s pulsations later found in data from *Ariel V* (Davison, Watson & Pye 1977). The binary orbital ephemeris is well known, with an orbital period of 3.7 d and an eccentricity $e = 0.174 \pm 0.015$ (Clark 2000). Detailed analysis of BATSE data has revealed a long term spin-up at an average rate of $\dot{\nu} = 1.8 \times 10^{-14}\,\mathrm{Hz\,s^{-1}}$ (Rubin et al. 1994). The short term changes in ν, however, are consistent with being due to a random walk in frequency and support the wind accretion hypothesis. Extensive theoretical work has been done by Bulik et al. (1992) and Bulik et al. (1995) to model the polar cap emission structure and magnetic field geometry for this source.

A CRSF was discovered in a spectrum obtained with the *Ginga* satellite by Clark et al. (1990). The feature, centered at $\sim$20 keV, was found to vary by $\sim$15% through the pulse. There is no evidence for a $\sim$40 keV harmonic in the spectrum, both phase resolved and averaged (Mihara 1995, and this work). A non-harmonically spaced feature at $51.9^{+4.2}_{-3.0}$ keV has been reported by Robba et al. (1999) using observations taken with the *Beppo*SAX instrument, although my *RXTE* spectrum fails to confirm this feature.

The observation analyzed here (see Fig. 3.12) spanned nearly the entire binary orbit of the system (excepting the interval during the X-ray eclipse). In addition to the phase averaged parameterization, I have also conducted a pulse phase resolved analysis, the results of which are given in §4.3.1. I would like to point out here, however, the pattern in the residuals that "peaks" just above 10 keV. While appearing similar to the residuals seen in 4U 1907+09, the size of this deviation is smaller, only $\pm$1.5%. I briefly discuss this pattern in §3.2.4.

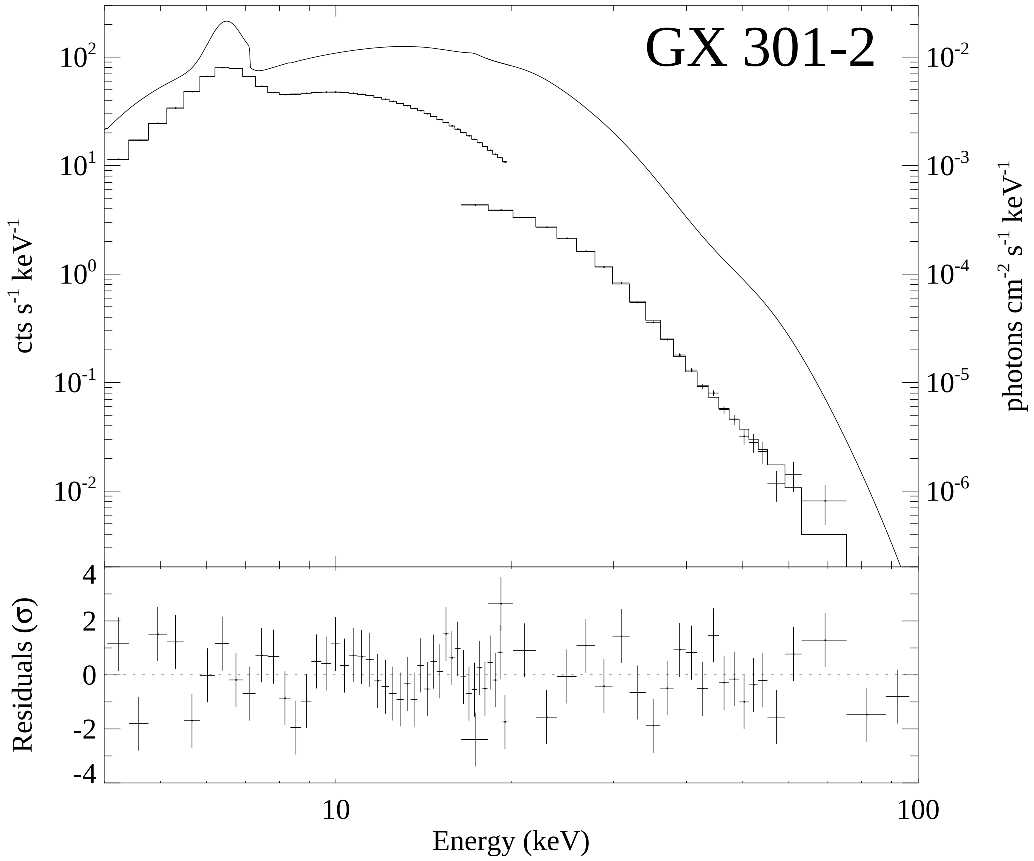

Figure 3.13: Top: Spectrum of GX 301−2, fit with a smoothed PLCUT continuum, Fe-K line, and a shallow CRSF. Shown are the counts spectrum (crosses), inferred photon spectrum (smooth curve) and model folded through the instrumental responses (histogram). The CRSF is apparent in the photon spectrum at ~45 keV. Bottom: Residuals to the fit, plotted in units of σ.

3.1.9 GX 301−2

The HMXB pulsar GX 301−2 (4U 1223−62) is a wind fed neutron star in a 41.5 day eccentric ($e = 0.47$) orbit around the supergiant companion Wray 977 (Sato et al. 1986). Pulsations from GX 301−2 were first detected by White et al. (1976) at ~700 s. Between 1975 and 1985, the neutron star showed no long term evidence for either spin-up or spin-down, which is consistent with the pulsar accreting from the wind of its companion star. After 1985 there was a prolonged period of spin-up at a rate $\dot{\nu} \approx 2 \times 10^{-13}\,\mathrm{Hz\,s^{-1}}$ (Nagase 1989). This trend may, at least in part, be due to rapid ~30 d spin-up episodes ($\dot{\nu} \approx (3-5) \times 10^{-12}\,\mathrm{Hz\,s^{-1}}$) discovered with the BATSE (Koh et al. 1997). Other than these episodes, which probably indicate the temporary formation of an accretion disk, no net changes in ν have been observed with the BATSE.

The pulsar undergoes regular flares during orbital phase $\sim$1.4 d before periastron passage, along with a smaller flare near apastron (Pravdo et al. 1995; Koh et al. 1997). The primary flare is probably due to passage through the mass outflow from the companion star which is directed primarily perpendicular to its rotational axis. The X-ray spectrum is characterized by a large and variable absorption column and a strong Fe-K line (White & Swank 1984; Leahy et al. 1989; Leahy & Matsuoka 1990).

There have been reports of a CRSF in this source at 35.6 ± 1.6 keV using observations obtained with the *Ginga* satellite at a reduced high-voltage, extending the spectral range out to 60 keV (Makishima & Mihara 1992; Mihara 1995). But due to uncertainties in the background subtraction above 36 keV and limited high energy statistics, the detection of the CRSF was not a firm one (Makishima & Mihara 1992; Makishima et al. 1999). With the *RXTE*, however, we have been able to confirm the presence of a CRSF in the spectrum at the energy $E_{\mathrm{c}} = 42.4^{+3.8}_{-2.5}$ keV.

The *RXTE* spectrum presented here (see Fig. 3.13) was obtained during a normal, non-flaring state of GX 301−2. The low-energy absorption measured with the *RXTE* is quite large, with $N_{\mathrm{H}} = (2.8 \pm 0.1) \times 10^{23}\,\mathrm{cm}^{-2}$. This is slightly larger than what was observed with *Tenma* (Leahy & Matsuoka 1990) and *Ginga* (Mihara 1995), although as mentioned above the low-energy absorption column is known to be variable. The *RXTE* spectrum also exhibits a prominent Fe-K line, with an 1.1 keV EW. Like other accreting pulsars there is an indication of a systematic residual centered near 10 keV, only here it is much less pronounced ($\sim \pm 0.5\%$).

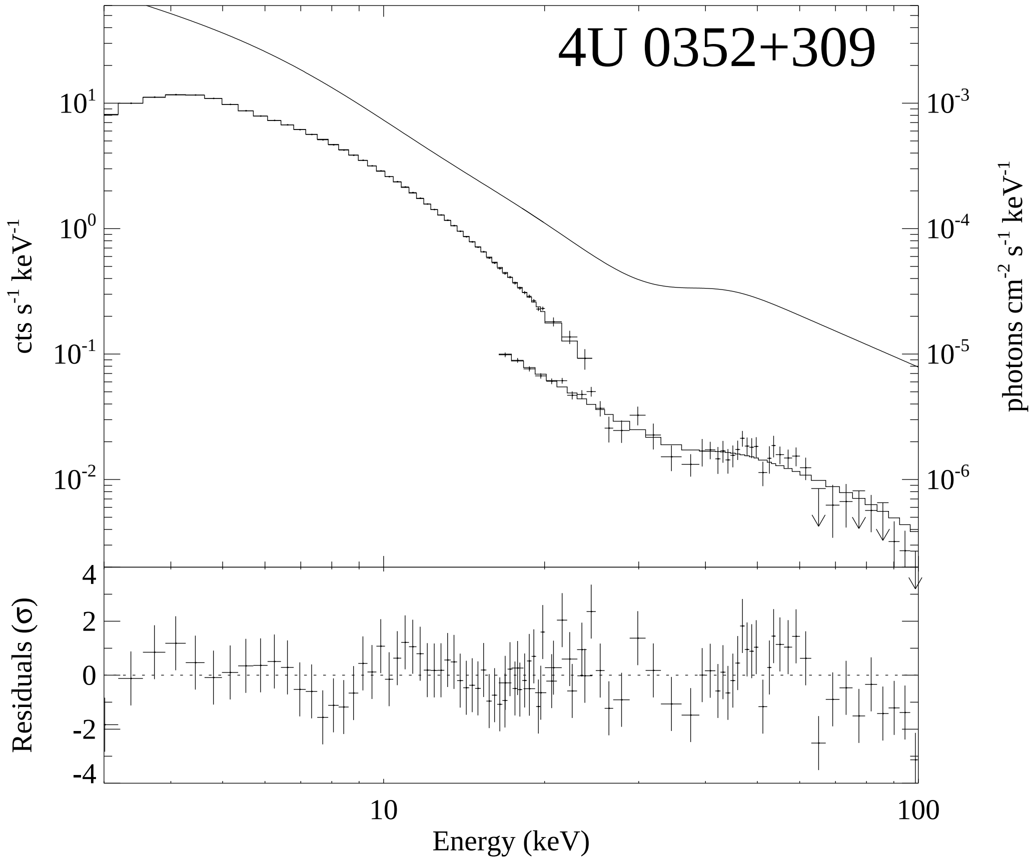

Figure 3.14: Top: Spectrum of 4U 0352+309, fit with a blackbody, a power-law, and a shallow CRSF. Shown are the counts spectrum (crosses), inferred photon spectrum (smooth curve) and model folded through the instrumental responses (histogram). The CRSF is apparent in both the counts and photon spectra at ~30 keV. Bottom: Residuals to the fit, plotted in units of σ.

3.1.10 4U 0352+309 (X Per)

The X-ray source 4U 0352+309 is an unusually low luminosity (4.2×10^{34} ergs s^{-1}) pulsar in a HMXB system with the Be star X Persei (X Per). It is also unusual in the sense that while most Be/X-ray binary systems are transient in nature, 4U 0352+309 is a source of persistent X-ray emission. This is perhaps due to the relatively wide and nearly circular orbit of the system (Delgado-Martí et al. 2001). Its ~837 s pulsation period was discovered with the *UHURU* satellite (White et al. 1976; White, Mason & Sanford 1977), and is still one of the longest periods of any known accreting pulsar (see Table 1.1). The distance to the system, based on optical observations of the companion X Per, is 0.95 ± 0.20 kpc (Telting et al. 1998).

As part of my analysis of *RXTE* archival data I discovered a CRSF in 4U 0352+309 (see ApJ, 552, 738, also reprinted in Chapter 5). I found that while the source spectrum is not well fit by the standard pulsar continuum, it can be modeled successfully by a blackbody plus a power-law modified by a CRSF. Chapter 5 contains a detailed pulse phase resolved spectral analysis of the source.

3.2 Fits and Results

With all of the phase averaged spectra fit in a consistent way with the same model, I can now discuss any correlations observed and therefore the average properties of this class of sources. The spectral shape parameterizations are given in Table 3.4, and the surface magnetic fields of these 10 pulsars are given in Table 3.5. Of particular interest is how the CRSF parameters ($E_{\rm c}$, $\sigma_{\rm c}$, $\tau_{\rm c}$) relate to the other three (Γ, $E_{\rm cut}$, $E_{\rm fold}$), and thus how the standard pulsar continuum is affected by the magnetic field. This also might make it possible to infer the magnetic moments of sources whose spectra do not contain a CRSF. First, however, I would like to stress that these phase averaged PLCUT fits are not necessarily the best fits to the data. In fact, sources such as 4U 1907+09 and 4U 1535−52 are poorly fit in the region 8–12 keV by a PLCUT continuum. These fits should not be used as definitive *RXTE* measurements of these spectra.

To identify how many meaningful, independent variables existed in the parameter space, along with the major linear correlations, I conducted a principle components analysis (Babu & Feigelson 1996) followed by a correlation analysis (Bevington 1969) on the 6 shape parameters.

A principle components analysis of k different parameters seeks to identify a set of q unique variables ($q \leq k$) that can completely describe the dataset. If the data in k-space is highly correlated, then this analysis will substantially reduce the dimensionality of the dataset. Principle component analysis works by first finding the direction in k-space where the cloud of data points are most elongated by a least squared minimization of the variance. This defines the first principle component. The data are then collapsed along this axis, leaving a $(k-1)$ space without this source of variation. This procedure is repeated a total of k times, giving the second,

Table 3.4: Source PLCUT Parameterizations

Source	Γ	E_{cut}	E_{fold}	E_{c}	σ_{c}	τ_{c}	χ^2_{red}/DOF
Her X−1	$0.93^{+0.01}_{-0.02}$	$22.0^{+1.4}_{-0.8}$	$10.8^{+0.2}_{-0.3}$	$40.4^{+0.8}_{-0.3}$	$6.4^{+1.1}_{-0.4}$	$0.76^{+0.10}_{-0.08}$	0.691/76
4U 0115+63	$0.26^{+0.10}_{-0.02}$	$10.0^{+0.5}_{-0.4}$	$9.3^{+0.5}_{-0.2}$	$16.4^{+0.4\,a}_{-1.0}$	$3.6^{+0.5}_{-1.0}$	$0.78^{+0.07}_{-0.22}$	1.105/83
Cen X−3	$1.24^{+0.01}_{-0.02}$	$21.3^{+0.2}_{-0.4}$	$6.67^{+0.09}_{-0.06}$	$30.4^{+0.3}_{-0.4}$	7.1 ± 0.2	1.08 ± 0.02	1.536/114
4U 1626−67	0.88 ± 0.05	6.8 ± 0.3	$38.8^{+5.5}_{-4.6}$	$39.3^{+0.6}_{-1.1}$	$6.6^{+0.6}_{-0.7}$	2.1 ± 0.2	1.263/122
XTE J1946+274	$1.14^{+0.02}_{-0.03}$	$22.0^{+0.8}_{-0.9}$	$8.3^{+0.5}_{-0.4}$	$34.9^{+1.9}_{-0.8}$	$4.8^{+3.2}_{-1.6}$	0.2 ± 0.1	1.067/52
Vela X−1	$0.00^{+0.09}_{-0.01}$	$17.9^{+0.3}_{-0.4}$	$8.8^{+0.2}_{-0.1}$	$24.4^{+0.5}_{-1.1}$	$0.9^{+0.9}_{-0.8}$	$0.16^{+1.13}_{-0.07}$	0.879/64
4U 1907+09	$1.236^{+0.007}_{-0.012}$	13.5 ± 0.2	9.8 ± 0.6	18.3 ± 0.4	1.6 ± 0.2	0.26 ± 0.04	1.827/95
4U 1538−52	$1.161^{+0.003}_{-0.014}$	$13.57^{+0.04}_{-0.05}$	11.9 ± 0.1	$20.66^{+0.05}_{-0.06}$	2.15 ± 0.04	0.50 ± 0.01	2.207/116
GX 301−2	-0.02 ± 0.04	$17.3^{+0.1}_{-0.2}$	$6.7^{+0.7}_{-0.3}$	$42.4^{+3.8}_{-2.5}$	$8.0^{+1.8}_{-2.6}$	$0.5^{+0.3}_{-0.2}$	1.240/60
4U 0352+309	1.83 ± 0.03	57^{+12}_{-17}	50^{+107}_{-30}	$28.6^{+1.5}_{-1.7}$	9.0 ± 1.3	0.66 ± 0.12	0.876/80

a Due to the complex line shape of the fundamental, the simple GABS model used results in an energy that is too high. Using a more complex shape to accurately fit the resonance gives an energy of $E_{\text{c}} \approx 12\,\text{keV}$

Table 3.5: Pulsar Magnetic Fields

System	E_c keV	$B(1+z)^{-1} \times 10^{12}$ G	$B \times 10^{12}$ G [a]
Hercules X−1	$40.4^{+0.8}_{-0.3}$	3.5	4.5
4U 0115+63[b]	$11.6^{+0.2}_{-0.4}$	1.0	1.3
Centaurus X−3	$30.4^{+0.3}_{-0.4}$	2.6	3.4
4U 1626−67	$39.3^{+0.6}_{-1.1}$	3.4	4.4
XTE J1946+274	$34.9^{+1.9}_{-0.8}$	3.0	3.9
Vela X−1	$24.4^{+0.5}_{-1.1}$	2.1	2.7
4U 1907+09	18.3 ± 0.4	1.6	2.1
4U 1538−52	$20.66^{+0.05}_{-0.06}$	1.8	2.3
GX 301−2	$42.4^{+3.8}_{-2.5}$	3.7	4.8
4U 0352+309	$28.6^{+1.5}_{-1.7}$	2.5	3.2

a Assuming $R_{\rm ns} = 10\,{\rm km}$, $M_{\rm ns} = 1.4\,{\rm M}_\odot$, and scattering near the surface of the star
b Using 1/2 the energy of the second harmonic, see text

third, etc. principle component each time. The principle components define a new set of k variables, however only q will be significant.

The variances of the principle components are an indication of their relative importance. Data that is distributed randomly in k-space will generate nearly equal variances, while a dataset that is highly correlated will produce a few components with most of the variance and the rest will be negligible. The variances of the principle components obtained from my 6 shape parameters were 0.462, 0.263, 0.163, 0.073, 0.034, and 0.005. This indicates that my dataset can be reduced from 6 to 4–5 meaningful variables, or that there should exist 2 linear correlations.

While the principle component analysis found the number of linear correlations present in the dataset, a correlation analysis was needed to identify them. I performed the correlation analysis using the prescription given by Bevington (1969), the results of which are given in Table 3.6. Unfortunately this prescription did not include a method for including the errors on each point, and because of this these numbers should be merely used as a guide on where to search in the data. In this analysis, the coefficient for uncorrelated data is 0, while a perfect correlation/anticorrelation results in 1/−1 respectively. Here we see that the primary interdependence is between the CRSF line centroid energy and width, shown in bold, with a ~2% chance that this is due to a random signal in the data.

Table 3.6: Correlation Matrix, All Parameters

	Γ	$E_{\rm cut}$	$E_{\rm fold}$	$E_{\rm c}$	$\sigma_{\rm c}$	$\tau_{\rm c}$
Γ	1.00	0.56	0.51	−0.08	0.28	0.12
$E_{\rm cut}$	0.56	1.00	0.57	0.09	0.53	−0.21
$E_{\rm fold}$	0.51	0.57	1.00	0.15	0.49	0.50
$E_{\rm c}$	−0.08	0.09	0.15	1.00	**0.70**	0.37
$\sigma_{\rm c}$	0.28	0.53	0.49	**0.70**	1.00	0.46
$\tau_{\rm c}$	0.12	−0.21	0.50	0.37	0.46	1.00

There are 2 sources in my analysis whose continua are slightly different from the other 8 pulsars: 4U 0352+309 and 4U 1626−67. Although 4U 0352+309 has a CRSF like the rest of the pulsars presented here, it has a continuum this is quite unlike the standard pulsar spectral shape. In Chapter 5 I argue that this is because of its very low accretion rate, where the thermal component that is normally buried by the accretion mound has been partially revealed. Also, due to inefficient cooling at higher temperatures, the break in the spectrum is at a much higher energy, $E_{\rm cut} \gtrsim 50\,{\rm keV}$. For 4U 1626−67, a pulse phase resolved spectral analysis reveals that the cutoff energy changes from ~6 keV to ~27 keV through the pulse (see Chapter 4). Another reason why these two sources might be slightly different is that in both cases the binary systems are viewed nearly face on, while 6 of the remaining 8 are known to be viewed nearly edge on (see Table 3.1).

While I have not excluded either of these sources from my overall analysis, however when I exclude both 4U 1626−67 and 4U 0352+309 from the correlation analysis a new dependency becomes apparent (see Table 3.7). There is now an association between the PLCUT cutoff energy $E_{\rm cut}$ and the CRSF line energy, with a ~0.5% probability of the correlation being due simply to chance. Additionally, the connection between the CRSF energy $E_{\rm c}$ and width $\sigma_{\rm c}$ becomes tighter, with the same ~0.5% probability of a chance correlation.

Table 3.7: Correlation Matrix, Excluding 4U 1626−67 and 4U 0352+309

	Γ	$E_{\rm cut}$	$E_{\rm fold}$	$E_{\rm c}$	$\sigma_{\rm c}$	$\tau_{\rm c}$
Γ	1.00	0.25	0.31	−0.11	−0.02	0.17
$E_{\rm cut}$	0.25	1.00	−0.35	**0.78**	0.53	0.08
$E_{\rm fold}$	0.31	−0.35	1.00	−0.41	−0.57	−0.17
$E_{\rm c}$	−0.11	**0.78**	−0.41	1.00	**0.81**	0.12
$\sigma_{\rm c}$	−0.02	0.53	−0.57	**0.81**	1.00	0.60
$\tau_{\rm c}$	0.17	0.08	−0.17	0.12	0.60	1.00

3.2.1 $E_{\rm c}$ and $\sigma_{\rm c}$

In Fig. 3.15 I have plotted the fit values of CRSF energy $E_{\rm c}$ versus width $\sigma_{\rm c}$. This correlation in the data, although not new (Heindl et al. 1999a; Dal Fiume et al. 2000), is both somewhat expected and yet surprising. However, with searches of this nature there is always the concern that the interrelations between the parameters of the model or selection effects might be the cause, and not a result of the underlying physics. The choice of the PLCUT model was made to minimize this; however, I conducted 2 Monte Carlo simulations to ensure that the effect is a real one.

The first test I performed was to investigate if the correlation was a result of the fitting procedure itself. To test this I observed how a set of Monte Carlo simulated *RXTE* Spectra, whose input parameters formed a grid in the $E_{\rm c}/\sigma_{\rm c}$ plane, were transformed by the fitting procedure. If there were systematic movement towards a correlation in the simulations then the result presented here would be suspect. To implement this I simulated 6 *RXTE* spectra (with differing depths $\tau_{\rm c}$) at each point on a 6×6 grid in the $E_{\rm c}$ versus $\sigma_{\rm c}$ plane. The simulated observations were 15 ks of a pulsar with moderate flux ($F_{\rm x} = 10^{-9}\,{\rm ergs\,cm^{-2}\,s^{-1}}$ in 2–10 keV). This is a conservative assumption, allowing fitting systematics and not counting statistics to dominate the fitting. Once the simulations were done I fit each of the resulting 216 spectra, and then plotted $E_{\rm c}$ versus $\sigma_{\rm c}$ (see Fig. 3.16). While there was some movement in the fit values from the original grid points, there was no systematic trend towards a correlation in the data. Therefore it is safe to conclude that the correlation between $E_{\rm c}$ and $\sigma_{\rm c}$ is not an artifact of how the data was fit or the models used.

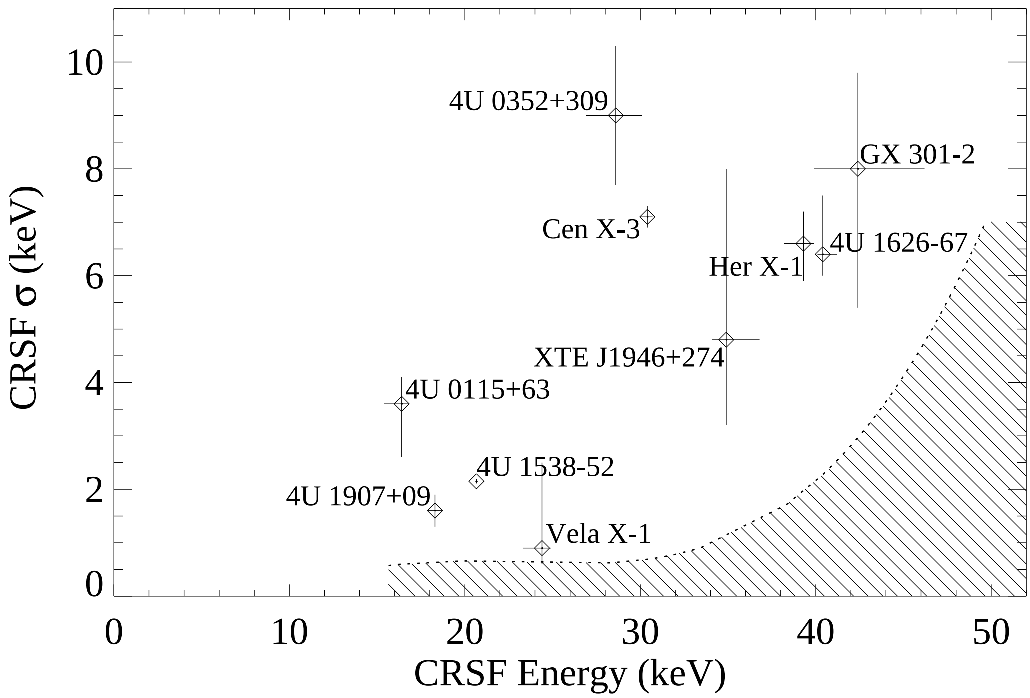

Figure 3.15: CRSF centroid energy E_c versus CRSF width σ_c. The correlation between the two parameters is obvious. The shaded regions indicates the 99% confidence limit for detection of a CRSF based upon the results of Monte Carlo simulations. CRSFs in this region would not be distinguishable from the underlying continua (see text). This line is based upon a conservative estimate of observing time and source flux. Increasing either of these parameters would allow for the detection of a lines at higher energies, and therefore move the shaded region to the right.

The next Monte Carlo simulation was done to see how selection biases might account for the observed correlation. Given the difficulties in identifying shallow lines, especially at higher energies, a priori one would expect some bias in the data. Using the same 15 ks observations, I simulated 30 spectra at each point on a 17×11 grid in the E_c/σ_c plane. I fit each of the resulting spectra initially without a CRSF, and then noted the change in χ^2 upon adding one to the model. The dotted line in Fig. 3.15 shows the contour corresponding to $\Delta\chi^2$ of 9.21 (99% for two degrees of freedom, Lampton, Margon & Bowyer 1976), with the hatched region indicating where a CRSF is indistinguishable from the continuum.

This non-detection region is easily understood. Broad features, especially at high energies where the continuum is falling steeply and statistics are running out, are nearly impossible to identify given the uncertainties in the phenomenological continuum models. And while the red wing of broad CRSFs at these energies will affect the continuum where the statistics are better, it again becomes a question of distinguishing between a real cyclotron feature and the choice of phenomenological model for the continuum. Also, narrow lines at all energies are difficult to detect given the finite energy resolution of not just HEXTE, but all modern hard X-ray satellite instruments.

Although this region does follow the trend in the data, its exact position depends on both the source flux and the length of the observation. As either increases, so will the ability to resolve lines at higher energies and thus move the dotted line to the right. Therefore it is unlikely that the absence of narrow lines at high energies can be completely explained as a selection effect. Also, selection effects cannot account at all for the lack of broad lines at lower energies.

The results of the two Monte Carlo simulations clearly show that the observed correlation between the CRSF energy E_c and width σ_c, although not a narrow one, is indeed real. This is not entirely surprising since a correlation of this nature is expected from theory.

The electrons in the scattering region, although quantized perpendicular are free to move parallel to the magnetic field, and therefore constitute a 1-dimensional gas (Mészáros 1992). For cold electrons the observed CRSF width would be nearly a δ-function. If, however, the electron is moving with a velocity v, then for a photon to be scattered it must be at the CRSF energy in the electron rest frame. Therefore, in the laboratory frame the energy that is scattered is $E' = E_c[1 - (v/c)\cos(\theta)]$. For a Maxwell-Boltzmann distribution of electrons, the observed CRSF FWHM is given by Mészáros & Nagel (1985a):

$$\Gamma_c \approx E_c \left(\frac{8\,\ln(2)\,kT_e}{m_e c^2} \right)^{1/2} |\cos(\theta)| \tag{3.1}$$

Where kT_e is the characteristic electron temperature, E_c the cyclotron resonance energy, and θ the viewing angle to the magnetic field. This gives a very straightforward dependence on the CRSF width σ_c on energy E_c as observed in Fig. 3.15. There is, however, a term involving the viewing angle θ. At small angles to the magnetic field ($\cos(\theta) \sim 1$), the motions of the electrons along the magnetic field lines will result in a maximal Doppler broadening of the feature, while at large angles ($\cos(\theta) \ll 1$) the

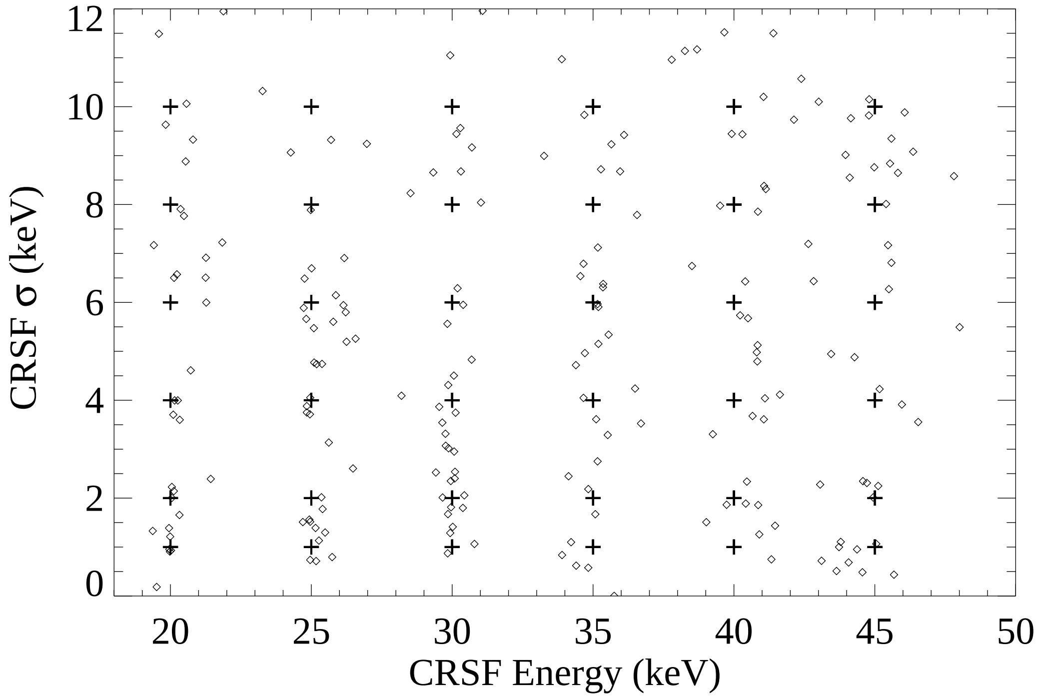

Figure 3.16: Monte Carlo results of fitting simulated *RXTE* spectra (see text). Six spectra were simulated at each grid point (crosses), and then fit using the PLCUT and GABS models. The fit results are shown (without errors) as the small diamonds. Although there is some deviation away from the grid points, there is no systematic movement that might explain the observed correlation.

effects of thermal broadening are small and the line is expected to be very narrow.

What is unusual about the correlation seen here is that a priori all of the systems should be viewed at *random* values of $\cos(\theta)$, and thus completely smear out the correlation. Therefore this implies that for sources where CRSFs are observed there is an observational bias towards a specific viewing angle θ. Interestingly, 6 of the 10 CRSF systems discussed here are also among the few accreting X-ray pulsars that exhibit eclipses (Her X−1, Cen X−3, Vela X−1, and 4U 1538−52) or are known to be viewed nearly edge on (GX 301−2, 4U 1907+09). This combination of a selection on a narrow range of viewing angles θ, with a bias towards systems with a large inclination, seems to imply that there is a preferred offset angle between the dipole and spin axes. The implication of this is discussed in Chapter 8.

This could be an indication as to why CRSFs have not been observed in sources such as 2S 1417−624, GS 1843+00, and GS 1843−024, where observational limitations such as source brightness and integration length were not a factor (see Chapter 7).

The orientation of their binary planes, and therefore our view of the polar emission regions, are not favorable to the detection of CRSFs. This also implies that should the inclination angles of systems such as 4U 0115+63 and XTE J1946+274 be measured, it will be found that they are observed nearly edge on.

There are three obvious counter examples, however, to this potential bias towards a high inclination angle. The binary systems 4U 1626−67 and 4U 0352+309 both exhibit CRSFs in their X-ray spectra, yet both are thought to be viewed nearly face on (Chakrabarty 1998; Delgado-Martí et al. 2001). Also, so far a CRSF has eluded detection in the eclipsing X-ray pulsar OAO 1657−415. This could simply be because the cyclotron energy of the B-field is outside the effective *RXTE* and *Beppo*SAX detection ranges, and observations with the *INTEGRAL* satellite should be able to answer this question.

The observed correlation is quite broad, and this might be due in part to the phase averaged spectrum averaging over a range of $\cos(\theta)$ for each source. This effect, while certainly present, is not expected to be large for two reasons. First, due to the viewing geometry it is unlikely that the observed range in $\cos(\theta)$ is the full [0,1] for a given source. Instead our view of the polar region will be some smaller subset as the neutron star rotates. Second, for most of the sources in question the FLC at the CRSF energy is a relatively simple single pulse. As noted for Cen X−3, the emission from the peak of this main pulse will dominate the phase average spectrum, further reducing the effective range of $\cos(\theta)$ sampled. Future pulse phase resolved fits, using phases chosen to isolate a specific $\cos(\theta)$, will test this result and produce a much tighter correlation if Eq. 3.1 is valid.

Assuming that Eq. 3.1 is correct, then the existence of the correlation also indicates a small range of polar cap temperatures despite over 3 orders of magnitude difference in luminosity (or alternatively, mass accretion rate). As matter falls onto the polar cap it forms an accretion structure (see §1.4.3), where in steady state the amount of matter falling in balances the matter spreading out at the base. The small spread in temperatures seen could indicate that the mound parameters such as area, density profile, etc., naturally find steady state values that produce a narrow range of electron temperatures, irrespective of mass accretion rate.

The small range in electron temperatures can also be explained if the temperature itself is tied to the magnetic field strength. In numerical simulations by Lamb, Wang & Wasserman (1990) of isotropic injection into an optically thick plasma dominated by cyclotron line cooling and heating, the temperature is found to vary as $kT_e \sim E_c/4$. These simulations were originally done assuming the hard power-law spectra of $\gamma-$ray bursts, and therefore are not directly applicable to the softer continua of accreting X-ray pulsars. Still, such a dependence of electron temperature kT_eon the magnetic field is consistent with the observed correlation between the cyclotron energy and width. The statistics of the data are such that fits to the correlation in Fig. 3.15 are unable to distinguish between the two scenarios; with $kT_e \propto E_c$ being marginally preferred over $kT_e \propto E_c^{1.5}$, but not at a statistically significant level.

Araya & Harding (1999) cite two caveats to the use of equation 3.1 to infer the electron temperature and viewing angle. The first is that a relativistic treatment of the scattering produces asymmetric broadening of the line even at $\theta = 90°$. Second, Monte Carlo simulations indicate that the line profiles of the fundamental can be quite complex (see §1.5.1). The relativistic cross sections for resonant scattering of photons depends on the angle of photon to the magnetic field. Since the scattered photons are emitted isotropically, the effect of the angular dependence of the cross section is a non-isotropic angular redistribution of photons. Although these simulations preserve the general sense of Eq. 3.1, with lines at higher energies and temperatures being broader, these other effects make a detailed inference of the electron temperature in terms of the CRSF width problematic.

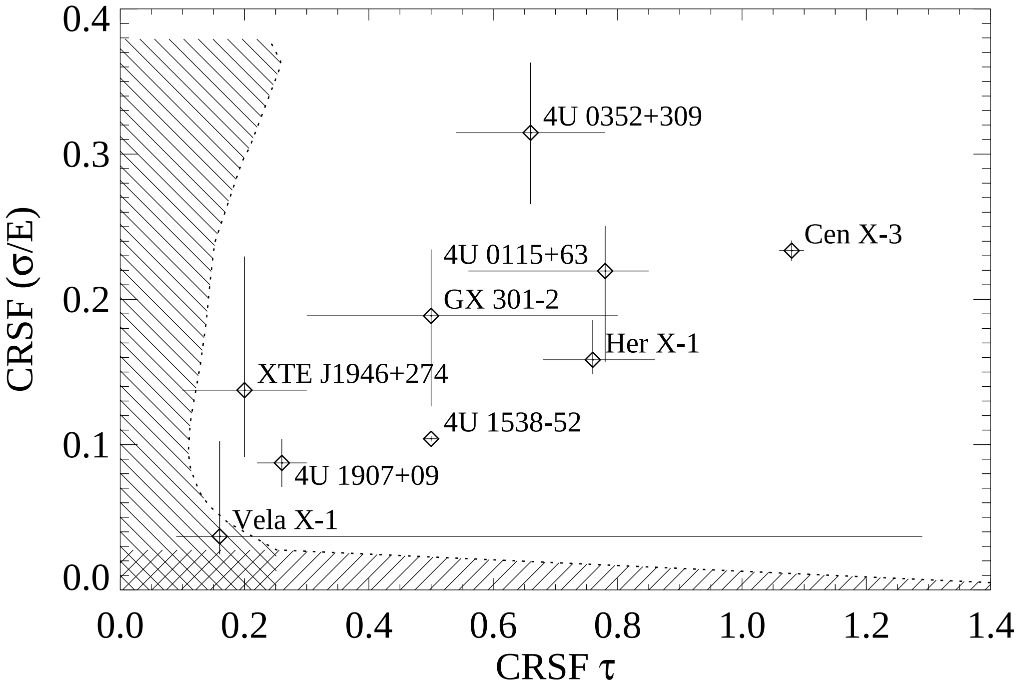

Figure 3.17: CRSF optical depth τ_c versus fractional CRSF width (σ_c/E_c). A high degree of correlation is readily apparent in the data.

3.2.2 τ_c and Fractional σ_c

In Figure 3.17 I have plotted the CRSF optical depth τ_c versus the fractional width σ_c/E_c. This is a much tighter correlation than E_c versus σ_c, and has not been reported before. In §3.2.1 I noted that as the energies of the lines increased, so did their width. This can be easily be understood in terms of Doppler broadening of the lines themselves. This correlation indicates that as CRSFs increase in depth, the width of the feature as a percentage of the resonance energy increases as well. Or that as CRSFs become broader, they become deeper.

As in §3.2.1, to test for systematic effects I did a similar sort of Monte Carlo analysis. I first simulated six,15 ks *RXTE* spectra with CRSFs at various energies on a 6×6 grid in the τ_c versus (σ_c/E_c) plane. I then fit each of the resulting 216 spectra, the results of which are plotted in Fig. 3.18. Again, although there was scatter in the fit values away from the initial grid points, there was no systematic movement that could explain the observed correlation.

To test for a selection bias I next simulated spectra 30 spectra at each point on a 12×11 grid, each with a CRSF at 30 keV. I fitted each of the resulting spectra without a CRSF, and noted the improvement (or lack thereof) in χ^2 after the addition of an absorption line to the model. The resulting $\Delta\chi^2$ of 9.21 (99% for two degrees of freedom, Lampton, Margon & Bowyer 1976) contour is plotted as a dotted line in Figure 3.17, with the hatched regions indicating where the observations were not sensitive to the presence of a CRSF in the spectrum. The region along the x-axis, narrow features at all depths, is simply due to the finite spectral resolution of the HEXTE. The region that follows the y-axis, shallow features at all widths, is due to the difficulties in distinguishing shallow CRSFs from the continuum. The dotted line itself (along with the shaded areas) is meant as a guide to the eye, and some minor movement is inevitabe due to changes in the CRSF energy or shape of the underlying continuum. The observed correlation between depth τ_c and fractional width σ_c/E_c cannot, however, be explained merely in terms of either model biases or selection effects. Therefore it is safe to conclude that this is a real, physical effect.

This observation, that CRSFs become fractionally broader as they become deeper is, in fact, *opposite* of what is expected from the relativistic cross sections alone (see Fig. 1.6, also Araya-Góchez & Harding 2000)). In the calculations of the cross sections, resonant photons that travel perpendicular to the magnetic field have a greater chance of scattering than those propagating along the field (see Fig. 1.6), giving rise to a deeper line. Conversely, off resonance photons along the B-field are more likely to scatter than those perpendicular. This combination gives cross sections that move from shallow and broad to narrow and deep as a function of photon propagation angle. Since the correlation shown here is in the opposite sense, other factors such as angular redistribution of photons and photon spawning must be important in the formation of observed CRSFs. Indeed, in simulations of Araya-Góchez & Harding (2000), the predicted shape of the fundamental CRSF can be quite complex (see Figs. 1.7 and 1.8), and depends greatly on the magnetic field strength, photon injection and scattering geometries, and viewing angle. This makes a comparison of this phase averaged work to the results of their simulations problematic, if not impossible.

It is interesting to note that the fundamental CRSF of Vela X$-$1 (Kreykenbohm et al. 2002), which sits marginally outside the nominal detection area, is still considered somewhat controversial. It is on the threshold of detectability in relatively short

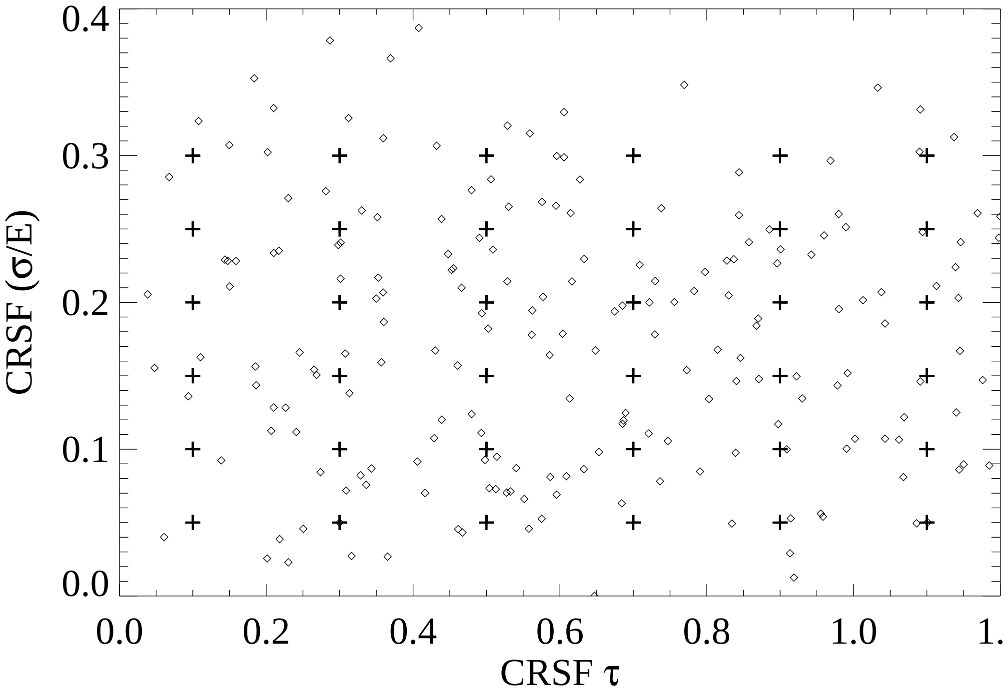

Figure 3.18: Monte Carlo results of fitting simulated *RXTE* spectra (see text). Six spectra were simulated at each grid point (crosses), and then fit using the PLCUT and GABS models. The fit results are shown (without errors) as the small diamonds. Although there is some deviation away away from the grid points, there is no systematic movement that might explain the observed correlation.

integration times (15 ks for the purposes of the simulations), and therefore might easily be indistinguishable from the continuum in a given dataset. This could explain why it has been seen in some observations (e.g. Mihara 1995; Kretschmar et al. 1997; Kreykenbohm et al. 1999) and not in others (e.g. Orlandini et al. 1998).

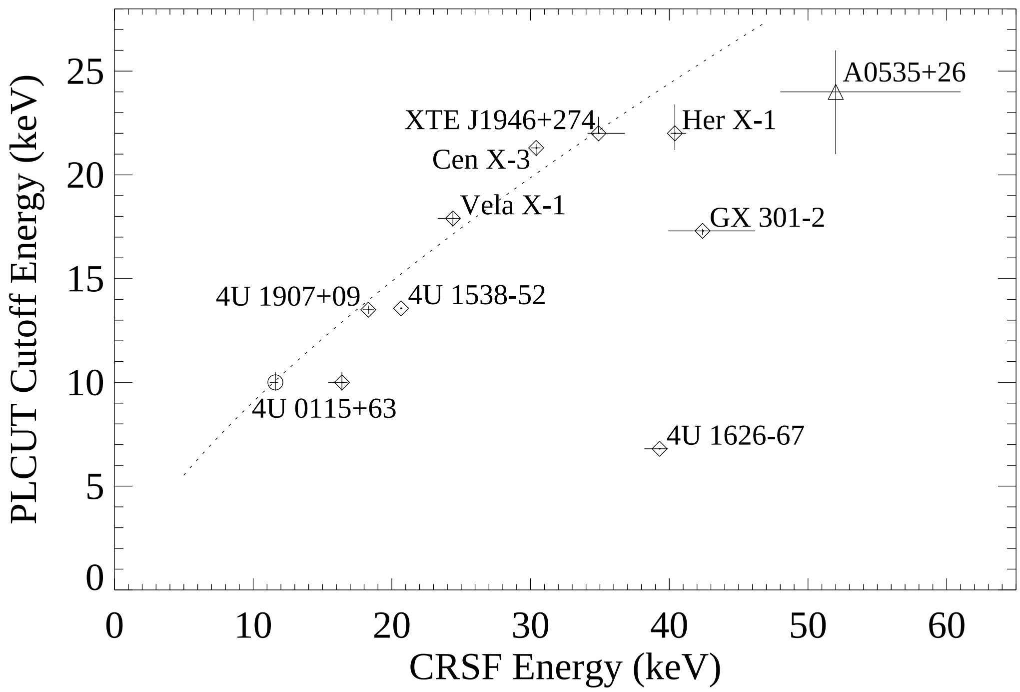

Figure 3.19: CRSF centroid energy E_c versus PLCUT cutoff energy E_{cut}. Two CRSF energies are shown for 4U 0115+63, the diamond indicating the fit value (and therefore the center of the feature as modeled with a Gaussian absorption feature) and a circle at 1/2 the energy of the second harmonic (and thus the B-field strength). See §3.1.2 for details. The HEXE measurement of A0535+26 (Kendziorra et al. 1994) is shown as a diamond. The new CRSF source XTE J1946+47, along with Cen X−3 and Her X−1, indicate a deviation in the power-law correlation (shown as a dotted line) observed by Makishima et al. (1999).

3.2.3 E_c and E_{cut}

The second result to come out of the correlation analysis above was a relationship between the CRSF energy E_c and the cutoff energy E_{cut}. A relationship between the two parameters was first noticed by Makishima & Mihara (1992) and later refined by Makishima et al. (1999). There, however, the authors used CRSF energies obtained with several different instruments and derived using a variety of continuum models. For the PLCUT cutoff energies the authors used fits without a CRSF to *Ginga* observations that were often non-contemporaneous. They found that the relationship was consistent with a power law, $E_{cut} \propto E_c^{0.7}$, indicating a saturation as compared to a linear correlation. My work has the advantage that each point is derived from a uniform model fit to a single spectrum. Also, with the exception of A0535+26, all points are from the same set of instruments.

As indicated by the dotted line, my results confirms the relationship noted by Makishima et al. (1999), at least for CRSF energies below ∼35 keV. Above 35 keV, however, there is an indication of a change in slope in the correlation. If correct, this flattening of $E_{\rm cut}$ is more abrupt than the rather smooth turnover of the $E_{\rm c}^{0.7}$ power law. This change in slope also suggests that the relation between the cyclotron and cutoff energies can instead be described by two linear relations, one below ∼35 keV and one above. The complex correlation between the CRSF energy (or more specifically the B-field strength) and the cutoff energy implies that the break in the spectra is related to the B-field, although it is not necessarily a magnetic effect. A similar, yet physically distinct, possibility is that the break is a function of another physical parameter, such as the electron temperature $kT_{\rm e}$. It is this intermediate quantity that is proportional to the magnetic field, up to a saturation point. The cutoff energy would then saturate as well, causing the observed roll over in the cutoff energy.

The actual functional form of the dependence between the two fit parameters is unclear. As mentioned above it might be simply a change in slope, or that $E_{\rm cut}$ is asymptotically approaching a saturation value. Interestingly, the change in slope occurs at ∼35 keV, and the cyclotron energy is ∼7% of the rest mass of the electron. Therefore the roll over might be an indication that relativistic effects in the creation of the continuum, are beginning to become important at those fields. This is, however, highly speculative. Whatever the cause, future spectral models of accreting X-ray pulsars will need to reproduce this feature.

For illustrative purposes I have included the results to fits of HEXE data for the source A0535+26 (indicated with a triangle in Fig. 3.19, Kendziorra et al. 1994). In this fit the continuum was modeled with a PLCUT, however the feature itself was modeled with the CYCLABS and not the GABS model (see §2.2.5). The two models generally give similar CRSF centroid energies, and given the size of the errors on the measurement the differences are negligible. Like Vela X−1, the energy of the fundamental is considered somewhat controversial. For A0535+26 there is a prominent feature at ∼110 keV (Grove et al. 1995), with the presence of the fundamental at ∼55 keV being less certain. If the fundamental is at 55 keV then this is consistent with my observed correlation, while if it is at 110 keV then it strengthens the apparent saturation.

Not shown in this plot is the source 4U 0352+309, which has a cutoff energy of $E_{\rm cut} \gtrsim 60$ (see Chapter 5). However, as I mentioned in §3.1.10, the spectrum of 4U 0352+309 is unusual when compared to other accreting X-ray pulsars. The pulse phase resolved spectrum of 4U 1626−67 is different as well. In particular, the cutoff energy $E_{\rm cut}$ is a strong function of pulse phase, changing by a factor of 4.5 through the pulse (see Table 4.3). This change in the cutoff energy as a function of rotation phase is unlike what is seen in other sources, and therefore it is not surprising that the phase average value for this source does not fall on the observed correlation. The bimodal variation in the cutoff energy is discussed in §4.4.2.

The third point that lies off of the correlation is GX 301−2. It is interesting to notice, however, that there is no discrepancy if the fundamental CRSF lies *not* at 42 keV, but at 21 keV instead. This may be an indication that the fundamental feature, as in Vela X−1, is shallow and difficult to detect. Since the CRSF parameters of energy, width, and depth are known to change with pulse phase, a full pulse phase resolved analysis could answer this question. Unfortunately the archival *RXTE* was obtained in a mode where such an analysis is impossible.

Since I am inferring the effect of the magnetic field on the standard pulsar continuum here, I have plotted two values of 4U 0115+63. The higher value (plotted as a diamond) is the result of the parameterization, and is the center of the absorption feature as modeled with the GABS analytic form. The second (plotted as a circle) is at 1/2 the energy of the second harmonic, and therefore is a better estimate of the pulsar magnetic field (see §3.1.2). I did not make this distinction in the previous 2 sections because those were investigations into the CRSF shapes themselves, and the shape of the CRSF in 4U 0115+63 as parameterized with the GABS model is centered at ~16 keV. Here, however, since the CRSF energy is used to measure the B-field the distinction is necessary.

3.2.4 The Feature at 10 keV

One interesting feature in most of these PLCUT fits is the wiggle, or "bump," in the spectrum in the range 8–12 keV. It might easily be mistaken for a CRSF, especially given the size of the residuals in, for example, the spectrum of 4U 1907+09 (see Fig. 3.11). This feature is evident in the spectra of many accreting X-ray pulsars, including those that do not otherwise exhibit a CRSF(e.g. GS 1843+00, see §7.2.3). While it often appears as a simple dip, it can also evidence itself as a pure bump (e.g. Her X−1, see §3.1.1) or a pseudo-P-Cygni profile. Since this bump is consistently at or near 10 keV, irrespective the CRSF energy, the feature therefore is probably not a magnetic effect.

It is not just apparent in *RXTE* spectra either. In Mihara (1995), the residuals in fits using the NPEX model to *Ginga* observations (e.g. 4U 1538−52, 4U 1907+09, and V0331+53) show a systematic structure around 10 keV. Upon closer inspection, pulse phase resolved spectroscopy indicates that the feature changes through the pulse. This ∼10 keV bump is also evident in the residuals seen with the *Beppo*SAX High Pressure Gas Scintillation Proportional Counter (HPGSPC) in Cen X−3 (Santangelo et al. 1998). Since this feature has been seen in a number of sources by several satellites, and yet is not present in other sources (like the Crab nebula/pulsar) it is safe to conclude that it is an inherent feature in the spectra of accreting pulsars.

This bump almost certainly arises from improper modeling of the continuum with a simple power-law, the net result the PLCUT and effective result of the FDCO below the cutoff energy. This also may account for the different shapes that are observed, rather than physical changes in the conditions creating the feature. The NPEX model, with two components that each have an independent normalization, can mimic this feature somewhat. Still, as seen in Mihara (1995), the model is only marginally successful at accounting for the feature for most sources.

The exact nature and physical cause of the bump is still unknown. The collecting area of the PCA, which is 50% larger than the previously largest proportional counter flow (the *Ginga* LAC) has made it something that can no longer be ignored. Future theoretical models for accreting X-ray pulsar spectra will need to address the nature and formation of this feature.

3.3 Summary

There are three principle results of this class analysis of the spectra and cyclotron features of accreting X-ray pulsars. The first two results involve correlations among the shape parameters of the CRSFs themselves. I find that the observed CRSFs widths are roughly proportional to their energy. If the widths are primarily due to Doppler broadening, then this implies a viewing angle selection bias in finding sources that exhibit cyclotron features. Since 6 of the 10 sources discussed here are in systems that are viewed nearly edge on, a selection bias on viewing angles further implies a preferred offset angle between the dipole and spin axes of the neutron star.

The next result is that, at least for the fundamental features, deeper CRSFs are also fractionally (scaled by the centroid energy) broader. This is difficult to understand simply in terms of the relativistic cross sections alone, which are in the *opposite* sense. This implies that other effects, such as photon spawning or the non-isotropic angular redistribution of photons, are important and should continue to be considered in theoretical efforts.

Lastly, I find a correlation between the magnetic field strength and the spectral cutoff energy. The existence of a correlation indicates that the observed spectral break is either a magnetic effect, or perhaps is tied to the magnetic field through some intermediate quantity. In the correlation itself there is a departure from the power-law observed by Makishima et al. (1999), either a roll over or break in the slope, near a cyclotron resonance energy of 35 keV. This might be an indication that the break is indeed tied to another quantity, such as the electron temperature, that is then tied to the magnetic field up to a saturation point.

I also discussed a departure in observed pulsar spectra from the standard pulsar continuum shape. While the standard shape is still applicable over most of the hard X-ray band, modern satellites have shown that it is inadequate near 10 keV. This highlights the need for theoretical work in how the X-ray continuum in these pulsars is formed, and when fitting spectra a departure away from the purely phenomenological models currently being used.

Chapter 4

Phase Resolved Spectroscopy

4.1 Introduction

One of the unique advantages of pulsars over other sources is their well defined spin period. For accreting pulsars this arises from the structures at the magnetic poles, which are the primary sources of hard X-ray emission in the system (see §1.4.3). Because these regions are small compared to the neutron star, as the neutron star spins their projected area on the plane of the sky is modulated. This is further enhanced by the fact that much of their emission is beamed, thereby increasing the rotational modulation. Both of these effects allow for very precise timing of the pulsar spin. This, in turn, allows for the study of the emission as a function of neutron star rotation phase.

The FLCs of pulsars can be decomposed into two components; "fan" and "pencil" beams (described below). As the neutron star rotates, the combination of beams and how they change with energy, the various angles, and general relativistic light bending around the surface of the neutron star, will determine the FLC seen by a distant observer. The pulse profiles of accreting pulsars are typically complex functions of both phase and energy (White, Swank & Holt 1983). Because of this two dimensional nature of accreting X-ray pulsar spectra, there are limits to what can be understood from spectra averaged over the entire pulse. A better approach is to treat the observed spectra in two dimensions, tracking both pulse phase and energy. This allows for the study the the spectral evolution as a function of star rotation and, more fundamentally, the pulsar polar cap structure from different viewing angles. The *RXTE*, with its large collecting area, collects many counts in each phase bin and is therefore ideal for this type of study.

In this chapter I further the analysis in Chapter 3 by resolving the X-ray spectrum as a function of pulse phase for the sources 4U 1538−52, 4U 1626−67, and 4U 1907+09. I qualitatively compare the spectra I obtained with the Monte Carlo results of Araya-Góchez & Harding (2000) and use this information to infer information about the emission geometry. In this analysis I used a combination of FLCs and pulse phase resolved spectroscopy to determine the emission geometry and geography of pulsars. As seen in Figs. 1.7 and 1.8 (from Araya-Góchez & Harding 2000), CRSF shapes are very sensitive to the viewing angle, injection pattern, and scattering geometry.

There are several caveats, however, to the direct application of these simulations to accreting X-ray pulsars. As mentioned in §1.5.1, the Monte Carlo results assume a very hard spectrum in the scattering region, one that is better suited to γ−ray bursts than accreting pulsars. Also, since this was a qualitative analysis I was only able to compare the general features of the predicted line shapes with what was observed. Doing rigorous fits with a more realistic continuum, and allowing for variations in parameters such as the electron temperature, density, and local B-field strength, will almost certainly produce results that better match the observations.

In the first section I outline how the various angles and geometry of pulsars are described, along with a brief discussion of the 2 emission beam patterns and their resulting FLCs. I then present the results of a pulse phase resolved spectral analysis of 4U 1538-62, 4U 1626-67, and 4U 1907+09. For each source I compare the observed CRSFs to the Monte Carlo results, and discuss how the suggested emission geometry

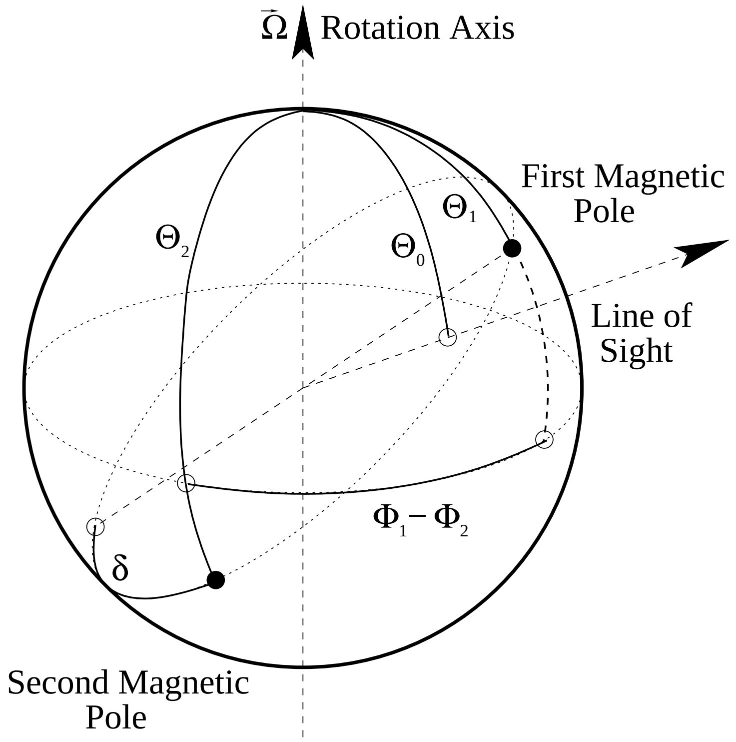

Figure 4.1: Diagram illustrating the various angles used to describe the surface geography of the neutron star. Spherical coordinates are used, with the z-axis along the rotation axis. The locations of the two magnetic poles are described by the polar angles Θ_1 and Θ_2, and the angular distance δ which is the offset from a purely dipolar configuration. The angle between the rotation axis and the line of sight is defined to be Θ_0. (after Blum & Kraus (2000), Fig. 1).

compares to what is inferred from the FLC of the source. I conclude the chapter with a brief summary.

4.2 Pulsar Geometry and Geography

In the discussion of pulsars in §1.4, I noted that if the magnetic and spin axes were not aligned then pulsations were seen. The specifics of how the two axes are misaligned can in general be quite complex. There are several main angles used to describe the geography of the neutron star surface (see Fig. 4.1). First, using spherical coordinates with the z-axis aligned with the neutron star rotation axis, the location of the magnetic poles are given by the angles (Θ_1, Φ_1) and (Θ_2, Φ_2). In the simple case of a centered dipole, specifying the coordinates of one pole defines the location of the other. The angle between the rotation axis and the observer's line of sight is Θ_0. The angle of the i^{th} magnetic pole with the line of sight, which varies with rotation phase φ, is $\gamma_i(\varphi)$.

To study the emission as a function of pulsation phase, FLCs are often used. As discussed in §2.2.2, a FLC is generated by first converting photon arrival times into rotation phase φ ($0 \leq \varphi < 1$) using the pulsation period of the star, and then generating a light curve by binning on phase instead of time. For an example of an FLC see Fig. 4.4.

In some models used to explain pulsar folded light curves, there is also an offset angle δ of the second pole from the antipode of the first pole. This "distorted dipole" is illustrated in Fig. 4.1 and discussed in detail in Kraus et al. (1995). This configuration has the dipole going through the center of the star, and while the B-fields at the two polar caps are equal in magnitude they are no longer parallel. This provides an asymmetry that is useful in the fitting of observed FLCs. In this case, the positions of the two poles are described with Θ_1, Θ_2, δ, and $\Delta\Phi = \Phi_1 - \Phi_2$.

Another modification from a simple, centered dipole is to assume a field that is offset from the center of the neutron star by a vector $\vec{\mathbf{r}}$ (Burderi et al. 2000). Here the magnetic field lines at one pole are parallel to the lines at the other. However, the B-fields at the two poles are no longer necessarily equal in magnitude. The field lines are also no longer parallel to the surface normal at either poles. In practice it is difficult to distinguish this "offset dipole" from a distorted dipole observationally.

When discussing pulsar emission and folded light curves, a superposition of contributions from both poles is generally considered. As mentioned briefly above, there are two emission patterns that are usually considered; the "fan" and "pencil" beam geometries (see Fig 4.2). A fan beam arises from a column geometry with the emission concentrated in a plane perpendicular to the dipole axis. On the other hand, a slab geometry produces a broad pencil beam concentrated along the magnetic dipole axis. The relative contributions of the two beam patterns depends largely on the geometry of the emission region and can vary as a function of energy. When fitting observed FLCs, the effect of light bending around the neutron star on these two emission patterns is also very important.

As mentioned above, a fan beam is generally modeled as having a flux that is

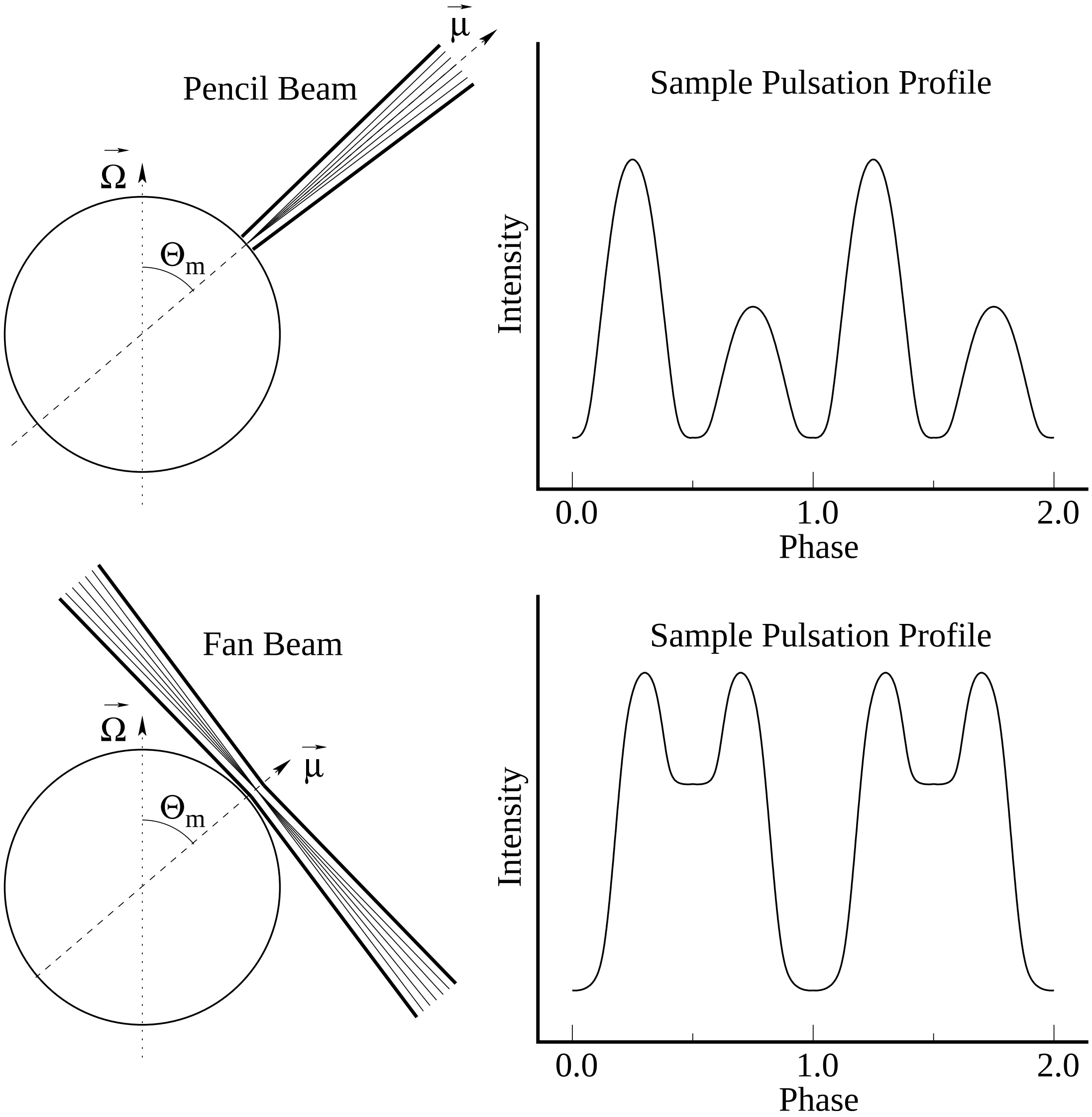

Figure 4.2: Left: Diagram (not to scale) illustrating idealized "pencil" (top) and "fan" (bottom) beam emission geometries. In both cases the patterns are cylindrically symmetric around the dipole axis $\vec{\mu}$ of the neutron star. In the pencil beam, emission is focused along the magnetic field lines at the surface, while in the case of a fan beam the emission is perpendicular. In general there is emission from both poles, although here only a single pole is illustrated for each case. The thick lines on the beams simply indicate the opening angles. Right: Theoretical FLCs, plotted twice in phase, associated with the two emission geometries for a particular set of Θ_m and Θ_0 (see text).

maximal at the dipolar equator and decreases with decreasing polar angle until it reaches zero at the magnetic poles. Assuming an undistorted, centered dipole ($\delta = 0$), then the angle between the spin and dipole axes Θ_m is the smaller of Θ_1 and Θ_2. Depending on whether or not the edge of the fan passes through the line of sight, the following pulsation profiles will be observed:

1. If $\Theta_m + \Theta_0 < \pi/2$, then a single peak will be observed, with the minimum corresponding to the point of closest approach to the line of sight (the minimum in γ) of the dipole axis.

2. If $\Theta_m + \Theta_0 > \pi/2$, then two maxima with equal heights will be seen. In this case there the two minima will have unequal levels unless $\Theta_m = \pi/2$ (see Fig. 4.2, top panel).

If there is an offset angle δ, then the emission will be the superposition of two fan beams, each with emission concentrated in the plane tangential to their respective magnetic pole.

Pencil beams are in effect the opposite: where emission is beamed along the dipolar axis and drops to zero at the magnetic equator. If each pole is considered to be a source of emission, and again the field configuration is an undistorted dipole ($\delta = 0$), the following pulsation profiles are observed:

1. If $\Theta_m + \Theta_0 < \pi/2$, only a single pole, and therefore a single pulse, is observed.

2. If $\Theta_m + \Theta_0 > \pi/2$, two pulses of unequal amplitude are observed, each arising from a different pole. The pulses will be separated by 180° in phase and will be separated by two equal minima (see Fig. 4.2, bottom panel).

The introduction of an offset angle δ can help account for simple peaks that are not spaced by 180°.

4.3 4U 1538−52

The 528 s pulsar 4U 1538−52 is in a 3.7 d eclipsing binary orbit with the B0 Iab star QV Nor. To date the *RXTE* has made 38 observations of the source, for a total of 426 ks of on-source time. Presented here are the results of a set of 11 pointings made in the first week of 1997 (see Table 4.1). These observations were obtained over the course of 1997 January 3–5, spanning nearly the entire binary orbit (sans eclipse). The PCA light curve of the observation is shown in Fig. 4.3.

Detailed analysis of the spectra and FLC of 4U 1538−52 has been carried out by Bulik et al. (1992) and Bulik et al. (1995) using data from the *Ginga* satellite. The geometric model used was the distorted dipole discussed above, and pencil beam emission was assumed from each pole (although the relative luminosity between the two poles was kept as a free parameter). This is assumption was reasonable given the shape of the FLC (see Fig 4.4). Spectral fits were done using a model where the infalling photons heat the deep layers of the neutron star atmosphere, producing an initial spectrum of photons. As the photons propagate outward through the accretion structure until they finally escape, they are scattered by electrons in cyclotron resonances. For more details on the radiative transport model see (Bulik 1993). In the best fits of Bulik et al. (1995) the observing angle $\Theta_0 \simeq 81^\circ$, which is consistent with the spin axes of the neutron star being nearly aligned with the angular momentum of the binary system. The polar angles were $\Theta_1 \simeq 25^\circ$ and $\Theta_2 \simeq 153^\circ$. The fit offset angle between the two emission regions was quite large, $\delta \simeq 25^\circ$.

4.3.1 Data and Analysis

The 3–100 keV flux during this set of observations was $1.03 \times 10^{-9}\,\mathrm{ergs\,cm^{-2}\,s^{-1}}$. At a distance of 6.4 kpc (Reynolds, Bell & Hilditch 1992), the luminosity of the source was $5.02 \times 10^{36}\,\mathrm{ergs\,s^{-1}}$. Because the time resolution of PCA standard 2 data is only 16 s, for the phase resolved analysis I used event data with 1 ms time resolution instead (the full datamode was `E_1ms_128M_0_1s`). I first filtered the event files for the top layer of PCUs 0,1 and 2, and then accumulated those files using a similar procedure as for standard 2 data (see Chapter 2). The source counting rate was high enough to estimate the PCA background using the SkyVLE model in all observations

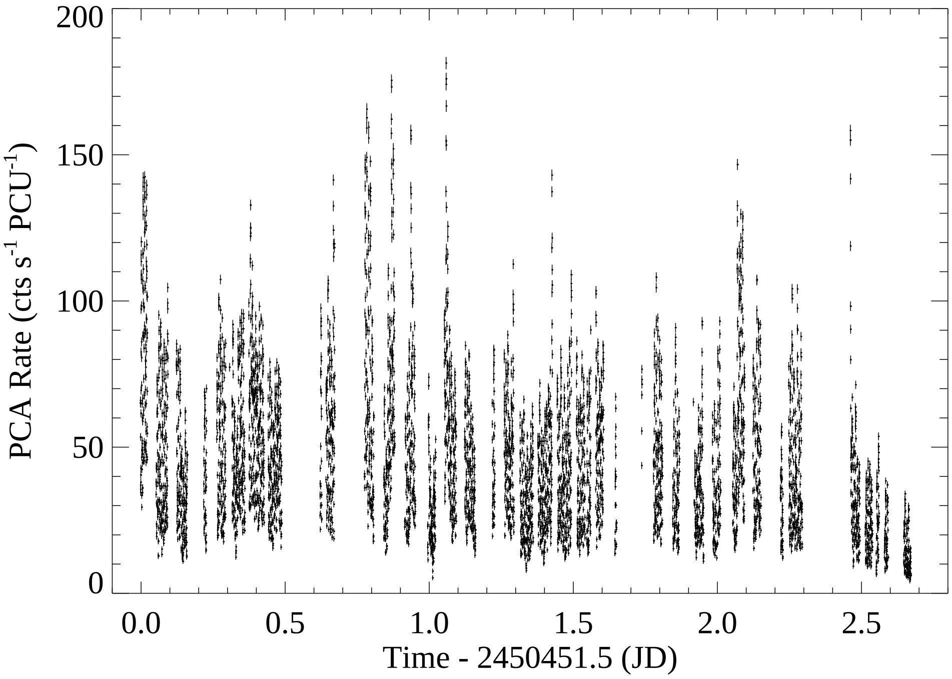

Figure 4.3: PCA light curve (top layer only, 16 s time resolution, entire energy range) for 4U 1538−52. The large modulation in the counting rate is due to the 528 s pulsation period.

except number 11. In that observation the Faint model was used. I used 0.4% PCA systematic errors in the 2–25 keV range. Since the HEXTE instrument was in event mode, I accumulated spectra normally.

The pulsation period I derived using the method outlined in §2.2.2, centered at MJD[1] 50451.807, was 528.84165(8) s. For this analysis I used a PCA light curve with 2^{-3} s time resolution and the orbital ephemeris of Rubin et al. (1997). Using this period I accumulated the PCA and HEXTE event data into pulse phase resolved spectra using our version of the `fasebin` `FTOOL`. Initially I used 64 phase bins to better resolve the temporal structure of the pulses. For the spectral analysis, however, I rebinned these into 8 phase bins. The resulting folded light curves at various energies, including the binning used, are shown in Fig. 4.4.

To avoid the complexities of the low-energy spectrum, I only analyzed data above 10 keV. Since the source is only 2°.1 out of the Galactic plane, there is contamination due to soft diffuse Galactic emission (Valinia & Marshall 1998). The additional presence of an Fe-K line and both local and interstellar absorption, make obtaining

1 Modified Julian Day (MJD) is Julian Day JD - 2400000.5

Table 4.1: 4U 1538−52 Observations

#	Date	Start Time	PCA		HEXTE	
		(UTC)	Exposure (ks)	Rate[a] (cts s^{-1} PCU^{-1})	Exposure (ks)	Rate[b] (cts s^{-1})
1	1997 Jan 3	00:00	8.9	47.60±0.05	5.8	5.5±0.2
2	1997 Jan 3	05:12	16.0	46.67±0.03	9.9	4.7±0.1
3	1997 Jan 3	14:47	14.8	71.87±0.04	9.6	8.7±0.1
4	1997 Jan 3	23:44	8.9	41.33±0.04	6.1	4.4±0.2
5	1997 Jan 4	05:09	23.0	38.55±0.03	13.5	4.1±0.1
6	1997 Jan 4	17:44	4.8	39.83±0.06	3.1	4.8±0.3
7	1997 Jan 4	21:14	4.8	33.28±0.06	3.7	3.7±0.3
8	1997 Jan 5	01:08	6.0	52.03±0.06	2.3	7.1±0.3
9	1997 Jan 5	05:09	4.8	37.80±0.06	3.0	4.2±0.2
10	1997 Jan 5	11:07	6.9	27.24±0.04	3.9	3.8±0.2
11	1997 Jan 5	15:03	2.1	13.58±0.06	1.3	2.6±0.4

[a] in 3–20 keV
[b] in 15–100 keV

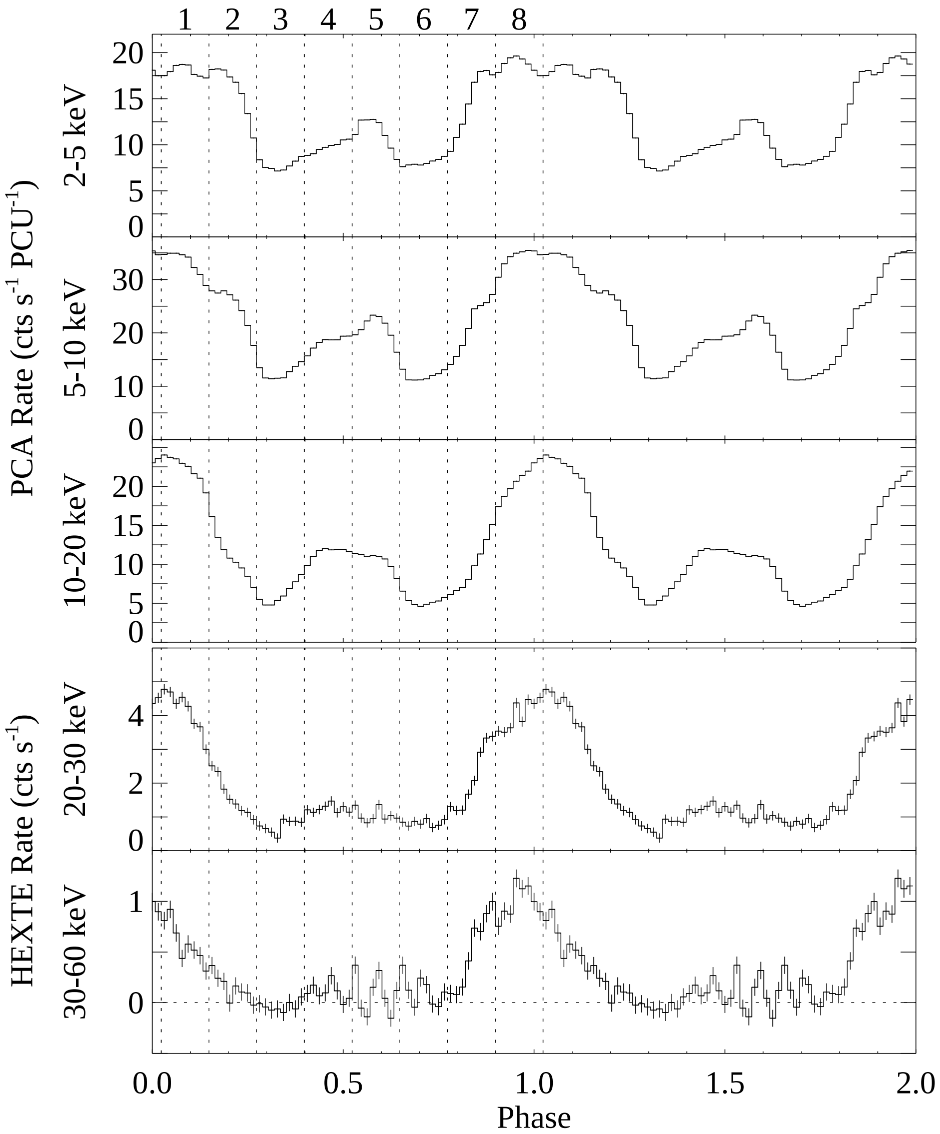

Figure 4.4: The *RXTE* light curve of 4U 1538−52 for both the PCA and HEXTE instruments, folded at the pulsation frequency. Note the differing scales and offsets in the various panes. As is common in accreting X-ray pulsars, the pulse shape is more complex at lower energies, with a simpler shape and higher pulsed fraction at higher energies.

good fits below 10 keV problematic. By ignoring these components the core of the analysis, which is primarily an investigation on how the $\gtrsim 10$ keV spectrum changes with pulsation phase, remains unaffected.

When fitting, I found that the PLCUT model gave the best fits to the data (see §2.2.4). When using the FDCO continuum I found that, for most phases, the photon index Γ was poorly constrained although the fits themselves had a similar range of

χ^2. The NPEX model suffered from a similar drawback, with neither of the power-law indices constrained. The relative analytic simplicity of the PLCUT form, along with its historical significance and the ability to directly compare the results here with those in Chapter 3, made its application useful. I modeled the CRSF using the Gaussian absorption feature given in Eq. 2.5.

4.3.2 Results and Discussion

Fits to the 8 spectral phase bins, along with the inferred photon spectra, are shown in Fig. 4.5. The results of the fitting are given in Table 4.2, and plotted as a function of pulse phase in Fig. 4.6. As was found in *Ginga* observations (Clark et al. 1990), there is an absorption feature near 20 keV required in all phases, and this feature varies with rotation. Also, the feature is strongest in the smaller of the two peaks, evidenced as a maximum in the CRSF depth parameter τ_c during phase bins 4 and 5. Like Hercules X$-$1, there does not seem to be any evidence for a CRSF second harmonic in the spectrum. This is especially true during the main peak, where there is a significant detection of the source beyond $\sim$40 keV where a second harmonic would be expected. Additionally, the CRSF energy follows the peaks in pulsation light curve. The CRSF width peaks during the rise of the pain pulse, but is relatively constant otherwise. The 20.7 keV CRSF in the spectrum implies a magnetic field of $B = 1.8(1+z) \times 10^{12}$ G ($B = 2.3 \times 10^{12}$ G assuming a canonical neutron star).

The FLC (see Fig. 4.4)is similar to what has been seen with *Ginga* (Clark et al. 1990). There are two peaks of unequal height, with the secondary peak much softer than the main pulse. As with most accreting X-ray pulsars, the pulse shape becomes simpler and has a higher pulsed fraction with increasing energy (White, Swank & Holt 1983). As was also the case with *Ginga*, the secondary pulse decomposes into several smaller peaks at energies above $\sim$30 keV. The cause of this is unknown.

The CRSF energy E_c of 4U 1538+52 was found to vary as a function of pulsation phase. This is similar to what is observed in Her X$-$1 (Soong et al. 1990) and Cen X$-$3 (Heindl & Chakrabarty 1999; Burderi et al. 2000), while different from sources such as 4U 1626$-$67 and 4U 1907+09 (discussed below). While it is unclear exactly why a variation is seen in some sources but not in others, several models

Table 4.2: 4U 1538−52 Pulse Phase Resolved Fit Parameters

	Pulse Phase							
Parameter	1	2	3	4	5	6	7	8
Γ	$0.64^{+0.04}_{-0.03}$	$1.35^{+0.04}_{-0.05}$	$1.2^{+0.1}_{-0.2}$	$0.67^{+0.02}_{-0.03}$	0.7 ± 0.2	$1.24^{+0.08}_{-0.16}$	$0.4^{+0.4}_{-0.3}$	$0.7^{+0.2}_{-0.3}$
$E_{\rm cut}$	13.6 ± 0.1	$17.1^{+0.6}_{-0.5}$	16.8 ± 0.5	13.3 ± 0.2	$16.5^{+0.8}_{-0.6}$	$13.2^{+0.6}_{-0.5}$	$14.3^{+0.4}_{-0.3}$	$14.6^{+0.4}_{-1.7}$
$E_{\rm fold}$	9.1 ± 0.2	$8.3^{+0.8}_{-0.7}$	$5.9^{+1.0}_{-0.8}$	7.6 ± 0.4	5.6 ± 0.5	11.1 ± 1.3	$8.1^{+2.5}_{-1.3}$	10.5 ± 1.5
$E_{\rm c}$	21.6 ± 0.2	$20.5^{+0.5}_{-0.4}$	$19.4^{+0.3}_{-0.5}$	21.0 ± 0.2	20.3 ± 0.3	$19.7^{+0.5}_{-0.4}$	18.9 ± 0.5	$20.6^{+0.2}_{-0.3}$
$\sigma_{\rm c}$	1.9 ± 0.2	$2.6^{+0.4}_{-0.3}$	$2.8^{+0.6}_{-0.4}$	1.7 ± 0.1	$3.6^{+0.5}_{-0.3}$	$2.6^{+0.8}_{-0.5}$	6.0 ± 1.2	4.4 ± 0.6
$\tau_{\rm c}$	0.44 ± 0.03	$0.41^{+0.08}_{-0.07}$	0.6 ± 0.1	1.23 ± 0.08	1.5 ± 0.1	$0.51^{+0.10}_{-0.09}$	$1.1^{+0.2}_{-0.3}$	$0.7^{+0.2}_{-0.1}$
$\chi^2_{\rm red}$/DOF	2.588/51	0.939/49	1.325/47	1.905/48	1.231/48	1.569/47	1.573/48	1.615/51

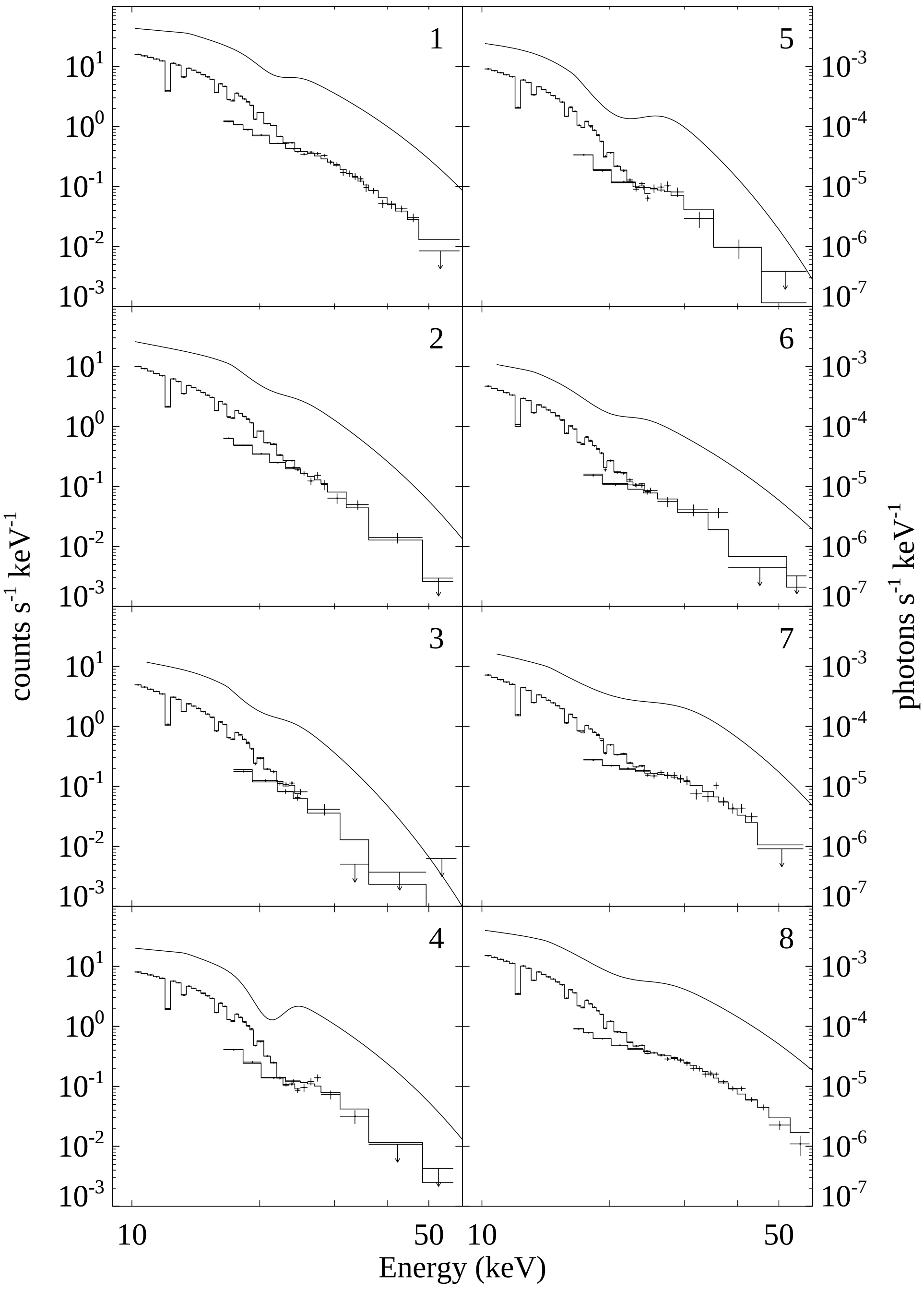

Figure 4.5: Pulse phase resolved joint PCA/HEXTE spectra of 4U 1538−52 in 8 pulse phase bins, as defined in Fig. 4.4. Each panel contains the observed counts (crosses), inferred photon spectrum (solid line), and the inferred spectrum folded through the instrumental response (histograms). The cyclotron feature clearly changes with pulsation phase, being most pronounced during the smaller pulse, phases 4 and 5. The irregular pattern in the PCA counts spectra is due to summing PCUs with slightly different gain corrections. The generation of the PCA response takes this into account, with continuum models predicted to have more (or less) counts per bin in the same manner as the data.

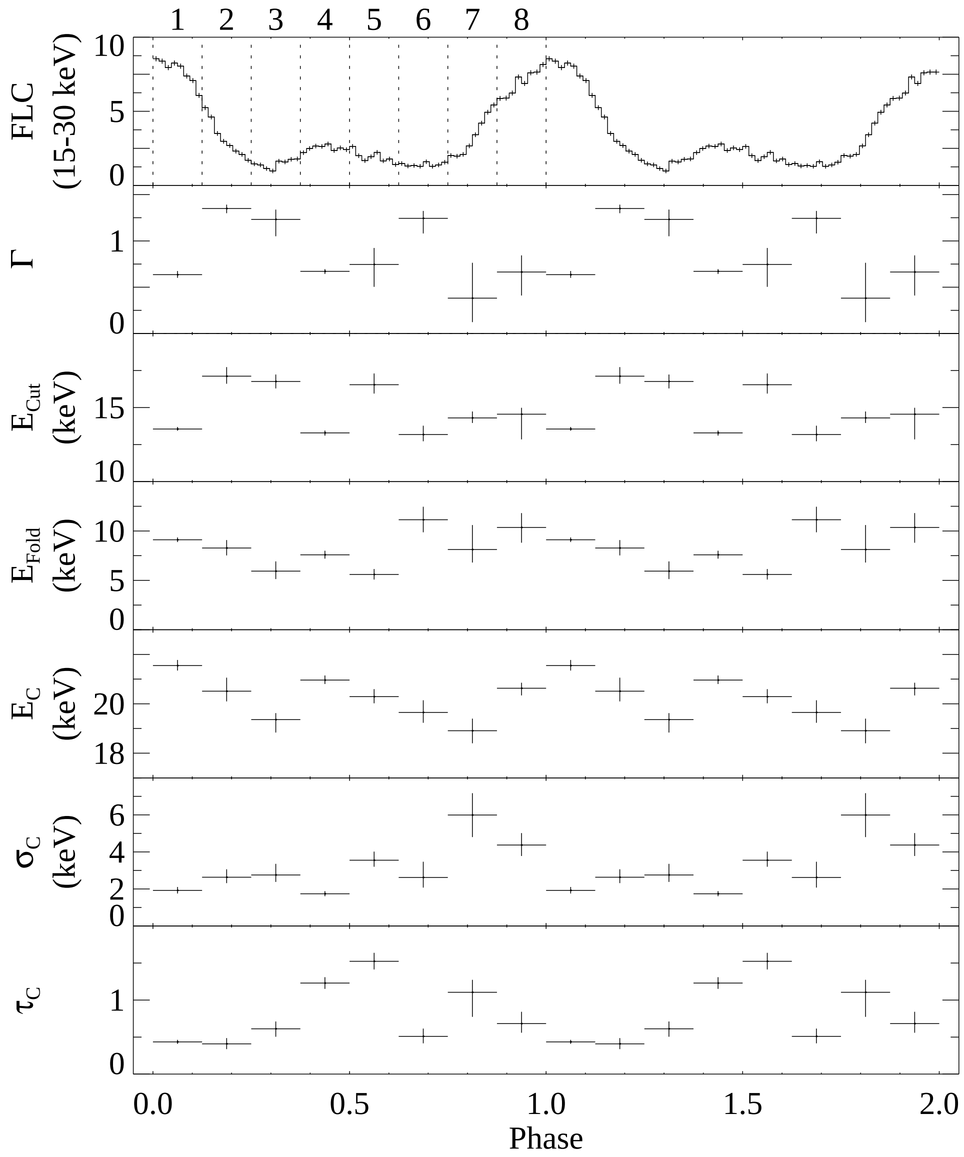

Figure 4.6: Fit parameters as a function of pulsation phase for 4U 1538−52, plotted twice for clarity. The phase bins are as defined in Fig. 4.4. For ease of reference, the HEXTE 15–30 keV FLC is presented in the top pane.

have been proposed. Since the strength of a dipole field changes as r^{-3}, a simple explanation is that the height of the line forming region above the pole changes as a function of pulsation phase (Mihara 1995). Another method is to exploit both the r^{-3} (and the $\cos(\theta)$) dependence of the field by allowing the angle between the dipole axis and the surface normal at the polar caps be no longer parallel. This is easily achieved by having the dipole significantly offset from the center of the neutron star

(Burderi et al. 2000). Recently Weth (2001) has suggested that the variations in line energy could be due to Doppler shifts in the accretion stream itself, although this model does have problems explaining sources where variability is not seen.

It is of interest to compare the observed line shapes to the simulations of Araya-Góchez & Harding (2000) for a 1.7×10^{12} G magnetic field (see Fig. 1.7). When matching the line shapes there are two main considerations: the observed feature is broad and shallow in all phases, and there are no CRSF harmonics detected above the fundamental. Also, since X-ray eclipses are seen the binary system must be viewed nearly edge on, and therefore the rotation axis of the pulsar can be assumed to be nearly perpendicular to the line of sight.

First, assuming that the angle between the magnetic field and the spin axes is small, then the viewing angle to the magnetic field will be nearly perpendicular ($\Theta_0 \simeq 90°$). For isotropic injection of photons, both the slab and cylindrical scattering plasmas produce several prominent higher harmonics. These are not seen observationally. Furthermore, for the case of cylindrical scattering geometry the fundamental is entirely in emission. Although the feature at 10 keV seen in the phase averaged spectrum (see §3.1.8) might be this emission peak and the 20 keV line the second harmonic, the lack of a harmonic at 30 keV makes this interpretation doubtful. For the injection of a fan beam the model predictions are similar, with shallow or non-existent fundamentals followed by several prominent higher harmonics. The FLC, which exhibits two peaks of unequal amplitude, suggests a pencil beam emission pattern (§4.2). Assuming a cone injection into the scattering plasma, the profile predicted for the fundamental feature is a broad emission feature with little or no evidence for higher harmonics. Again, this is not what is observed.

In the models of Araya-Góchez & Harding (2000), the geometry that qualitatively matches best with the observations of 4U 1538−52 is the combination of a pencil beam propagating though a slab of scattering material, and viewed nearly *face on* ($\Theta_0 \sim 90°$, also referred to as an orthogonal rotator since the spin and dipole axes are perpendicular). If the viewing angle to the magnetic field is small, then the predicted line shape is a single, broad feature at the resonance energy. Each peak in the FLC would be due to an individual pole rotating through the field of view, and the reduced emission in the secondary peak either due to inclination effects or possibly a smaller

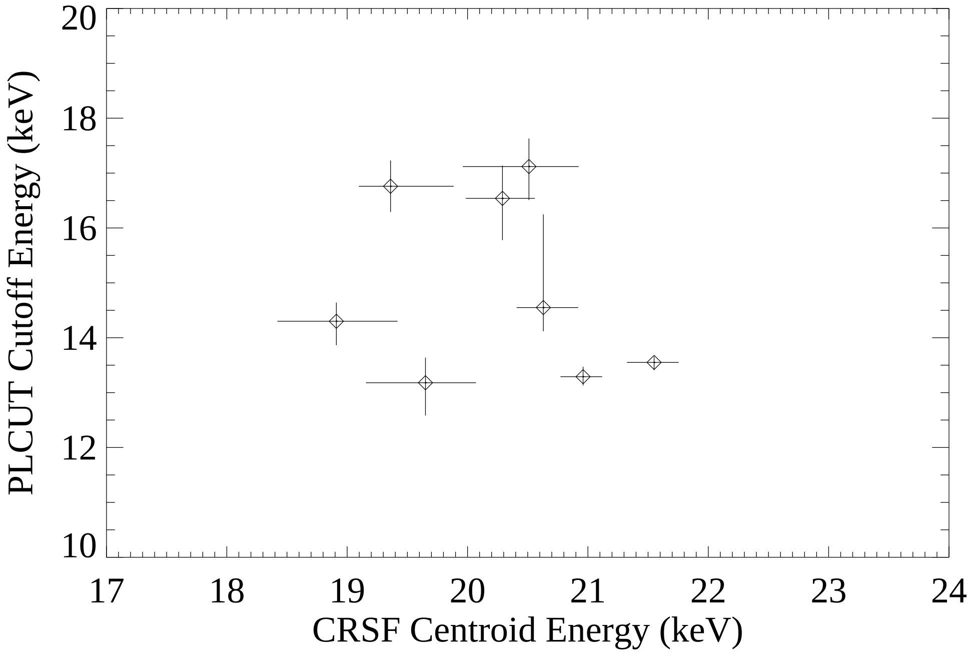

Figure 4.7: The pulse phase resolved fit values of E_c versus E_{cut} for 4U 1538−52, using the same parameterization as in §3.2.3. Unlike the phase averaged case across many sources, there is no clear correlation in the phase resolved data.

accretion rate.

The problem with the interpretation of the system as an orthogonal rotator, however, lies in the phases away from the two pulse peaks. At intermediate viewing angles the simulations predict prominent emission wings on the fundamental. These are not seen during the rising or falling phases. Also, between the two peaks in the interpulse phases both poles are presumably being viewed nearly edge on. Based on the simulations one would expect the CRSF to disappear, but instead the feature is still observed. Possibly gravitational light bending causes the observed emission to be dominated by the two poles at all phases, however this seems unlikely. Therefore, based upon the simulations alone, it cannot be determined if 4U 1538−52 is an orthogonal rotator.

This certainly does not mean that the simulations of (Araya-Góchez & Harding 2000) are incorrect. Rather, that given the caveats in §§1.5.1 and 4.1, they may not be directly applicable to this system. It should also be noted that these interpretations are not based on rigorous fits to the simulations. Instead they are the result of comparing the general features of the predicted line shapes with what is observed.

Using the 529 s pulsation period, the 5×10^{36} ergs s^{-1} luminosity, and assuming that the neutron star is spinning in equilibrium with the inner edge of an accretion disk, the magnetic dipole moment of the neutron star can be inferred from accretion torque theory (see §1.5.2). Using this formulation, the dipole moment is $\mu = 2.7\times10^{32}$ G cm^3, giving a polar cap magnetic field of 5.4×10^{14} G. Since the measured B-field from the CRSF energy is only 2.3×10^{12} G, which is over 200 times smaller, the neutron star is not spinning in equilibrium with the inner edge of an accretion disk. Instead I conclude that it is accreting primarily from the wind of its companion, and that if an accretion disk forms it is only transitory. This is supported by the lack of any periodic long term optical variability that might be associated with the presence of an accretion disk (Pakull et al. 1983), as is seen in sources such as Her X−1 and SMC X−1.

In Fig. 4.7 I have plotted the fit CRSF centroid energy E_c versus the PLCUT cutoff energy $E_{\rm cut}$. A strong, nonlinear correlation between these two parameters was noticed in §3.2.3 using phase averaged spectra from a number of sources. This indicated that the phase average value of the cutoff energy is related to the magnetic field. Here, however, there is almost no correlation between the two parameters despite the use of the same spectral model and fitting techniques. Therefore, while the magnetic field apparently sets the gross value of the cutoff energy, the variations seen as a function of pulsation phase are not sensitive to the changes in the local magnetic field for that phase.

The lack of a correlation in the phase resolved data could be due to the observed spectral cutoff being determined in a region distinct from where the cyclotron scattering occurs. This might be the case if the observed spectrum is generated deep within the neutron star atmosphere, and then propagates outward through the upper layers. In this way the cutoff energy can be determined by the bulk magnetic field strength, however there can still be small variations around the average value that are due to radiative transport through the material and not the observed CRSF energy.

4.4 4U 1626−67

The 7.66 s pulsar 4U 1626−67 shares a 42 min orbit (Middleditch et al. 1981) with the low-mass dwarf star KZ TrA. The system has the lowest known mass function for a pulsar (Levine et al. 1988), with a limit of $a_{\mathrm{x}} \sin i < 8$ lt-ms (Shinoda et al. 1990). The timing history of 4U 1626−67 is characterized by a sudden change from steady spin-up to steady spin-down in 1990 June (Chakrabarty et al. 1997). A $\sim$40 mHz quasi-periodic oscillation has been observed in the X-ray emission (Shinoda et al. 1990; Angelini et al. 1995; Kommers, Chakrabarty & Lewin 1998). This QPO probably arises through the interaction between the pulsar magnetosphere and the inner edge of the accretion disk (Alpar & Shaham 1985; Lamb et al. 1985).

It is thought that material proceeds onto the neutron star through an accretion disk. The optical counterpart of 4U 1626−67 has a strong ultraviolet excess (McClintock et al. 1977), and pulsations have been detected with the same period as the X-ray pulsar (Ilovaisky, Motch & Chevalier 1978). This emission is understood to be primarily due to the reprocessing in an accretion disk of X-ray flux from the pulsar (Chester 1979; McClintock et al. 1980). The exact nature of the mass transfer from the companion star to the disk is still unknown, however. Since neon is a product of helium burning, the existence of a bright neon line emission complex suggests a helium-burning star that underfills its Roche lobe (Angelini et al. 1995). Chakrabarty (1998), however, finds that mass transfer via a radiative driven wind is inconsistent with optical observations. For reasonable estimates of the companion star mass, Chakrabarty (1998) concludes that the inclination angle of the system must be small (i.e. the binary orbital plane is being viewed nearly face on).

Historically the hard X-ray (2–250 keV) spectrum of 4U 1626−67 has been fit with an absorbed $\sim$0.6 keV blackbody, plus a power-law that is exponentially cutoff above $\sim$20 keV. This form is typical of accreting X-ray pulsars (White, Swank & Holt 1983). Doing a pulse phase resolved analysis of *ASCA* data, Angelini et al. (1995) found evidence for a very weak Fe-K emission line just after the low-energy double peak structure (see Fig. 4.9, phases $\sim$0.5-0.7). The line had an equivalent width of 80 ± 42 eV. Additionally, *ASCA* and *Beppo*SAX observed a bright neon line emission complex near 1 keV (Angelini et al. 1995; Owens, Oosterbroek & Parmar 1997). Both

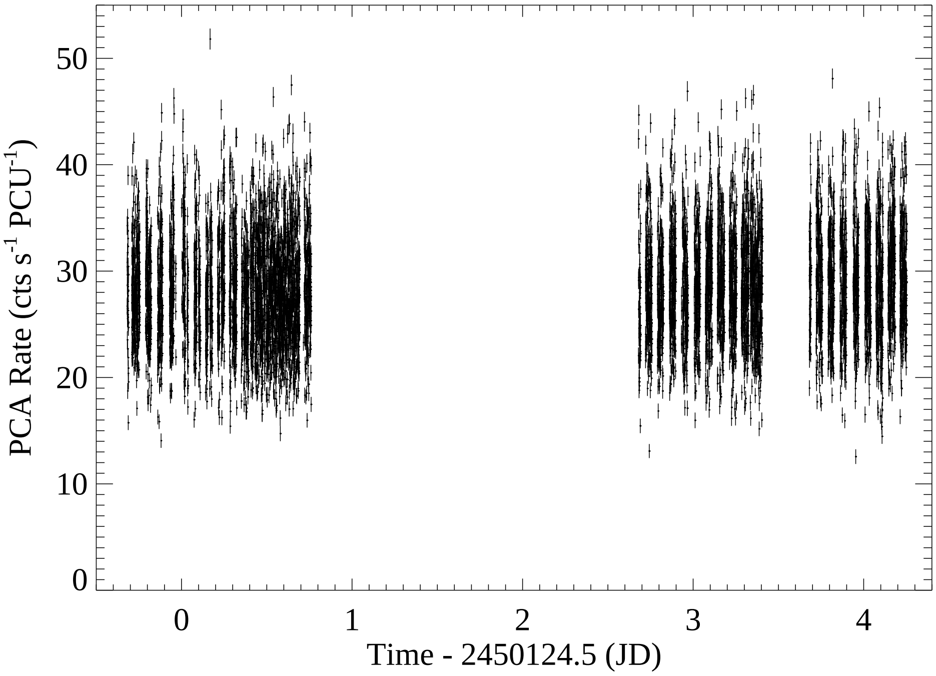

Figure 4.8: PCA light curve (top layer only, 16 s time resolution, entire energy range) for 4U 1626−67. The modulation in the counting rate is due to the 528 s pulsation period.

the *RXTE* and the *Beppo*SAX satellites observed a $\sim$ 39 keV CRSF in the spectrum of 4U 1626+67 (Heindl & Chakrabarty 1999; Orlandini et al. 1998), which implies a magnetic field strength of $B = 3.4(1+z) \times 10^{12}$ G in the scattering region, or $B = 4.4 \times 10^{12}$ G for a canonical neutron star.

Although 4U 1626−67 has a period and luminosity that is similar to the anomalous X-ray pulsars (discussed in §1.4.2), the similarities end there. In particular, the spectrum of 4U 1626−67 is quite different from the soft (Γ~3–4) spectrum of AXPs. The spin histories of 4U 1626−67 and AXPs differ as well, with the anomalous pulsars experiencing nearly constant spin-down while 4U 1626−67 has exhibited both spin states. Because of these differences it is safe to conclude that 4U 1626−67 falls in the AXP period and luminosity range by chance, and not due to a relation with the class of anomalous X-ray pulsars.

4.4.1 Data and Analysis

As of March 2001, the *RXTE* has made 20 pointed observations of the source, for a total time of 274.3 ks. Here I discuss data from 3 long observations made between 1996

February 10–14. The source remained fairly constant in both luminosity and spectral shape over the course of the four day observation, allowing me to add together the individual pointings and obtain enough sensitivity to pulse phase resolve the CRSF.

This was very early in the mission, during the PCA Gain Epoch 1. Not only were all 5 PCUs operating during the entire set of pointings, this was also before the failure of one of the pulse height analyzers in cluster B of the HEXTE (see §2.1.2). This allowed for the accumulation of spectra from all 8 of the HEXTE detectors. The PCA was on-source for a total of 121 ks. The total HEXTE on-source livetime was 71.6 ks for both clusters. The 3–25 keV count rate in the PCA was 27.34±0.04 cts s^{-1} PCU^{-1}, while the 15–100 keV rate was 5.94±0.04 cts s^{-1} in HEXTE. The 3–100 keV source flux during the observation was 7.3×10^{-10} ergs cm^{-2} s^{-1}. Assuming a distance of 6 kpc this implies a source luminosity of 3.2×10^{36} ergs s^{-1}.

I first accumulated and analyzed phase averaged source spectra using the standard analysis outlined in §2.2. Since the 16 s second time resolution of the PCA standard 2 data is inadequate to pulse phase resolve a 7 s pulsar, I instead used the PCA `GoodXenon` event mode data, using the top layer only but with all detectors. Due to the low counting rate in the PCA I used the Faint model to estimate the background. To estimate the size of the systematic errors in the PCA Epoch 1 (version 2.43) response matrix, I analyzed Crab data taken several days after the 4U 1626−67 observations. The calibration of the PCA during epochs 1 & 2 is less well understood than in later epochs, so the systematic errors are expected to be larger. As discussed in §2.2, I fit the Crab spectrum to a combination of two power-laws. The first the first with a fit photon index of 2.17±0.01, and the second with the 2–10 keV normalization fixed to be 10% of the primary. I then increased the size of the systematic errors until I achieved a reduced $\chi^2$of unity. This analysis lead me to use 0.81% systematic errors in the 3–24 keV range, and 6.6% above 24 keV.

To determine the pulsation period, I started with 22.7 ks of PCA `GoodXenon` data and generated a light curved with 2^{-8} s time resolution. I then used the method outlined in §2.2.2, and determined a period of 7.6673669(2) s centered on MJD 50124.441. Using this period I accumulated the PCA and HEXTE event data into pulse phase resolved spectra using our version of the `fasebin` `FTOOL`. The resulting folded light curves at various energies, including the binning for the spectral analysis, are shown

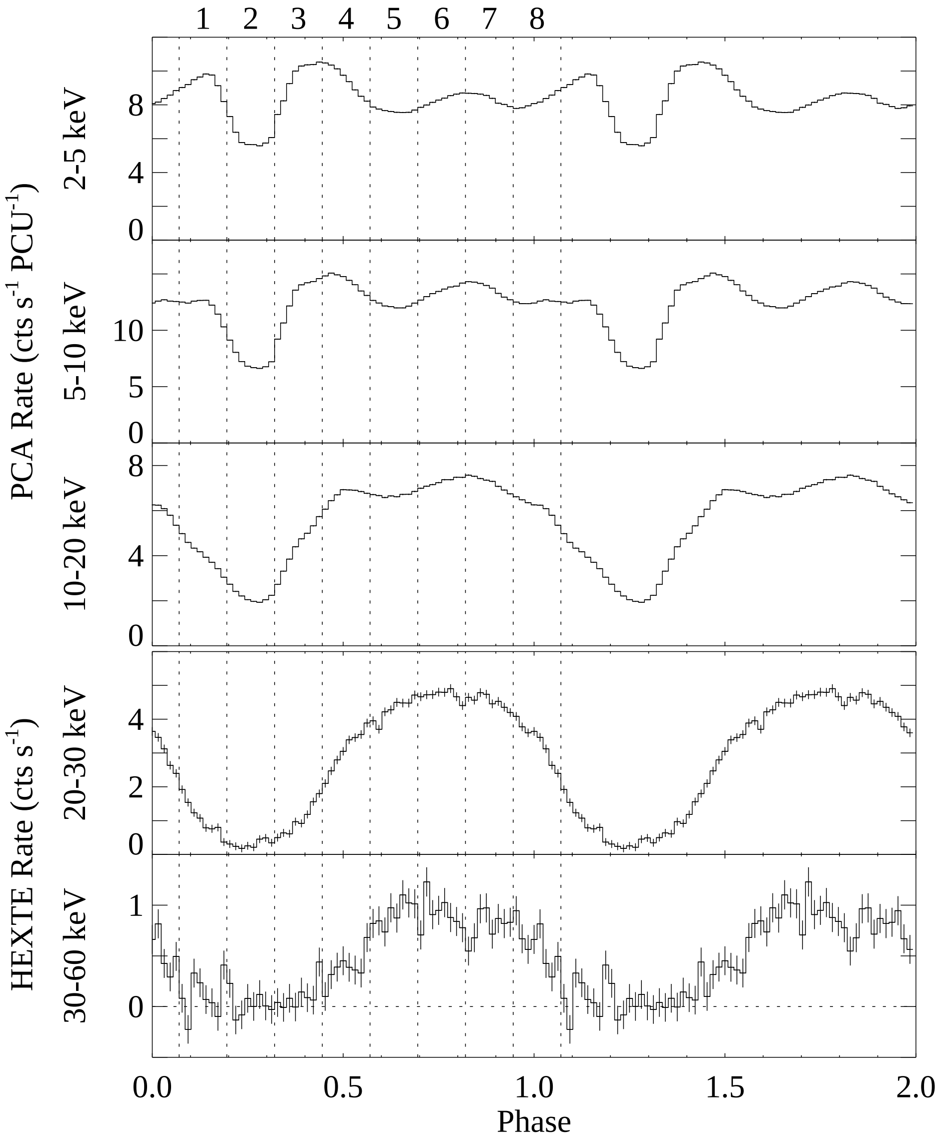

Figure 4.9: The *RXTE* light curve of 4U 1626−67 for both the PCA and HEXTE instruments, folded at the pulsation frequency. Note the differing scales and offsets in the various panes. As is common in accreting X-ray pulsars, the pulse shape is more complex at lower energies, with a simpler shape and higher pulsed fraction at higher energies.

in Fig. 4.9.

I modeled the joint PCA/HEXTE spectra in the 3–100 keV range using a PLCUT continuum model (see §2.2.4). I found that the FDCO model fit the spectrum well in phases 4–8; however, the fits during the low-energy double peaks at phase minimum (see Fig. 4.9) were very poor. The NPEX continuum had similar problems. In addition to this standard pulsar continuum shape and low-energy interstellar absorption, most phases required a blackbody component as well. The *RXTE* observations did not require an iron line in any of the phases, however the upper limits are consistent with the *ASCA* results (Angelini et al. 1995).

4.4.2 Results and Discussion

The spectrum in each phase bin, along with the inferred photon spectrum, is shown in Fig. 4.10. The results of pulse phase resolved fitting can be seen in Table 4.3 and have been plotted in Fig. 4.11. Since the pulse shape at high energies ($\gtrsim 20\,\mathrm{keV}$) is relatively simple, unless otherwise specified when I refer to pulse phase minimum and maximum it will be with respect to the HEXTE folded light curves.

In the phase resolved spectra, away from phase minimum, the average blackbody temperature was $kT = 0.33^{+0.02}_{-0.03}\,\mathrm{keV}$. This is not only consistent with, but nearly identical to, the phase average *Beppo*SAX value of $0.33 \pm 0.02\,\mathrm{keV}$ (Owens, Oosterbroek & Parmar 1997). Unfortunately the normalization of the black-body component, which would allow for an estimation of the area of the emission region, is virtually unconstrained. This is due, at least in part, to the difficulties in simultaneously constraining both the blackbody and low-energy absorption components. Both components affect the lowest few PCA channels, and in general the two components can be varied simultaneously to give similar fits. So while the addition of a black-body component is necessary to properly fit the data, its normalization is unknown.

The measured absorption column, again away from pulse minimum, was consistent with being constant and had an average value of $N_{\mathrm{H}} = (2.5^{+0.4}_{-0.5}) \times 10^{22}\,\mathrm{cm}^{-2}$. This is significantly larger than the $8 \times 10^{21}\,\mathrm{cm}^{-2}$ column measured with the *Beppo*SAX satellite (Owens, Oosterbroek & Parmar 1997). As mentioned above, however, this measurement is problematic for the *RXTE* when there is also a soft component. Therefore it is unlikely that I am measuring a significantly increased absorption column. Instead the formal errors on both N_{H} and kT are most likely underestimated.

The fits of the the blackbody and absorption components in phase bins 1–3 are quite unlike the rest of the phases. A much lower absorption column ($5 \times 10^{21}\,\mathrm{cm}^{-2}$) is inferred from the the fits, and the blackbody component is either missing (phases 1 and 3) or at nearly twice the temperature (phase 2). In these phase bins the spectrum

Table 4.3: 4U 1626−67 Pulse Phase Resolved Fit Parameters

	Pulse Phase							
Parameter	1	2	3	4	5	6	7	8
$N_{\rm H}\,(10^{22}{\rm cm}^{-2})$	$0.54^{+0.1}_{-0.09}$	< 1.4	$0.4^{+0.7}_{-0.4}$	$1.8^{+2.2}_{-1.7}$	2 ± 1	$2.7^{+0.6}_{-0.9}$	3 ± 1	$2.6^{+0.6}_{-1.2}$
kT (keV)	–	$0.75^{+0.07}_{-0.13}$	–	$0.39^{+0.09}_{-0.14}$	$0.33^{+0.05}_{-0.07}$	$0.33^{+0.05}_{-0.05}$	$0.31^{+0.04}_{-0.06}$	$0.33^{+0.04}_{-0.07}$
Γ	1.00 ± 0.01	$0.3^{+0.3}_{-0.4}$	$0.92^{+0.11}_{-0.08}$	0.8 ± 0.1	0.75 ± 0.03	0.80 ± 0.03	0.81 ± 0.04	0.90 ± 0.05
A^{a}	$272.9^{+4.9}_{-0.8}$	148^{+11}_{-8}	284^{+24}_{-5}	298^{+17}_{-12}	243^{+8}_{-7}	276^{+5}_{-7}	279^{+5}_{-8}	264^{+8}_{-8}
$E_{\rm cut}$ (keV)	6.63 ± 0.08	6.5 ± 0.2	$6.6^{+0.4}_{-0.3}$	$6.7^{+0.9}_{-0.8}$	$21.3^{+0.3}_{-0.5}$	22.0 ± 0.5	27 ± 2	27 ± 2
$E_{\rm fold}$ (keV)	12.6 ± 0.2	$5.8^{+1.1}_{-0.9}$	13^{+3}_{-1}	37^{+15}_{-10}	9 ± 1	9.3 ± 0.5	8 ± 1	8 ± 2
$E_{\rm c0}$ (keV)	36 ± 6	–	63^{+80}_{-17}	39 ± 2	36 ± 2	38^{+2}_{-1}	38 ± 2	40^{+4}_{-3}
$\sigma_{\rm c0}$ (keV)	5^{+3}_{-1}	–	15^{+10}_{-6}	7 ± 1	2 ± 2	3 ± 2	$7.6^{+1.2}_{-0.6}$	$10.4^{+0.9}_{-1.4}$
$\tau_{\rm c0}$	$1.1^{+0.8}_{-0.5}$	–	$8^{+\infty}_{-6}$	$3.0^{+0.6}_{-0.9}$	$1.3^{+\infty}_{-0.6}$	$1.7^{+\infty}_{-0.6}$	$1.4^{+0.2}_{-0.3}$	$1.6^{+0.3}_{-0.5}$
$E_{\rm c1}$ (keV)	78^{+86}_{-1}	–	–	84^{+56}_{-10}	–	–	–	–
$\sigma_{\rm c1}$ (keV)	19^{+21}_{-1}	–	–	12^{+8}_{-4}	–	–	–	–
$\tau_{\rm c1}$	6^{+27}_{-1}	–	–	> 8	–	–	–	–
$\chi^2_{\rm red}$/DOF	0.905/75	0.834/79	0.643/78	0.693/73	0.823/76	0.993/76	1.086/76	1.300/76

a $10^{-12}\,{\rm ergs\,cm^{-2}\,s^{-1}}$ in 2–10 keV

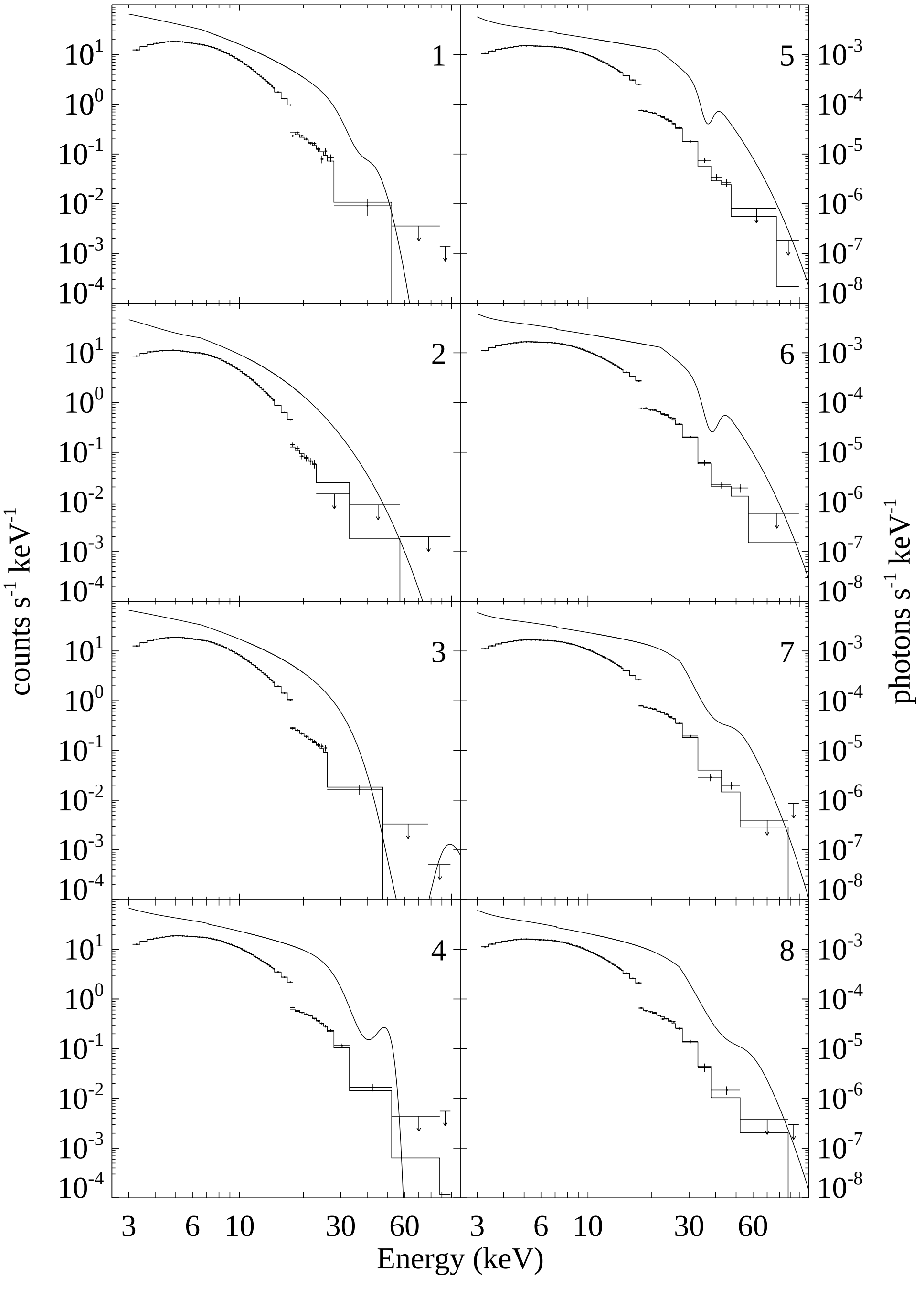

Figure 4.10: Pulse phase resolved joint PCA/HEXTE spectra of 4U 1626−67 in 8 pulse phase bins, as defined in Fig. 4.9. Each panel contains the observed counts (crosses), inferred photon spectrum (solid line), and the inferred spectrum folded through the instrumental response (histograms).

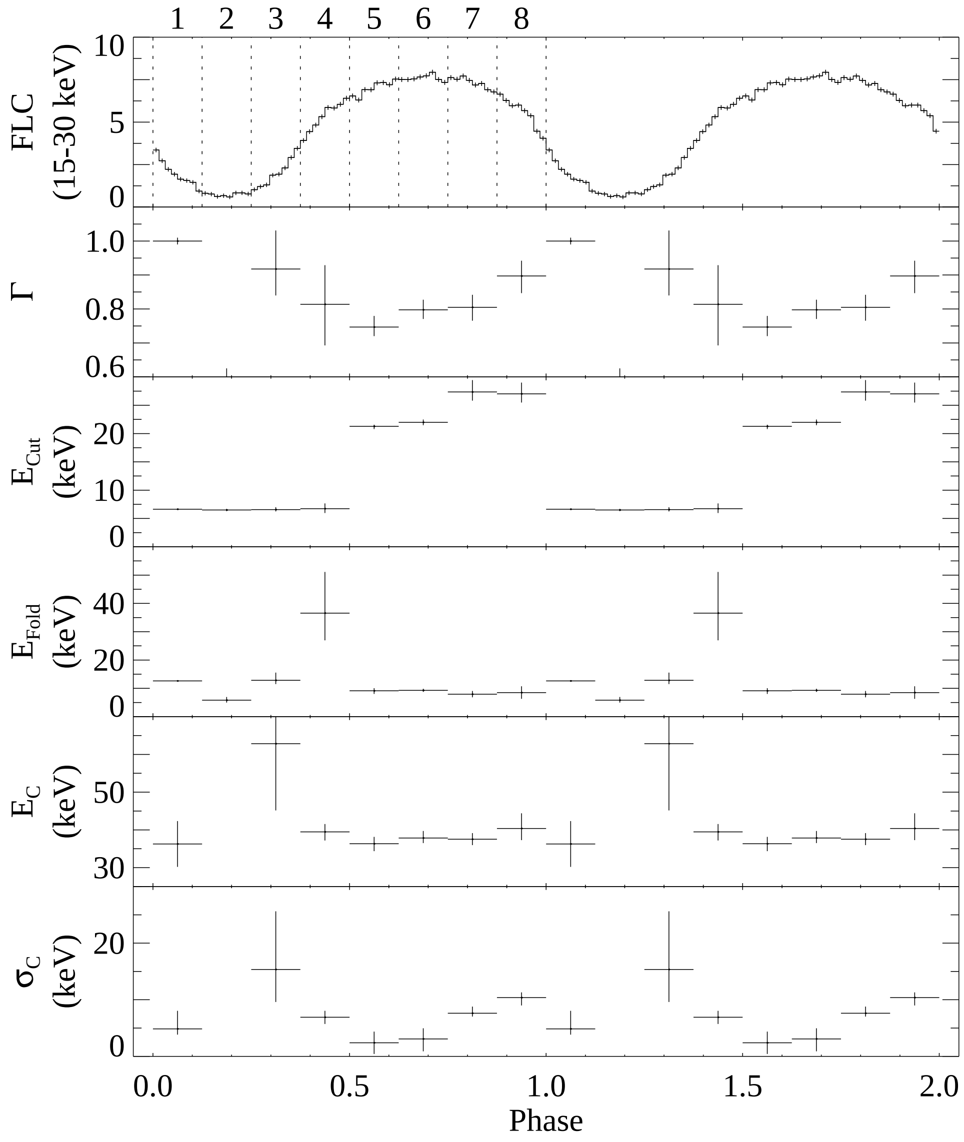

Figure 4.11: Fit parameters as a function of pulsation phase for 4U 1626−67, plotted twice for clarity. The phase bins are as defined in Fig. 4.9. For ease of reference, the HEXTE 15–30 keV FLC is presented in the top pane.

is very soft, and the low-energy component changes very quickly with phase. Even with my relatively narrow pulse phase bins I am averaging over quite a bit of structure in the FLC at the lowest energies (see Fig. 4.9).

The CRSF centroid energy is constant, to within errors, through the pulse peak, implying that a nearly constant magnetic field is seen as the hard X-rays sweep past. This is different than sources like Her X−1 (Soong et al. 1990), Cen X−3 (Heindl &

Chakrabarty 1999; Burderi et al. 2000), and 4U 1538−52 (Clark et al. 1990§4.3.2), where the CRSF energy changes by as much as 20% through the pulse. Fits through the pulse minimum do not require a CRSF in the fits and so limits on variability cannot be placed there. This is due to the source being nearly 100% pulsed at the cyclotron energy.

In phases 1 and 4 (the fall and rise of the pulse) the addition of a CRSF *second* harmonic significantly improved the fits (see Table 4.3). The addition of a second harmonic also significantly improves the phase average fits, with an FTEST probability of 1.6×10^{-11} for a chance improvement in the fits. I also note that, although the errors are large, the best fit energies of the second harmonic CRSFs are twice that of the first, giving harmonically spaced lines as expected. Modeling the fundamental CRSF with the CYCLABS model (with its high energy tail, see §2.2.5) actually gives a slightly worse χ^2, and so cannot account for the steeper cutoff in these phases. If this feature is confirmed, then this is the first evidence for its existence.

Here, however, I can only postulate the presence of a CRSF second harmonic the spectrum. With the steeply falling continuum the second CRSF is only seen in its effects of its red wing on the high energy continuum. This could also be explained by the continuum rolling off faster than $e^{-E/E_{\rm cut}}$. However this seems unlikely given the success of this form when applied to other accreting pulsars (as well as 4U 1626−67 in other phases). Therefore I speculate that there might indeed be a second harmonic CRSF in this source.

If the binary system is indeed viewed nearly face on (Chakrabarty 1998), then the relatively simple sinusoidal shape seen above 20 keV in the FLC can be interpreted as a single hot spot radiating isotropically. The sinusoidal shape is then simply due to the observed area of the emission region being modulated by the rotation of the pulsar. In this picture the other polar cap is hidden from view by the neutron star itself.

The width σ_c of the CRSF, excluding phase bins 2 and 3 where a feature is barely detected, does systematically change as a function of pulse phase. This is most dramatic during the peak of the main pulse. There the CRSF width reaches a minimum (σ_c~2 keV) in the rise of the peak (phase bins 5 and 6), and a maximum (σ_c~9 keV) just after (phase bins 7 and 8). If the CRSF width σ_c is interpreted as due to Doppler broadening (Mészáros & Nagel 1985a), then one would expect a variation as the star rotated the polar magnetic field through the field of view. In this picture, for a constant CRSF energy E_c and electron temperature kT_e, $\Delta E \propto |\cos(\theta)|$ where θ is the viewing angle with respect to the B-field (see Eq. 3.1).

Since it is plausible that only a single magnetic polar cap is being observed, the interpretation of the CRSF width σ_c as due to Doppler broadening becomes much cleaner. In particular, because the emission reaches a maximum before the CRSF width, this implies that the normal to the magnetic polar area reaches the point of closest approach to the line of sight *before* the the magnetic field vector does. This assumes that the emission region is small so that the magnetic field lines can be approximated as nearly parallel. If this is true, then the lag in phase of the CRSF width allows for an estimate of the angle between the magnetic field and the surface normal. This angle might be due to a slight offset $\vec{\mathbf{r}}$ of the dipole moment from the center of the star. Since it is unlikely that we ever observe the emission region completely face on, only the azimuthal component of this angle can be measured. In my fits, where the star's rotation is only resolved into 8 bins, the angle between the B-field and polar cap surface normal is somewhere in the $\sim$45°–90°range. Future observations that allow for a much higher phase resolution are required to properly measure this angle.

The interpretation that the source is viewed nearly face on is consistent with the line shapes predicted by Araya-Góchez & Harding (2000). In their simulations of scattering in a 4.4×10^{12} G magnetic field nearly parallel to the line of sight (see Fig 1.8), lines shapes similar to those observed are predicted for pencil beam injection into both slab and cylinder geometries. As the viewing angle increases, however, the line shapes become very complex. This requires that, while our view of the emission region is modulated by the rotation, it never rotates far from face on. In this case the angle between the spin and rotation axes Θ_1 is small.

Just as with 4U 1538−52 (see Fig. 4.7), the spectral cutoff energy E_c does not vary proportionally with the CRSF centroid energy. In particular, there is an apparent jump in the cutoff energy as a function of pulse phase (see Fig. 4.11). The E_{cut} is modest ($\sim$6 keV) during the minimum and increases discontinuously during the maximum (21-27 keV). This behavior persists with the FDCO continuum, as well as in fits to the PCA data alone (where the cutoff energy moves beyond the PCA range during the pulse maximum). This indicates that the jump is a property of the source, and not an artifact of the modeling. Therefore again there is evidence that while the cutoff energy is a function of the magnetic field, it is either due to a large-scale average B-field strength or else the continuum is formed in a region that is distinct from where the scattering occurs (see §4.3.2).

From the 39.9 keV CRSF I derive a polar cap surface magnetic field of $B = 3.4(1+z) \times 10^{12}$ G (or $B = 4.4 \times 10^{12}$ G for a canonical neutron star). This implies a neutron star magnetic moment of $\mu = 2.2 \times 10^{30}\,\mathrm{G\,cm^3}$. For a source luminosity of $3.2 \times 10^{36}\,\mathrm{ergs\,s^{-1}}$ and a spin period of 7.67 s, the inferred magnetic moment of the pulsar from accretion torque theory (Ghosh & Lamb 1979, see also §1.5.2) is $\mu = 1.5 \times 10^{30}\,\mathrm{G\,cm^3}$(setting $\xi = 1$). This implies a surface field strength of $B = 3.0 \times 10^{12}$ G.

The magnetic moments derived from the CRSF and inferred from accretion torque theory are in very good agreement. This is especially impressive since the theory is technically only applicable in cases where the neutron star is spinning up, while during these observations the source was spinning down. Because of this agreement between the two methods, the pulsar is most likely spinning very near equilibrium with the inner edge of an accretion disk.

Since accretion torque theory is sensitive to the magnetic field at a radius equal to a few-hundred neutron star radii, it is a measure of only the dipole component of the B-field. The agreement between this measure of the magnetic moment and the CRSF, which depends on the magnetic field strength at the neutron star surface, implies that higher order magnetic multipole terms do not dominate in the polar emission region. In particular, the quadrupole term of the star's magnetic field must be small.

4.5 4U 1907+09

The 440 s X-ray pulsar 4U 1907+09 was discovered with the *UHURU* satellite (Giacconi et al. 1971b). Using data from the *Ariel V* satellite, Marshall & Ricketts (1980) determined the 8.38 d orbital period from a folded light curve which showed a pronounced primary flare and a dimmer, irregular secondary flare. Later observations with *Tenma* confirmed the existence of two orbital phase-locked flares (Makishima et al. 1984). The source is a wind fed neutron star, although the exact spectral type of the companion is still under some debate. It has been suggested to be either an OB supergiant (Schwartz et al. 1980), or possibly a Be (Iye 1986; Roberts et al. 2001) companion star.

Recent *RXTE* observations have shown several interesting new phenomena in the source. in't Zand, Strohmayer & Baykal (1997) discovered a dipping behavior in the source, where the 2–15 keV flux fades below the background level during intervals lasting from minutes to perhaps 1.5 hours. The dips are not tied to any particular orbital phases, nor are they associated with enhancements in the column density of cold circumstellar material that might be screening the flux. Therefore the authors conclude that the likely cause for the dips are cessations of the mass accretion, possibly due to an inhomogeneous wind from the companion star.

in't Zand, Baykal & Strohmayer (1998) report the discovery of ~18 s oscillations during a flare from the source that lasted ~1 h. In other sources such a QPO is often interpreted in terms of the magnetic beat frequency model (Alpar & Shaham 1985; Lamb et al. 1985, see also §3.1.2). The authors suggest the flare QPO could be such a feature, and that the frequent formation of a transient, retrograde accretion disk might be responsible for the consistent spin-down of the pulsar.

A ~21 keV CRSF was discovered in 4U 1907+09 by Makishima & Mihara (1992) using *Ginga* observations. This feature was later confirmed, along with the discovery of a second harmonic at ~39 keV, by Cusumano et al. (1998) using a 70 ks *Beppo*SAX observation.

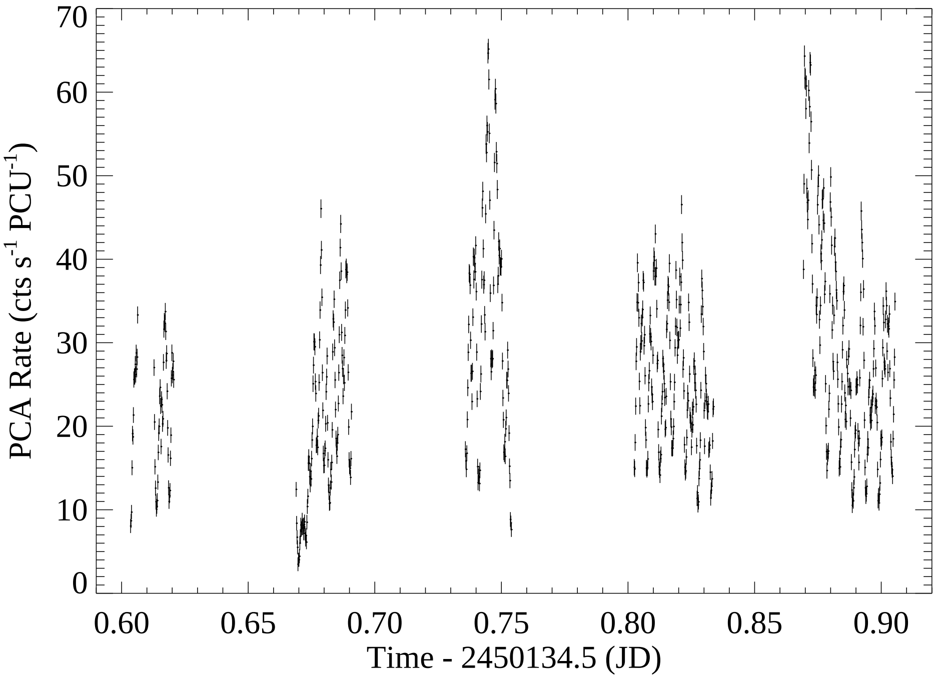

Figure 4.12: PCA light curve (all layers, 16 s time resolution, entire energy range) for 4U 1907+09. The modulation in the counting rate is due to the 528 s pulsation period.

4.5.1 Data and Analysis

As of 2001 March, the *RXTE* has made 57 pointed observations of 4U 1907+09, for a total observing time of 414.6 ks. The observation presented here was obtained on 1996 February 21. Like with 4U 1626-67, this was during PCA gain epoch 1, and before the loss of spectral information from one of the HEXTE detectors in Cluster B (see §2.1.2). This data, which was chosen for its duration, is a subset of a larger series of observations used for other purposes by in't Zand, Strohmayer & Baykal (1997) and in't Zand, Baykal & Strohmayer (1998). I have chosen a sequence that is nearly contiguous and is free from both X-ray dips and flares. This was done to minimize any spectral variability that might be associated with these features. Since this was during PCA epoch 1, the PCA systematic errors I used were 0.8% in the 3–25 keV range.

The PCA datamode used for the observation (`E_16us_64M_0_1s`) did not include detector or layer information. Since the 16 s time resolution of the PCA standard 2 data is inadequate to phase resolve even a 440 s pulse, I accumulated the event data for the entire detector volume instead. Due to the extreme faintness of the source I used the PCA Faint background model. The HEXTE data modes used were standard event modes, and therefore I accumulated the spectra from those detectors in the standard manner.

The pulsation period I derived, centered at MJD 50133.574, was 440.373589(1) s. I used the method outlined in §2.2.2, using a PCA light curve with 2^{-3} s time resolution and the orbital ephemeris of in't Zand, Baykal & Strohmayer (1998). With this period, I accumulated the HEXTE and filtered PCA event files into pulse phase resolved spectra using our version of the `fasebin` `FTOOL` (see §2.2.2). The resulting folded light curves at various energies, including the binning used for the spectral analysis, are shown in Fig. 4.13.

When fitting, I only analyzed the PCA above 10 keV. This was done because, like 4U 1538−52, there is low-energy contamination in the *RXTE* field of view due to emission from other than 4U 1907+09. The pulsar is only $\sim 0^{\circ}.5$ above the Galactic plane, so there is a considerable contribution due to diffuse Galactic emission (Valinia & Marshall 1998). There may also be some extra soft flux due to the supernova remnant W49B, which is only $52'$ off-axis. These factors make obtaining good fits below 10 keV problematic. By ignoring these components the core of the analysis, which is primarily an investigation on how the higher energy spectral components change with pulsation phase, remains unaffected.

I found that the PLCUT model gave the best fits to the data. Much the same as with 4U 1538−52, when using the FDCO continuum I found that the photon index Γ was virtually unconstrained, and neither of the NPEX power-law indices were constrained. The relative analytic simplicity of the PLCUT form along with the ability compare the results here with those in Chapter 3, made its application here desirable.

Cusumano et al. (1998) have reported the detection of a CRSF second harmonic using observations obtained with the *Beppo*SAX satellite. While there are hints of this feature in the fit residuals to the *RXTE* data, the detection of the source is not significant out to high enough energies to confirm the presence of a 40 keV feature.

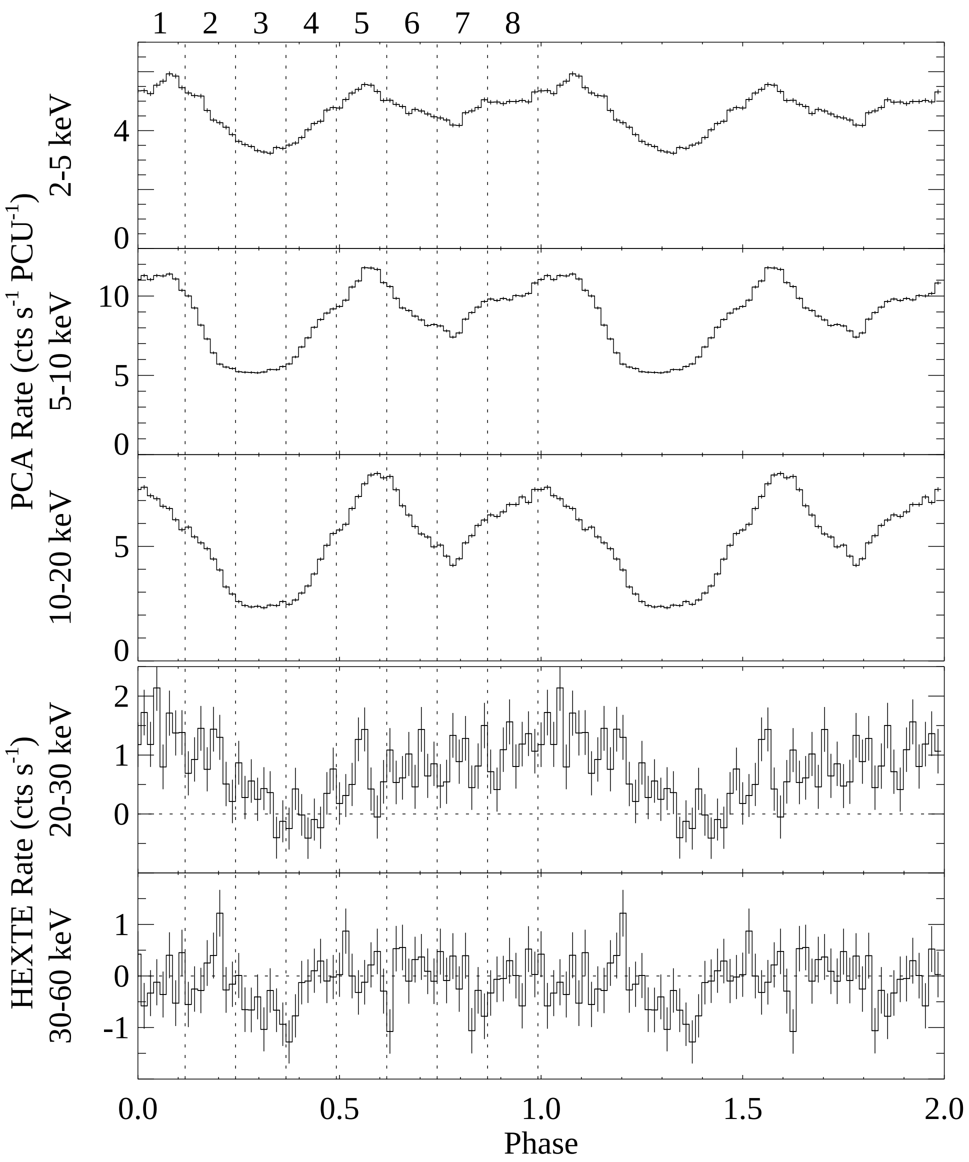

Figure 4.13: The *RXTE* light curve of 4U 1907+09 for both the PCA and HEXTE instruments, folded at the pulsation frequency. Note the differing scales and offsets in the various panes. As is common in accreting X-ray pulsars, the pulse shape is more complex at lower energies, with a simpler shape and higher pulsed fraction at higher energies.

4.5.2 Results and Discussion

The spectra of the 8 phase bins analyzed, along with the resulting fits, are plotted in Fig. 4.14. The results of these fits are given in Table 4.4 and plotted as a function of phase in Fig. 4.15.

The FLC, especially at intermediate energies (5–20 keV), consists of two large

Table 4.4: 4U 1907+09 Pulse Phase Resolved Fit Parameters

	Pulse Phase							
Parameter	1	2	3	4	5	6	7	8
Γ	$0.2^{+1.1}_{-0.5}$	$0.6^{+0.4}_{-2.5}$	$1.1^{+0.4}_{-2.7}$	1.2 ± 0.3	0.6 ± 0.2	$0.3^{+0.2}_{-0.8}$	$1.00^{+0.08}_{-0.22}$	$0.7^{+0.2}_{-0.4}$
$E_{\rm cut}$	$12.6^{+1.2}_{-0.5}$	22.6 ± 1.9	$12.0^{+0.9}_{-2.1}$	12.2 ± 0.3	$12.9^{+0.2}_{-0.3}$	$12.9^{+0.9}_{-0.6}$	$13.2^{+0.8}_{-0.9}$	$20.4^{+2.7}_{-6.2}$
$E_{\rm fold}$	$5.1^{+5.8}_{-1.4}$	$1.9^{+3.3}_{-1.8}$	$7.5^{+2.0}_{-4.5}$	4.3 ± 0.4	$4.4^{+0.8}_{-0.4}$	6.9 ± 1.6	$9.8^{+3.7}_{-2.4}$	$3.9^{+1.6}_{-1.7}$
$\tau_{\rm c}$	$1.1^{+3.2}_{-0.9}$	$0.7^{+0.9}_{-0.2}$	—	—	$0.5^{+1.8}_{-0.2}$	$0.9^{+5.9}_{-0.5}$	0.4 ± 0.2	0.9 ± 0.5
$E_{\rm c}$	$13.8^{+2.8}_{-4.4}$	$19.5^{+3.3}_{-1.0}$	—	—	$18.4^{+0.9}_{-0.5}$	$22.6^{+8.9}_{-1.6}$	$20.9^{+1.9}_{-1.5}$	$20.1^{+2.1}_{-2.4}$
$\sigma_{\rm c}$	$6.1^{+4.4}_{-3.9}$	$3.4^{+5.2}_{-1.2}$	—	—	$1.0^{+1.1}_{-0.9}$	$3.5^{+14.6}_{-1.4}$	$1.9^{+1.8}_{-1.7}$	$3.0^{+1.6}_{-2.7}$
$\chi^2_{\rm red}$/DOF	0.934/17	0.667/17	1.702/19	1.172/19	0.499/16	0.817/17	1.559/16	0.718/17

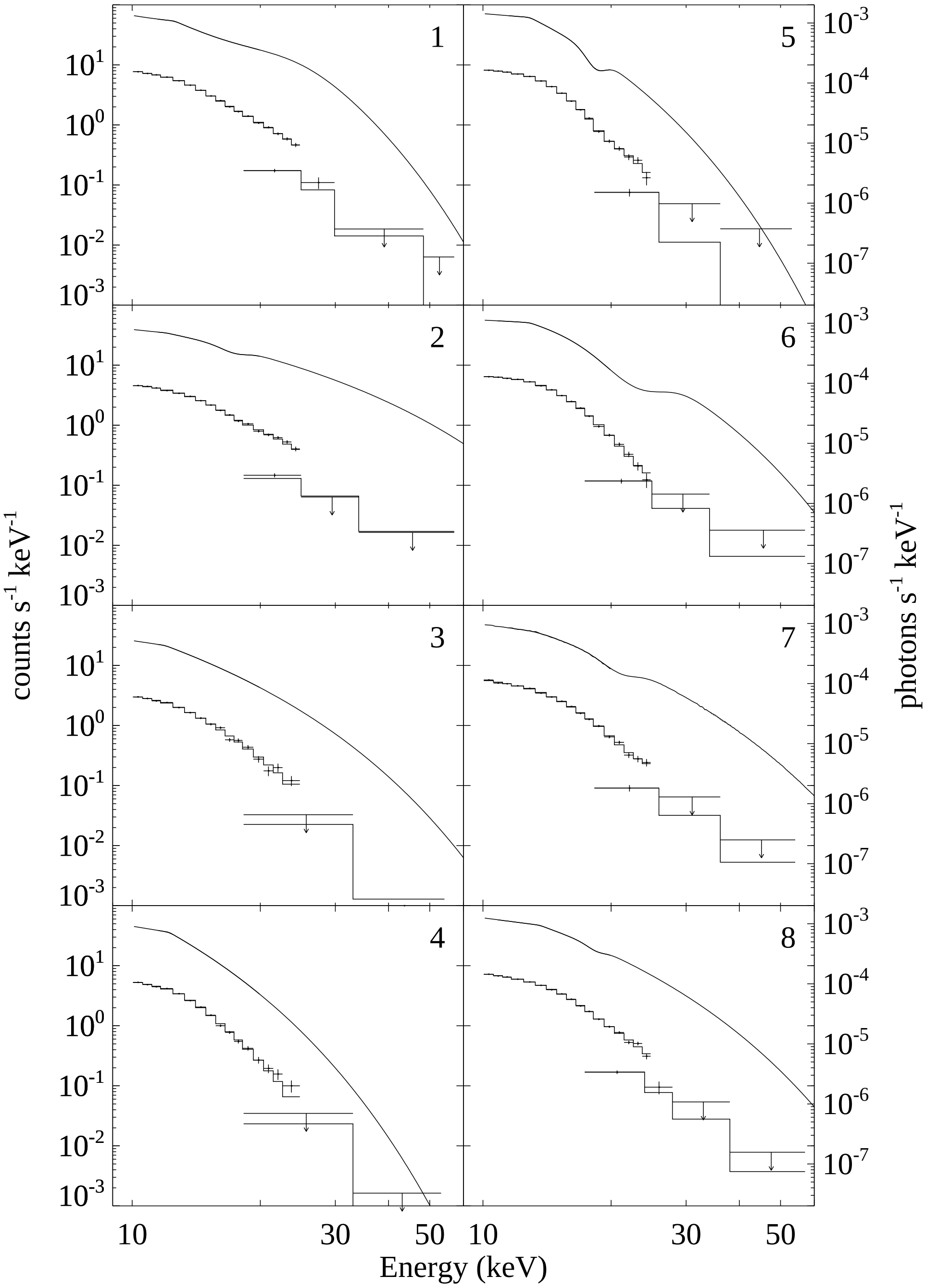

Figure 4.14: Pulse phase resolved joint PCA/HEXTE spectra of 4U 1907+09 in 8 pulse phase bins, as defined in Fig. 4.13. Each panel contains the observed counts (crosses), inferred photon spectrum (solid line), and the inferred spectrum folded through the instrumental response (histograms).

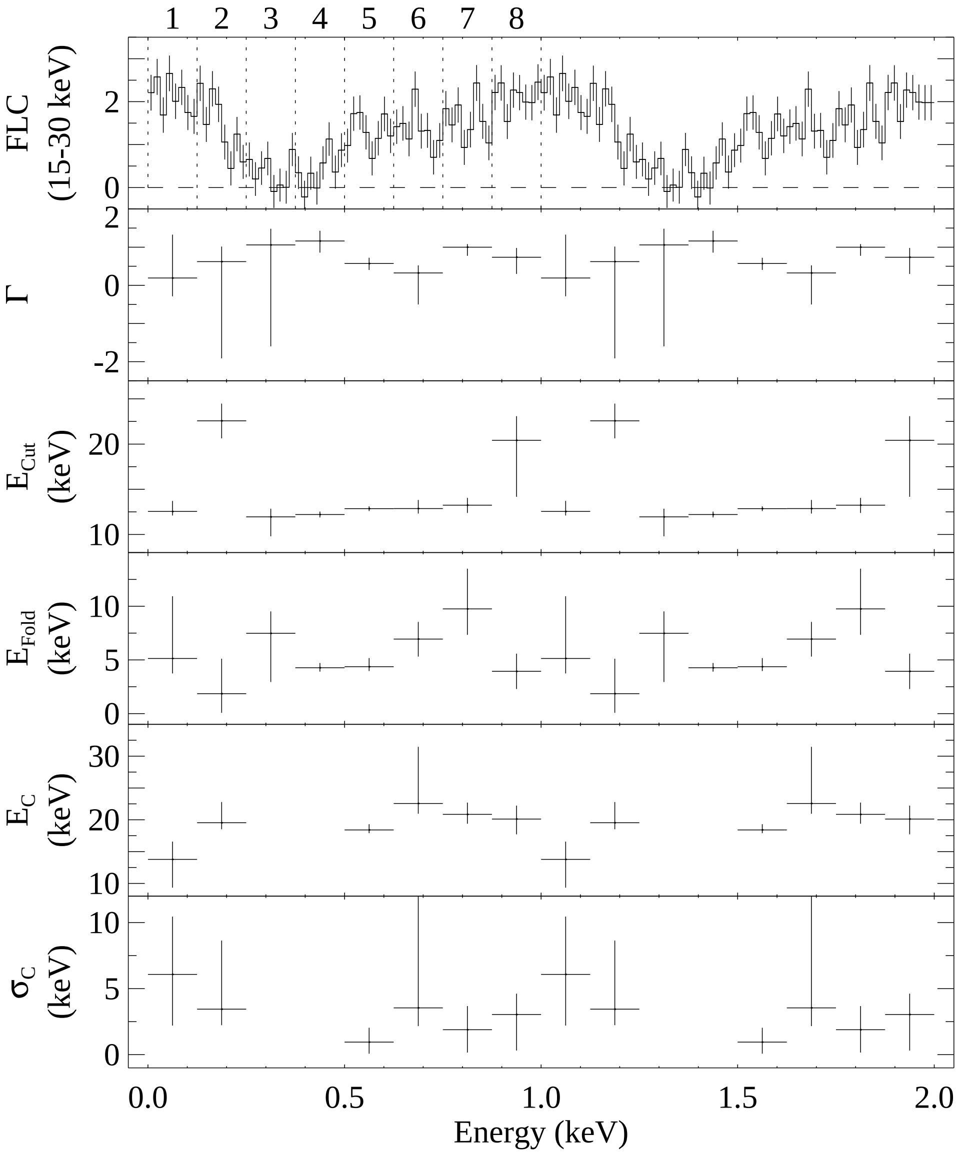

Figure 4.15: Fit parameters as a function of pulsation phase for 4U 1907+09, plotted twice for clarity. The phase bins are as defined in Fig. 4.13. For ease of reference, the HEXTE 15–30 keV FLC is presented in the top pane.

peaks separated by unequal minima. This shape suggests that the emission is primarily that of a fan beam and that the pulsar is observed relatively edge on ($\Theta_{\rm m}+\Theta_0 > \pi/2$, see §4.1). Two broad pencil beams in a distorted dipole configuration (δ ~large), however, cannot be ruled out by the FLC alone. In this case the unequal minima are due to a blending of the emission from the two poles, and the opening angles of the two beams are required to be quite large. The azimuthal component of the offset angle, calculated as the phase difference between the two peaks in the 10–20 keV FLC, is $\delta_\Phi \simeq 28°$. I used this energy range since it is where each peak is reasonably symmetric, and thus have more defined "centers." This angle δ_Φ is quite large, although similar to what has been estimated for Vela X-1 ($\delta \sim 30°$) and 4U 1538-52 ($\delta \sim 25°$) (Bulik et al. 1995).

To within errors, and for the phases where a CRSF was required, the centroid energy E_c remained constant as a function of pulse phase. The distribution of energies about the mean gives a chi-squared of χ^2=4.726 for 6 degrees of freedom. This indicates that while the observed emission region is changing with rotation phase, the observed magnetic field is remaining constant.

The CRSF width remained constant as well, although there is a hint of a systematic increase across the two pulses. If the CRSF width σ_c is due to Doppler broadening (Mészáros & Nagel 1985a, also §3.2.1), then a variation in the width with rotation phase is expected. Since the amplitude of such a variation is almost non-existent, this implies that we are observing the emission region at nearly constant values of θ. The errors, however, are quite large (see Fig. 4.15) and so future observations are needed to verify this. The lack of variation in the width does, however, support the idea that the rotation axis of the neutron star is nearly perpendicular to the line of sight.

If the emission regions are viewed nearly edge on throughout the pulse, this supports the interpretation of the FLC as a fan beam since the broad opening angles required in the pencil beam interpretation would require that the viewing angle to the magnetic field change considerably as the beam moved through and out of the line of sight. The analyses of Iye (1986) and more recently Roberts et al. (2001), indicate that the system has a large orbital inclination. Therefore the CRSF width and FLC shape, combined with estimates of the system inclination angle, indicate that Θ_m is small.

The phase average value of the CRSF energy is 18.3 keV, implying a magnetic field in the scattering region of $B = 1.6(1+z)$ G (or $B \simeq 2.1 \times 10^{12}$ G for a canonical neutron star). The magnetic moment of the star is therefore $\mu \simeq 1.0 \times 10^{30}\,\mathrm{G\,cm^3}$. The 3–100 keV flux is 3.15×10^{-10}. The distance to the source is between 2.4 and 5.9 kpc (van Kerkwijk, van Oijen & van den Heuvel 1989), giving a source luminosity during this observation in the range $(0.2-1.3) \times 10^{36}\,\mathrm{ergs\,s^{-1}}$. Using accretion torque theory, the dipole moment implied by this luminosity range is $4.5 \times 10^{31} - 1.1 \times 10^{32}\,\mathrm{G\,cm^3}$. This translates to a surface field at the magnetic poles of $9.0 \times 10^{13} - 2.2 \times 10^{14}$. This is range of values is 1–2 orders of magnitude larger than that measured by the CRSF energy, implying that the systems is not spinning in equilibrium with an accretion disk. This indicates that the neutron star is accreting material from a fast stellar wind and not through Roche-lobe overflow.

4.6 Summary

One important result is that while there exists a strong correlation between the spectral cutoff energy E_{cut} and the cyclotron energy E_{c} in the phase averaged spectra (see §3.2.3), I find that this does not extend to pulse phase resolved analyses. These analyses indicate that the break in the continuum is not sensitive to the local magnetic field where the cyclotron scattering occurs. Instead, the lack of a correlation in the phase resolved data could be due the observed spectral cutoff being determined in a region distinct from the cyclotron scattering site. This might be the case if the observed spectrum is generated deep within the neutron star atmosphere, and then propagates outward through the upper layers. The cutoff energy is then determined by an average magnetic field strength across the polar cap; however, there can still be small variations across the accretion mound.

Qualitative matches between the line shapes predicted by the Monte Carlo simulations of Araya-Góchez & Harding (2000) and the observations seem to predict that the polar regions of these 3 pulsars are being viewed nearly face on. For the sources 4U 1538-52 and 4U 1907+09 this is inconsistent with analyses of their FLCs, which seem to prefer emission regions being viewed close to edge on. Also, since both of these binary systems are viewed nearly edge on and therefore have rotation axes that are nearly perpendicular to the line of sight, the observed CRSF profiles should match the Monte Carlo simulations from other viewing angles as the polar regions rotate in and out of sight.

It is doubtful, however, that the difficulties in matching emission geometry inferred from the FLCs and the lines shapes from the Monte Carlo simulations are due to a flaw in the simulations themselves. Instead, the discrepancy is probably due to the many simplifications made. In particular, these models assume a very hard input spectrum, one more suited to $\gamma-$ray bursts than accreting pulsars. While these input spectra do allow for an easier identification and interpretation of effects such as photon spawning, relativistic angular distribution, and geometry, they do mean that the results are not directly applicable to accreting X-ray pulsars (Araya & Harding 1999). Future work (e.g., Kretschmar et al. 2000), with a more realistic input spectrum along with additional scattering geometries, should produce better results.

Finally, simply fitting spectra or FLCs alone is not enough to disentangle and understand the emission of accreting X-ray pulsars. However, by interpreting the two in combination, a self consistent picture can start to be formulated. Therefore I propose a method using a combination of FLCs and pulse phase resolved spectroscopy to determine the emission geometry and geography of pulsars. As seen in Figs. 1.7 and 1.8, CRSF shapes are very sensitive to the viewing angle. By fitting spectra as a function of phase the geometry of the emission region can be constrained (e.g. Bulik et al. 1992, 1995). The FLCs of the source can then also be modeled, using a combination of beam patterns and properly taking into account the effects of light bending, giving another set of constraints on the emission region (e.g. Kraus et al. 1995). The results of the two methods should agree, with the simultaneous solution hopefully unique. The eventual goal would be to fit a 2-dimensional histogram of counts versus both energy and rotation phase, giving a complete description of the pulsar emission.

Chapter 5

Discovery of a CRSF in 4U 0352+309 (X Per)

5.1 Abstract

We have discovered a ∼29 keV Cyclotron Resonance Scattering Feature (CRSF) in the X-ray spectrum of 4U 0352+309 (X Per) using observations taken with the *Rossi X-ray Timing Explorer*. 4U 0352+309 is a persistent low luminosity ($L_X = 4.2 \times 10^{34}\,\mathrm{ergs\,s^{-1}}$) X-ray pulsar, with a 837 s period and which accretes material from the Be star X Per. The X-ray spectrum, unusual when compared to brighter accreting pulsars, may be due to the low-mass accretion rate and could be typical of the new class of persistent low luminosity Be/X-ray binary pulsars. We attempted spectral fits with continuum models used historically for 4U 0352+309, and found that all were improved by the addition of a CRSF at $\sim 29\,\mathrm{keV}$. The model that best fit the observations is a combination of a $1.45 \pm 0.02\,\mathrm{keV}$ blackbody with a $5.4 \times 10^{8}\,\mathrm{cm}^2$

area, and a power-law with a 1.83 ± 0.03 photon index modified by the CRSF. In these fits the CRSF energy is $28.6^{+1.5}_{-1.7}$ keV, implying a magnetic field strength of $2.5(1+z) \times 10^{12}$ G in the scattering region (where z is the gravitational redshift). Phase resolved analysis shows that the blackbody and cyclotron line energies are consistent with being constant through the pulse.

5.2 Introduction

The X-ray source 4U 0352+309 is a persistent, low luminosity pulsar in a binary orbit with the Be star X Persei (X Per). Its $\sim$837 s pulsation period was discovered with the *UHURU* satellite (White et al. 1976; White, Mason & Sanford 1977), and is still one of the longest periods of any known accreting pulsar (Bildsten et al. 1997, and references therein). The distance to the system, based on optical observations of the companion X Per, is 0.95 ± 0.20 kpc (Telting et al. 1998). Recently, Delgado-Martí et al. (2001) have determined a complete orbital ephemeris of the system using data from the *Rossi X-ray Timing Explorer* (*RXTE*).

Like many accreting pulsars, the history of the pulse period of 4U 0352+309 shows both episodes of spin-up and spin-down (White et al. 1976; Robba et al. 1996; Di Salvo et al. 1998, and references therein). The neutron star experienced a large apparent torque reversal around 1978. 4U 1626−67 (Chakrabarty et al. 1997) and GX 1+4 (Makishima et al. 1988) have exhibited similar torque reversals, and in both sources the mean spin-up and spin-down rates were similar in absolute magnitude. Previous to 1978 the spin history of 4U 0352+309 was erratic; however, there was a general trend toward spin-up at a rate of $\dot{P}_{\rm spin}/P_{\rm spin} = -1.5 \times 10^{-4}\,{\rm yr}^{-1}$ (Delgado-Martí et al. 2001). Since 1978, although the spin period measurements have been infrequent the star has been spinning down at an average rate of $\dot{P}_{\rm spin}/P_{\rm spin} = 1.3 \times 10^{-4}\,{\rm yr}^{-1}$ (Delgado-Martí et al. 2001). Unfortunately there are not enough spin period measurements to distinguish between steady spin down, as might be due to disk accretion, or the erratic torque fluctuations that would be expected from wind accretion.

An unusual aspect of 4U 0352+309 is the source's X-ray spectrum. Most accreting X-ray pulsar spectra are well described by a standard model: a simple power-law with a photon index of $\sim$1 that is exponentially cutoff above $\sim$20 keV (White, Swank &

Holt 1983). 4U 0352+309, on the other hand, does not follow this standard spectral shape and as a result has been fit with a variety of different models. Observations lacking response below ~2 keV have typically been fit with thin thermal bremsstrahlung emission in the temperature range 7–12 keV (Becker et al. 1979; White et al. 1976, 1982) or thermal bremsstrahlung with a high energy tail (Mushotzky et al. 1997; Frontera et al. 1979; Worrall et al. 1981; White et al. 1982; Frontera et al. 1985). Observations obtained with the *Tenma* (Murakami et al. 1987), *EXOSAT* (Robba & Warwick 1989), and *Ginga* (Robba et al. 1996) satellites were fit by the standard model for binary X-ray pulsars, but required very low cutoff energies (in the range of 0.6–1.7 keV) that are atypical of most accreting pulsars (White, Swank & Holt 1983). Furthermore the *Ginga* result, where the data extended to higher energies, showed evidence for a hard tail above ~15 keV. Recently Di Salvo et al. (1998) fit the broad band (0.1–200 keV) *Beppo*SAX X-ray spectrum with a combination of two power-laws. The first, which was important at lower energies, had a simple high-energy cutoff and was identical in form to the standard spectral model for accreting pulsars. The second power-law, which dominated above ~15 keV, had both high and low-energy cutoffs.

With the broad energy ranges and good spectral resolution of satellites such as the *RXTE* and *Beppo*SAX, several new Cyclotron Resonance Scattering Features (CRSFs) have been discovered in well known accreting pulsars. Two of the most notable recent discoveries are Cen X$-$3 (Santangelo et al. 1998; Heindl & Chakrabarty 1999) and 4U 1626$-$67 (Orlandini et al. 1998; Heindl & Chakrabarty 1999). These line-like spectral features are thought to be due to resonant scattering by electrons in Landau orbits in the $\sim 10^{12}$ G magnetic field of the neutron star. The CRSF centroid energy is given by $E_{\rm c} = 11.6 \frac{B}{10^{12}\,{\rm G}} (1+z)^{-1}\,{\rm keV}$, where z is the gravitational redshift in the scattering region and B_{12} is the magnetic field in units of 10^{12} Gauss. Thus CRSFs give a direct measurement of the average magnetic field in the scattering region near the neutron star surface. Without a CRSF the magnetic dipole moment of the star can only be inferred from measurements of the luminosity (a function of the often uncertain distance) and spin period using accretion torque theory (Ghosh & Lamb 1979). Even the radio pulsar magnetic fields are estimated, not directly measured, assuming dipole radiation and measuring the period and period derivative

(Manchester & Taylor 1977).

5.3 Observations and Analysis

The observations of 4U 0352+309 studied here were made using the two pointed instruments on the *RXTE*. The Proportional Counter Array (PCA, Jahoda et al. 1996) is a set of five identical Xenon proportional counters (Proportional Counter Units, or PCUs) sensitive in the energy range 2–60 keV. The PCA can, and sometimes does, operate with one or more of the individual PCUs turned off. This is done to extend the lifetime of the instrument, but reduces the effective area during those observations. The High Energy X-ray Timing Experiment (HEXTE, Rothschild et al. 1998) consists of two clusters of 4 NaI(Tl)/CsI(Na) phoswich scintillation detectors (15–250 keV) that rock on and off source, simultaneously measuring both source and background counts. One of the detectors in Cluster B suffered a failed pulse height analyzer early in the mission and no longer provides any spectral information, effectively reducing the area of that cluster by 25%. The PCA and HEXTE fields of view are co-aligned on-source and are collimated to the same 1° full width half maximum (FWHM) region.

We have used data from 40 pointings from the *RXTE* public archive (see Table 5.1) spanning from 1998 July 1 through 1999 February 27, roughly one binary orbit of the system. This is a subset of the observations used by Delgado-Martí et al. (2001), allowing us to use their orbital ephemeris in our timing analysis. These observations were chosen for their relatively short intervals between pointings (on average 6 days), which minimizes the possibility of long-term spectral variability and yet provides enough data for a suitable detection of the source. See Fig. 5.1 for the *RXTE*/ASM history of the source, along with the times of the *RXTE* pointings.

For the PCA we used GoodXenon mode data with PCUs 0, 1, and 2 only, as these were the only PCA detectors that were on during all of the observations. The total PCA on-source exposure was 161 ks with 3 PCUs, and the on-source livetime in HEXTE was 54.6 ks per cluster. The average PCA 3–25 keV counting rate was 20.6 ± 0.1 cts s^{-1} PCU^{-1}. In HEXTE the counting rate was 1.78 ± 0.06 cts s^{-1} in Cluster A and 1.30 ± 0.05 cts s^{-1} in Cluster B. The average 3–100 keV X-ray flux from the

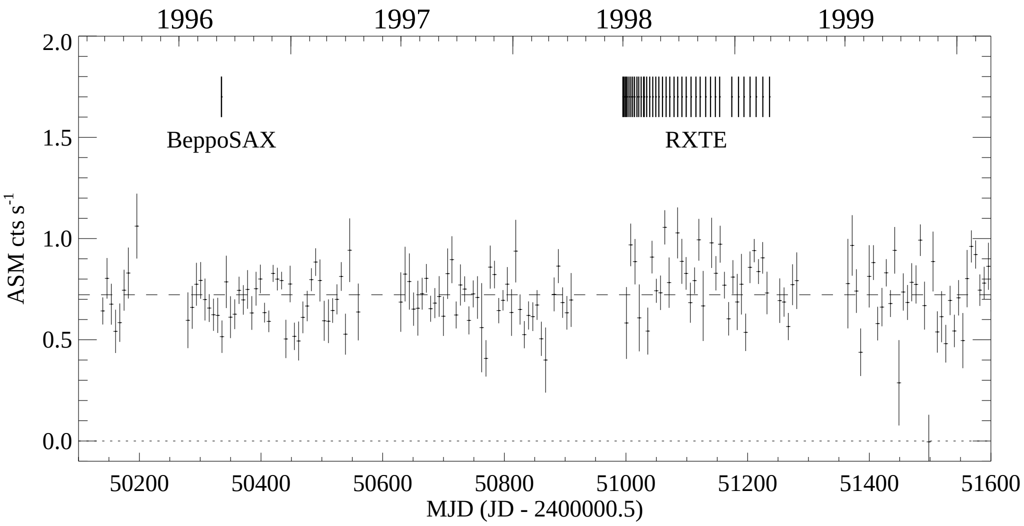

Figure 5.1: Counting rate of 4U 0352+309 in the ASM, binned as weekly averages. The thick bars near the top of the plot indicate where observations were made with the *RXTE* pointed instruments, as well as the *Beppo*SAX observation (Di Salvo et al. 1998) for comparison. The average ASM counting rate (0.72$\pm$0.1 cps) is shown as a dashed line. The average rate during the period of *RXTE* pointed observations is 0.82$\pm$0.02 cts s^{-1}, above the overall source average. For comparison, the Crab Pulsar is $\sim$75 cts/sec in the ASM.

source over the course of the observations was 3.9×10^{-10} ergs cm^{-2} s^{-1}. At a distance of 0.95 kpc (Telting et al. 1998) the source luminosity is 4.2×10^{34} ergs s^{-1}. This is at least two orders of magnitude less than the typical 10^{36}-10^{38} ergs s^{-1} luminosities seen in other persistent accreting pulsars or transient pulsars while in outburst.

The phase averaged PCA and HEXTE spectra were accumulated using version 5.0.1 of the HEASoft tools. Even though the average PCA counting rate was below the 40 cts s^{-1} PCU^{-1} threshold for using the Faint source background model, the large pulse modulation often brought the instantaneous counting well above, at times over 100 cts s^{-1} PCU^{-1}. Since we cannot, at this time, phase resolve the background spectra of the PCA, we were forced to use the bright-source SkyVLE model. The Faint source model, which relies partly on average counting rates, significantly over-predicted the background level. In particular, the modeled Faint source background was larger than the measured source plus background for the phase minimum at all energies. The SkyVLE model, on the other hand, predicted a background rate that was less than source plus background for all four phases. These models also gave background subtractions that were consistent with zero at high energies, where

Table 5.1: 4U 0352+309 Observations

Date	On-Source Time (ks)	Date	On-Source Time (ks)
1998 Jul 1	5.00	1998 Sep 10	4.94
1998 Jul 2	5.16	1998 Sep 16	5.26
1998 Jul 4	5.16	1998 Sep 23	4.04
1998 Jul 6	3.36	1998 Sep 29	5.62
1998 Jul 8	4.60	1998 Oct 6	4.74
1998 Jul 11	6.42	1998 Oct 13	5.54
1998 Jul 14	5.78	1998 Oct 21	5.00
1998 Jul 17	5.06	1998 Oct 29	5.32
1998 Jul 20	5.46	1998 Nov 5	5.60
1998 Jul 24	4.62	1998 Nov 14	5.00
1998 Jul 27	5.68	1998 Nov 22	5.32
1998 Jul 31	5.42	1998 Nov 30	5.54
1998 Aug 4	1.24	1998 Dec 7	5.36
1998 Aug 5	3.30	1998 Dec 27	5.00
1998 Aug 9	5.00	1999 Jan 7	5.00
1998 Aug 14	5.00	1999 Jan 16	5.08
1998 Aug 19	5.48	1999 Jan 26	5.48
1998 Aug 24	5.36	1999 Feb 5	5.00
1998 Aug 29	5.00	1999 Feb 16	5.78
1998 Sep 4	5.00	1999 Feb 27	4.92

4U 0352+309 was too weak to detect. Therefore we concluded that it was appropriate to use the the SkyVLE models for our PCA background subtraction. Since the HEXTE uses a measured background accumulated in the same way as the source pointings, it did not suffer these problems. The estimated error of the HEXTE background subtraction is a few tenths of a percent (Rothschild et al. 1998), while the source flux of 4U 0352+309 is 1.7% of background.

In order to study the evolution of the spectrum through the pulse, and to aid in the search for CRSFs, we performed pulse phase resolved spectral analysis as well. The spectra of accreting X-ray pulsars can vary considerably with pulse phase (White, Swank & Holt 1983). This is easily seen in the Folded Light Curves (FLCs) of these sources, where the general trend is toward more complicated pulse shapes at lower energies, and larger pulsed fractions at higher energies. This two dimensional nature can make interpreting spectra averaged over an entire pulse period problematic.

We corrected photon arrival times to both the solar system and the binary system barycenters using the ephemeris of Delgado-Martí et al. (2001) and accumulated spectra using a locally modified version of the `fasebin` phase resolved accumulation `FTOOL`. The `fasebin` `FTOOL` produces a two dimensional counts histogram versus both phase and energy, allowing for an analysis of spectra as a function of phase, or folded light curves as a function of energy. Modifications to the `fasebin` `FTOOL` were made to take the HEXTE deadtime corrections into account properly and to allow for phase resolving the HEXTE background files. Phase resolving the background is important for long period pulsars, where the background level can vary over the course of a single pulse. Given the relatively simple, saw-tooth like pulse shape of 4U 0352+309 and the faintness of the source, we divided the pulse into four phase bins; Peak, Fall, Min, and Rise (See Fig. 5.2).

The uncertainties in the PCA spectra, with its large collecting area and thus excellent counting statistics, are dominated by the systematic errors in the response matrix and background modeling (Wilms et al. 1999). To estimate the size of the systematic errors in the PCA version 2.43 response matrix, we analyzed observations of the Crab nebula and pulsar as recommended by the PCA team (Jahoda 2000b). To be able to compare directly to our 4U 0352+309 composite spectrum, we summed 10 Crab observations taken between 1998 July 27 and 1999 February 24, for a total PCA exposure of 8 ks. To fit these data, we used a combination of two power-laws. The first power-law, with a best fit photon index of $2.21^{+0.03}_{-0.02}$, was to account for the nebular flux. The second, which modeled emission from the pulsar, had a photon index of $1.9^{+0.7}_{-0.1}$ and a 2–10 keV normalization fixed to be 10% of the first (Jahoda 2000a; Knight 1982). We then examined the best fit and increased the size of the systematic errors as a function of energy until we achieved a reduced χ^2 of unity. The second power-law is important in this type of analysis, since ignoring the contribution of the pulsar would have led us to estimate larger systematic errors.

The systematic errors we used were 0.4% in the range 2–12.5 keV, 0.3% in 12.5–20.5 keV, and 2.4% above 20.5 keV. These are slightly smaller than the errors used by other authors (e.g. Wilms et al. 1999; Barret et al. 2000), due in part to the dual power-law model used and improvements in the current response matrices (PCARSP V2.43). The effects of increasing the systematic errors reduces the formal significance of the CRSF by improving χ^2, as well as increasing the uncertainties of the fit pa-

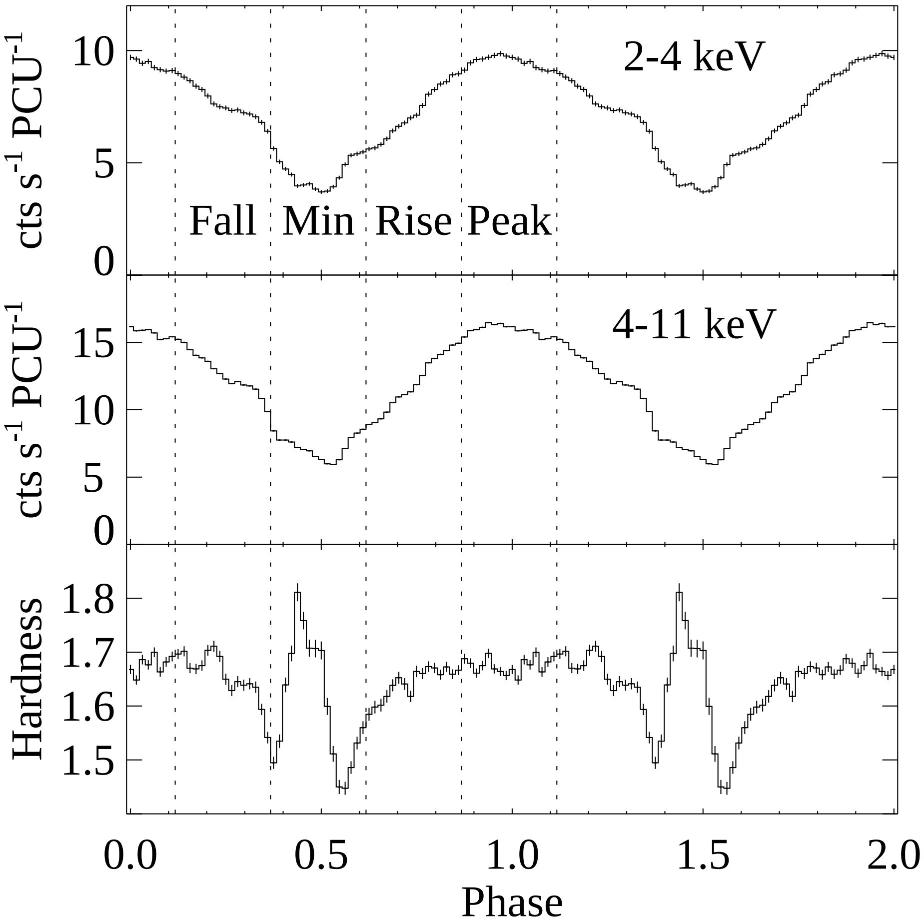

Figure 5.2: TOP: PCA folded light curve in the 2–4 keV range. The phase intervals used in the spectral analysis (Peak, Fall, Min, and Rise) are indicated by the dotted lines. MIDDLE: Folded light curve in the 4–11 keV range. BOTTOM: Hardness ratio, defined as ratio of counts in the 4–11 keV band to those in 2–4 keV. As in previous observations Robba & Warwick (1989); Robba et al. (1996) there is a prominent peak in the hardness during the pulse minimum. This indicates that the average X-ray spectrum of 4U 0352+309 is relatively constant. We do note, however, that when the *Beppo*SAX satellite observed the source (Di Salvo et al. 1998) the hardness spike was much less prominent.

rameters. However, such an increase does not affect the overall shape of the residual errors, especially the line-like shape in the HEXTE data around 30 keV. The errors of the HEXTE data are dominated by the counting statistics (Rothschild et al. 1998), so systematic errors were not applied.

In our analysis of 4U 0352+309 we truncated the PCA energy range at 25 keV. This was done to minimize the effects of the large systematic errors above 20 keV, while still allowing a significant overlap between the PCA and HEXTE energy ranges.

We fit the PCA simultaneously with data from both HEXTE clusters in the range 16–100 keV, with the overall normalization of each HEXTE cluster allowed to vary with respect to the PCA in the fits.

5.3.1 Spectral Variability

One of our major concerns was the validity of summing a large number of short pointings, taken over the course of 8 months, into a single set of spectra. This is especially dangerous when searching for CRSFs, as averaging different power-law slopes could artificially create a dip-like or inflection feature in the spectrum. The pulse profile of 4U 0352+309 is also known to vary from pulse to pulse (Delgado-Martí et al. 2001), and due to the long pulse period there are fewer than 6 pulses in any given 5 ks observation. Furthermore, the X-ray spectra of accretion powered pulsars, especially wind fed systems, can vary dramatically with both time and luminosity (Kreykenbohm et al. 1999). We took great care to ensure that the spectra we analyzed were free from these effects.

Since the separation of 4U 0352+309 and X Per is quite large (2.2 AU, Delgado-Martí et al. 2001), the system is almost certainly wind fed. But because of the modest eccentricity (e=0.11, Delgado-Martí et al. 2001), we did not expect the effects of the stellar wind to vary dramatically with the orbit. Furthermore, the small inferred inclination angle ($i \sim 23° - 30°$, Delgado-Martí et al. 2001) implies that the system is not being viewed through a (possibly variable) stellar or accretion disk. Because of this we did not expect significant variations in the absorption column, and thus in low-energy spectral shape, over time. Additionally, although no single observation was long enough to make a significant detection of a CRSF, the longest single pointing suggested that there might indeed be one. Therefore we were motivated to investigate whether we could discuss the average spectrum of 4U 0352+309.

First we tested whether or not the pulse shape converged to an average, repeatable shape. We divided the 40 pointings into 5 contiguous sets of observations, with each segment containing approximately 38 pulses. We then did a two component fit of each of the five 3–25 keV FLCs to the average FLC, allowing for both an additive offset in rate and an overall multiplicative factor. This allowed for possible errors in

Table 5.2: Five Interval Ratios

	Reduced $\chi^{2\,a}$				
Pulse Phase	Seg 0	Seg 1	Seg 2	Seg 3	Seg 4
Peak	0.784	1.119	1.446	0.839	0.923
Fall	1.026	1.212	0.522	0.663	0.888
Min	0.968	1.321	1.045	1.819	0.386
Rise	1.114	0.966	0.751	1.232	1.049

a See §5.3.1

the background subtraction and tested the repeatability of the overall shape, but was insensitive to changes in pulsed fraction. The fit offsets were small, only 3–4% of the rate in each phase bin. The scatter around the mean FLC gave reduced χ^2s of 1.05, 0.66, 0.59, 0.67, and 0.91 in the 5 data segments. So, as with other accreting pulsars, the pulse shape variations of 4U 0352+309 converge to an average pulse shape that is stable at least over several months.

Next we sought to verify whether the average pulse was similar to previous observations. In particular 4U 0352+309 has shown a peak in hardness at pulse minimum (Robba & Warwick 1989; Robba et al. 1996; Di Salvo et al. 1998). Using the spectra from our phase resolved analysis we generated folded light curves in the 2–4 and 4–11 keV bands and created a hardness ratio through the pulse (Fig. 5.2). As in previous observations, we see a nearly constant hardness ratio though the peak of the pulse as well as a hard spike at pulse minimum. This consistent behavior suggests that summing a series of short observations would be nearly equivalent to a single long pointing. We also note that the hard spike is very prominent in our data, similar to what was observed with *EXOSAT* (Robba & Warwick 1989) and *Ginga* (Robba et al. 1996), while the spike was much less pronounced during the *Beppo*SAX observation (Di Salvo et al. 1998).

Lastly, we investigated whether or not the spectral shapes in the five data segments were consistent with the average spectral shape. To account for the fact that the 5 intervals had different amounts of time in different parts of the pulse, we used background subtracted spectra that were also resolved into our 4 phase bins (see above), giving a total of 20 spectra to be tested. Then, for the 5 segments in each phase bin, we took the ratio of the 3–25 keV PCA counts to that of the total counts spectrum (also background subtracted) for that phase bin, and calculated the reduced χ^2 assuming a constant ratio. This was done for all 4 phases. See Table 5.2 for the results of this analysis. We found that the spectral shape in the 5 data segments, at least in the 3–25 keV range, is consistent with being constant. Therefore, due to the stability of the pulse and spectral shapes over the course of our observations, we concluded that summing data from all of the observations would not introduce a significant artifact in a given phase bin or for the phase averaged spectrum.

5.3.2 Spectral Fitting

Identifying CRSFs in the spectrum of accreting pulsars can be problematic, especially when the underlying continuum is unknown. However, in the case of 4U 0352+309 a large feature is clearly visible at ~50 keV in the counts spectra of the source (Fig. 5.3), and is especially evident in the falling edge of the pulse peak. This same feature is also visible in a shorter observation (~10 ks) made early on in the *RXTE* mission. This feature is not present in counts spectra successfully fit with the standard model of accreting pulsars, but would be expected if there were also resonant cyclotron scattering present in the source. We were therefore motivated to find a simple and physically reasonable continuum spectrum that would describe the data.

In our fits we fixed the neutral hydrogen column to be $1.5 \times 10^{21}\mathrm{cm}^{-2}$, based on measurements from satellites with significant response below 1 keV (for example *ROSAT*, Haberl 1994; Mavromatakis 1993, *BBXRT*, Schlegel et al. 1993, *Copernicus*, Mason et al. 1976, and *Beppo*SAX, Di Salvo et al. 1998). This is an order of magnitude smaller than measurements made by instruments lacking response below ~2 keV (e.g. White et al. 1982; Murakami et al. 1987; Robba et al. 1996). It is difficult for these instruments (e.g. *Ginga* and *RXTE*) to measure such a low column. The fitting is also complicated by the fact that there is a change or break in spectrum at ~2 keV, as revealed by instruments such as *EXOSAT* (Robba & Warwick 1989) and *BBXRT* (Schlegel et al. 1993). This change can explain why instruments without low-energy response systematically measure a column which is larger by an order of magnitude.

Starting with models used historically for 4U 0352+309 (see §5.2), we first attempted to fit the *RXTE* data with a thermal bremsstrahlung model both with and

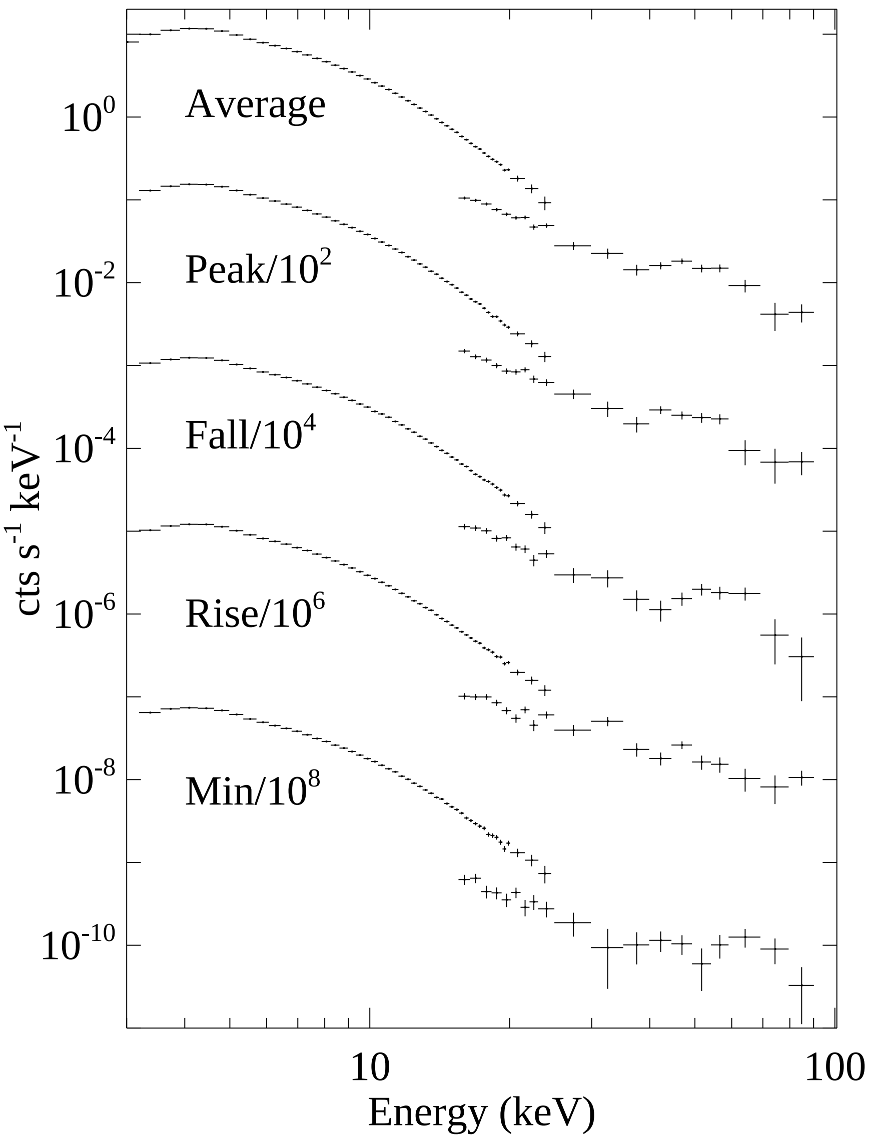

Figure 5.3: Plot of the raw PCA and HEXTE counts for the phase average spectrum and four phase bins defined in Fig. 5.2. The PCA is shown from 3–25 keV while the HEXTE is 16–100 keV. The CRSF is visible as in inflection in the phase average counts, and especially so in the falling edge.

without a power-law tail. We found that these models gave poor fits to the data when the absorption column was fixed at $1.5\times10^{21}\,\mathrm{cm}^{-2}$. When the amount of absorption was allowed to vary we achieved acceptable fits, but these required an unreasonably large column ($1-3\times10^{22}\,\mathrm{cm}^{-2}$) and were consistent with previous observations where a thin thermal plasma model has been applied to > 2 keV data. The thermal model also suffers from no iron line ever being detected in this source (with an upper limit on the equivalent width of $\sim$6 eV, Di Salvo et al. 1998). Because of this and the large inferred absorption column we have rejected the bremsstrahlung and bremsstrahlung plus power law tail continuum models.

In the *RXTE* band, the standard model used to describe accreting X-ray pulsars is a power-law that breaks into a power-law times an exponential at a characteristic cutoff energy. Historically this has been realized in the PLCUT form

$$\mathrm{PLCUT}(E) = A\ E^{-\Gamma} \times \begin{cases} 1 & (E \leq E_{\mathrm{cut}}) \\ \mathrm{e}^{-(E-E_{\mathrm{cut}})/E_{\mathrm{fold}}} & (E > E_{\mathrm{cut}}) \end{cases}$$

where Γ is the photon power-law index, and E_{cut} and E_{fold} are the cutoff and folding energies respectively. Other analytical forms have been used as well, such as the Fermi-Dirac form of the cutoff (FDCO, Tanaka 1986) and the Negative and Positive power-law Exponential model (NPEX, Mihara 1995). For a full review of the various phenomenological models see Kreykenbohm et al. (1999). This generic spectral shape can be interpreted as due to Comptonization of soft photons by the hot accreting electrons, with the cutoff and folding energies determined by the temperature of the infalling electrons.

When we applied these models (PLCUT, FDCO, and NPEX) we found that they were inadequate to describe the shape of the spectra. As with *Ginga* (Robba et al. 1996), there appeared to be a power-law tail extending beyond $\sim$15 keV. Our inferred values of cutoff energy were below 3 keV (and outside the PCA energy range), also consistent with previous results. Moreover, the "tail" at higher energies was still present when we fit the pulse peak minus pulse minimum, confirming that it is pulsed emission from 4U 0352+309 and not a contaminating background source such as an AGN. However, the simple addition of an extra power-law to the model, or even a second PLCUT, still gave unacceptable fits. Specifically these were unable to account for the dip seen at $\sim$35 keV. This motivated us to try other two component models.

Di Salvo et al. (1998) fit the *Beppo*SAX spectrum of 4U 0352+309 with a dual PLCUT model. The first PLCUT had a cutoff energy of $\sim$2 keV. The second, which was only important above $\sim$ 15keV where there was "extra" emission, had a cutoff energy of 66 keV and an exponentially shaped low-energy absorption term with a 44 keV folding energy. The cross over of the two components was at $\sim$15 keV, and the second component fits the excess "tail" not described by the lower energy component. We applied this model to our observations as well and achieved a reduced χ^2 of 1.25 for 79 degrees of freedom for the phase averaged spectrum. The shape of the spectrum, however, was noticeably different from that obtained by Di Salvo et al. (1998). In particular, the high energy photon index we obtained was smaller (although within errors, 1.5±0.6 vs. 2.6±1.1) and the low-energy exponential absorption folding energy an order of magnitude less ($2.7^{+3.3}_{-2.2}$ vs. 44.3±4.5 keV). Furthermore, the *RXTE* fits using this model were improved by the addition of a CRSF at ~30 keV, giving a reduced $\chi^2$of 0.753 for 76 degrees of freedom. This difference between the spectra obtained with the *Beppo*SAX and the *RXTE* satellites could be real, possibly connected with variations of the source luminosity. The 1–10 keV flux during the *Beppo*SAX observation was $1.7\times10^{-10}\,\mathrm{ergs\,cm^{-2}\,s^{-1}}$ (Di Salvo et al. 1998), while the 1.7–10 keV flux in our observation was $2.1\times10^{-10}\,\mathrm{ergs\,cm^{-2}\,s^{-1}}$, or 23% higher. Furthermore, the *RXTE*/ASM source flux in the week spanning the *Beppo*SAX observation was $0.52\pm0.08\,\mathrm{cts\,s^{-1}}$, which is below the source average (Fig. 5.1).

Nelson et al. (1995) suggested that the spectrum of accreting low-luminosity neutron stars ($L_\mathrm{X} \lesssim \times10^{34}\,\mathrm{ergs\,cm^{-2}\,s^{-1}}$) could exhibit a cyclotron *emission* line. This feature is expected to be broad ($E/\Delta E \sim 2-4$), peak at energies below the fundamental cyclotron energy of the magnetic field, and be sharply cutoff above the cyclotron energy. Di Salvo et al. (1998) interpreted the second PLCUT in their spectrum as evidence for this feature. Since the second component in our fits was different from that obtained with the *Beppo*SAX, and quite unlike an emission line, we attempted to test the Nelson et al. (1995) prediction with some slightly different models. We fit the phase averaged spectrum with the standard PLCUT and FDCO forms, plus an additional Gaussian shaped emission line, both with and without a high-energy cutoff. The Gaussian was meant to fit the peak near 50 keV, while the cutoff was used to truncate the high-energy wing of the Gaussian to simulate the predicted steep fall at the cyclotron energy. The folding energy of the cutoff associated with the Gaussian component was allowed to vary, but constrained to be within 0.1–10 keV. We found that the presence of a cutoff did not change the fits significantly, and we were unable to achieve any reasonable fits using an emission line model.

We have found a two component model that both best described the data and

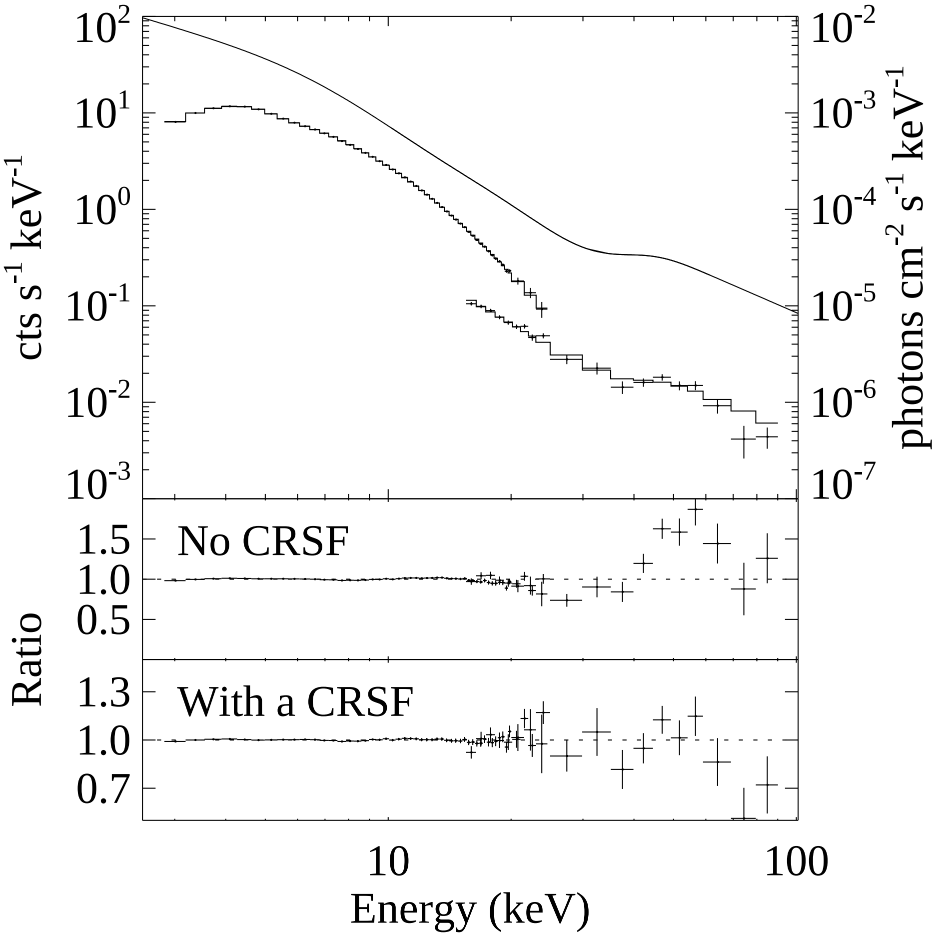

Figure 5.4: Top: Plot of the phase averaged counts spectra (crosses) fit with a combination of a black body and power law (histograms). The input model is also shown (smooth line). Middle: Ratio of data to model without (top) and with (bottom) a CRSF at ∼29 keV. Bottom: The residuals to the fit, in units of sigma, both without (top) and with (bottom) a ∼29 keV CRSF. The PCA points contain the systematic errors discussed in the text (see §5.3)

had a simple physical interpretation. The first component was a ∼1.4 keV black-body, the second a power-law with a photon index $\Gamma \sim 1.8$ and a broad absorption feature centered at 29 keV. See Table 5.3 for the best fit parameters and Fig. 5.4 for the phase averaged spectrum.

As in previous observations of the source we found no evidence of an Fe-K line in the spectrum, with a 90% confidence upper limit on the equivalent width of 13 eV for a Gaussian line centered at 6.4 keV and with a 0.5 keV sigma. This is consistent with the ∼6 eV upper limit of Di Salvo et al. (1998). In the phase average fits, the inferred area of the black body was 5.4×10^{8} cm^{2}, consistent with standard values

Table 5.3: Black-Body / Power-Law fits

Parameter	Pulse Phase				Phase
	Peak	Fall	Min	Rise	Average
$N_{\rm H}$ (10^{22} cm^{-2})[a]	0.15	0.15	0.15	0.15	0.15
kT (keV)	1.42±0.02	$1.47^{+0.03}_{-0.02}$	$1.43^{+0.06}_{-0.05}$	$1.39^{+0.04}_{-0.03}$	1.45±0.02
$R_{\rm BB}$ (m)	160±30	130±30	100±40	150±30	130±30
Γ	1.79±0.04	$1.84^{+0.06}_{-0.05}$	$1.80^{+0.10}_{-0.08}$	$1.77^{+0.05}_{-0.04}$	1.83±0.03
A[b]	$1.63^{+0.07}_{-0.06}$	$1.51^{+0.13}_{-0.08}$	$1.1^{+0.4}_{-0.2}$	$1.30^{+0.08}_{-0.06}$	$1.35^{+0.06}_{-0.05}$
$E_{\rm c}$ (keV)	$27.7^{+2.1}_{-2.5}$	32.7±2.8	31 ± 6	$20.9^{+3.6}_{-1.7}$	$28.6^{+1.5}_{-1.7}$
$\tau_{\rm c}$	0.64±0.16	0.70±0.20	0.8 ± 0.4	$0.34^{+0.14}_{-0.11}$	0.66±0.12
$\sigma_{\rm c}$ (keV)	7.9±1.5	$11.2^{+3.0}_{-2.5}$	13^{+8}_{-6}	$5.7^{+2.9}_{-1.5}$	9.0±1.3
$\chi^2_{\rm red}$/DOF	0.933/80	0.997/80	0.746/80	0.995/80	0.876/80
F-test[c]	5×10^{-15}	2×10^{-6}	4×10^{-5}	1×10^{-7}	1×10^{-18}

a Not allowed to vary
b 2–10 keV Power-Law Flux, in units of 10^{-10} ergs cm^{-2} s^{-1}
c Improvement in fit by the addition of a CRSF

for the magnetic polar cap of a neutron star. The black-body temperature remained constant, to within errors, with pulse phase. We note, however, that the formal errors on the black-body component are small (only 20 eV for the temperature). Factors such as the fixed value for the absorption column and the spectrum below 1 keV, which is not measured with the *RXTE* and was fit with a slightly different shape in the *Beppo*SAX data(Di Salvo et al. 1998), affect these results. Therefore the actual errors for both the temperature and area are almost certainly larger. See Fig. 5.5 for the two model components in the inferred phase average photon spectrum.

The absorption line model used in the fits was a multiplicative exponential of the form $\mathrm{e}^{-\tau(\mathrm{E})}$, where τ is the optical depth of the absorption as a function of energy. The functional form of τ is given by the Gaussian GABS(E) = $\tau_{\rm c}\ \mathrm{e}^{-(E-E_{\rm c})^2/(2\sigma_{\rm c}^2)}$ where $E_{\rm c}$ is the centroid energy (also called line energy), $\sigma_{\rm c}$ is the width, and $\tau_{\rm c}$ is the optical depth at the CRSF energy. We interpret this feature as a 29 keV CRSF. It was present in all four phases; however, it was only weakly detected during the rise of the pulse. In Fig. 5.6 we plot the ratio of the data to the best fit model, both before and after the addition of a CRSF to the model. Because there are simply more counts at energies below the centroid energy, the errors are smaller and have a greater effect on the fitting process. When fitting without a CRSF, these smaller errors drive

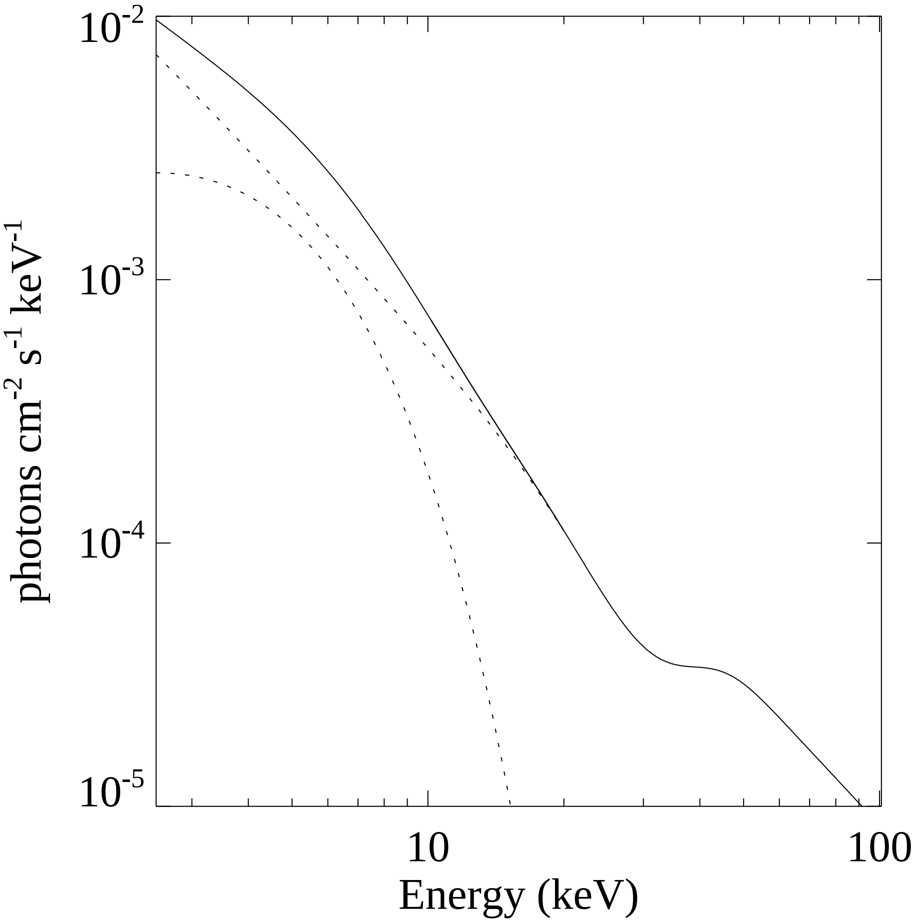

Figure 5.5: The inferred model from the phase averaged spectral fits, along with the black body and power-law components show individually as dotted lines. The CRSF is visible as a notch in the power-law.

the continuum to fit the low side of the line and under predict the continuum at higher energies. This gives rise to a dip followed by a rise in a ratio plot – a classic signature of a CRSF. These dips are especially evident in the pulse fall and minimum in Fig. 5.6.

The CRSF does, however, appear near the 33.17 keV K-edge of Iodine, where there is a dramatic change in the response properties in the HEXTE NaI scintillators. In a ratio plot (Fig. 5.4), the trough of the feature is below 30 keV, and shows a deviation from the model of approximately 20%. There is a similar structure in the HEXTE ratios of power-law fits to the Crab nebula/pulsar using the released matrices. This structure, however, is significantly smaller (less than 1%) and is centered above 30 keV. Additionally, when we take the ratio of the 4U 0352+309 counts spectrum to

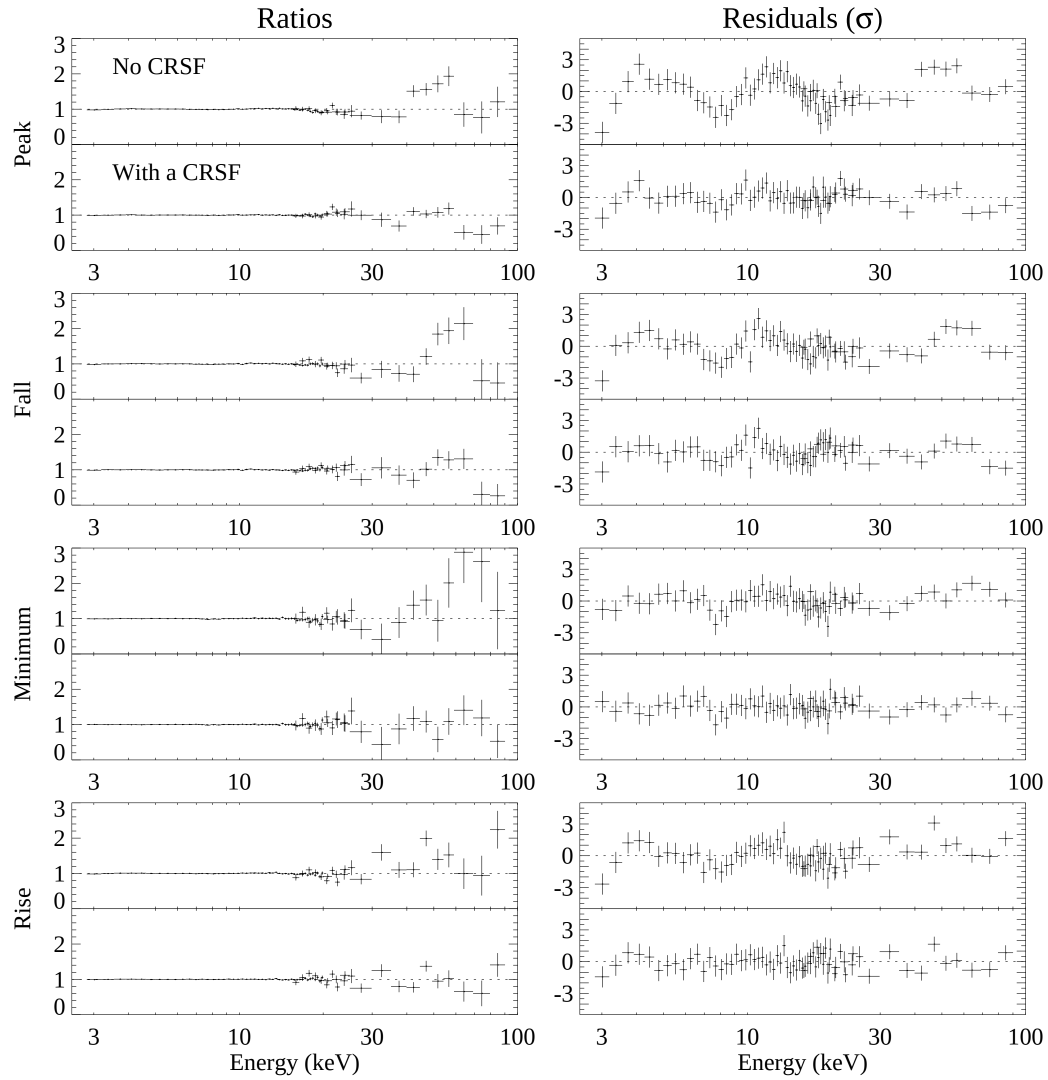

Figure 5.6: The ratios (left column) and residuals (right column) of the data to the best fit model before (top panels) and after (bottom panels) the addition of a CRSF to the model, in the four phase bins. In addition to errors due to the counting statistics, the PCA points contain the systematic errors discussed in the text (see §5.3). Due to the falling nature of the continuum, there are more counts at energies below the line centroid, and therefore these data have a larger effect on the fitting procedure. When fit without an absorption line this leads to a continuum that hugs the lower edge of the line and an under prediction at energies above the line. In a ratio plot this manifests itself as a dip followed by an excess, and is a classic signature of a CRSF. This signature is especially evident in the pulse fall and minimum. Although we do not find strong evidence for a spectral cutoff (see §5.4), the highest few HEXTE energy bins in each of the panels are an indication that there might be a high-energy cutoff.

that of the Crab, we still see a line-like structure. Since the spectrum of 4U 0352+309 is a power-law (with the exception of the CRSF) in the HEXTE band, this ratio is, to first order, free of instrumental effects. Lastly, we fit the data using a set of intermediate response matrices provided by the HEXTE instrument team. The released version of the HEXTE response matrices are derived from these, but have had the diagonal elements adjusted slightly to give a smooth fit to the Crab and account for calibration errors near the K-edge. The intermediate matrices, which are based solely upon modeling of the detectors and calibration data, have residual errors that are $\pm 2\%$ in the region of the K-edge. When we fit our 4U 0352+309 spectrum with these unreleased matrices χ^2 becomes worse; however, the line width and energy remain unchanged. Due of this analysis we conclude that the feature is intrinsic to the source, and not due to any instrumental problems or artifacts. We further conclude that the CRSF fit parameters are not significantly affected by the instrumental calibration.

From the pulse peak through minimum the CRSF energy is constant to within errors and is quite broad. The fit parameters are also consistent with the phase averaged spectrum. At pulse minimum a feature can be clearly seen in the pattern of ratios, although the statistics in this phase bin are quite low. The addition of a CRSF is not formally required by the fits, since a reduced χ^2 of 0.96 can be achieved without it. However, the addition of a CRSF at 30 ± 6 keV greatly improves the fits, with an F-test chance probability of 3.5×10^{-5}.

The fit CRSF during the pulse rise is quite different than the other phases. Specifically, it appears at a lower energy than in the other three phases (21 instead of $\sim$29 keV) and with a shallower depth. The CRSF also falls in the region of overlap between the PCA and HEXTE instruments, and due to its width is not completely resolved by either instrument. Because of this the fitted CRSF might be an artifact. We do note, however, that the width of the CRSF is, as a percentage of the centroid value, similar to the other three phases, and the temperature of the soft component and power-law index are consistent with the other pulse phases.

We also conducted a search for a CRSF second harmonic. Multiple harmonics have been detected in sources such as 4U 0115+63 (Heindl et al. 1999; Santangelo et al. 1999) and 4U 1907+09 (Cusumano et al. 1998), and so it is not unreasonable to search for one in this source as well. There appears, however, to be no evidence for a higher harmonic at $\sim$60 keV. Our statistics in that range are poor and resolving a line would be difficult. Using the phase average spectra we added a CRSF fixed at twice the energy and width of the fundamental. We then increased the depth parameter until the χ^2 changed by 2.7 (for one interesting parameter), and were able to obtain a 90% confidence upper limit of 0.25 on the depth of a second harmonic.

5.4 Discussion

Since the discovery of the first cyclotron resonance scattering feature in the spectrum of Her X−1 (Trümper et al. 1978), there have been only about a dozen firm detections of CRSFs out of the ~50 known accreting X-ray pulsars (Makishima et al. 1999). With this analysis we have added another, namely 4U 0352+309. The magnetic field at the polar cap implied by a 29 keV CRSF is $2.5(1+z) \times 10^{12}$ G (where z is the gravitational redshift in the scattering region). Assuming the radius and mass of the neutron star to be 10 km and $1.4\,M_\odot$ respectively, and that the cyclotron scattering is occurring at the magnetic polar cap, then the magnetic field is 3.3×10^{12} G. This field strength is well within the range of other accreting pulsars as measured by CRSFs, and also near the 2×10^{12} G peak in the distribution of radio pulsar fields (Taylor, Manchester & Lyne 1993). This implies that there is nothing unusual about the magnetic field strength of 4U 0352+309.

It is often useful to discuss the magnetic dipole moment μ of the neutron star since the magnetic field strength is a strong function of position. For a purely dipolar field, the dipole moment is given by $\mu = 0.5\,B\,R^3$, where B is the magnetic field strength at the polar cap and R the radius of the neutron star (Shapiro & Teukolsky 1983; Jackson 1975). So, for a polar cap field of 3.3×10^{12} G, the magnetic dipole moment of 4U 0352+309 is 1.7×10^{30} G cm^3.

In our two component continuum, we identify the power-law as the normal accreting pulsar continuum shape in the low accretion rate limit. While the spectrum of most accreting pulsars are exponentially cutoff above a characteristic energy E_{cut} (White, Swank & Holt 1983), our fits of 4U 0352+309 did not strongly require such a cutoff. When we substituted a PLCUT for the simple power-law in our model (see §5.3.2), the cutoff and folding energies were $E_{\mathrm{cut}} = 57^{+12}_{-17}$ and $E_{\mathrm{fold}} = 50^{+107}_{-30}$ respectively, with an F-test chance probability of 6×10^{-3}. This is consistent with the results of Di Salvo et al. (1998) when fitting *Beppo*SAX data: $E_{\rm cut} = 66^{+28}_{-14}$ and $E_{\rm fold} = 44^{+54}_{-22}$. However, when we used the slightly different FDCO, the cutoff and folding energies were completely unconstrained. Because of the large errors and model dependence, we find there is at most weak evidence for an exponential cutoff in our spectrum of 4U 0352+309.

Assuming that the bulk motion of the electrons is small, as might be the case below an accretion shock (Burnard, Arons & Klein 1991), then the power-law component could be a Comptonized spectrum due to the electrons in the accretion column. In the case of 4U 0352+309 the low accretion rate would lead to less efficient cooling of the infalling electrons, and therefore a higher electron temperature (Hayakawa 1985). In this model the exponential cutoff is at the electron temperature (Rybicki & Lightman 1979), which could explain the high energy ($\gtrsim 60\,\mathrm{keV}$) of any roll over in the spectrum: the temperature of the infalling electrons has increased the cutoff energy to beyond our sensitive detection band. Using the the photon index Γ and cutoff energy $E_{\rm cut}$, the electron scattering depth $\tau_{\rm es}$ can be estimated (Rybicki & Lightman 1979). For an index of $\Gamma = 1.83$ and a $60\,\mathrm{keV}$ cutoff, the optical depth to electron scattering is $\tau_{\rm es} \sim 1$.

These hotter electrons can also account for the broad width of the CRSF. It is thought that line widths are due, at least in part, to thermal Doppler broadening by the electrons (Mészáros & Nagel 1985a,b). Because the motion of the electrons responsible for the scattering is quantized perpendicular to the field lines but free parallel to them, the width of the line should increase as the viewing angle approaches the field direction. Mészáros & Nagel (1985a) predict that the width should go as

$$\Gamma_{\rm c} \approx E_{\rm c} \left(\frac{8\, \ln(2)\, kT_{\rm e}}{m_{\rm e} c^2} \right)^{1/2} |\cos(\theta)|$$

where $T_{\rm e}$ is the electron temperature, $m_{\rm e}c^2$ is the electron rest mass, and θ is the viewing angle with respect to the field. If we assume that the electron temperature is $\gtrsim 60\,\mathrm{keV}$ (as indicated by the cutoff energy), then the CRSF width is $\sigma_{\rm c} \gtrsim 0.34 E_{\rm c} \cos(\theta)$. Delgado-Martí et al. (2001) estimate the inclination angle of the system to be $i \sim 23^\circ - 30^\circ$, so if the magnetic and spin axes are not greatly offset then $\cos(\theta) \sim 0.9$. Therefore the width of the CRSF, while being quite wide, is roughly consistent with the estimates of the infalling electron temperature and viewing geometry.

The value of 1.7×10^{30} G cm^3 for the dipole moment derived from the CRSF is very different from what is estimated from accretion torque theory if the pulsar is spinning in equilibrium with the inner edge of an accretion disk (Ghosh & Lamb 1979). In the case of 4U 0352+309, with 837 s spin period and 4.2×10^{34} ergs s^{-1} luminosity, the implied magnetic dipole moment is $\gtrsim 4.1 \times 10^{31}$ G cm^3 (depending on the model used for the magnetospheric radius), or at least 24 times larger than what we measure. Using the observed luminosity and magnetic field strength, accretion torque theory predicts the equilibrium spin period to be in the range 20–50 s. However, instead of spinning up to this period the general trend is currently towards spinning down (although it has been measured only infrequently, Di Salvo et al. 1998). One explanation for this is to assume that the star is *not* currently spinning in equilibrium with an accretion disk. Indeed, it is unlikely that a persistent accretion disk is even present in this system. For a disk to form, the radius at which the captured wind material would go into a Keplerian orbit should be larger than the magnetospheric radius (Shapiro & Lightman 1976; Wang 1981; Li & van den Heuvel 1996). For typical wind velocities ($v \gtrsim 600$ km s^{-1}) and wide binary separations ($P_{\rm orb} \gtrsim 100$ days), a disk will be unable to form. Instead the accretion is quasi-spherical beyond the magnetospheric radius, while inside the behavior of matter is governed by the magnetic field. Therefore accretion torque theory does not apply in the case of 4U 0352+309, and there is no discrepancy between the magnetic field strength and pulse period.

5.5 Summary

We have discovered a cyclotron resonant scattering feature at 29 keV in the spectrum of 4U 0352+309. The feature is strongest in the peak and falling edge of the pulsed emission, but also evident in the phase average spectrum. The CRSF energy implies a magnetic field strength at the polar cap of 3.3×10^{12} G. 4U 0352+309 is also the lowest luminosity pulsar in which a CRSF has been observed. We have fit the continuum spectrum with a combination of a black body plus a power-law. Both of the components exist in the on-pulse minus off-pulse spectra, showing that they are indeed coming from the pulsar magnetic polar cap. The inferred area of the soft component is $5.4 \times 10^8\,\mathrm{cm}^2$, consistent with being emission from the magnetic polar cap of the pulsar. The power-law component, although being quantitatively different than other, more luminous accreting X-ray pulsars, is at least qualitatively similar. The main differences are a steeper photon index ($\Gamma = 1.8$) and the apparent lack of an exponential cutoff. We find that accretion torque theory does not fit the values of luminosity, spin period, and magnetic field strength, implying that the pulsar is not spinning in equilibrium with an accretion disk.

5.6 Acknowledgments

We would like to thank the referee for his helpful and insightful comments. This work was supported by NASA grant NAS5-30720 and NSF Travel Grant NSF INT-9815741.

This chapter has previously appeared in *The Astrophysical Journal* as "Discovery of a Cyclotron Resonant Scattering Feature in the RXTE Spectrum of 4U 0352+309 (X Per)," W. Coburn, W. A. Heindl, D. E. Gruber, R. E. Rothschild, R. Staubert, J. Wilms, and I. Kreykenbohm 2001, volume 552, pages 738-747.

Chapter 6

Discovery of a CRSF in XTE J1946+274

6.1 Abstract

We report on observations of the transient accreting pulsar XTE J1946+274 with the *Rossi X-ray Timing Explorer*. These observations, made during the course of the 1998 September–November outburst, reveal an apparent absorption feature in the hard X-ray spectrum near 35 keV. We interpret this feature as a "cyclotron line" resulting from resonant scattering by electrons in quantized Landau levels in the strong neutron star magnetic field. We determine a centroid line energy of $36.2^{+0.5}_{-0.7}$ keV, which implies a magnetic field strength of $3.1(1+z) \times 10^{12}$ G, where z is the gravitational redshift of the scattering region. The optical depth, $\tau_c = 0.33^{+0.07}_{-0.06}$, and width, $\sigma_c = 3.37^{+0.92}_{-0.75}$ keV, are typical of known cyclotron lines in other pulsars. This discovery makes XTE J1946+274 one of about a dozen pulsars with securely detected

cyclotron lines and the resulting direct magnetic field measurement.

6.2 Introduction

The transient accreting X-ray pulsar XTE J1946+274 was discovered during an outburst in 1998 September. Its persistent emission was identified with the All Sky Monitor (ASM) on board the *Rossi X-ray Timing Explorer* (*RXTE*) (Smith & Takeshima 1998). At the same time, 15.8 second pulsations were observed with the *CGRO*/BATSE, with the pulsating source designated GRO J1944+26 (Wilson et al. 1998). The best X-ray position ($1'$ radius, 90% confidence) comes from observations with the MECS instrument on-board *Beppo*SAX (Campana et al. 1998). The position falls within the *Ariel V* error region for the transient source 3A 1946+274, making it likely that the two objects are identical (Campana et al. 1998).

The initial outburst (see Fig. 6.1), which reached $\sim$6 cts s^{-1} in the *RXTE*/ASM, lasted about 100 days and was followed by a series of smaller flares. Campana, Israel & Stella (1999) discussed the extended *RXTE*/ASM lightcurve. They found that the flaring was nearly periodic with a repetition period of $\sim$80 d. They interpret this as either the binary orbital period or half of the binary orbital period, with flares occurring either once or twice per orbit, respectively. Either case is consistent with the known orbital period range of Be/X-ray binary pulsars. Given its probable orbital period and the outburst characteristics, XTE J1946+274 is most likely another example of a Be star/X-ray binary pulsar transient. This class of binaries accounts for over half of the known accreting pulsars (Liu, van Paradijs & van den Heuvel 2000).

Several observations (see Figure 6.1) were made with the *RXTE* pointed instruments spanning the peak of the initial outburst. In this *Letter*, we report on the spectral analysis of these observations and, in particular, the discovery of a cyclotron line at $\sim$35 keV. Santangelo et al. (2002) report their independent discovery of the XTE J1946+274 cyclotron line with *Beppo*SAX in this volume.

Cyclotron lines, or more precisely cyclotron resonance scattering features, result from the scattering of X-rays by electrons in quantized Landau orbits in the $\sim 10^{12}$ G fields near the magnetic poles of accretion powered pulsars. The characteristic energy of the Landau transition scales with the magnetic field as $E_c = (11.6\,\mathrm{keV})(1+z)^{-1}B_{12}$, where E_c is the cyclotron line energy in keV, z is the gravitational redshift in the scattering region, and B_{12} is the magnetic field in units of 10^{12} G. Because of this proportionality, cyclotron lines give us the only direct measure of the neutron star magnetic field. In general, harmonically spaced lines (corresponding to higher order Landau transitions) may exist (see for example Heindl et al. 1999; Heindl et al. 1999b; Santangelo et al. 1999). Depending on the temperature and geometry of the emitting and scattering material and the viewing angle with respect to the magnetic field, the line profiles may be broad and complex (e.g. Araya-Góchez & Harding 2000; Kretschmar et al. 2000). To date, about a dozen pulsars have well-established cyclotron lines, for the most part discovered with *Ginga*, *RXTE*, and *Beppo*SAX (see for example Makishima et al. 1999; Heindl et al. 1999b; Dal Fiume et al. 1999). With this work, we add one more object to these ranks.

6.3 Observations

During the XTE J1946+274 outburst, 12 pointed observations were made with the Proportional Counter Array (PCA) and the High Energy X-ray Timing Experiment (HEXTE) on-board the *RXTE* (see Tab. 6.1). The PCA (Jahoda et al. 1996) is a set of 5 identical Xenon proportional counter units (PCUs) sensitive in the energy range 2–60 keV with a total effective area of $\sim$7000 cm^2. The HEXTE (Rothschild et al. 1998) consists of two arrays ("clusters A and B") of 4 NaI(Tl)/CsI(Na) phoswich scintillation counters (15–250 keV) totaling $\sim$1600 cm^2. Early in the *RXTE* mission, the pulse height analyzer of a single cluster B phoswich failed, so its data are not useful for spectral analyses. Thus, the effective area of cluster B is $\sim$3/4 of cluster A. The HEXTE clusters alternate pointing between target and nearby blank fields in order to measure the background. The PCA and HEXTE fields of view are collimated to the same 1° full width half maximum (FHWM) region.

Table 6.1 lists the observation dates and the PCA and HEXTE counting rates. In order to extend the life of the PCA detectors, most observations are currently made with one or more PCUs turned off. All the observations here were performed with PCUs 0, 1, and 2 on. Because PCUs 3 and 4 were sometimes off, they have been

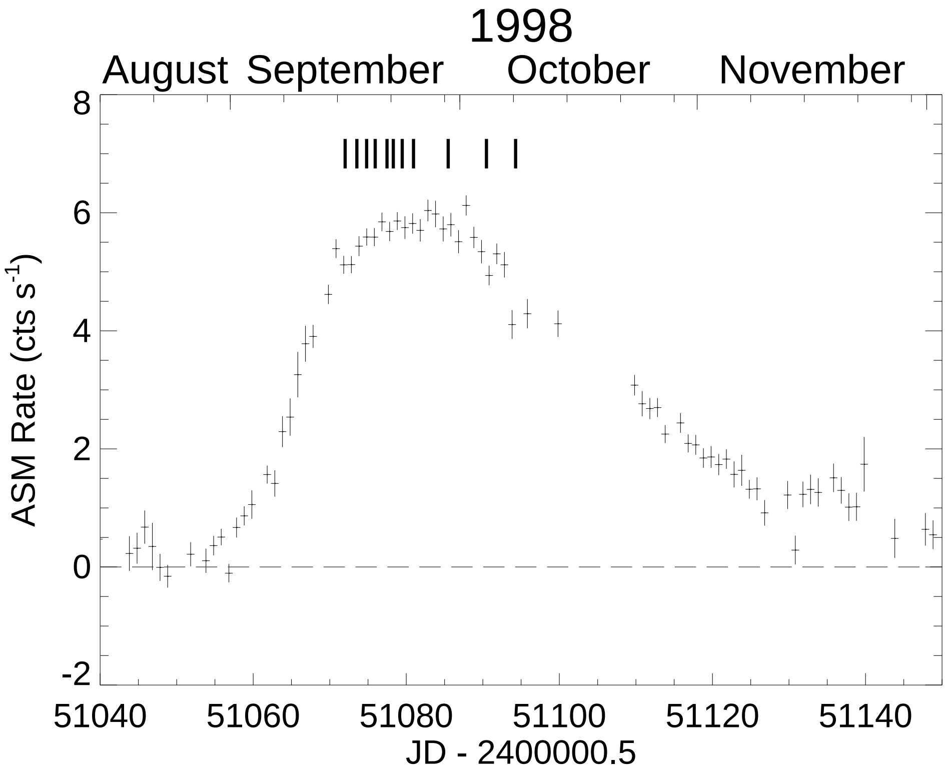

Figure 6.1: The *RXTE*/ASM lightcurve for the 1998 September outburst of XTE J1946+274. Bars at the top indicate the PCA/HEXTE observations (Table 6.1).

excluded from this analysis.

The ASM lightcurve of the initial outburst is shown in Figure 6.1. Vertical bars at the top the plot indicate the times of the pointed observations.

6.4 Analysis

For each observation, we accumulated source and background spectra from the PCA standard 2 data and the HEXTE event mode data. We used the `FTOOLs` 5.0.1 and the procedures detailed by Wilms et al. (1999).

In order to take advantage of the best PCA calibrations, we limited the data to detector layer 1 only. We summed the spectra for the 3 active PCUs (numbers 0, 1, and 2) to form a single pulse height spectrum. We used the bright source background model (appropriate for the high counting rate of XTE J1946+274) to estimate the PCA background. Because of the high PCA counting rate of XTE J1946+274 and the

Table 6.1: XTE J1946+274 Observations

		PCA		HEXTE	
	Date[a]	Time[b]	Rate[c]	Time[b]	Rate [d]
1	Sep 16	1.42	195.0 ± 0.2	0.84	30.1 ± 0.5
2	Sep 17	2.35	208.2 ± 0.2	1.50	33.6 ± 0.4
3	Sep 18	2.51	217.5 ± 0.2	1.64	34.6 ± 0.3
4	Sep 19	2.94	216.3 ± 0.2	1.85	33.3 ± 0.3
5	Sep 21	2.69	250.0 ± 0.2	1.76	37.9 ± 0.4
6	Sep 22	3.82	254.5 ± 0.2	2.42	38.5 ± 0.3
7	Sep 23	2.70	243.0 ± 0.2	1.75	37.6 ± 0.4
8	Sep 24	1.54	258.4 ± 0.2	1.09	38.0 ± 0.4
9	Sep 29	4.93	244.9 ± 0.4	3.26	36.4 ± 0.2
10	Oct 4	2.93	219.7 ± 0.2	1.81	33.1 ± 0.3
11	Oct 8	2.77	200.6 ± 0.2	1.79	30.7 ± 0.4
12	Oct 14	1.08	167.9 ± 0.2	0.71	25.4 ± 0.5
	Total[e]	30.6	230.7 ± 0.3	19.7	35.3 ± 0.1

a 1998
b exposure (ks)
c cts s^{-1} PCU^{-1}, 3–20 keV
d cts s^{-1}, 16–100 keV
e Observations 1 – 11. Observation 12 was excluded from the analysis (see §6.4).

duration of the observations, the statistical errors in the energy spectra ($\ll 1\%$) were small compared to the uncertainties in the instrument calibration. It was therefore necessary to include systematic uncertainties on the PCA data in order to achieve a reasonable fit to the data. We determined the size of these errors through the procedures recommended by the PCA team (Jahoda 2000a) and explained in Coburn et al. (2001). In short, we fit contemporaneous observations of the Crab Nebula and Pulsar to a two power law model, using the XTE J1946+274 response matrices. This model allows for different power law indices for the pulsar and nebular components (Knight 1982). We adjusted the systematic errors until a reduced chi-squared of one was achieved – at a level of 0.3% per channel below 20 keV. Above 20 keV, the systematic errors became unacceptably large, $\gtrsim$5%, so we chose to ignore these PCA data, rather than apply large systematic errors. Below 20 keV, we adopted 0.3% systematics for our XTE J1946+274 fits.

We accumulated the HEXTE cluster A and B spectra separately then summed them to form joint source and background spectra for each observation. For the analysis of these summed spectra, we added the cluster A and B response matrices, weighted by the cluster effective areas (4:3, respectively). Fits with this matrix to a single power law model, appropriate in the HEXTE energy band, to the Crab have residuals of $\pm 1\%$. This is smaller than the statistical uncertainties, so we applied no additional systematic errors to the HEXTE data.

Because the observations were spread over $\sim$1 month and a range of $\sim$40% in flux, we were concerned that changes in the source spectrum could affect our analysis. To search for spectral changes, we calculated for each observation the ratio of the net PCA counts spectrum to the total PCA spectrum of all observations (see Figure 6.2). In all but observation 12, we found that above 8 keV, the ratio was nearly flat, indicating that only the flux, and not the spectral shape, had changed. In observation 12 (the last and dimmest observation – see Table 6.1), significant spectral changes were observed, and this pointing was eliminated from our analysis. Observations 1 to 11 showed no changes in spectral shape at a level of $\sim$1–2% between 8–20 keV. Below 8 keV, systematic changes of up to $\sim$5% were seen, particularly in the lowest energy channels. These changes are consistent with $\lesssim$10% variations in the absorbing column and the iron line emission. Such variations are not unexpected during a Be/X-ray binary outburst, and they are likely not indicative of changes in the underlying continuum emission. For this reason, we concluded that by excluding data below 8 keV we could then safely combine observations 1 to 11.

After accumulating observations 1 through 11 as described above, we attempted to fit the PCA and HEXTE spectra jointly with a set of continuum models typically used for accreting pulsars. While there is a notable lack of adequate theoretical models, pulsar spectra are heuristically well-described by a power-law at low energies which breaks to an exponentially cut-off power-law at high energies (White, Swank & Holt 1983). Kreykenbohm et al. (1999) review several models with such an asymptotic behavior – the exponentially cut-off power law (PLCUT, White, Swank & Holt 1983), the Fermi-Dirac cut-off (FDCUT, Tanaka 1986), and a combination of two power-laws with a positive and a negative exponent (NPEX, Mihara 1995). None of these models provided an acceptable fit to the XTE J1946+274 spectrum. All models left significant, cyclotron line-like residuals near 35 keV (see Figure 6.3). We therefore

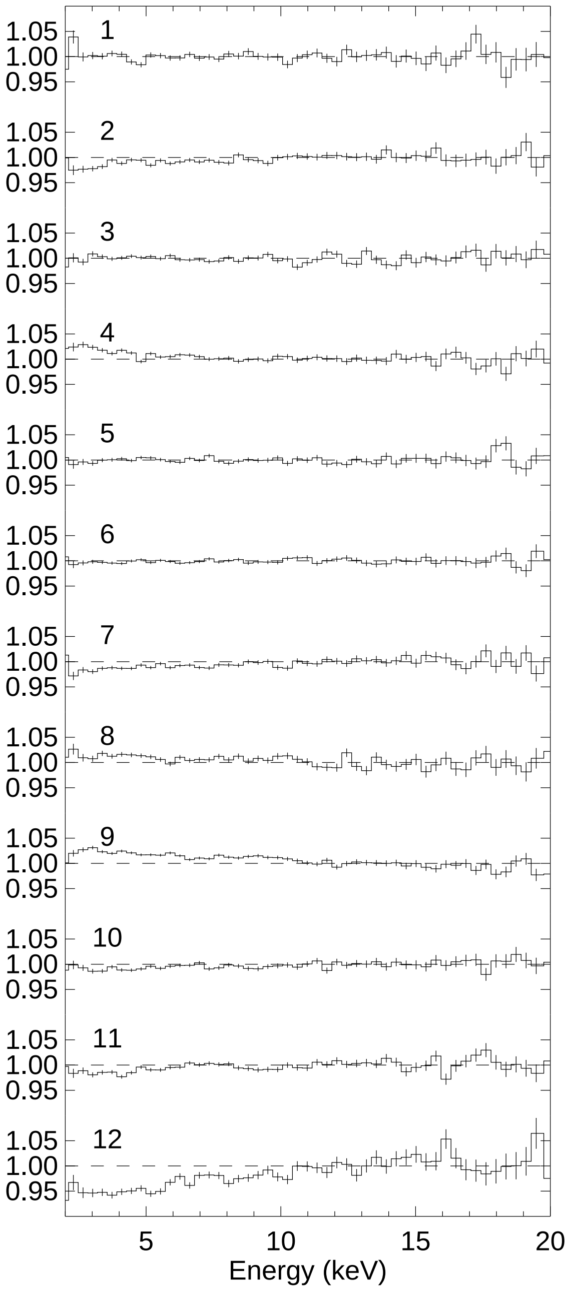

Figure 6.2: Ratios of the net PCA counts spectra from the twelve observations (Table 6.1) to the total spectrum, normalized to the 8–20 keV counting rate. While a small residual slope is apparent in observation 9, deviations above 8 keV were less than 2%, so this spectrum was included in the analysis. However, owing to the overall steep slope of its ratio and large deviations from one, observation 12 was eliminated.

added to each model a cyclotron absorption term with a Gaussian optical depth profile:

$$\tau(E) = \tau_c \times e^{-(E-E_c)^2/2\sigma_c^2}. \tag{6.1}$$

Adding the Gaussian absorption line greatly improved the fits. The best fit was achieved with the NPEX continuum, given by:

$$\mathrm{NPEX}(E) \propto (E^{-\Gamma_1} + \alpha E^{+\Gamma_2}) \times e^{-(E/E_{\mathrm{fold}})} \tag{6.2}$$

where NPEX(E) is the photon flux at energy E; Γ_1 and Γ_2 are the indices of the falling and rising power law components, with α their relative normalizations; and E_{fold} is the exponential folding energy. Our best-fit model was of the form Flux $\propto$ NPEX(E) $\cdot\, \mathrm{e}^{-\tau(E)}$. In this case, the reduced χ^2 changed (with the addition of the line) from 3.61 to 0.97 for 52 and 49 degrees of freedom respectively. The resulting F-Test probability for this to be a chance improvement is 1.2×10^{-14}. Table 6.2 gives the best fit parameters for this model.

6.5 Results and Discussion

Figure 6.3 shows the best fit model and residuals together with the inferred incident photon spectrum. It also shows residuals to the best NPEX model without a cyclotron line. The cyclotron line is apparent in the NPEX-only residuals around 35 keV. From the cyclotron line energy, we deduce a magnetic field strength in the scattering region of $3.1(1+z) \times 10^{12}$ G. The line is weakly resolved with the HEXTE energy resolution of ~8 keV (FHWM, at 35 keV), and the fitted width of the line is $9.3^{+2.5}_{-2.1}$% of the line energy. This is on the low side, but within the range, of typical values determined with the Gaussian absorption profile model Coburn (2001). In general, the cyclotron lines observed with *RXTE* have been inconsistent with narrow lines.

We also searched for a harmonic line near 70 keV, but, as is evident in Figure 6.3, the falling high energy continuum provides inadequate statistics to make a sensitive search for such a feature.

Table 6.2: Best fit spectral parameters for an NPEX times Gaussian absorption profile model.

Parameter	value
Continuum	
Γ_1	$1.38^{+0.27}_{-0.10}$
Γ_2	$2.80^{+0.14}_{-0.27}$
α	$(3.1^{+3.2}_{-1.8}) \times 10^{-4}$
E_{fold} (keV)	$5.54^{+0.16}_{-0.13}$
Flux[a]	5.5×10^{-9}
Cyclotron line	
τ_{c}	$0.33^{+0.07}_{-0.06}$
E_{c} (keV)	$36.2^{+0.5}_{-0.7}$
σ_{c} (keV)	$3.37^{+0.92}_{-0.75}$
χ^2_r/degrees of freedom	0.97/49

[a] ergs $\mathrm{cm}^{-2}\,\mathrm{s}^{-1}$, 2–10 keV

Figure 6.4 (after Coburn 2001) shows the spectral cut-off energy plotted against the cyclotron line energy for 8 pulsars measured with *RXTE*. Also shown is the (somewhat controversial) HEXE/TTM result for A0535+26 (Kendziorra et al. 1994). For uniformity, the pulse-phase average spectra of all sources were fit with the PLCUT continuum:

$$\mathrm{PLCUT}(E) = A\ E^{-\Gamma} \times \begin{cases} 1 & (E \leq E_{\mathrm{cut}}) \\ \mathrm{e}^{-(E-E_{\mathrm{cut}})/E_{\mathrm{fold}}} & (E > E_{\mathrm{cut}}) \end{cases} \tag{6.3}$$

smoothed at E_{cut} (see Coburn 2001 for details). Two sources are excluded from the plot: 4U 1626-67, whose cut-off energy varies by a factor of four with pulse phase (Coburn 2001), and the low luminosity ($\sim 4 \times 10^{34}$ ergs s^{-1}) object 4U 0352+309 (X Per) whose spectrum is not well fit by the usual pulsar models. Due to the complex shape of the 4U 0115+63 fundamental line and the resulting uncertainty in its centroid energy (Heindl et al. 1999b), its plotted energy is half of the first harmonic value.

A clear correlation exists between the line energy and spectral cut-off indicating that the cut-off is related to the magnetic field. Makishima & Mihara (1992)

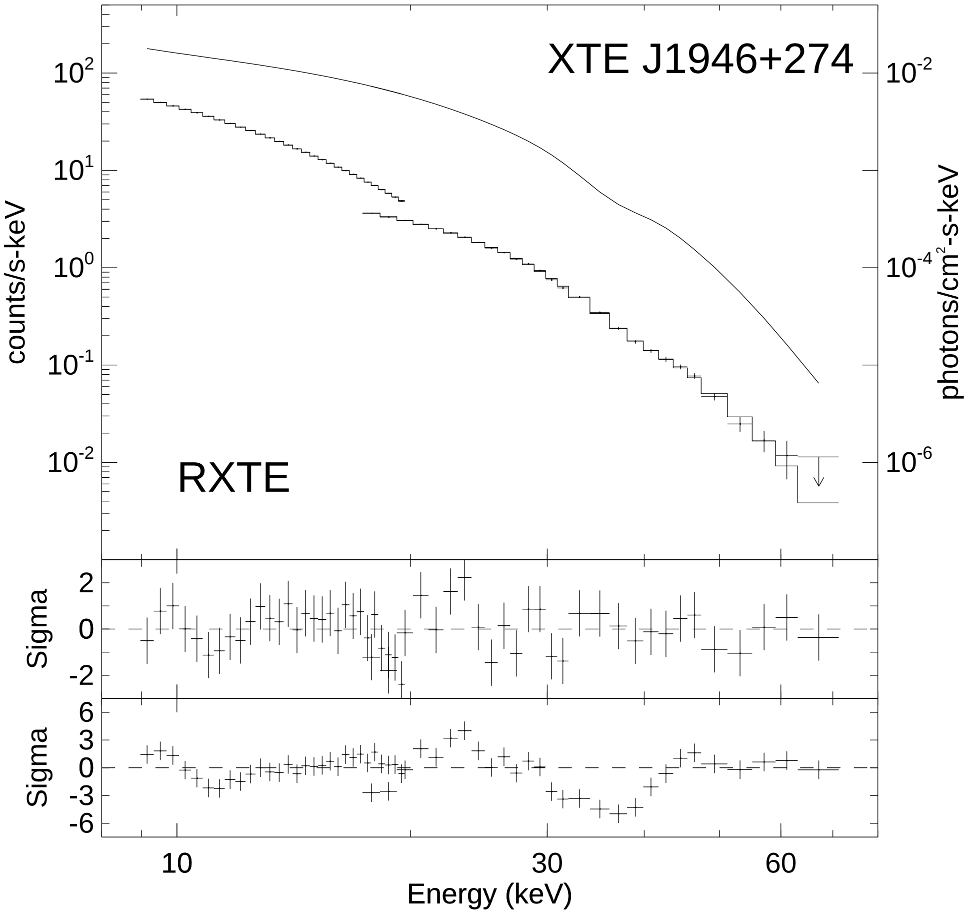

Figure 6.3: The joint PCA/HEXTE spectrum of XTE J1946+274. Top panel shows the data (crosses), the best fit NPEX model with a cyclotron line (histograms), and the inferred incident photon spectrum (smooth curve). See Table 6.2 for fit parameters. The middle and bottom panels show the residuals for the best fit model and the best fit NPEX model with no cyclotron line.

and Makishima et al. (1999) first noted this relationship by plotting cyclotron line energies from *Ginga* and other instruments, derived with a variety of continuum models, against the PLCUT cut-off energy from sometimes non-contemporaneous *Ginga* observations. They found that the relationship was consistent with a power law, $E_{\rm c} \propto E_{\rm cut}^{1.4}$ (or, $E_{\rm cut} \propto E_{\rm c}^{0.7}$), indicating a saturation as compared to a linear correlation. Figure 6.4 has the advantage that each point is derived from a uniform model fit to a single spectrum. And, with the exception of A0535+26, all points are from the same set of instruments. XTE J1946+274 fits nicely on the correlation, and below 30 keV, the slope is consistent with $E_{\rm cut} \propto E_{\rm c}^{0.7}$. However, there appears to be

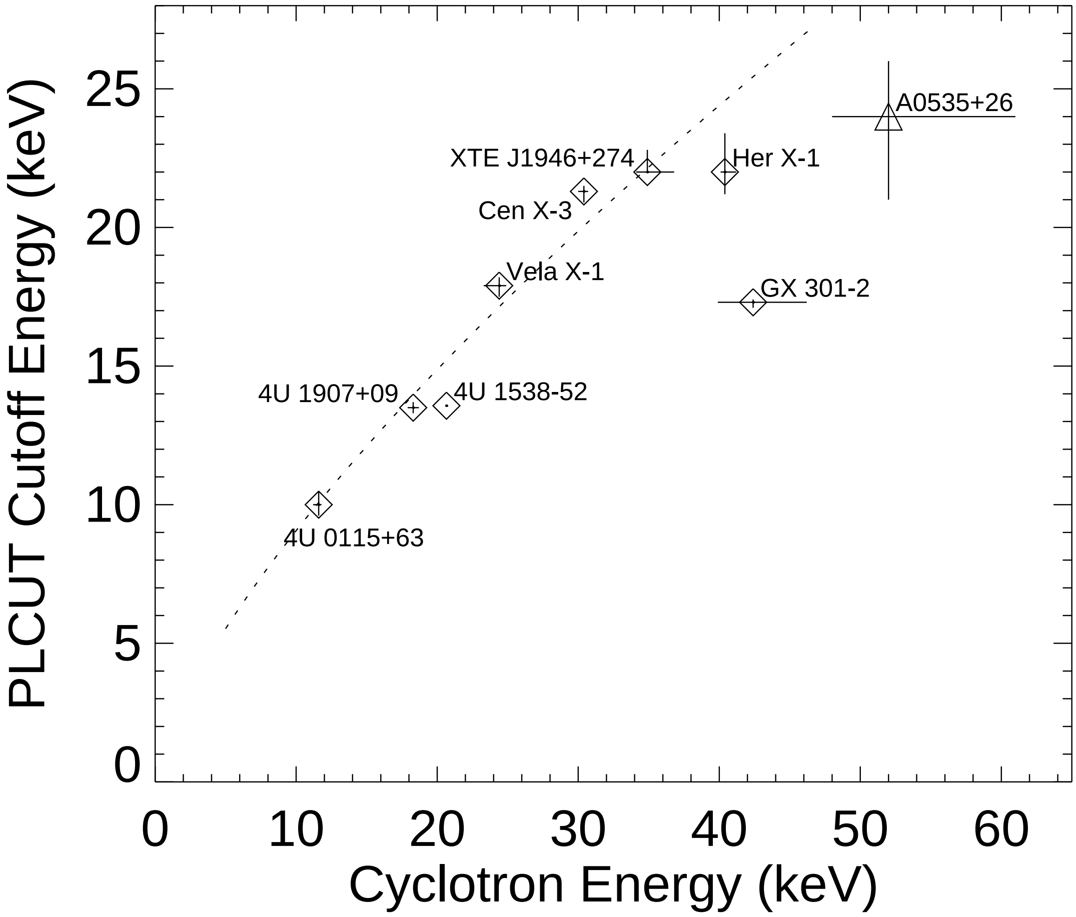

Figure 6.4: Spectral cut-off energy as a function of cyclotron line energy. A possible saturation of the correlation is seen at energies above 30 keV. All points are from *RXTE* except A0535+26 which is from HEXE/TTM (Kendziorra et al. 1994). The line is a power law with $E_{\rm cut} \propto E_{\rm c}^{0.7}$ (Makishima et al. 1999). See text for parameter definitions.

a break in the relationship above $\sim$30 keV. If correct, this flattening of $E_{\rm cut}$ is more abrupt than the rather smooth turnover of the $E_{\rm c}^{0.7}$ power law and suggests that the processes responsible for the formation of the continuum saturate at higher magnetic fields.

With XTE J1946+274, we have added a 13^{th} accreting pulsar to the list of objects with secure cyclotron line detections. Nearly all of these have been confirmed, and several were discovered, with *RXTE* and *Beppo*SAX. As shown in Figure 6.4, we have begun detailed studies of these objects as a class. In particular, since ten of the thirteen sources have been observed with *RXTE*, we are applying uniform analyses to all these objects to further understand the line forming regions. First results of such studies, including correlations between other line parameters, are given in Coburn (2001).

6.6 Acknowledgements

ASM data are provided by the *RXTE*/ASM teams at MIT and at the *RXTE* SOF and GOF at NASA's GSFC. This work was supported by NASA grant NAS5-30720, NSF travel grant INT-9815741, DFG grant Sta 173/25-1, and a travel grant from the DAAD.

This chapter has been recommended for publication to the *The Astrophysical Journal Letters* as "Discovery of a Cyclotron Resonance Scattering Feature in the X-ray Spectrum of XTE J1946+274," W. A. Heindl, W. Coburn, D. E. Gruber, R. E. Rothschild, I. Kreykenbohm, J. Wilms, and R. Staubert, 2001.

Chapter 7

CRSF Searches

Many of the observations of CRSFs in accreting X-ray pulsars to date concern their discovery. There is little written, however, about which pulsars do not exhibit CRSFs. Therefore in addition to discovering new CRSFs, I sought to quantify our knowledge of sources where CRSFs are *not* detected. To do this I derived upper limits on the optical depths of lines, as a function of energy and width, for 12 pulsars observed with the *RXTE*. In this way I distinguish between sources where CRSFs are ruled out with a high degree of confidence, and those where magnetic features might still be hiding in spectra with poor counting statistics. In some cases lines can be ruled out over the entire 10–80 keV range. In others, due to a combination of low source flux and short observing time, the limits are much weaker.

7.1 Strategy

I first screened the source data with several criteria, the first was to minimize the spectral variability of the source. Many X-ray pulsars, especially systems accreting from a wind like Vela X−1, have an X-ray continuum that varies from observation to observation (Kreykenbohm et al. 1999). Simply summing these together can lead to both false positives as well as wash out real features. So I searched the archive for datasets with single, long observations ($\gtrsim 10$ ks) to ensure that there was enough exposure to resolve a CRSF, while also minimizing possible continuum variability. If there were no single long integration then a dataset was chosen that had a number of observations over as short an interval of time as possible. The second criteria I used was the source flux. This was to help ensure enough counting statistics to resolve a CRSF, and therefore observations where the source was brighter were preferred over similar pointings at a lower flux level.

I accumulated the data for both the PCA and the HEXTE using the standard methods and software tools (see Chapter 2). For the PCA I used only the detector combination that was operating during the entire observation or set of observations. Also, due to the faintness of many of the sources, I accumulated only data from the top layer of the PCA to minimize the detector internal background. For the background estimation I used the Faint source background models if the source flux was below 40 cts s^{-1}, and SkyVLE models for sources where the count rate was above. I used PCA systematics of 0.5%, and analyzed data in the range 3–25 keV. This level of systematic error was chosen to be slightly conservative, since it was unfeasible to fit contemporaneous Crab observations for each pulsar.

I accumulated the HEXTE data was in the standard way, taking proper account of the non-functioning pulse height analyzer in cluster B when appropriate. To improve the signal in the HEXTE instrument as well as streamline the analysis, I summed the two clusters together to form a single spectrum, along with their background files and response matrices. I then rebinned the resulting source pointing spectra using the **grppha** `FTOOL` such that there was a minimum of 10^4 counts (source plus background) in each spectral bin.

I then generated PCA light curves for each set of observations to help screen the data. I analyzed segments of data that were $\gtrsim 10$ ks individually, as well as shorter observations with high count rates. If the count rate remained nearly constant and the observation spanned less than a day (or at most several) then I assumed that the spectra did not vary much and the entire observation was summed. Once segments of data were chosen, the spectra from the different observations were summed together.

In each case I found a best fit using either the PLCUT or the FDCO, depending on which model was a better fit (see §2.2.4). I also allowed for low-energy photoelectric absorption along the line of sight (using the phabs model in XSPEC), and added a Gaussian shaped emission Fe-K line and or Fe-edge as needed.

Starting with the best fit, I added Gaussian shaped absorption lines (GABS, see §2.2.5) with fixed energies (10, 20, 30, 40, 60, and 80 keV) and widths (0.75 keV or narrow, $0.1E_{\rm c}$, $0.2E_{\rm c}$, and $0.3E_{\rm c}$). I then increased the depth of the line, fitting the spectrum at each iteration to allow the continuum to adjust, until the χ^2 increased by 9.0 (99.73% confidence Lampton, Margon & Bowyer 1976). In this way I found the largest optical depth, for a grid of energies and widths, that was consistent with the data at the $3-\sigma$ level. Due to the various model components (Fe-K lines, blackbodies, Fe-edges, etc.) that describe the 2–10 keV spectra of pulsars, I did not extend my upper limit analysis below 10 keV. These model components can easily compensate for a deep CRSF with physically unreasonable parameters and thus lead to an overestimation of the upper limits.

Figure 7.1 shows the results of searches on Monte Carlo simulations of *RXTE* data for different observation lengths and source fluxes. In all cases the input spectrum was a FDCO continuum with Γ=1.0, $E_{\rm cut}$=10, and $E_{\rm fold}$=15 and no CRSF. I have also included an interstellar absorption column ($N_{\rm H} = 7.5 \times 10^{-21}\,{\rm cm}^{-2}$) and an Fe-K line at 6.4 keV with $\sigma = 0.7$ keV. For the dim case the simulated 3–100 keV source flux was $1.8 \times 10^{-10}\,{\rm ergs\,cm^{-2}\,s^{-1}}$, while for the bright source it was 10 times as high.

In the 4 panes of Fig. 7.1 I plot the 3-σ upper limits on the optical depth τ as a function of CRSF energy and width. The dotted line, at an optical depth $\tau = 0.5$, is a useful fiducial threshold since the observed lines lie in the range $\tau = 0.3 - 1$. Where the upper limits are above the dotted line I cannot rule out the existence of a CRSF in the spectrum at that energy and width. These plots show clearly that in order to confidently exclude a CRSF in a source, the pulsar needs to be both bright and observed for a significant ($\gtrsim 100$ ks) amount of time.

In many cases the limiting optical depths are quite small, in some cases as low as $\tau_{\rm c} \sim 10^{-2}$. I would like to point out that identifying such a shallow line as a CRSF in the *RXTE* data would be nearly impossible; the effect of such a feature

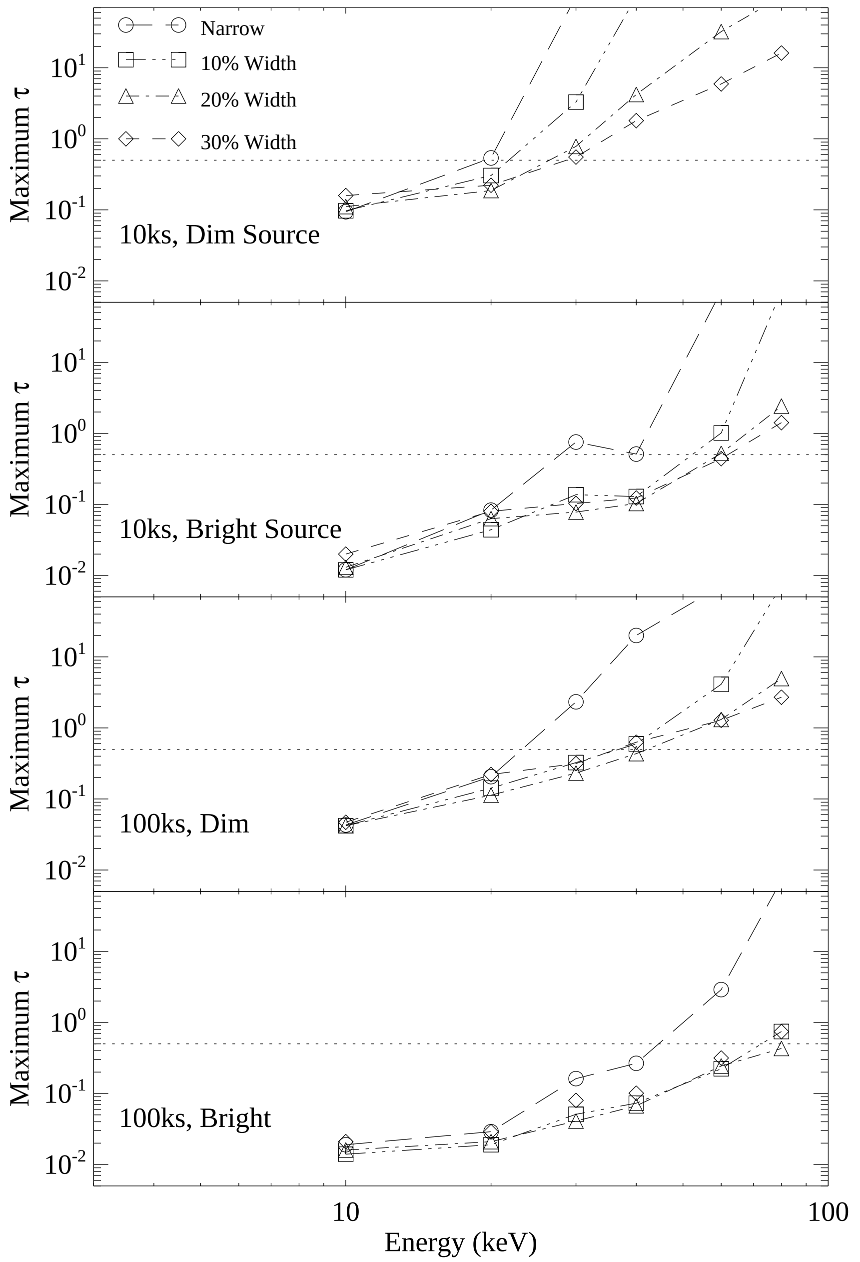

Figure 7.1: Upper limits to CRSF depth in Monte Carlo *RXTE* data with no CRSF for two different observation lengths (10 and 100 ks) and at two 3–100 keV source fluxes (1.8×10^{-10} and $1.8 \times 10^{-9}\,\mathrm{ergs\,cm^{-2}\,s^{-1}}$).

on the underlying (and uncertain) continuum would be too small. Also, because of the uncertainties in the PCA response matrix and background subtraction, a 3–σ detection of a line at such a depth would be a tenuous claim. Instead, these small limits should be taken as evidence that if there were a CRSF in the spectrum that was similar to known features, it would have been clearly detected.

The results of this analysis show that for many sources narrow features, especially at higher energies, are virtually undetectable by the current generation of hard X-ray satellites (the *Beppo*SAX is similar to the *RXTE* in sensitivity to CRSFs). For very broad lines ($\sigma_c \gtrsim 20$) detection is slightly easier since the effect of their red wings on the continuum is noticeable even if the source is not detected at the resonance energy. However, given the phenomenological nature of the current continuum models, distinguishing a real feature from a poorly modeled continuum is problematic. Since higher energy CRSFs modify an exponentially falling continuum, what is needed for their detection are large areas, low internal background, and long integration times. Also, to search for narrow lines excellent energy resolution is also required. Unfortunately, this means putting several square meters of germanium detectors in orbit, something that is currently unfeasible. In the interim, there is certainly the possibility that the European Space Agency's *INTEGRAL* satellite, with its higher energy range (15 keV–10 MeV) and excellent spectral resolution, will observe potential narrow CRSFs.

The following pages contain two figures for each source. The first is the background subtracted PCA light curve of the observations used in the analysis, summed over the entire PCA energy range. In these plots the time resolution is 16 s, and each bin is plotted as a cross indicating the 16 s width and error in the counting rate. The large variation (or smearing) seen is due to the pulsation period.

The second figure is the source spectrum with three panes. The top panel contains the phase averaged *RXTE* counts spectrum (crosses) along with the best fit model (histograms). In the cases where upper limits are given in the counts spectra these are at the 2-σ level. Additionally, the inferred photon spectrum is shown (smooth line), with the corresponding vertical axis read on the right-hand side of the pane. The middle panel contains the residuals of the fit, shown in units of σ. The bottom panel is nearly identical to the panes in Fig. 7.1, with the upper limits on CRSF depths plotted as a function of CRSF energy and width. In many of these sources the lack of an observed CRSF in the spectrum can easily be attributed to statistics and length of the observation.

Table 7.1: Sources and Observations Usedin the Upper Limit Analysis

Source	Observation Date	$P_{\rm spin}$ (s)	Exposure (ks) PCA	Exposure (ks) HEXTE	Flux[a] ($\rm ergs\,cm^{-2}\,s^{-1}$)	PCUs
2S 1553−542	1997 Sep 18	9.27	3.9	2.4	2.20×10^{-10}	0,1,2
2S 1417−62	2000 Jan 11–12	17.2	46.7	28.9	2.24×10^{-9}	0,2
GS 1843+00	1997 March 5	29.5	9.5	5.8	5.89×10^{-9}	All
OAO 1657−415	1997 Nov 10–11	37.7	26.4	16.8	3.44×10^{-10}	All
EXO 2030+375	1996 Jul 1–10	42.1	58.6	46.6	1.22×10^{-9}	All
GS 1843−024	1998 Sep 17–29	94.8	31.4	20.6	1.74×10^{-9}	0,1,2
GRO J2058+42	1998 Feb 5	110	7.7	5.7	3.61×10^{-10}	0,1,2
Scutum X−1	1997 Jun 20–21	111	20.3	12.7	2.28×10^{-10}	0,1,2,3
GX 1+4	1996 Jul 19–20	120	51.2	31.1	2.86×10^{-10}	0,1,2
XTE J1858+034	1998 Feb 24	221	7.4	4.5	5.86×10^{-10}	All
EXO 1722−363	1998 Oct 31	414	9.3	5.4	3.39×10^{-10}	All
RX J0146.9+6121	1997 Jul 11	1413	8.0	5.2	1.07×10^{-10}	All

[a] in 3–100 keV

7.2 Individual Sources

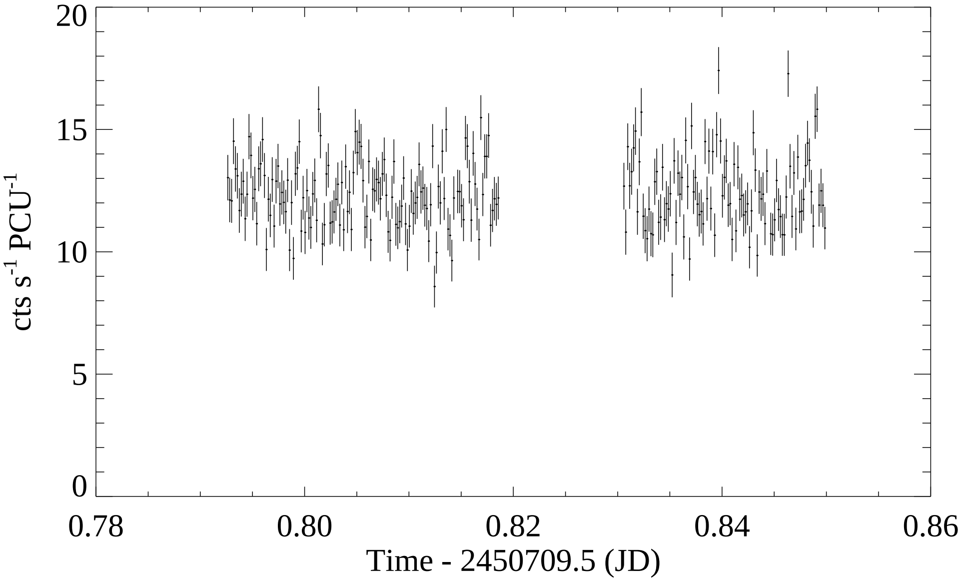

Figure 7.2: The PCA light curve during the observation of 2S 1553−542.

7.2.1 2S 1553−542

The source 2S 1553−542 is a 9.27 s (Kelley, Rappaport & Ayasli 1983) transient pulsar with an unknown companion. The PCA light curve of the 1997 Sep 18 observation is given in Fig. 7.2. The length of this observation is less than our 10 ks selection criterion. It was used, however, because it was the longest observation of the source in the *RXTE* data archive. I fit the source spectrum (see Fig. 7.3) with a FDCO continuum, along with interstellar absorption and a narrow Fe-K line. Since the source was only detected out to ~30 keV, I am unable to place meaningful limits above ~15 keV.

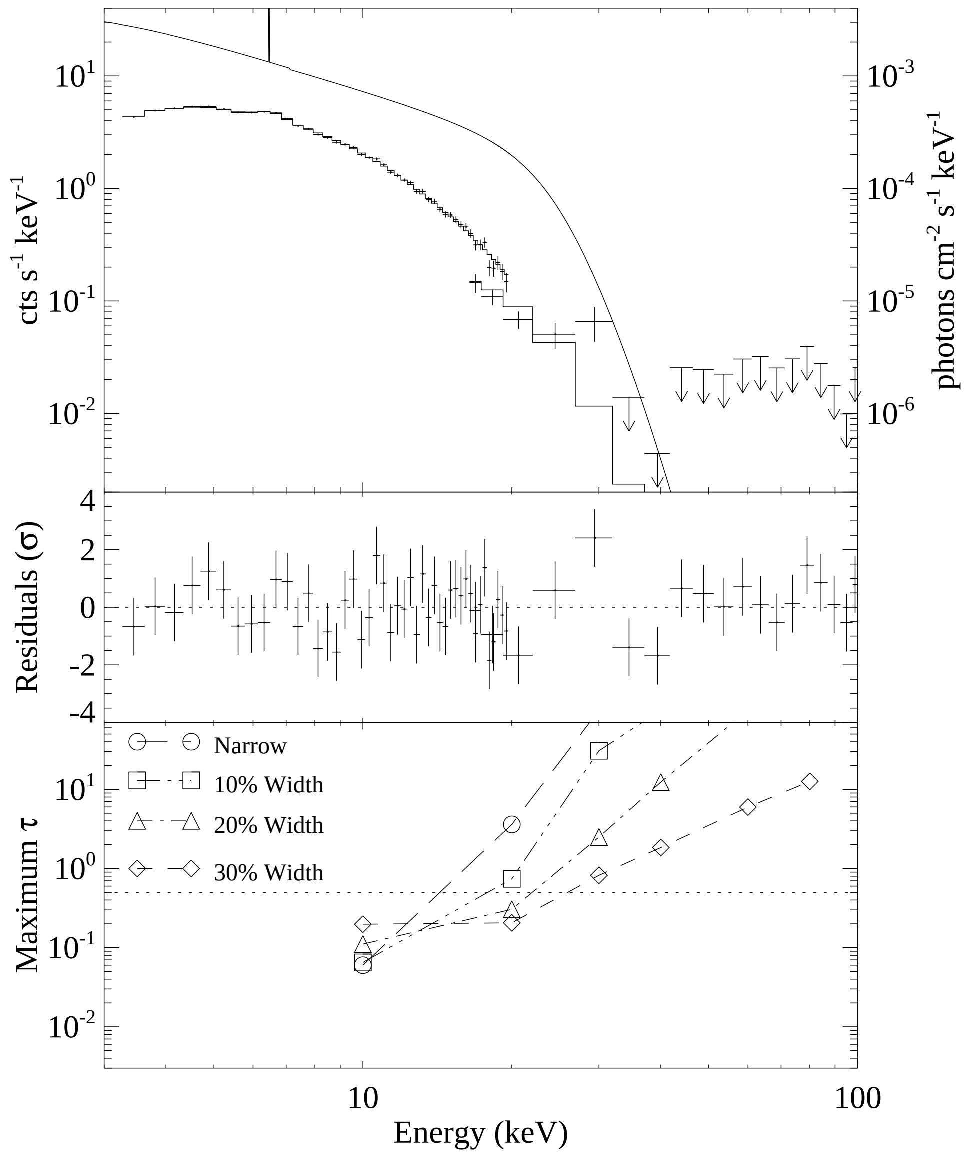

Figure 7.3: Top: Counts spectrum of 2S 1553−542 (crosses), best fit model (histograms, see text), and inferred photon spectrum (continuous line). Middle: Residuals to the fit in units of σ. Bottom: Upper limits on CRSF depths τ_c as a function of energy E_c and either fractional width (σ_c/E_c) or a narrow (0.75 keV) feature.

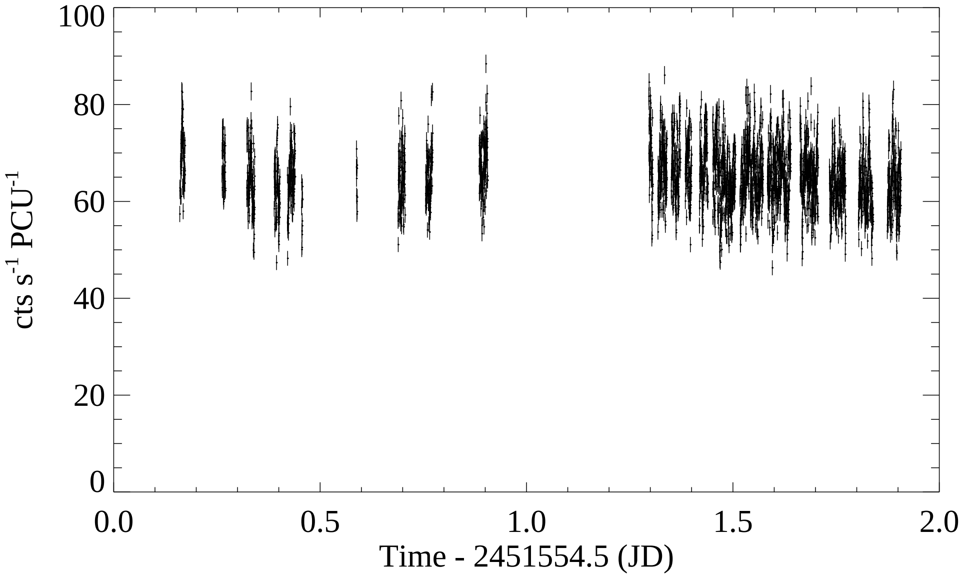

Figure 7.4: PCA light curve of this observation of 2S 1417−62.

7.2.2 2S 1417−62

The source 2S 1417−62 is a ∼17.6 s transient pulsar with an OBe companion (Finger, Wilson & Chakrabarty 1996). The observations here were taken during an outburst of the source, and the PCA light curve is shown in Fig. 7.4. I fit the source spectrum (see Fig. 7.5) with a PLCUT continuum, broad Fe-K line, and interstellar absorption. I can rule out the presence of broad CRSFs over almost the entire energy range, as well as a narrow feature out to ∼50 keV.

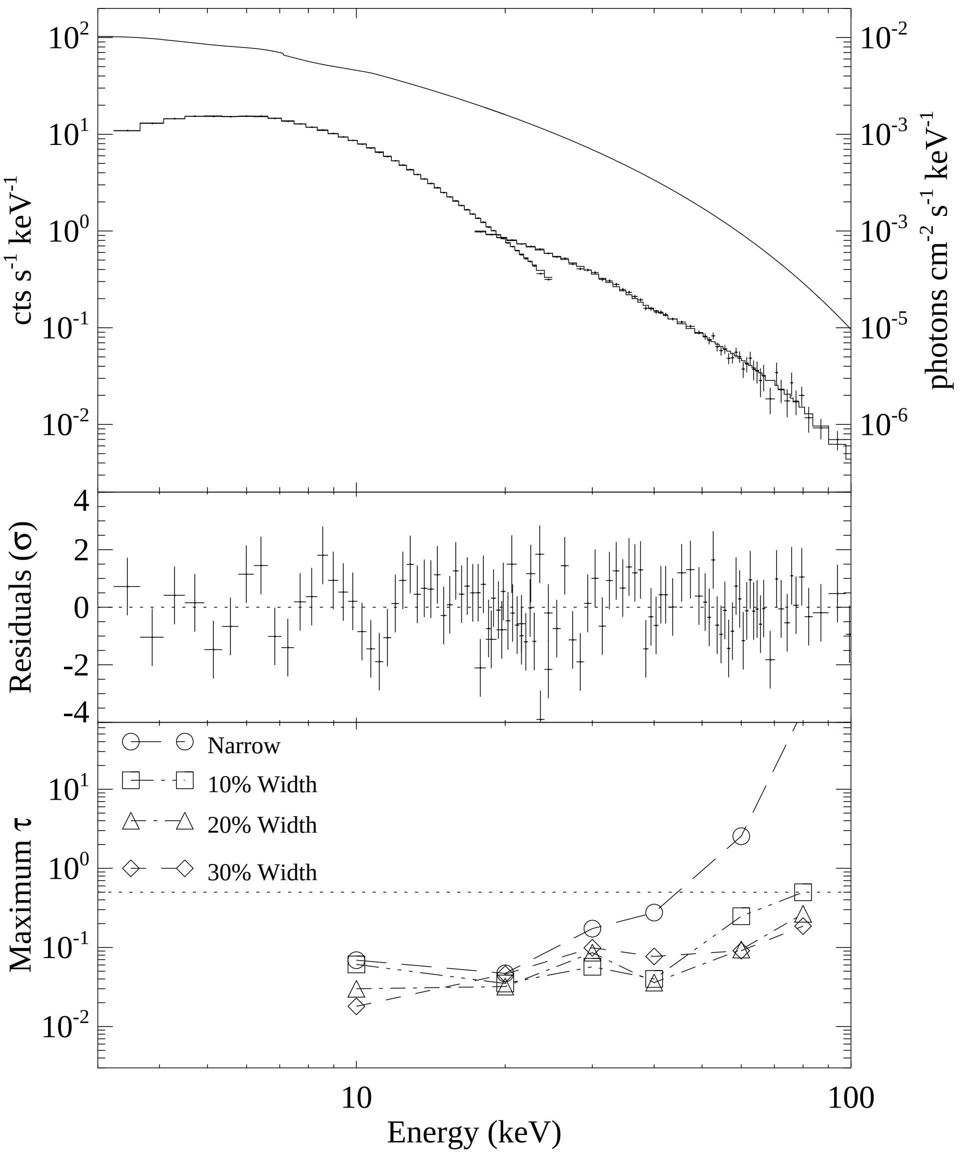

Figure 7.5: Top: Counts spectrum of 2S 1417−624 (crosses), best fit model (histograms, see text), and inferred photon spectrum (continuous line). Middle: Residuals to the fit in units of σ. Bottom: Upper limits on CRSF depths τ_c as a function of energy E_c and either fractional width (σ_c/E_c) or a narrow (0.75 keV) feature.

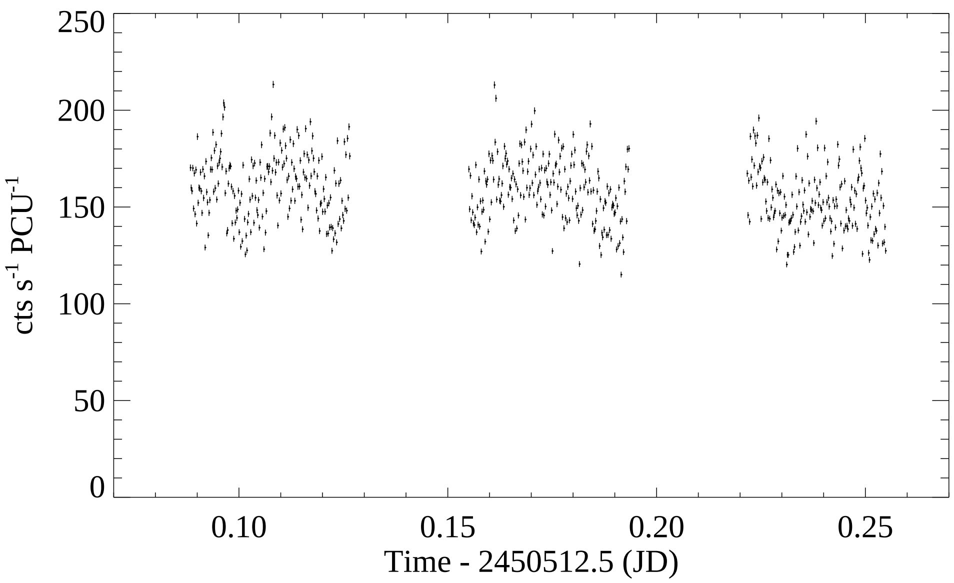

Figure 7.6: The PCA light curve during the observation of GS 1843+00.

7.2.3 GS 1843+00

The source GS 1843+00 is a ~29.5 s transient pulsar with an unknown companion (Koyama et al. 1990a). The PCA light curve of the 1997 March 5 observation is given in Fig. 7.6. A possible ~20 keV CRSF has been suggested by Mihara (1995), but this has not been confirmed in either my analysis of *RXTE* data or in *Beppo*SAX observations (Piraino et al. 2000).

I fit source spectrum (see Fig. 7.7) with a FDCO continuum model plus a blackbody and interstellar absorption. There is a pattern of residuals near 10 keV which are a ±1% deviation from the model. This pattern at 10 keV is seen in many pulsars, and see §3.2.4 for a brief discussion. Due to the highly significant spectrum I can exclude the presence of broad CRSFs out to ~80 keV, and narrow features out to nearly 60 keV.

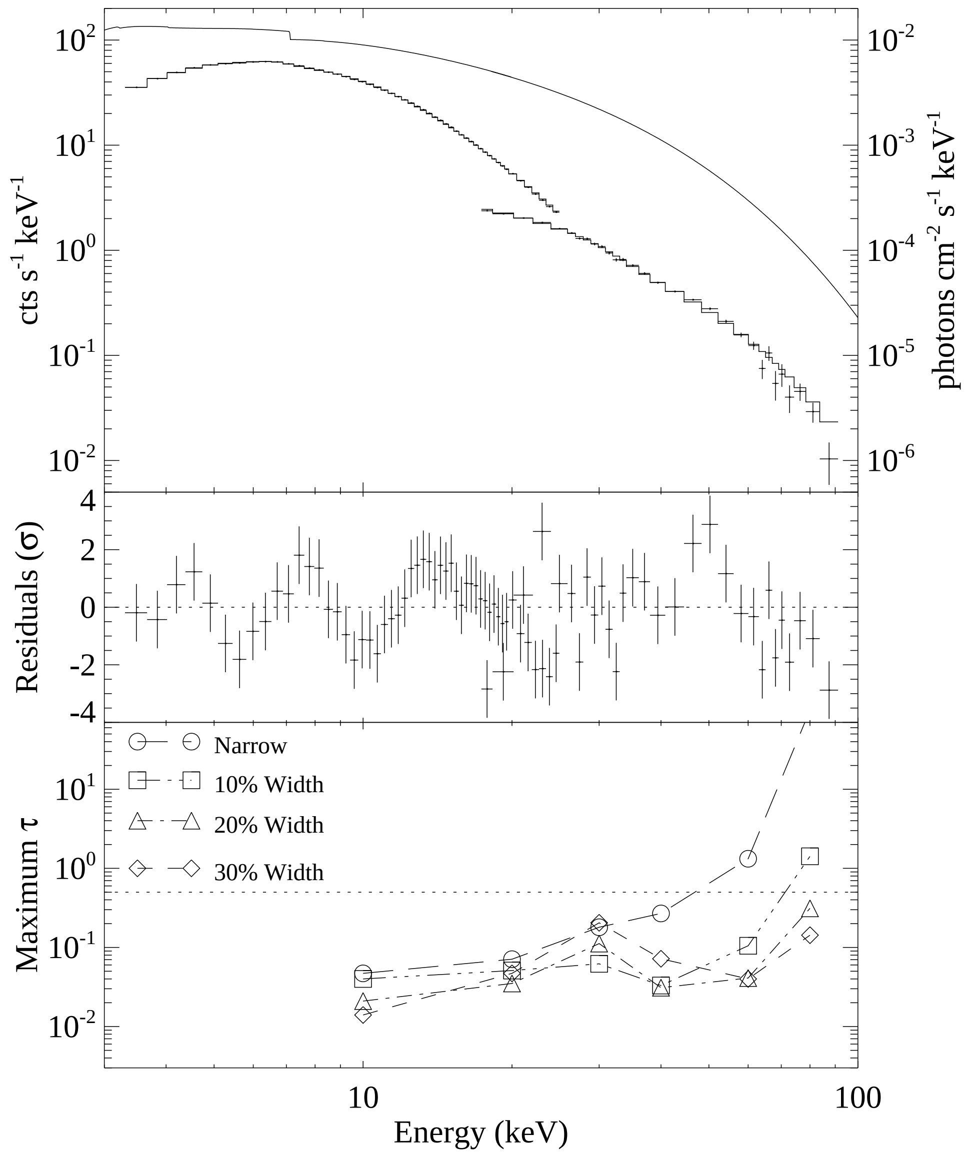

Figure 7.7: Top: Counts spectrum of GS 1843+00 (crosses), best fit model (histograms, see text), and inferred photon spectrum (continuous line). Middle: Residuals to the fit in units of σ. Bottom: Upper limits on CRSF depths $\tau_{\rm c}$ as a function of energy $E_{\rm c}$ and either fractional width ($\sigma_{\rm c}/E_{\rm c}$) or a narrow (0.75 keV) feature.

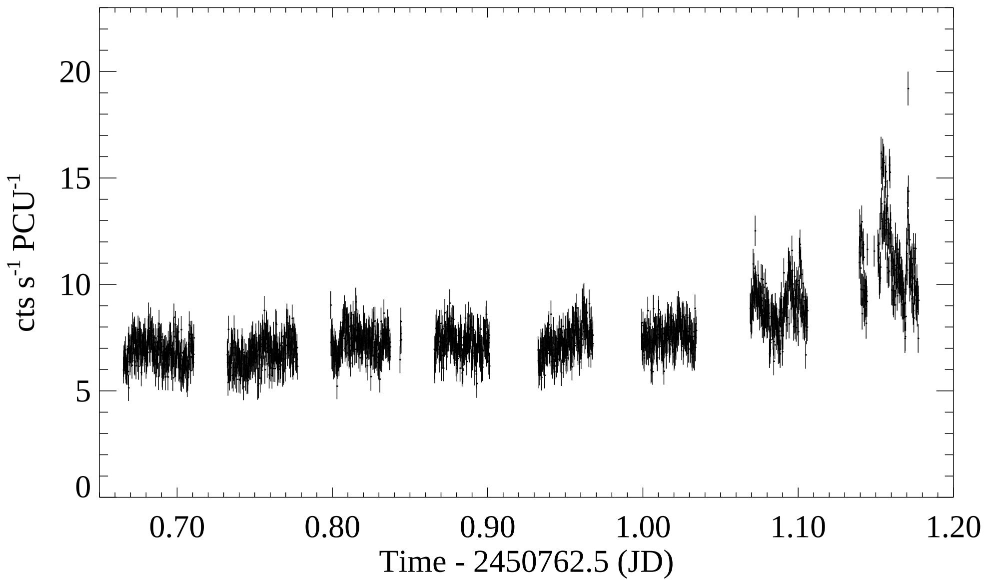

Figure 7.8: PCA light curve during the observation of OAO 1657−415.

7.2.4 OAO 1657−415

The ~37.7 s pulsar OAO 1657−415 is a persistent HMXB with a type B0-6 Iab Star (Chakrabarty et al. 1993). The *RXTE* has observed the source ~82 times since launch. I have used data obtained between 1997 November 10–11 observations, which were both the longest and among the brightest (see Fig. 7.8. I fit the source spectrum (see Fig. 7.9) with a PLCUT continuum, an Fe-K line and Fe-edge, black-body, and interstellar absorption. I can exclude a narrow line only to ~20 keV, and a broad feature to ~30 keV.

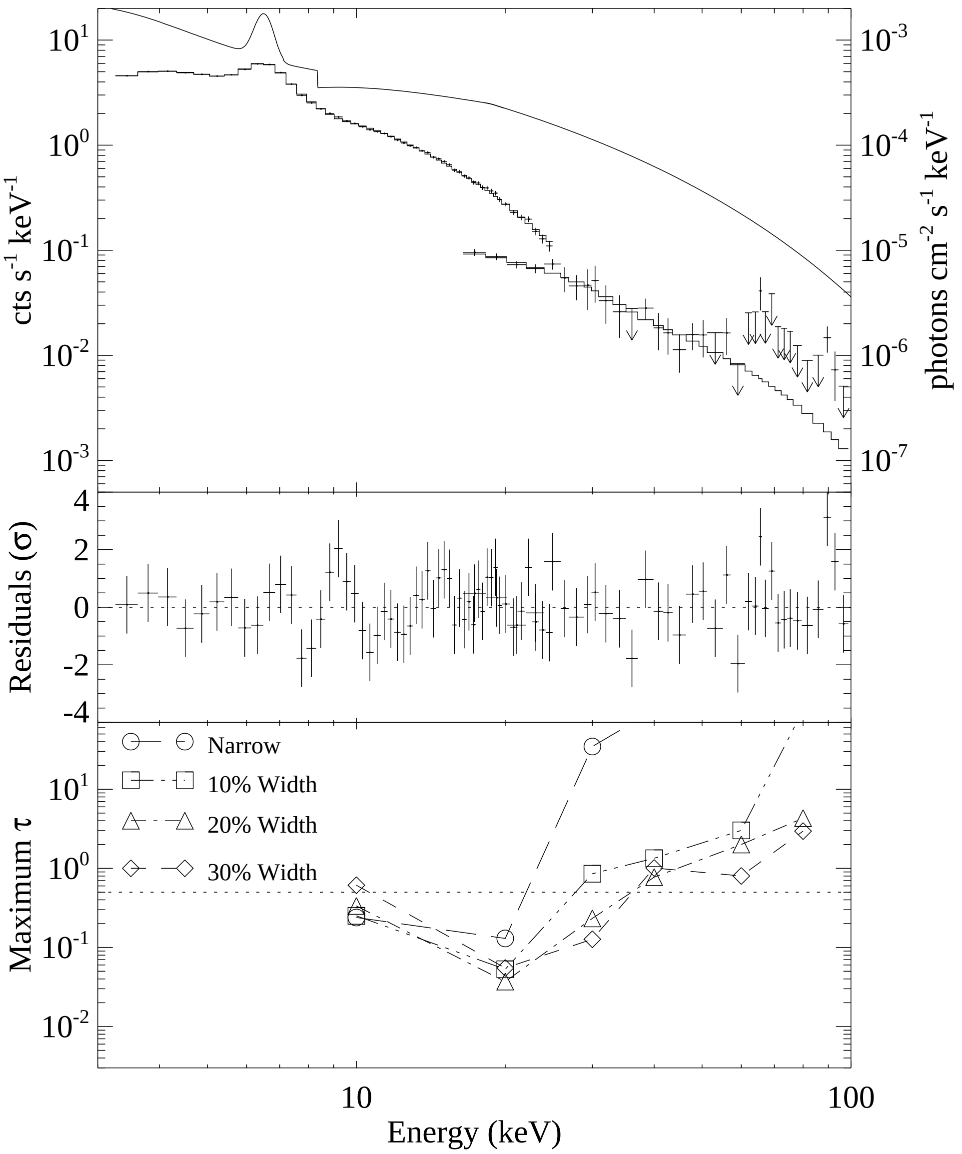

Figure 7.9: Top: Counts spectrum of OAO 1657−415 (crosses), best fit model (histograms, see text), and inferred photon spectrum (continuous line). Middle: Residuals to the fit in units of σ. Bottom: Upper limits on CRSF depths τ_c as a function of energy E_c and either fractional width (σ_c/E_c) or a narrow (0.75 keV) feature.

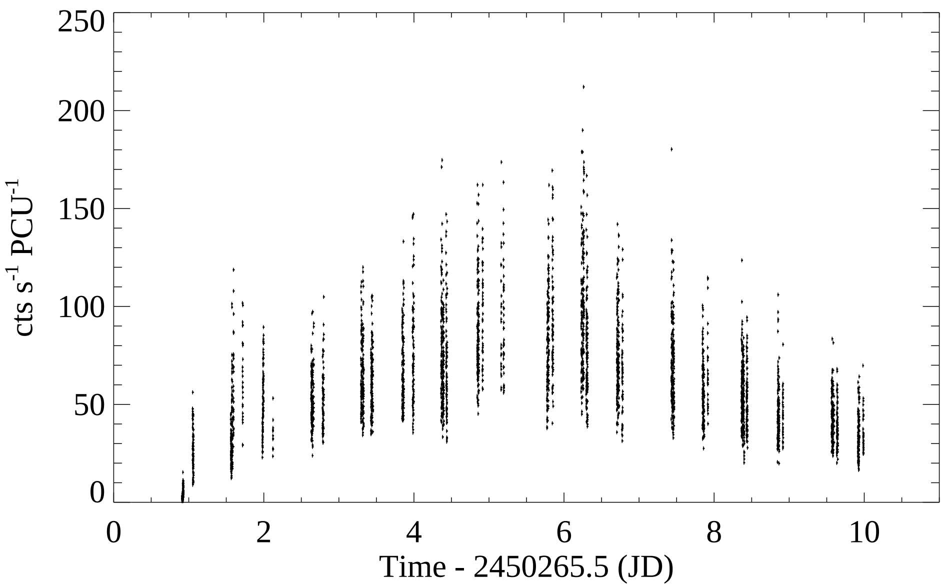

Figure 7.10: PCA light curve during the observation of EXO 2030+375.

7.2.5 EXO 2030+375

The source EXO 2030+375 is a ~42.1 s transient pulsar with a Be star companion. The *RXTE* observed an outburst of this source during 1996 July 1–10. The PCA light curve is given in Fig. 7.10. The *RXTE* made 25 short (~5 ks) observations, which I have summed together for this analysis. This is a longer baseline than I would normally use, and as such the resulting spectrum might be contaminated slightly due to spectral variability. A ~36 keV CRSF has been reported from this dataset previously (Reig & Coe 1999), although only data from HEXTE cluster A was used in the analysis. When both clusters are used there is no evidence of a CRSF in the HEXTE spectrum.

I fit the source spectrum (see Fig. 7.11) with a PLCUT continuum, a black-body, broad Fe-K line and Fe-edge, and interstellar absorption. I can rule out the presence of broad CRSFs in the 10–60 keV range, and a narrow line up to 40 keV.

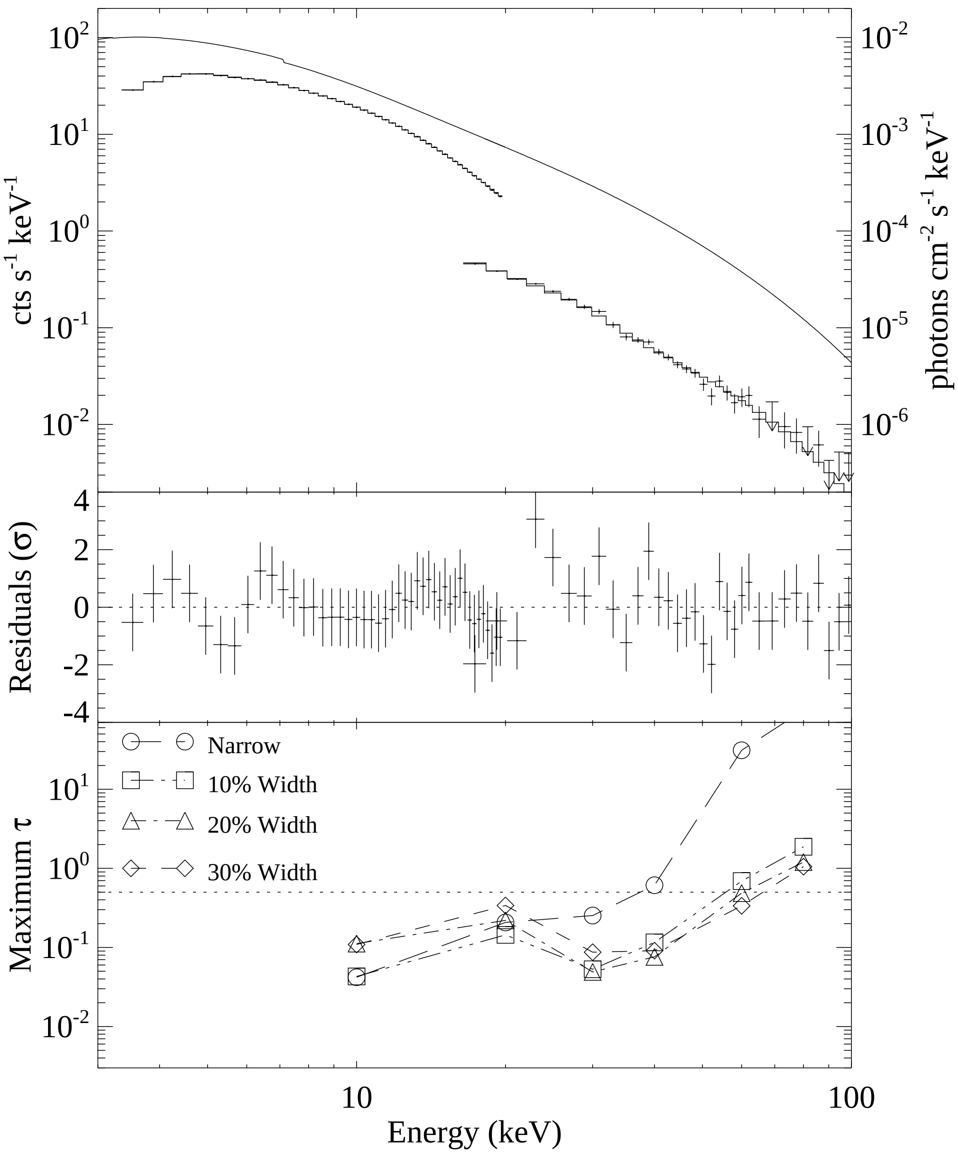

Figure 7.11: Top: Counts spectrum of EXO 2030+375 (crosses), best fit model (histograms, see text), and inferred photon spectrum (continuous line). Middle: Residuals to the fit in units of σ. Bottom: Upper limits on CRSF depths τ_c as a function of energy E_c and either fractional width (σ_c/E_c) or a narrow (0.75 keV) feature.

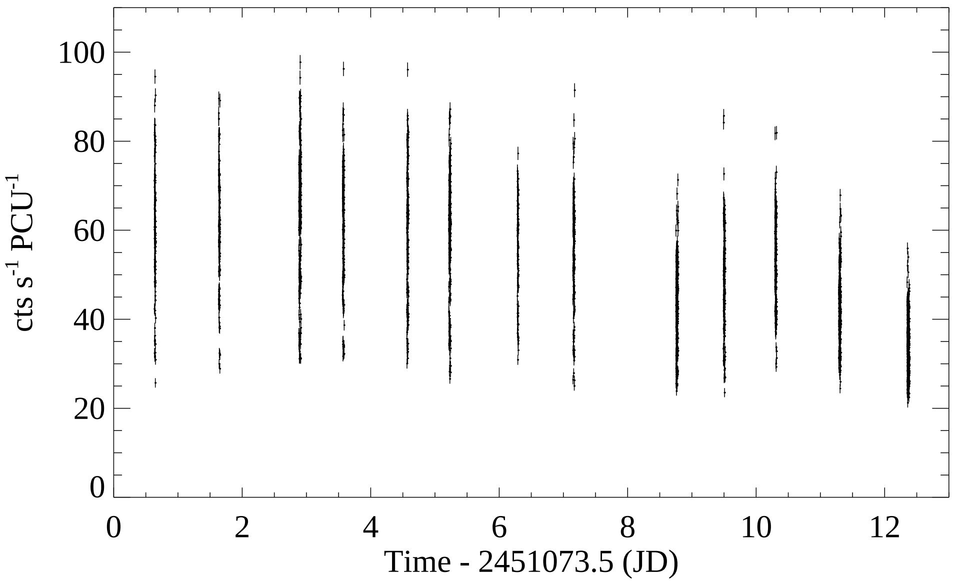

Figure 7.12: The PCA light curve during the observation of GS 1843−024.

7.2.6 GS 1843−024

The source GS 1843−024 is a transient ~94.8 s pulsar with an unknown companion (Koyama et al. 1990b). I have chosen a subset of 13 observations because of the relatively constant counting rate (see Fig. 7.12), despite the two week interval they are spread over. I fit the source spectrum (see Fig. 7.13) with a PLCUT continuum, black-body, Fe-K line, and interstellar absorption. I can exclude broad CRSF features over the entire energy range, and a narrow feature up to ~60 keV.

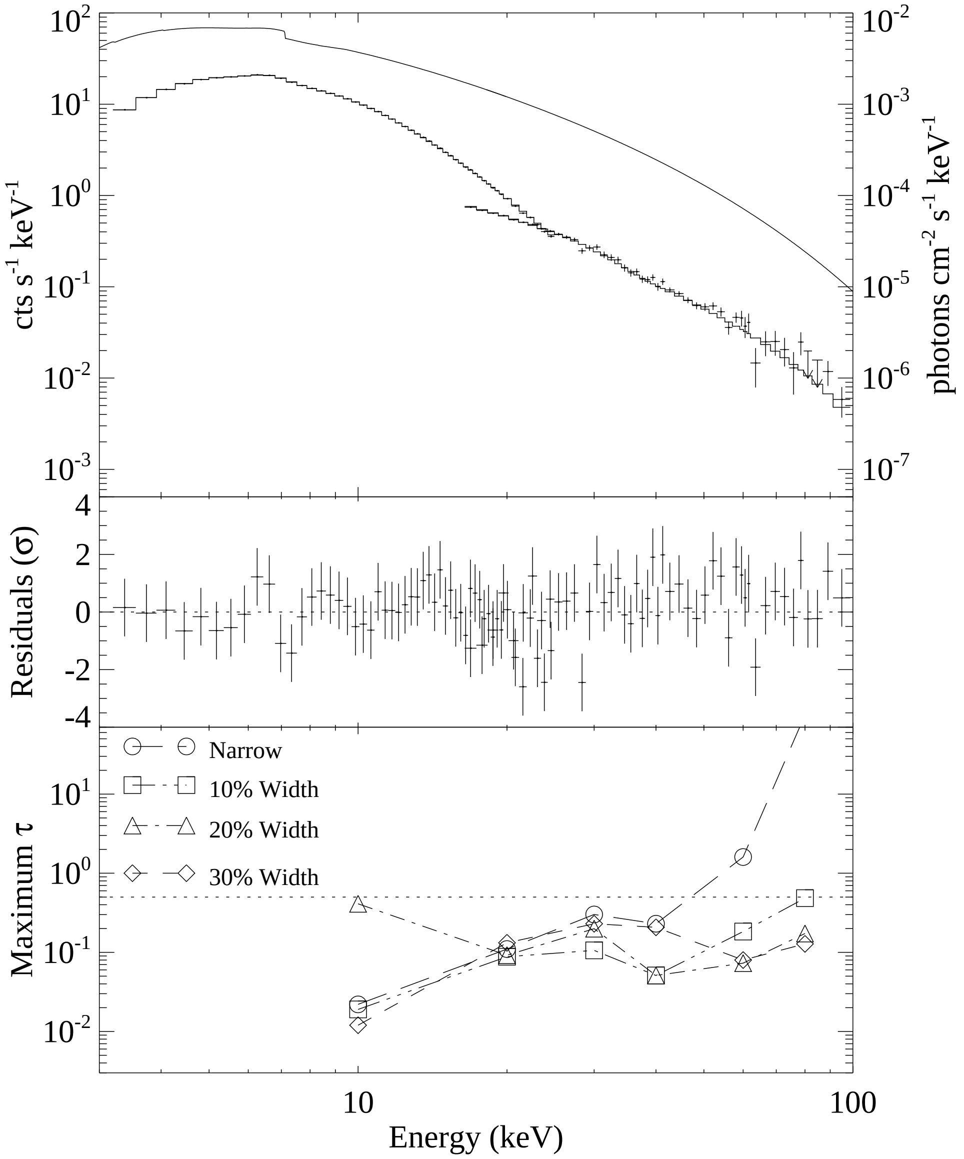

Figure 7.13: Top: Counts spectrum of GS 1843−024 (crosses), best fit model (histograms, see text), and inferred photon spectrum (continuous line). Middle: Residuals to the fit in units of σ. Bottom: Upper limits on CRSF depths τ_c as a function of energy E_c and either fractional width (σ_c/E_c) or a narrow (0.75 keV) feature.

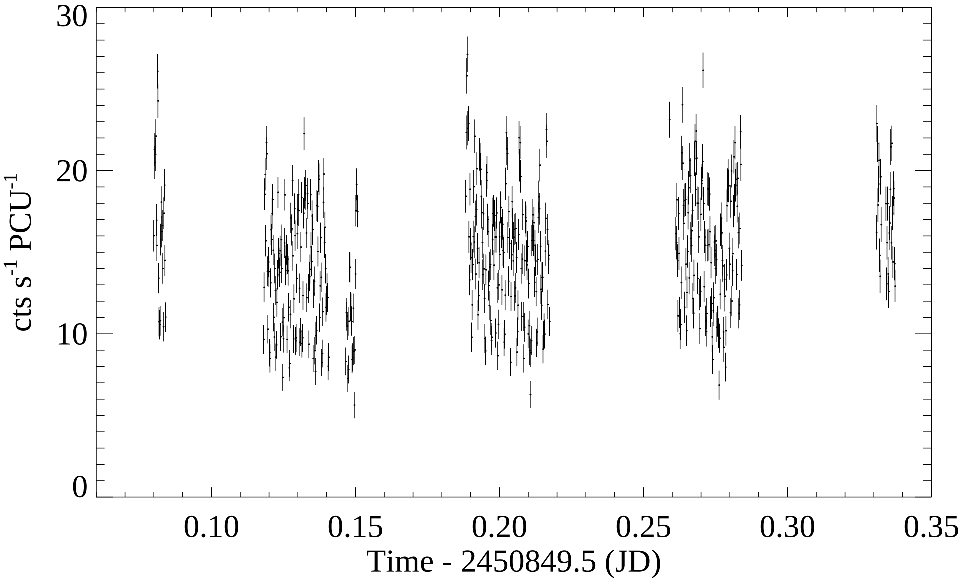

Figure 7.14: PCA light curve during the observation of GRO J2058+42.

7.2.7 GRO J2058+42

The ~110 s pulsar GRO J2058+42 is a transient source with an unknown companion discovered by the *CGRO*/BATSE (Wilson et al. 1995). The *RXTE* made 15 observations from 1998 January 23 through 1998 March 30, with the source brightest on 1998 February 5. The PCA light curve of that observation is given in Fig. 7.14). I fit the spectrum (see Fig. 7.15) with a PLCUT continuum plus low-energy absorption. Due to the very low source flux I cannot rule out the existence of a CRSF above ~20 keV.

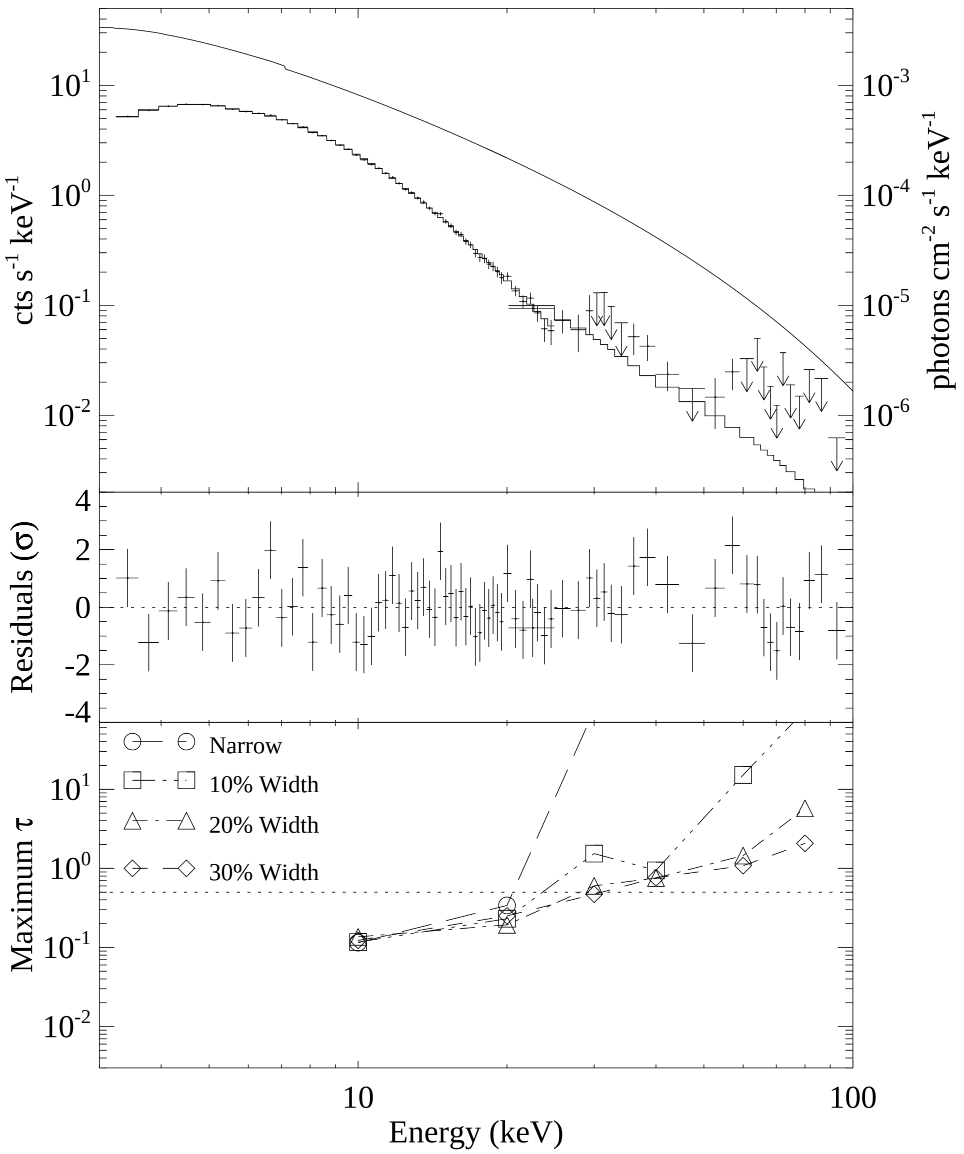

Figure 7.15: Top: Counts spectrum of GRO J2058+42 (crosses), best fit model (histograms, see text), and inferred photon spectrum (continuous line). Middle: Residuals to the fit in units of σ. Bottom: Upper limits on CRSF depths τ_c as a function of energy E_c and either fractional width (σ_c/E_c) or a narrow (0.75 keV) feature.

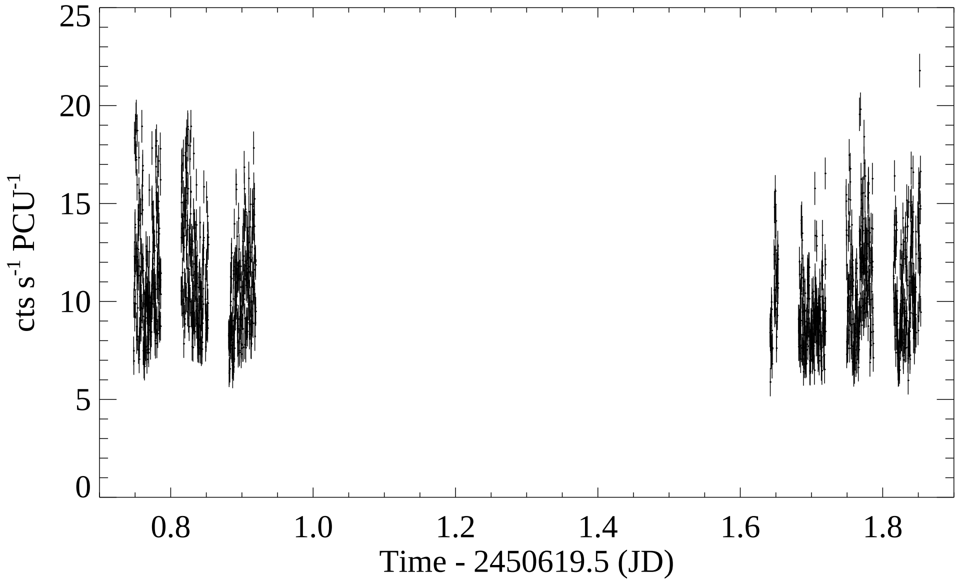

Figure 7.16: PCA light curve during the observation of Sct X−1.

7.2.8 Sct X−1

The transient pulsar Scutum X−1 (Sct X−1) has a 111 s pulsation period and unknown companion (Koyama et al. 1991). The PCA light curve of the 1997 June 20–21 observation is given in Fig. 7.16. I fit the spectrum (Fig. 7.17) with the FDCO continuum, with an Fe-K line and interstellar absorption. Due to the very low source flux I cannot rule out the existence of a CRSF above ~20 keV.

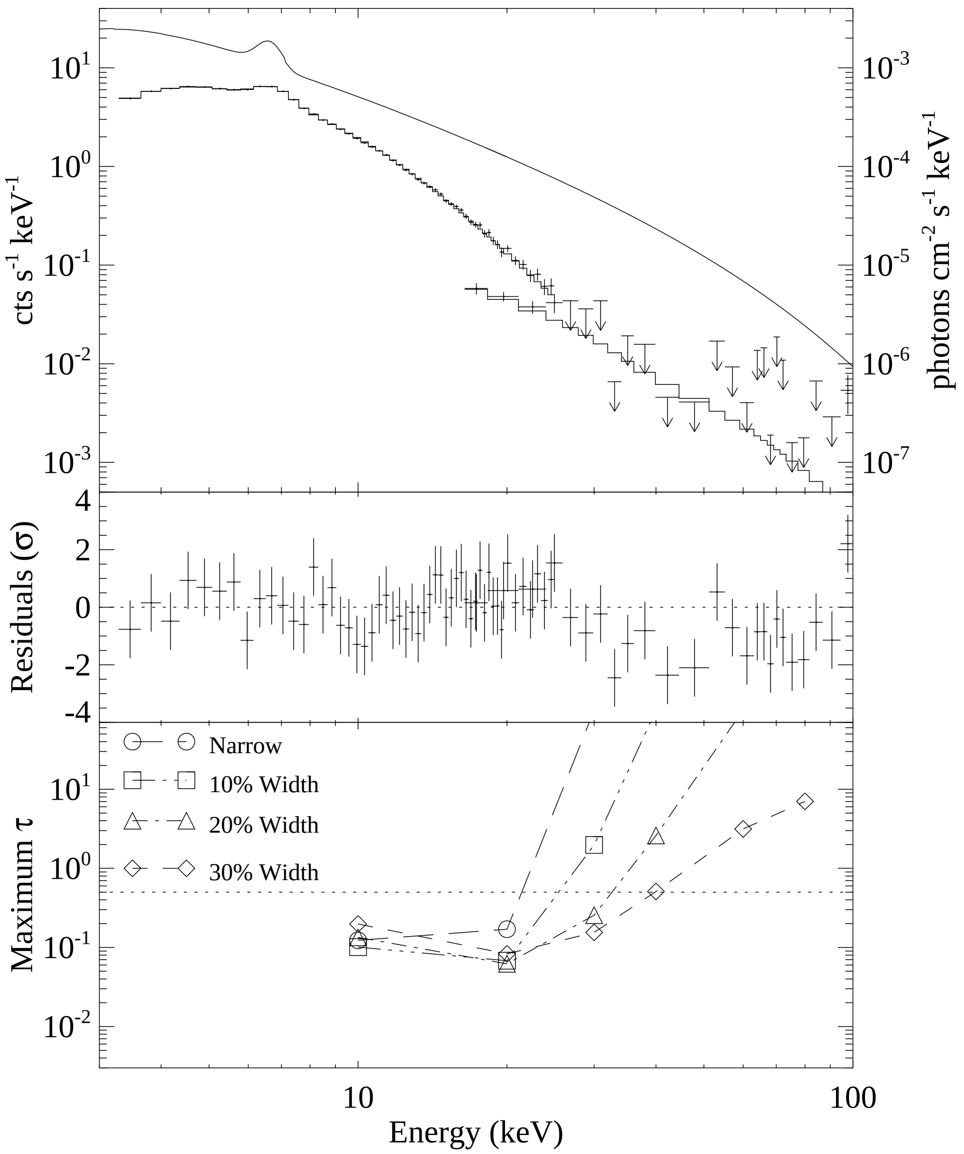

Figure 7.17: Top: Counts spectrum of Sct X−1 (crosses), best fit model (histograms, see text), and inferred photon spectrum (continuous line). Middle: Residuals to the fit in units of σ. Bottom: Upper limits on CRSF depths τ_c as a function of energy E_c and either fractional width (σ_c/E_c) or a narrow (0.75 keV) feature.

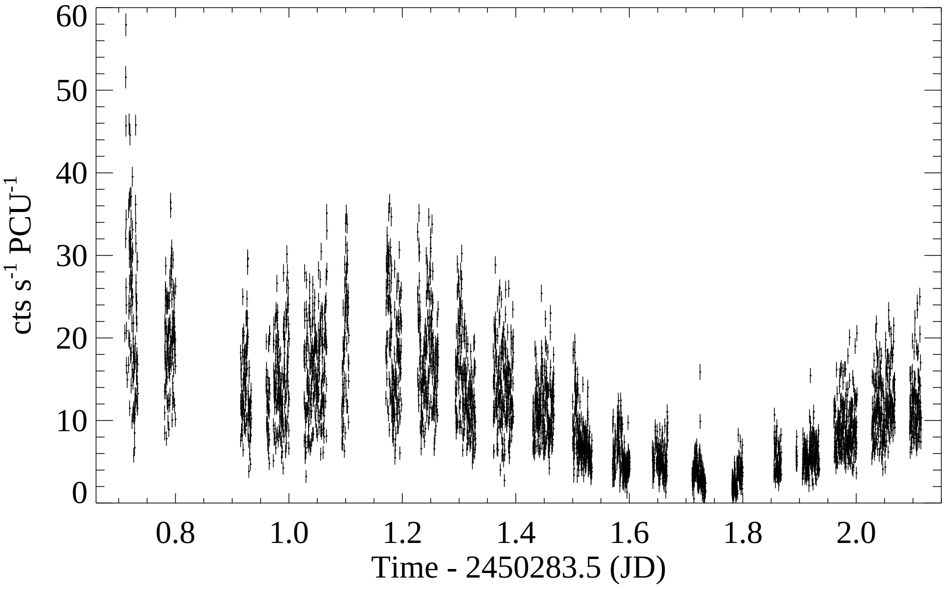

Figure 7.18: PCA light curve during the observation of GX 1+4.

7.2.9 GX 1+4

The ~120 s pulsar GX 1+4, along with its M6 III companion star V2116 Oph, is one of the five known accreting X-ray pulsars in LMXB systems. The PCA light curve of the 1996 July 19–20 *RXTE* observation is given in Fig. 7.18. I fit the spectrum (see Fig. 7.19) with a PLCUT continuum, an Fe-K line, and interstellar absorption. The spectrum does show a pattern of residuals near ~30 keV, although these are very poorly fit by an absorption feature. My analysis rules out the existence of broad CRSFs out to ~50–60 keV. However, a narrow line is permitted by the data above ~20 keV.

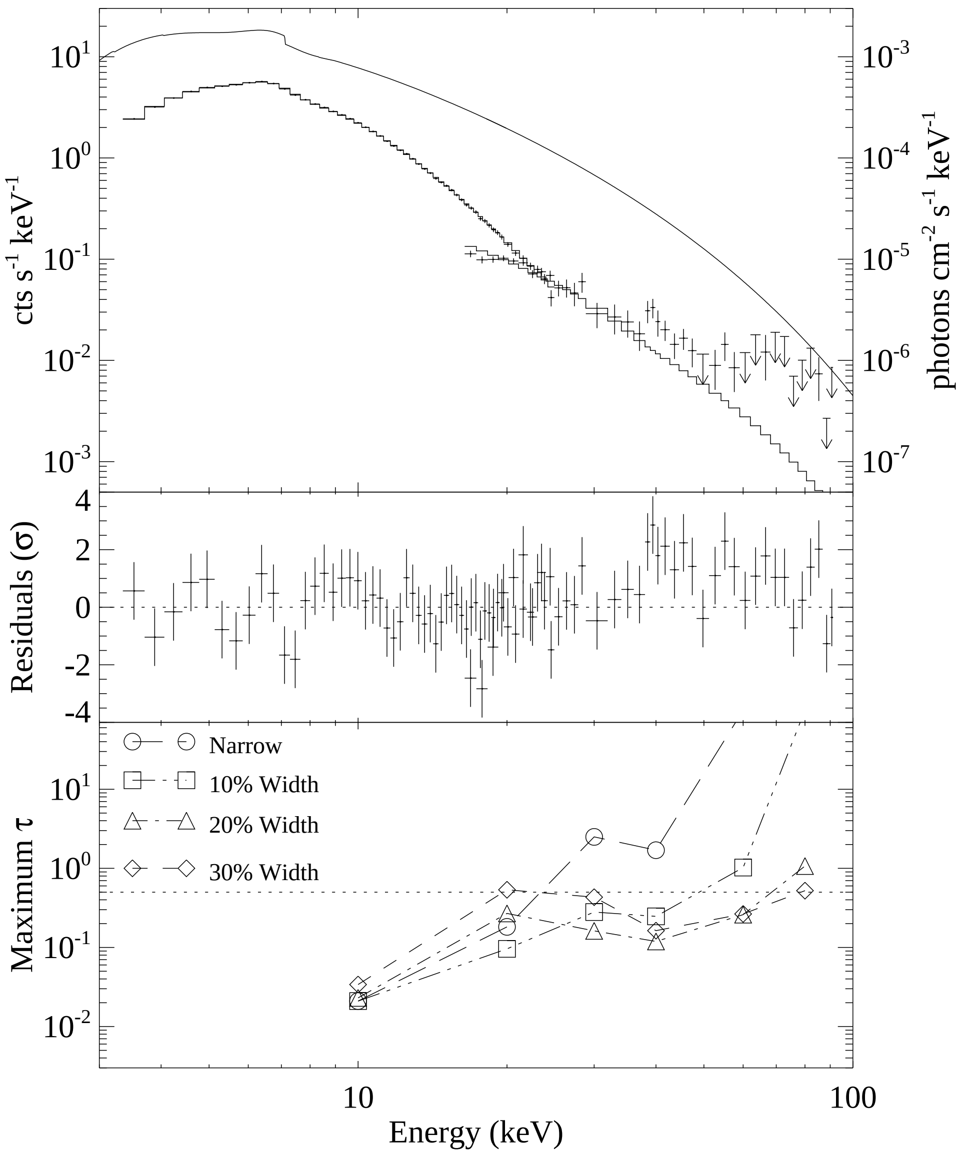

Figure 7.19: Top: Counts spectrum of GX 1+4 (crosses), best fit model (histograms, see text), and inferred photon spectrum (continuous line). Middle: Residuals to the fit in units of σ. Bottom: Upper limits on CRSF depths τ_c as a function of energy E_c and either fractional width (σ_c/E_c) or a narrow (0.75 keV) feature.

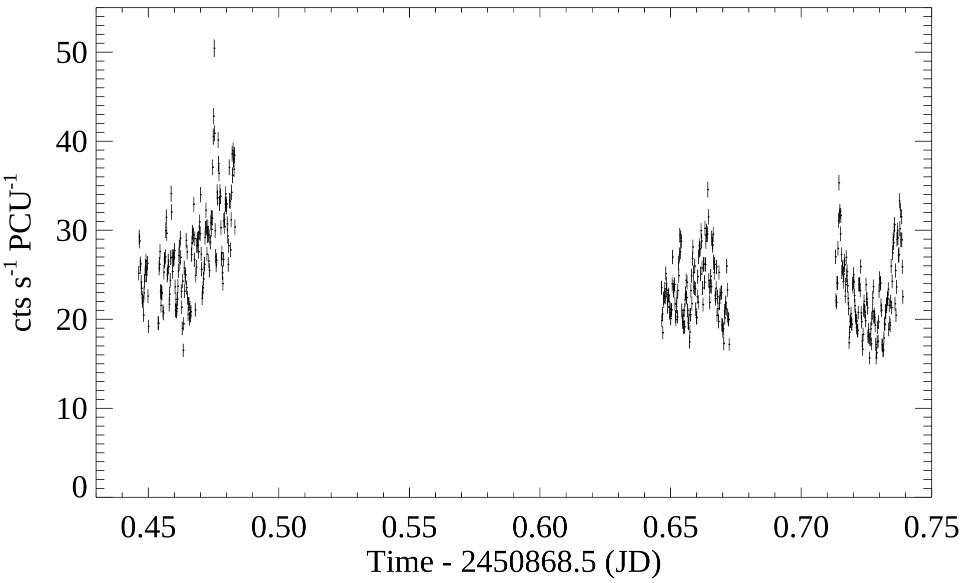

Figure 7.20: PCA light curve during the observation of XTE J1858+034.

7.2.10 XTE J1858+034

The transient source XTE J1858+034 was discovered with the *RXTE* (Remillard et al. 1998), and has a 221 s pulsation period (Takeshima et al. 1998). The companion star is currently unidentified. I have analyzed data from 3 pointings taken on 1998 February 24, with the PCA light curve is given in Fig. 7.20. I fit the spectrum (see Fig. 7.21) with an FDCO continuum, broad Fe-K line, and interstellar absorption. I can only exclude the presence of a CRSF below $\sim$20 keV.

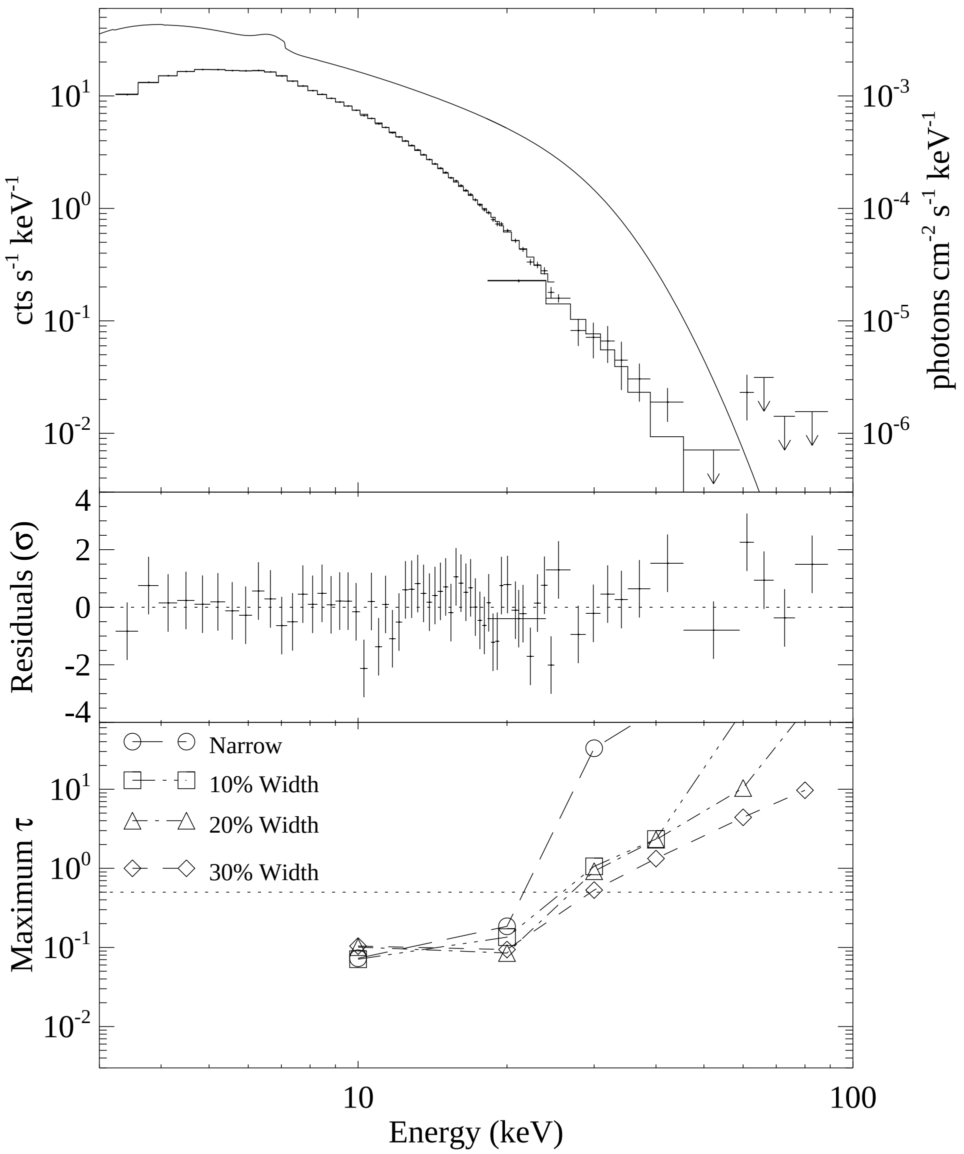

Figure 7.21: Top: Counts spectrum of XTE J1858+034 (crosses), best fit model (histograms, see text), and inferred photon spectrum (continuous line). Middle: Residuals to the fit in units of σ. Bottom: Upper limits on CRSF depths τ_c as a function of energy E_c and either fractional width (σ_c/E_c) or a narrow (0.75 keV) feature.

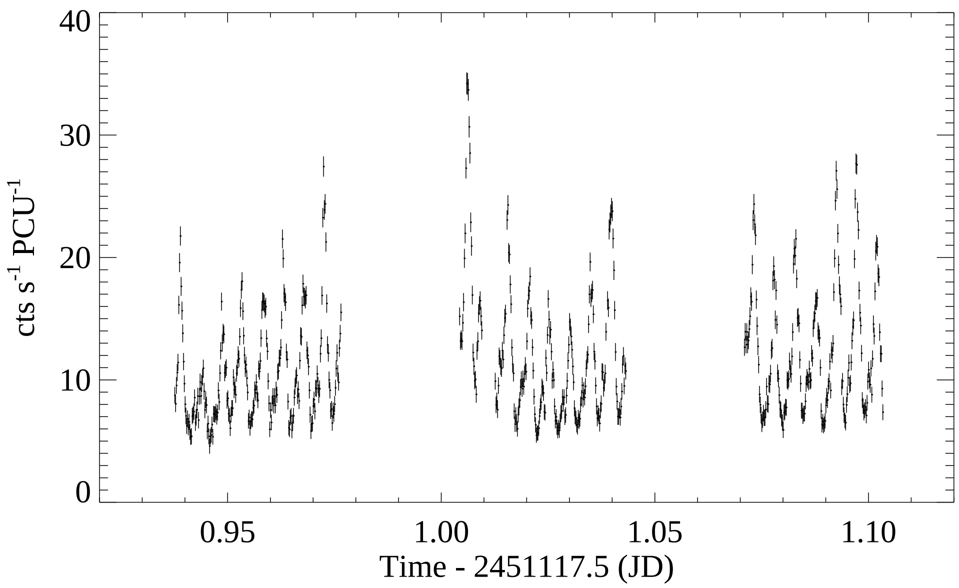

Figure 7.22: The PCA light curve during the observation of EXO 1722−363. The ∼414 s pulsations are clearly visible.

7.2.11 EXO 1722−363

The transient source EXO 1722−363 has a ∼414 s pulse period and unknown companion (Tawara et al. 1989). The source was observed by the *RXTE* on 1998 October 31, and the PCA light curve is given in Fig. 7.22. I fit the spectrum (see Fig. 7.23) with a PLCUT continuum, Fe-K line, and interstellar absorption. Due to the statistics of the observation I can rule out the two broadest CRSFs up to ∼30 keV, and the narrower features up to ∼20 keV.

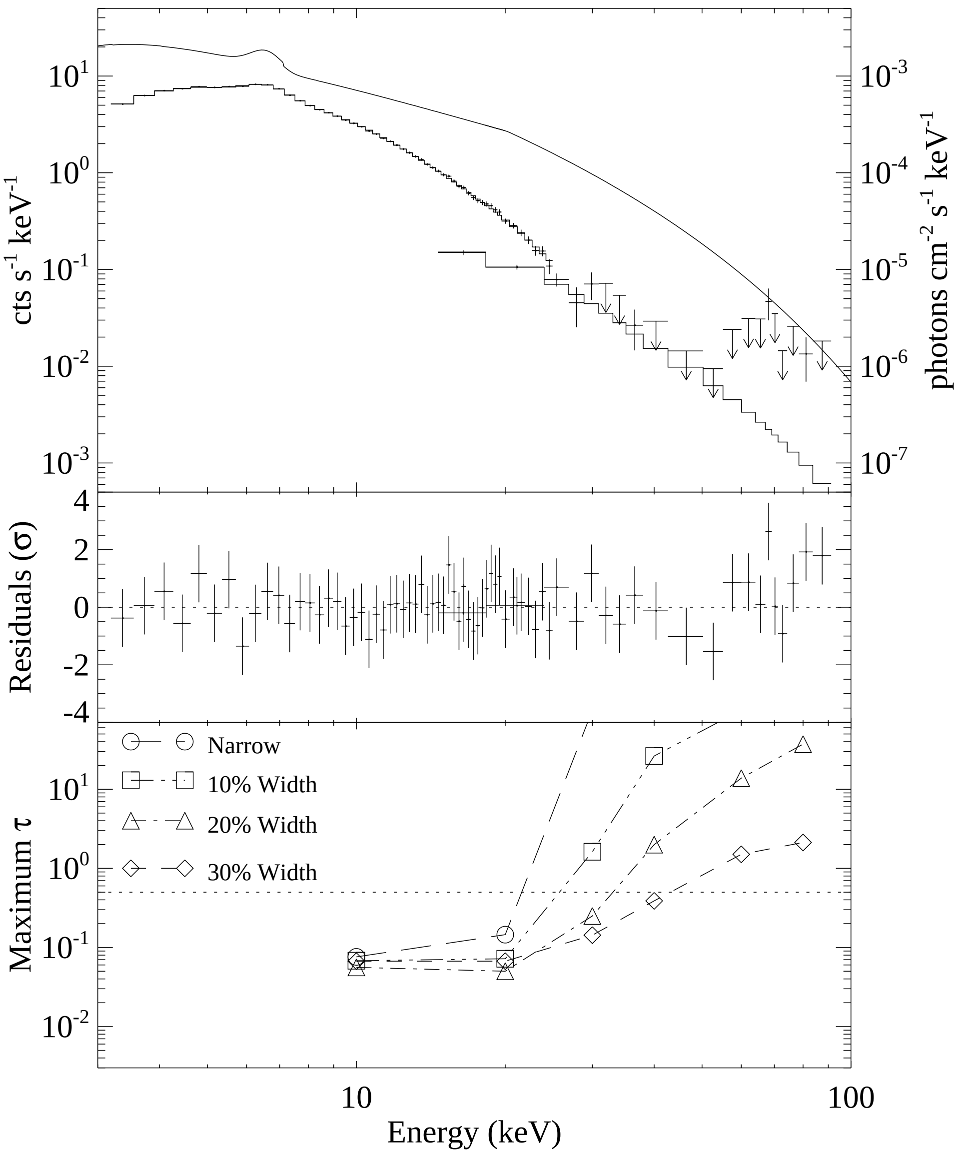

Figure 7.23: Top: Counts spectrum of EXO 1722−363 (crosses), best fit model (histograms, see text), and inferred photon spectrum (continuous line). Middle: Residuals to the fit in units of σ. Bottom: Upper limits on CRSF depths τ_c as a function of energy E_c and either fractional width (σ_c/E_c) or a narrow (0.75 keV) feature.

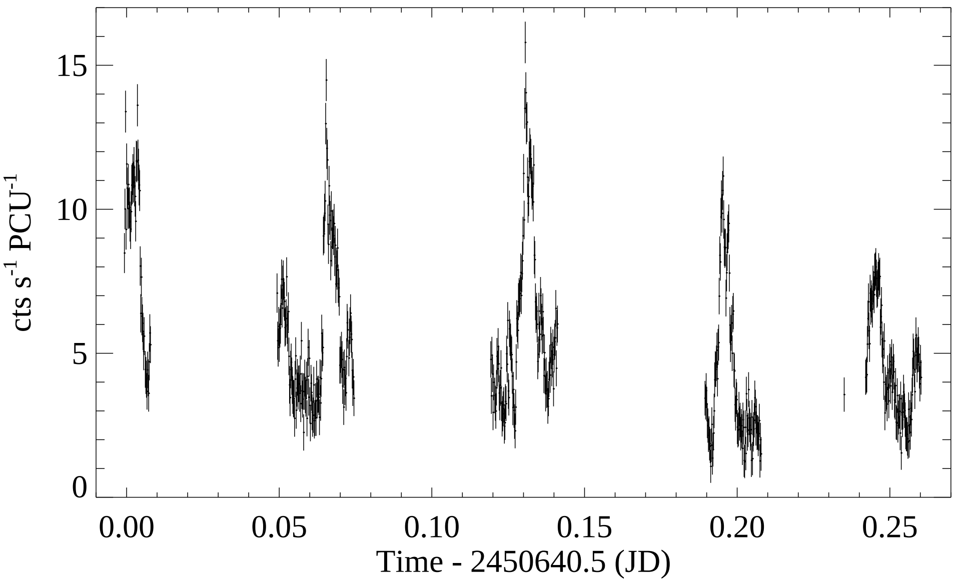

Figure 7.24: PCA light curve during the observation of RX J0146.9+6121. The pulsations of the source can be clearly seen.

7.2.12 RX J0146.9+6121

At 1413 s, the transient *ROSAT* source RX J0146.9+6121 has one of the longest known rotation periods of any pulsar. The source has been identified as a companion to the B5 IIIe star LS I+61°235 (Hellier 1994). The PCA light curve of the 1997 July 11 *RXTE* observation is given in Fig. 7.24. I fit the spectrum (see Fig. 7.25) with a PLCUT continuum and interstellar absorption. Due to the low luminosity and soft continuum I cannot exclude the existence of a CRSF from this spectrum.

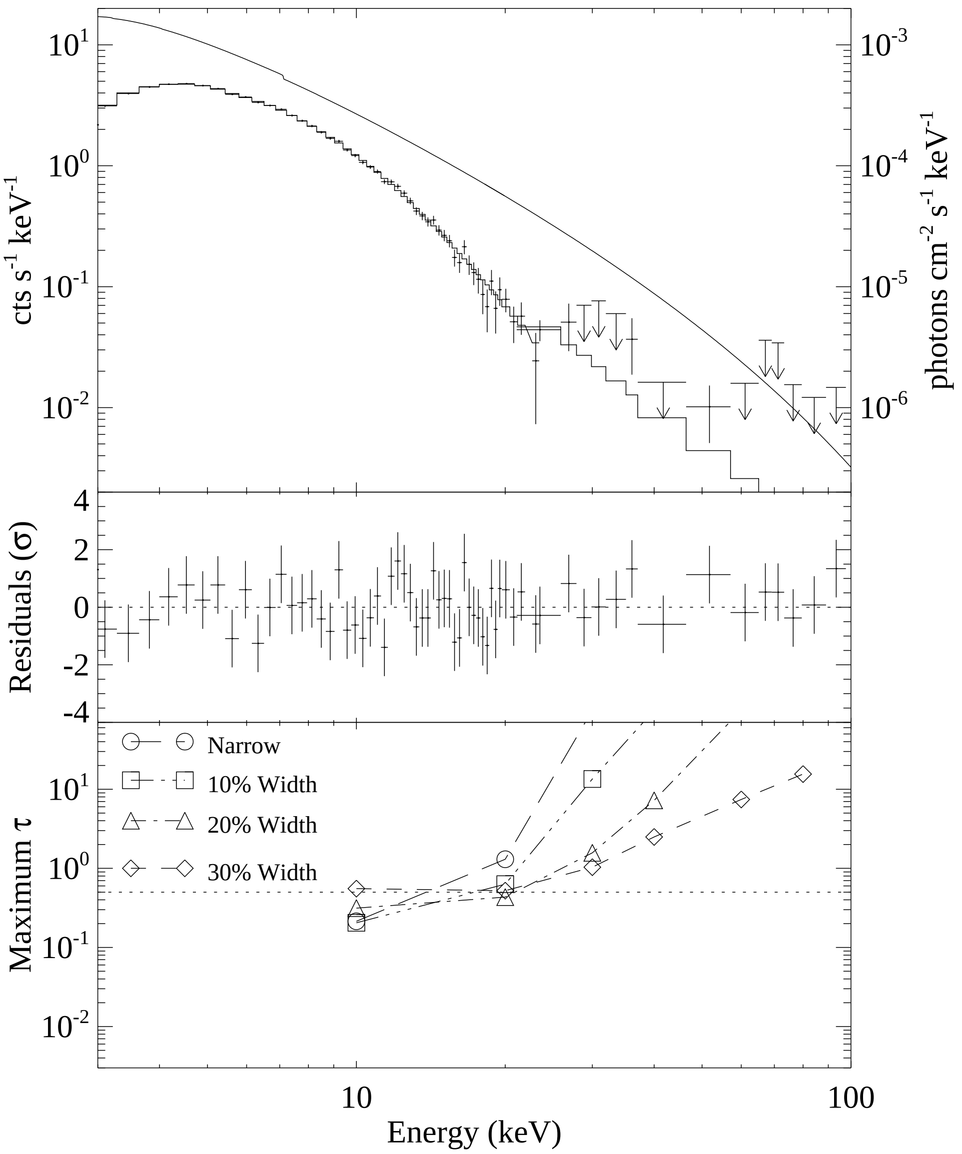

Figure 7.25: Top: Counts spectrum of RX J0146.9+6121 (crosses), best fit model (histograms, see text), and inferred photon spectrum (continuous line). Middle: Residuals to the fit in units of σ. Bottom: Upper limits on CRSF depths τ_c as a function of energy E_c and either fractional width (σ_c/E_c) or a narrow (0.75 keV) feature.

7.3 Tables of Upper Limits

The following 4 tables summarize the upper limits on CRSF depth τ_c, as a function of width σ_c and E_c, plotted in the previous pages. Values above the τ_c=0.5 fiducial, and therefore not firm limits, are shown in *italics*.

Table 7.2: Upper Limits on Optical Depths for Narrow CRSFs

	Optical Depth (Narrow)					
Source	10 keV	20 keV	30 keV	40 keV	60 keV	80 keV
2S 1553−542	0.060	*3.610*	*> 50*	*> 50*	*> 50*	*> 50*
2S 1417−624	0.069	0.047	0.173	0.276	*2.550*	*> 50*
GS 1843+00	0.047	0.071	0.180	0.269	*1.322*	*> 50*
OAO 1657−415	0.239	0.130	*34.70*	*> 50*	*> 50*	*> 50*
EXO 2030+375	0.042	0.207	0.253	*0.612*	*31.10*	*> 50*
GS 1843−024	0.022	0.110	0.301	0.230	*1.602*	*> 50*
GRO J2058+42	0.115	0.340	*> 50*	*> 50*	*> 50*	*> 50*
Sct X−1	0.123	0.170	*> 50*	*> 50*	*> 50*	*> 50*
GX 1+4	0.021	0.182	*2.497*	*1.696*	*> 50*	*> 50*
XTE J1858+034	0.073	0.185	*33.00*	*> 50*	*> 50*	*> 50*
EXO 1722−363	0.076	0.145	*> 50*	*> 50*	*> 50*	*> 50*
RX J0146.9+6121	0.214	*1.303*	*> 50*	*> 50*	*> 50*	*> 50*

Table 7.3: Upper Limits on Optical Depths for $\sigma_c = 0.1E_c$ CRSFs

	Optical Depth					
Source	10 keV	20 keV	30 keV	40 keV	60 keV	80 keV
2S 1553−542	0.065	*0.741*	*30.78*	*> 50*	*> 50*	*> 50*
2S 1417−624	0.061	0.035	0.057	0.040	0.248	0.498
GS 1843+00	0.040	0.051	0.062	0.033	0.105	*1.421*
OAO 1657−415	0.251	0.053	*0.854*	*1.340*	*3.021*	*> 50*
EXO 2030+375	0.043	0.144	0.053	0.116	0.691	*1.873*
GS 1843−024	0.019	0.088	0.106	0.051	0.183	0.484
GRO J2058+42	0.117	0.231	*1.536*	*0.944*	*15.14*	*> 50*
Sct X−1	0.101	0.068	*1.976*	*> 50*	*> 50*	*> 50*
GX 1+4	0.021	0.096	0.280	0.247	*1.024*	*> 50*
XTE J1858+034	0.071	0.135	*1.060*	*2.343*	*> 50*	*> 50*
EXO 1722−363	0.068	0.072	*1.622*	*26.30*	*> 50*	*> 50*
RX J0146.9+6121	0.205	*0.631*	*13.48*	*> 50*	*> 50*	*> 50*

Table 7.4: Upper Limits on Optical Depths for $\sigma_c = 0.2E_c$ CRSFs

Source	Optical Depth					
	10 keV	20 keV	30 keV	40 keV	60 keV	80 keV
2S 1553−542	0.111	0.305	*2.502*	*12.35*	*> 50*	*> 50*
2S 1417−624	0.030	0.032	0.086	0.036	0.094	0.266
GS 1843+00	0.021	0.035	0.112	0.031	0.041	0.312
OAO 1657−415	0.335	0.037	0.233	*0.774*	*2.001*	*4.310*
EXO 2030+375	0.112	0.220	0.049	0.076	0.486	*1.202*
GS 1843−024	0.411	0.092	0.199	0.051	0.073	0.173
GRO J2058+42	0.136	0.193	*0.601*	*0.753*	*1.451*	*5.741*
Sct X−1	0.134	0.062	0.256	*2.605*	*> 50*	*> 50*
GX 1+4	0.023	0.269	0.162	0.119	0.260	*1.070*
XTE J1858+034	0.101	0.085	*0.920*	*2.306*	*10.38*	*> 50*
EXO 1722−363	0.056	0.050	0.250	*1.994*	*13.80*	*37.15*
RX J0146.9+6121	0.314	0.433	*1.572*	*7.240*	*> 50*	*> 50*

Table 7.5: Upper Limits on Optical Depths for $\sigma_c = 0.3E_c$ CRSFs

Source	Optical Depth					
	10 keV	20 keV	30 keV	40 keV	60 keV	80 keV
2S 1553−542	0.198	0.206	*0.821*	*1.841*	*5.973*	*12.61*
2S 1417−624	0.018	0.046	0.099	0.077	0.091	0.186
GS 1843+00	0.014	0.047	0.205	0.072	0.040	0.143
OAO 1657−415	*0.611*	0.055	0.127	*1.010*	*0.801*	*2.953*
EXO 2030+375	0.109	0.339	0.087	0.091	0.336	*1.051*
GS 1843−024	0.012	0.132	0.230	0.207	0.080	0.128
GRO J2058+42	0.123	0.251	0.471	*0.760*	*1.082*	*2.069*
Sct X−1	0.198	0.083	0.155	*0.509*	*3.151*	*7.032*
GX 1+4	0.034	*0.536*	0.432	0.163	0.265	*0.522*
XTE J1858+034	0.104	0.094	*0.531*	*1.331*	*4.421*	*9.704*
EXO 1722−363	0.067	0.067	0.143	0.388	*1.504*	*2.125*
RX J0146.9+6121	*0.554*	*0.522*	*1.035*	*2.492*	*7.423*	*15.55*

7.4 Summary

As can be seen from the previous pages of figures, the current generation of hard X-ray instruments search a limited phase space for CRSFs. In particular narrow lines, especially those at higher energies, are difficult to detect. Unfortunately, the detection of lines at higher energies requires long integrations with large area detectors that have a low internal background. Unfortunately it is not currently feasible to put such a satellite into orbit.

The limited phase space does not imply, however, that current studies are missing large numbers of CRSFs. If accreting X-ray pulsars have a distribution of magnetic fields that is similar to that of radio pulsars, the majority of CRSFs should lie within the *RXTE* and *Beppo*SAX energy ranges (see Fig. 1.3). Also, the observed proportionality between CRSF energy E_c and width σ_c (see Fig. 3.16) indicates that CRSFs are naturally quite broad. Despite the difficulty in identifying CRSFs at high energies, the results of Monte Carlo simulations (see §3.2.1) show that the observed correlation is not due purely to this effect. Therefore the CRSFs formation process may preferentially produce broad lines, and it is unlikely that current studies are missing large numbers of narrow features.

The sources 2S 1417−62, GS 1843+00, and GS 1843−024, have highly significant detections in the *RXTE*. These pulsars are excellent candidates for a pulse phase resolved spectral analysis. A comparison of this analysis to those sources that do exhibit CRSFs may help determine why CRSFs are seen in some pulsar spectra and not others.

Chapter 8

Conclusions and Outlook

8.1 Conclusions

In this dissertation I have conducted a study of the magnetic polar regions of accreting X-ray pulsars. With their deep gravitational wells and high magnetic fields, the environments provide a unique laboratory for the study of matter in conditions unobtainable on Earth. I have shown that by studying both the spectra and light curves of many different sources, we can disentangle the geography of the neutron star and the geometry of the X-ray emitting region, and even begin to investigate the dominant processes of the emission itself. Eventually this might lead to an understanding of the physics of hot, ionized plasmas in 10^{12} G magnetic fields.

I have concentrated on the study of cyclotron resonant scattering features, and shown that they provide a very powerful probe of the emission regions of accreting X-ray pulsars. The B-fields of pulsars can be measured directly using CRSFs, and of the 22 accreting X-ray pulsars discussed in this work about half exhibited CRSFs in their hard X-ray spectra. Not only are CRSFs the *only* direct measure neutron star B-fields, but as shown by Araya-Góchez & Harding (2000) their profiles and harmonic content are sensitive to the physical conditions in the scattering region. Using these features I have discussed how the strong magnetic field influences the formation of the X-ray continua. I have also outlined a method of using CRSF line profiles in combination with FLCs to constrain the geometry of the emission region and relative locations of the polar caps on the neutron star.

As discussed in §3.2.3, there is a correlation between the spectral break energy $E_{\rm cut}$ and the strength of the B-field as measured by the CRSF energy $E_{\rm c}$. This confirms the $E_{\rm cut} \propto E_{\rm c}^{0.7}$ relation observed previously by Makishima et al. (1999), which was obtained by plotting CRSF energies from *Ginga* and other instruments, derived with a variety of continuum models, against the PLCUT cut-off energy in fits without a CRSF and using sometimes non-contemporaneous *Ginga* observations. The results of my analysis, which applied a consistent set of models to a consistent set of spectra, show that this relationship is more complex. In particular there seems to be evidence for a change in slope above $\sim$35 keV. So while the observed spectral break in these sources is indeed a magnetic feature, the effect of the B-field on the continuum is not a simple power-law. A similar, but physically distinct, possibility is that the magnetic field and spectral break are related through an intermediate quantity such as the electron temperature $kT_{\rm e}$. In this case the intermediate parameter is linearly proportional to the magnetic field up to a saturation point, and this is the cause of the curvature in the observed correlation.

This dependence of the cutoff energy on the magnetic field is not, however, a complete picture. In §4.6 I discussed the fact that as a function of pulsar rotation phase there is no correlation between the cutoff energy and the B-field strength in the scattering region in the three sources analyzed. This implies that the spectral cutoff is due to an average or bulk B-field in the polar regions, and the shape of the X-ray continuum is determined by conditions deep within the accretion structure. The variations seen in the cutoff energy with rotation phase, since they are not correlated with the cyclotron energy $E_{\rm c}$, are then possibly due to local, non magnetic effects in the emission region.

As discussed in detail in §3.2.2, the observed depths of the cyclotron features are correlated with the fractional width of the line (the width σ_c scaled by the resonance energy E_c). This correlation is such that fractionally broader lines are observed to be deeper. This is the opposite of what one would expect based upon the relativistic cyclotron scattering cross sections alone, where wider lines are expected to be shallower (see Fig 1.6). This implies that effects such as photon spawning, relativistic non-isotropic angular redistribution of photons, and the geometry of the scattering plasma are important. This observed correlation is also a feature that future modeling efforts will need to reproduce.

Furthermore, since Monte Carlo simulations indicate that a wide variety of line shapes are possible (Araya & Harding 1999; Araya-Góchez & Harding 2000; Kretschmar et al. 2000), the existence of a correlation at all is surprising. The predicted line shapes are functions of physical parameters such as electron temperature kT_e and emission geometry. Therefore the existence of a correlation suggests that the polar regions of different pulsars, and at different mass transfer rates, are similar. In particular this indicates that the number of different steady state configurations of accretion structures may be limited. Or alternatively, the range of accretion structure parameters that allow for the observation of a CRSF may be small.

The other correlation among the CRSF fit parameters is between the line energies and widths (see Fig 3.15). If the width is due primarily to Doppler broadening (Mészáros & Nagel 1985a; Mészáros 1992), then the CRSF width should go as:

$$\sigma_c \propto E_c (kT_e)^{1/2} \left|\cos(\theta)\right| \tag{8.1}$$

where $\cos(\theta)$ is the viewing angle with respect to the magnetic field. Since a correlation between energy and width is observed, this implies two things. First, that the electron temperatures in the scattering regions in systems where we see CRSF are virtually the same despite several orders of magnitude difference in X-ray luminosities ($10^{34} - 10^{37}\,\mathrm{ergs\,s^{-1}}$). Second, that there is a selection bias towards certain viewing angles θ in finding systems that exhibit CRSFs. Indeed, of the 10 sources where the *RXTE* observes CRSFs, 6 of them are in systems where the binary plane is viewed nearly edge on (see Table 3.1).

Using a toy model, Wang (1981) and Wang & Robnik (1982) predict that the angle Θ_m between the spin and magnetic dipole axis should change in response to accretion. This is due to a net torque on the dipole moment resulting from the accreted angular momentum. This torque will act to align ($\Theta_{\rm m} = 0$) the two axes during episodes of spin-down, and make them perpendicular ($\Theta_{\rm m} = \pi/2$) during spin-up. The characteristic time scale for this alignment was estimated to be $t \sim 10^4$ yr, which is similar to the timescale for a neutron star to come into spin equilibrium with an accretion disk (see §1.5.2) and much shorter than the ages of these pulsars. The authors suggest that most observed accreting X-ray pulsars began their lives as rapidly spinning ($P_{\rm spin} \lesssim 1$ s) neutron stars, and then experienced significant spin-down due to a low initial mass transfer and the propeller effect (Illarionov & Sunyaev 1975). This is reasonable given that the range of spin periods for radio pulsars is $10^{-3} - 10^{1}$ s, while for accreting pulsars it is $10^{-3} - 10^{5}$ s. In this picture there is expected to be a bias towards small values of $\Theta_{\rm m}$ provided that most neutron stars have not experienced significant spin-up torques during their lifetimes. This last assumption is probably not a safe one for most accreting X-ray pulsars; however, this model does underline the fact that accretion can affect the orientation of the dipole moment of the neutron star.

If this evolutionary scenario, or indeed any model that seeks to align the dipole and spin axes, is correct and $\Theta_{\rm m}$ is small for most accreting pulsars, then the bias toward edge on systems can be understood as a bias toward viewing neutron stars perpendicular to their magnetic dipole moment. If, in general, the two axes are nearly aligned then the reason we do not see CRSFs in more sources might simply be due to the distribution of inclinations of the systems. I note, however, that for any given pulsar with an unknown inclination angle, there is always the possibility that the cyclotron energy is out of the effective *RXTE* detection range. The bias towards finding CRSFs in systems viewed nearly edge on also implies that should an inclination angle ever be determined for the sources 4U 0115+63, XTE J1496+274, and A0535+63, it is likely to be large.

As mentioned in Chapter 3, there are three counter examples to this. Both 4U 0352+309 and 4U 1626−67 exhibit CRSFs and yet both binary systems are viewed nearly face on (Delgado-Martí et al. 2001; Chakrabarty 1998). While it is possible that these pulsars have been spun-up such that they are orthogonal rotators, the single peaked nature of their pulsation FLCs make this possibility seem unlikely. This would also require that that 4U 0352+309, which already has one of the longest spin periods known, be spun-down to a very long period to be spun back up to 837 s. The third counter example is the the eclipsing X-ray pulsar OAO 1657−415, where so far a CRSF has eluded detection. When fit with the PLCUT continuum, the CRSF energy implied from the cutoff energy is ∼26 keV. A feature at this energy with a depth greater than $E_c \sim 0.2$ can be excluded at the 3-σ level for CRSF widths broader than $0.2E_c$ (see §3.2.3 and §7.2.4).

8.2 Future Work

So far only a small subset of observations of accreting X-ray pulsars contained in the *RXTE* database have been analyzed in detail. Also, with every transient source that goes into outburst there is the possibility of discovering a new CRSF, or new higher harmonics in a source with a known CRSF. The continued efforts of the UC San Diego/University of Tübingen collaboration to obtain long (∼100 ks) and nearly continuous observations during outbursts of transient sources, along with making similar long observations of persistent sources, means that there exists a wealth of data well suited for pulse phase resolved analyses. Once that is finished there are still various timing, orbital phase resolved, and other results waiting to be obtained. The *RXTE* database is not alone, nor is it the end. Just as the *RXTE* and *Beppo*SAX satellites have extended our knowledge of accreting X-ray pulsars beyond the pioneering work of the *Ginga*, future missions such as *INTEGRAL* will extend our understanding beyond *RXTE* and *Beppo*SAX.

While pulse phase resolved spectroscopy is important for pulsars with known CRSFs, these techniques should not be limited to these sources alone. As noted previously, CRSFs can be quite variable with pulsation phase, and therefore there might be features in phase resolved data that are not obvious in a phase averaged spectrum. An example of this is Vela X−1, whose ∼24 keV fundamental feature was considered controversial (e.g. Orlandini et al. 1998) before a detailed phase resolved analysis was done (Kreykenbohm et al. 2002). Also, detailed studies of the FLCs of these pulsars will provide information about the emission geometry and various angles in systems without CRSFs. This knowledge, in turn, could lead to a better understanding of why cyclotron features are not seen in these sources. Is it simply a matter of the inclination angle of the system? Or are there other stable accretion structures that are unfavorable to CRSF production?

An important step in the interpretation of pulse phase resolved spectra is to make direct comparisons of the data with Monte Carlo simulations. The fundamental CRSF in 4U 0115+63 is only poorly fit with the simple models discussed in §2.2.5 (Heindl et al. 1999), and as the spectral resolution of satellite-borne detectors improves the flaws in these models will become more and more apparent. To this end our collaboration has begun a project using the Monte Carlo codes of Araya & Harding (1999) to generate models that can be used with the `XSPEC` X-ray spectral fitting package. To make the comparisons with observations more realistic, this code has been modified such that the assumed initial spectrum is similar to the standard pulsar continuum (Kretschmar et al. 2000). In this way quantitative statements based on fitting the data with simulations can be made, rather than just qualitative statements about line shapes and harmonic content. Once finished, these models will be released to the community.

Simply fitting pulse phase resolved spectra alone, however, is not enough to completely disentangle and understand the emission of accreting X-ray pulsars. A separate technique, the analysis of pulsar FLCs, can be used to help verify and constrain the results of fits to the Monte Carlo simulations. FLCs are already being used successfully to infer information about the emission beam geometry and the relative locations of the neutron star polar regions (e.g. Kraus et al. 1996; Scott, Leahy & Wilson 2000; Blum & Kraus 2000). In Chapter 4 I proposed a method using this combination to determine the emission geometry and geography of pulsars. The FLCs as a function of energy can then also be modeled, properly taking into account the effects of light bending, to give another set of constraints on the emission region (e.g. Kraus et al. 1995). The results of this and the spectroscopic method above should agree, with the simultaneous solution hopefully unique. To conduct this type of analysis our collaboration has recently obtained the code used by Kraus et al. (1995) to fit the FLCs of Her X−1 (Blum & Kraus 2000) and Cen X−3 (Kraus et al. 1996). These two different approaches used simultaneously will undoubtedly prove to be a very powerful diagnostic tool.

Using phase resolved observations of CRSFs compared with the Monte Carlo simulations, one can hope to unambiguously determine the viewing angles to the polar caps, along with estimates of the shape of the emission region and the temperature of the scattering electrons. Analysis of pulsar FLCs can potentially provide an independent test of the spectroscopic results, or at the least provide another set of constraints to determine a unique solution. With the marriage of timing and spectral information it should be possible to to fully model the pulsar emission geometry and geography. The ultimate goal, once good theoretical models of the X-ray spectra of accreting pulsars become available, will be to do simultaneous fits of both energy and phase. At this point the pulsar emission regions, which are truly a laboratory unlike any on Earth, will be open for use.

Appendix A

IAU Circulars

A.1 7126

4U 0115+63

W. A. Heindl and W. Coburn, University of California, San Diego, report: "The current outburst of the 3.6 s X-ray pulsar 4U 0115+63 (IAUC 7116) has been monitored with daily RXTE pointings since Mar. 3. The flux (2–10 keV) has increased from 5.6×10^{-9} (Mar. 3) to $1.1 \times 10^{-8}\,\mathrm{ergs\,cm^{-2}\,s^{-1}}$ on Mar. 12. Fitting the Mar. 3 joint PCA/HEXTE spectrum reveals cyclotron absorption features at about 14 and 21 keV. Because the phase-averaged spectra are complex due to pulse-phase spectral variability, these line energies are not well-determined. A cyclotron absorption feature was first seen in this source with HEAO 1 (Wheaton et al. 1979, Nature 282, 240). In addition to the short monitoring observations, we have made two long pointings on Mar. 7.16–7.45 and 11.89–12.32 UT. The second of these spanned periastron passage (according to the ephemeris of Bildsten et al. 1997, Ap.J. Suppl. 113, 367) at Mar. 11.95. During this observation, the source exhibited large oscillations with a timescale of about 500 s. The oscillation rms deviations were about 30 percent of the mean flux. Such slow oscillations are not consistent with the beat-frequency QPO model whose expected frequencies are of order 5 Hz. The oscillations may have been present during 2500 s of the Mar. 7 observation, but at greatly reduced amplitude. Additional observations are encouraged. The RXTE/ASM real-time light curve is available at http://heasarc.gsfc.nasa.gov/xte_weather/."

A.2 7487

4U 0115+63

W. Coburn, R. Rothschild, and W. A. Heindl, University of California at San Diego, report: "An outburst of the Be-transient X-ray pulsar 4U 0115+63 has been detected by the RXTE/ASM. The daily averaged ASM countrate began to increase on Aug. 27, which coincided with periastron of the source. In the first four days, the ASM countrate rose to > 7 counts/s. This is a faster rise than the 1999 Mar. outburst (IAUC 7116), which began several days after periastron, and a similar countrate was achieved 9 days after that. On 2000 Sept. 1.06 UT, the RXTE made a 1000 s pointed observation. Strong pulsations were detected at the 3.61 s pulse period, confirming that it is the pulsar currently in outburst. The 2–100 keV flux was $(6.5 \pm 0.3) \times 10^{-9}$ ergs cm^{-2} s^{-1}, and at a distance of 3500 pc had an X-ray luminosity of 9.6×10^{36} ergs s^{-1}. Preliminary fitting of the joint PCA/HEXTE spectrum reveals two cyclotron absorption features at about 15 and 23 keV, similar to what was observed the previous outburst (IAUC 7126). Because phase-averaged spectra are complex due to pulse-phase variability, these line energies are not well determined. Additional observations are encouraged. The RXTE/ASM real-time light curve is available at http://heasarc.gsfc.nasa.gov/xte_weather/."

Appendix B

Useful Information

B.1 Acronyms and Abbreviations

AXP:	Anomalous X-ray Pulsar
***ANS*:**	*Astronomische Nederlandse Satelliet*
***ASCA*:**	*Advanced Satellite for Cosmology and Astrophysics*
ASM:	All Sky Monitor
AXAF:	*Advanced X-ray Astrophysics Facility*
BATSE:	Burst And Transient Source Experiment
***Beppo*SAX:**	*Beppo Satellite per Astronomia X*
***BBXRT*:**	*Broad Band X-ray Telescope*
CASS:	Center for Astrophysics and Space Sciences
***CGRO*:**	*Compton Gamma-Ray Observatory*
CRSF:	Cyclotron Resonance Scattering Feature
CYCLABS:	Cyclotron Absorption
***CXO*:**	*Chandra X-ray Observatory*
DOF:	Degrees of Freedom
EA:	Event Analyzer
EDS:	Experiment Data System
ESA:	European Space Agency
***EXOSAT*:**	*European X-ray Observatory Satellite*
FDCO:	Fermi-Dirac cutoff Power-Law

FLC:	Folded Light Curve
FOV:	Field of View
FWHM:	Full Width at Half Maximum
FWZM:	Full Width at Zero Maximum
GABS:	Gaussian Absorption
GOF:	Guest Observer Facility
GSFC:	Goddard Space Flight Center
***HEAO*:**	*High Energy Astrophysical Observatory*
HEASARC:	High Energy Astrophysics Science Archive Research Center
***HESSI*:**	*High Energy Solar Spectroscopic Imager*
***HETE*:**	*High Energy Transient Explorer*
HEXTE:	High Energy X-ray Timing Experiment
HMXB:	High-Mass X-ray Binary
IAAT:	Institute for Astronomy and Astrophysics
IDL:	Interactive Data Language
***INTEGRAL*:**	*International Gamma-Ray Astrophysics Laboratory*
LAC:	Large Area Counter
LGM:	Little Green Men
LMXB:	Low-Mass X-ray Binary
LMC:	Large Magellanic Cloud
MDR:	Magnetic Dipole Radiation
MHD:	Magnetohydrodynamic
MIT:	Massachusetts Institute of Technology
MJD:	Modified Julian Day, MJD is Julian Day JD$-$2400000.5
NASA:	National Aeronautics and Space Administration
NPEX:	Negative and Positive power-law Exponential
OAO:	*Orbiting Astronomical Observatory*
OSO:	*Orbiting Solar Observatory*
PCA:	Proportional Counter Array
PCU:	Proportional Counter Unit
PHA:	Pulse Height Analyzer
PLCUT:	Power-Law with a High Energy Cutoff

PSPC:	Position-Sensitive Proportional Counter
QED:	Quantum Electrodynamic
QPO:	Quasi-Periodic Oscillation
***ROSAT*:**	*Röntgen Satellite*
***RXTE*:**	*Rossi X-ray Timing Explorer*
SAA:	South Atlantic Anomaly
SAS:	*Small Astronomy Satellite*
SG:	Supergiant
SGR:	Soft $\gamma-$ray Repeater
SMC:	Small Magellanic Cloud
SSC:	Scanning Shadow Camera
UCSD:	University of California, San Diego
UTC:	Universal Time Coordinated
***XMM*:**	*X-ray Multi-Mirror Mission*
XRB:	X-ray Binary
XTE:	*X-ray Timing Explorer* (see *RXTE*)

B.2 Constants and Conversions

Fine Structure Constant:	$\alpha = 7.3 \times 10^{-3}$
Speed of Light:	$c = 3.00 \times 10^{10}\,\mathrm{cm\,s^{-1}}$
Charge of an Electron:	$e = 4.80 \times 10^{-10}\,\mathrm{G\,cm^2}$
Gravitational Constant:	$G = 6.67 \times 10^{-8}\,\mathrm{gm^{-1}\,cm^3\,s^{-2}}$
Planck's Constant:	$\hbar = 1.05 \times 10^{-27}\,\mathrm{ergs\,s}$
	$= 6.58 \times 10^{-19}\,\mathrm{keV\,s}$
	$\hbar c = 1.973 \times 10^{-8}\,\mathrm{keV\,cm}$
Boltzman's Constant:	$k = 1.38 \times 10^{-16}\,\mathrm{ergs\,K^{-1}}$
	$= 8.61 \times 10^{-8}\,\mathrm{keV\,K^{-1}}$
Electron Mass:	$m_e = 9.11 \times 10^{-28}\,\mathrm{gm}$
	$= 511\,\mathrm{keV\,c^{-2}}$
Critical B-Field $[(m_e^2 c^3)/(\hbar e)]$:	$B_{\mathrm{QED}} = 4.4 \times 10^{13}\,\mathrm{G}$
Solar Mass:	$M_\odot = 1.99 \times 10^{33}\,\mathrm{gm}$
Solar Radius:	$R_\odot = 6.69 \times 10^{10}\,\mathrm{cm}$
Solar Luminosity	$L_\odot = 3.90 \times 10^{33}\,\mathrm{ergs\,s^{-1}}$
Neutron Star Mass ($1.4\,\mathrm{M_\odot}$):	$M_{\mathrm{ns}} = 2.8 \times 10^{33}\,\mathrm{gm}$
Neutron Star Radius ($10\,\mathrm{km}$):	$R_{\mathrm{ns}} = 1 \times 10^{6}\,\mathrm{cm}$
Earth Mass:	$M_\oplus = 5.68 \times 10^{27}\,\mathrm{gm}$
Earth Radius:	$R_\oplus = 6.37 \times 10^{8}\,\mathrm{cm}$

$$1\,\mathrm{Gauss} = 1\,\mathrm{gm^{1/2}\,cm^{-1/2}\,s^{-1}}$$

$$1\,\mathrm{keV} = 1.602 \times 10^{-9}\,\mathrm{ergs}$$

$$1\,\mathrm{kpc} = 3.09 \times 10^{21}\,\mathrm{cm}$$

$$1\,\mathrm{M_\odot\,yr^{-1}} = 6.31 \times 10^{25}\,\mathrm{gm\,s^{-1}}$$

Bibliography

Alpar, M. A., & Shaham, J., 1985, Nature, 316, 239

Angelini, L., White, N. E., Nagase, F., Kallman, T. R., Yoshida, A., Takeshima, T., Becker, C., & Paerels, F., 1995, ApJ, 449, L41

Anzer, U., & Boerner, G., 1980, A&A, 83, 133

Araya, R. A., & Harding, A. K., 1999, ApJ, 517, 334

Araya-Góchez, R. A., & Harding, A. K., 2000, ApJ, 544, 1067

Arnaud, K. A., 1996, in ASP Conf. Ser. 101: Astronomical Data Analysis Software and Systems V, ed. G. H. Jacoby, J. Barnes, Vol. 5, 17

Arnett, W. D., 1979, in Sources of Gravitational Radiation, ed. L. Smarr, (Cambridge/New York: Cambridge University Press), 311

Arnett, W. D., Schramm, D. N., & Truran, J. W., 1989, ApJ, 339, L25

Arons, J., 1993, ApJ, 408, 160

Arons, J., Burnard, D. J., Klein, R. I., McKee, C. F., Pudritz, R. E., & Lea, S. M., 1984, in High Energy Transients in Astrophysics, 215

Arons, J., & Lea, S. M., 1976, ApJ, 207, 914

Arons, J., & Lea, S. M., 1980, ApJ, 235, 1016

Avni, Y., & Bahcall, J. N., 1974, ApJ, 192, L139

Avni, Y., & Bahcall, J. N., 1975, ApJ, 197, 675

Baade, W., & Zwicky, F., 1934, Phys.Rev, 45, 138

Babu, G. J., & Feigelson, E. D., 1996, Astrostatistics: Interdisciplinary Statistics, (London: Chapman and Hall)

Barret, D., Olive, J. F., Boirin, L., Done, C., Skinner, G. K., & Grindlay, J. E., 2000, ApJ, 533, 329

Becker, R. H., Boldt, E. A., Holt, S. S., Pravdo, S. H., & Robinson-Saba, J., 1979, ApJ, 227, L21

Bendat, J. S., & Piersol, A. G., 2000, Random data: analyis and measurement procedures, (New York: Wiley), 3^{rd} edition

Bevington, P. R., 1969, Data reduction and error analysis for the physical sciences, (New York: McGraw-Hill)

Bhattacharya, D., 1995, in X-ray Binaries, ed. W. H. G. Lewin, J. van Paradijs, E. P. J. van den Weuvel, (Cambridge/New York: Cambridge University Press), 233

Bichenkov, E. I., & Shvetsov, G. A., 1997, Journal of Applied Mechanics and Technical Physics, 38, 578

Bildsten, L., Chakrabarty, D., Chiu, J., Finger, M. H., Koh, D. T., Nelson, R. W., Prince, T. A., Rubin, B. C., Scott, D. M., Stollberg, M., Vaughan, B. A., Wilson, C. A., & Wilson, R. B., et al., 1997, ApJS, 113, 367

Blum, S., & Kraus, U., 2000, ApJ, 529, 968

Bondi, H., & Hoyle, F., 1944, MNRAS, 104, 273

Buccheri, R., Bennett, K., Bignami, G. F., Bloemen, J. B. G. M., Boriakoff, V., Caraveo, P. A., Hermsen, W., Kanbach, G., Manchester, R. N., Masnou, J. L., Mayer-Hasselwander, H. A., Ozel, M. E., Paul, J. A., Sacco, B., Scarsi, L., & Strong, A. W., et al., 1983, A&A, 128, 245

Bulik, T., Mészáros, P., Woo, J. W., Hagase, F., & Makishima, K., 1992, ApJ, 395, 564

Bulik, T., Riffert, H., Mészáros, P., Makishima, K., Mihara, T., & Thomas, B., 1995, ApJ, 444, 405

Bulik, T. W., 1993, *Ph.D. thesis*, Pennsylvania State University, University Park, PA

Burderi, L., Di Salvo, T., Robba, N. R., La Barbera, A., & Guainazzi, M., 2000, ApJ, 530, 429

Burnard, D. J., Arons, J., & Klein, R., 1991, ApJ, 367, 575

Campana, S., Israel, G., & Stella, L., 1999, A&A, 352, L91

Campana, S., Israel, G. L., Stella, L., & Santangelo, A., 1998, IAU Circular, 7039, 2

Chadwick, J., 1932, Nature, 129, 312

Chakrabarty, D., 1996, *Ph.D. thesis*, California Insititute of Technology, Pasadena, CA

Chakrabarty, D., 1998, ApJ, 492, 342

Chakrabarty, D., Bildsten, L., Grunsfeld, J. M., Koh, D. T., Prince, T. A., Vaughan, B. A., Finger, M. H., Scott, D. M., & Wilson, R. B., et al., 1997, ApJ, 474, 414

Chakrabarty, D., Grunsfeld, J. M., Prince, T. A., Bildsten, L., Finger, M. H., Wilson, R. B., Fishman, G. J., Meegan, C. A., & Paciesas, W. S., et al., 1993, ApJ, 403, L33

Chakrabarty, D., & Morgan, E. H., 1998, Nature, 394, 346

Chatterjee, P., & Hernquist, L., 2000, ApJ, 543, 368

Chester, T. J., 1979, ApJ, 227, 569

Chitnis, V. R., Rao, A. R., Agrawal, P. C., & Manchanda, R. K., 1993, A&A, 268, 609

Clark, G. W., 2000, ApJ, 542, L131

Clark, G. W., Woo, J. W., Nagase, F., Makishima, K., & Sakao, T., 1990, ApJ, 353, 274

Coburn, W., 2001, *Ph.D. thesis*, University of California, San Diego, La Jolla, CA

Coburn, W., Heindl, W. A., Gruber, D. E., Rothschild, R. E., Staubert, R., Wilms, J., & Kreykenbohm, I., 2001, ApJ, 552, 738

Coburn, W., Heindl, W. A., Wilms, J., Gruber, D. E., Staubert, R., Rothschild,

R. E., Postnov, K. A., Shakura, N., Risse, P., Kreykenbohm, I., & Pelling, M. R., et al., 2000, ApJ, 543, 351

Coburn, W., Rothschild, R., & Heindl, W. A., 2000, IAU Circular, 7487, 1

Colgate, S. A., & White, R. H., 1966, ApJ, 143, 626

Comella, J. M., Craft, H. D., Lovelace, R. V. E., Sutton, J. M., & Tyler, G. L., 1969, Nature, 221, 453

Cook, M. C., & Page, C. G., 1987, MNRAS, 225, 381

Corbet, R. H. D., Smale, A. P., Ozaki, M., Koyama, K., & Iwasawa, K., 1995, ApJ, 443, 786

Corbet, R. H. D., Woo, J. W., & Nagase, F., 1993, A&A, 276, 52

Crampton, D., Hutchings, J. B., & Cowley, A. P., 1978, ApJ, 225, L63

Crosa, L., & Boynton, P. E., 1980, ApJ, 235, 999

Cusumano, G., Di Salvo, T., Burderi, L., Orlandini, M., Piraino, S., Robba, N., & Santangelo, A., 1998, A&A, 338, L79

Dal Fiume, D., Frontera, F., Masetti, N., Orlandini, M., Palazzi, E., Del Sordo, S., Santangelo, A., Segreto, A., Oosterbroek, T., & Parmar, A. N., et al., 1999, in The Fifth Compton Symposium, ed. M. L. McConnell, J. M. Ryan, Vol. 366, (New York: American Institute of Physics Press), 183

Dal Fiume, D., Orlandini, M., Del Sordo, S., Frontera, F., Oosterbroek, T., Palazzi, E., Parmar, A. N., Piraino, S., Santangelo, A., & Segreto, A., et al., 2000, in Broad Band X-ray Spectra of Cosmic Sources, ed. K. Makishima, L. Piro, T. Takahashi, COSPAR/Pergamon Press), 399

Davidson, K., 1973, Nature (Physical Science), 246, 1

Davidson, K., & Ostriker, J. P., 1973, ApJ, 179, 585

Davison, P. J. N., Watson, M. G., & Pye, J. P., 1977, MNRAS, 181, 73P

Deeter, J. E., Boynton, P. E., & Pravdo, S. H., 1981, ApJ, 247, 1003

Delgado-Martí, H., Levine, A. M., Pfahl, E., & Rappaport, S. A., 2001, ApJ, 546,

455

Di Salvo, T., Burderi, L., Robba, N. R., & Guainazzi, M., 1998, ApJ, 509, 897

Doxsey, R., Bradt, H. V., Levine, A., Murthy, G. T., Rappaport, S., & Spada, G., 1973, ApJ, 182, L25

Duncan, R. C., & Thompson, C., 1992, ApJ, 392, L9

Elsner, R. F., Ghosh, P., & Lamb, F. K., 1980, ApJ, 241, L155

Elsner, R. F., & Lamb, F. K., 1977, ApJ, 215, 897

Fabian, A. C., & Barcons, X., 1992, ARA&A, 30, 429

Fenimore, E. E., Conner, J. P., Epstein, R. I., Klebesadel, R. W., Laros, J. G., Yoshida, A., Fujii, M., Hayashida, K., Itoh, M., Murakami, T., Nishimura, J., Yamagami, Y., Kondo, I., & Kawai, N., et al., 1988, ApJ, 335, L71

Finger, M. H., Koh, D. T., Nelson, R. W., Prince, T. A., Vaughan, B. A., & Wilson, R. B., 1996, Nature, 381, 291

Finger, M. H., Wilson, R. B., & Chakrabarty, D., 1996, A&AS, 120, C209

Finger, M. H., Wilson, R. B., & Fishman, G. J., 1994, in The Second Compton Symposium, ed. C. E. Fichtel, N. Gehrels, J. P. Norris, (New York: American Institute of Physics Press), 304

Finger, M. H., Wilson, R. B., Harmon, B. A., Fishman, G. J., Meegan, C. A., & Paciesas, W. S., 1993, in Compton Gamma Ray Observatory, ed. M. Friedlander, N. Gehrels, D. J. Macomb, (New York: American Institute of Physics Press), 386

Forman, W., Jones, C., Cominsky, L., Julien, P., Murray, S., Peters, G., Tananbaum, H., & Giacconi, R., 1978, ApJS, 38, 357

Forman, W., Tananbaum, H., & Jones, C., 1976, ApJ, 206, L29

Friend, D. B., & Castor, J. I., 1982, ApJ, 261, 293

Frontera, F., Dal Fiume, D., Dusi, W., Morelli, E., & Spada, G., 1985, Advances in Space Research, 5, 125

Frontera, F., Fuligni, F., Morelli, E., & Venturea, G., 1979, ApJ, 229, 291

Ghosh, P., Angelini, L., & White, N. E., 1997, ApJ, 478, 713

Ghosh, P., & Lamb, F. K., 1979, ApJ, 234, 296

Giacconi, R., Gursky, H., Kellogg, E., Levinson, R., Schreier, E., & Tananbaum, H., 1973, ApJ, 184, 227

Giacconi, R., Gursky, H., Kellogg, E., Schreier, E., & Tananbaum, H., 1971a, ApJ, 167, L67

Giacconi, R., Kellogg, E., Gorenstein, P., Gursky, H., & Tananbaum, H., 1971b, ApJ, 165, L27

Giacconi, R., Murray, S., Gursky, H., Kellogg, E., Schreier, E., Matilsky, T., Koch, D., & Tananbaum, H., 1974, ApJS, 27, 37

Gold, T., 1968, Nature, 221, 25

Gottwald, M., Steinle, H., Graser, U., & Pietsch, W., 1991, A&AS, 89, 367

Grove, J. E., Strickman, M. S., Johnson, W. N., Kurfess, J. D., Kinzer, R. L., Starr, C. H., Jung, G. V., Kendziorra, E., Kretschmar, P., Maisack, M., & Staubert, R., et al., 1995, ApJ, 438, L25

Gruber, D. E., Heindl, W. A., Rothschild, R. E., Coburn, W., Staubert, R., Kreykenbohm, I., & Wilms, J., 2001, ApJ, 562, 499

Haberl, F., 1994, A&A, 283, 175

Haberl, F., & Sasaki, M., 2000, A&A, 359, 573

Haberl, F., & White, N. E., 1990, ApJ, 361, 225

Harding, A. K., 1994, in The Evolution of X-ray Binaries, ed. S. Holt, C. S. Day, (New York: American Institute of Physics Press), 429

Harding, A. K., & Daugherty, J. K., 1991, ApJ, 374, 687

Hayakawa, S., 1985, Phys. Rep., 121, 317

Heindl, W. A., & Chakrabarty, D., 1999, in Proceedings of the Symposium "Highlights in X-ray Astronomy in honour of Joachim Trümper's 65th birthday", ed. B. Aschenbach, M. J. Freyberg, Vol. 272, (Garching: Max-Planck Institute),

25

Heindl, W. A., & Coburn, W., 1999, IAU Circular, 7126, 2

Heindl, W. A., Coburn, W., Gruber, D. E., Pelling, M., Rothschild, R. E., Kretschmar, P., Kreykenbohm, I., Wilms, J., Pottschmidt, K., & Staubert, R., et al., 1999a, in The Fifth Compton Symposium, ed. M. L. McConnell, J. M. Ryan, Vol. 366, (New York: American Institute of Physics Press), 178

Heindl, W. A., Coburn, W., Gruber, D. E., Pelling, M., Rothschild, R. E., Wilms, J., Pottschmidt, K., & Staubert, R., 1999b, in The Fifth Compton Symposium, ed. M. L. McConnell, J. M. Ryan, Vol. 366, (New York: American Institute of Physics Press), 173

Heindl, W. A., Coburn, W., Gruber, D. E., Pelling, M. R., Rothschild, R. E., Wilms, J., Pottschmidt, K., & Staubert, R., 1999, ApJ, 521, L49

Hellier, C., 1994, IAU Circular, 5994, 2

Hewish, A., Bell, S. J., Pilkington, J. D. H., Scott, P. F., & Collins, R. A., 1968, Nature, 217, 709

Hoyle, F., Narlikar, J. V., & Wheeler, J. A., 1964, Nature, 203, 914

Hutchings, J. B., Cowley, A. P., Crampton, D., van Paradus, J., & White, N. E., 1979, ApJ, 229, 1079

Illarionov, A. F., & Sunyaev, R. A., 1975, A&A, 39, 185

Ilovaisky, S. A., Motch, C., & Chevalier, C., 1978, A&A, 70, L19

Inoue, H., Ogawara, Y., Waki, I., Ohashi, T., Hayakawa, S., Kunieda, H., Nagase, F., & Tsunemi, H., 1984, PASJ, 36, 709

in't Zand, J. J. M., Baykal, A., & Strohmayer, T. E., 1998, ApJ, 496, 386

in't Zand, J. J. M., Strohmayer, T. E., & Baykal, A., 1997, ApJ, 479, L47

Isenberg, M., Lamb, D. Q., & Wang, J. C. L., 1998a, ApJ, 493, 154

Isenberg, M., Lamb, D. Q., & Wang, J. C. L., 1998b, ApJ, 505, 688

Iye, M., 1986, PASJ, 38, 463

Jackson, J. D., 1975, Classical Electrodynamics, 2nd Edition, (New York: Wiley)

Jahoda, K., 2000a, in Rossi2000: Astrophysics with the Rossi X-ray Timing Explorer

Jahoda, K., 2000b, private communication

Jahoda, K., Swank, J. H., Giles, A. B., Stark, M. J., Strohmayer, T., Zhang, W., & Morgan, E. H., 1996, SPIE, 2808, 59

Joss, P. C., & Rappaport, S. A., 1976, Nature, 264, 219

Jung, G. V., 1989, ApJ, 338, 972

Kaper, L., Hammerschlag-Hensberge, G., & Zuiderwijk, E. J., 1994, A&A, 289, 846

Kelley, R. L., Rappaport, S., & Ayasli, S., 1983, ApJ, 274, 765

Kelley, R. L., Rappaport, S., Clark, G. W., & Petro, L. D., 1983, ApJ, 268, 790

Kendziorra, E., Kretschmar, P., Pan, H. C., Kunz, M., Maisack, M., Staubert, R., Pietsch, W., Truemper, J., Efremov, V., & Sunyaev, R., et al., 1994, A&A, 291, L31

Kendziorra, E., Mony, B., Kretschmar, P., Maisack, M., Staubert, R., Doebereiner, S., Englhauser, J., Pietsch, W., Reppin, C., & Trümper, J., et al., 1992, in The Compton Observatory Science Workshop, (Goddard Space Flight Center: NASA), 217, see N92-21874 12-90

Knight, F. K., 1982, ApJ, 260, 538

Knoll, G. F., 1979, Radiation detection and measurement, (New York: John Wiley and Sons, Inc.)

Koh, D. T., Bildsten, L., Chakrabarty, D., Nelson, R. W., Prince, T. A., Vaughan, B. A., Finger, M. H., Wilson, R. B., & Rubin, B. C., et al., 1997, ApJ, 479, 933

Kommers, J. M., Chakrabarty, D., & Lewin, W. H., 1998, ApJ, 497, L33

Koyama, K., Kawada, M., Takeuchi, Y., Tawara, Y., Ushimaru, N., Dotani, T., & Takizawa, M., 1990a, ApJ, 356, L47

Koyama, K., Kunieda, H., Takeuchi, Y., & Tawara, Y., 1990b, PASJ, 42, L59

Koyama, K., Kunieda, H., Takeuchi, Y., & Tawara, Y., 1991, ApJ, 370, L77

Kraus, U., Blum, S., Schulte, J., Ruder, H., & Mészáros, P., 1996, ApJ, 467, 794

Kraus, U., Nollert, H., Ruder, H., & Riffert, H., 1995, ApJ, 450, 763

Kretschmar, P., Araya-Gochez, R. A., Kreykenbohm, I., Wilms, J., Staubert, R., Heindl, W. A., Rothschild, R. E., & Gruber, D. E., 2000, in Proceedings of the Fourth INTEGRAL Symposium, (Alicante: ESA-SP), submitted

Kretschmar, P., Pan, H. C., Kendziorra, E., Maisack, M., Staubert, R., Skinner, G. K., Pietsch, W., Truemper, J., Efremov, V., & Sunyaev, R., et al., 1997, A&A, 325, 623

Kreykenbohm, I., Coburn, W., Wilms, J., Kretschmar, P., Staubert, R., Heindl, W. A., & Rothschild, R. E., 2002, A&A in press

Kreykenbohm, I., Kretschmar, P., Wilms, J., Staubert, R., Kendziorra, E., Gruber, D., Heindl, W. A., & Rothschild, R., 1999, A&A, 341, 141

Krzemiński, W., 1974, ApJ, 192, L135

Kuster, M., Wilms, J., Blum, S., Staubert, R., Gruber, D., Rothschild, R., & Heindl, W. A., 1999, in Proc. 3rd Integral Workshop, Astrophys. Lett. Comm., Vol. 38, 161

Lamb, D. Q., & Lamb, F. K., 1978, ApJ, 220, 291

Lamb, D. Q., Wang, J. C. L., & Wasserman, I. M., 1990, ApJ, 363, 670

Lamb, F. K., Pethick, C. J., & Pines, D., 1973, ApJ, 184, 271

Lamb, F. K., Shibazaki, N., Alpar, M. A., & Shaham, J., 1985, Nature, 317, 681

Lampton, M., Margon, B., & Bowyer, S., 1976, ApJ, 208, 177

Large, M. I., Vaughan, A. E., & Wielebinski, R., 1968, Nature, 220, 753

Latal, H. G., 1986, ApJ, 309, 372

Leahy, D. A., 1997, MNRAS, 287, 622

Leahy, D. A., & Matsuoka, M., 1990, ApJ, 355, 627

Leahy, D. A., Matsuoka, M., Kawai, N., & Makino, F., 1989, MNRAS, 237, 269

Levine, A., Ma, C. P., McClintock, J., Rappaport, S., van der Klis, M., & Verbunt, F., 1988, ApJ, 327, 732

Levine, A. M., Bradt, H., Cui, W., Jernigan, J. G., Morgan, E. H., Remillard, R., Shirey, R. E., & Smith, D. A., 1996, ApJ, 469, L33

Levine, A. M., Lang, F. L., Lewin, W. H. G., Primini, F. A., Dobson, C. A., Doty, J. P., Hoffman, J. A., Howe, S. K., Scheepmaker, A., Wheaton, W. A., Matteson, J. L., Baity, W. A., Gruber, D. E., Knight, F. K., Nolan, P. L., Pelling, R. M., Rothschild, R. E., & Peterson, L. E., et al., 1984, ApJS, 54, 581

Li, X., & van den Heuvel, E. P. J., 1996, A&A, 314, L13

Liu, Q. Z., van Paradijs, J., & van den Heuvel, E. P. J., 2000, A&AS, 147, 25

Lovelace, R. V. E., Romanova, M. M., & Bisnovatyi-Kogan, G. S., 1995, MNRAS, 275, 244

Makishima, K., Kawai, N., Koyama, K., Shibazaki, N., Nagase, F., & Nakagawa, M., 1984, PASJ, 36, 679

Makishima, K., & Mihara, T., 1992, in Frontiers of X-ray Astronomy (Proc. of the 28th Yamada Conf.), ed. Y. Tanaka, K. Koyama, (Tokyo: Uni. Acad. Press), 23

Makishima, K., Mihara, T., Nagase, F., & Tanaka, Y., 1999, ApJ, 525, 978

Makishima, K., Ohashi, T., Sakao, T., Dotani, T., Inoue, H., Koyama, H., Makino, F., Mitsuda, K., Nagase, F., Thomas, H. D., Turner, M. J. L., Kii, T., & Tawara, Y., et al., 1988, Nature, 333, 746

Maloney, P. R., & Begelman, M. C., 1997, ApJ, 491, L43

Manchester, R. N., & Taylor, J. H., 1977, Pulsars, (San Francisco: W. H. Freeman)

Marsden, D. C., 1999, *Ph.D. thesis*, University of California, San Diego, Ja Lolla, CA

Marshall, N., & Ricketts, M. J., 1980, MNRAS, 193, 7P

Mason, K. O., White, N. E., Sanford, P. W., Hawkins, F. J., Drake, J. F., & York, D. G., 1976, MNRAS, 176, 193

Matteson, J. L., (eds.) 1978, The UCSD/MIT hard X-ray and low energy gamma–ray experiment for HEAO–1 – Design and early results

Mavromatakis, F., 1993, A&A, 276, 353

McClintock, J. E., Bradt, H. V., Doxsey, R. E., Jernigan, J. G., Canizares, C. R., & Hiltner, W. A., 1977, Nature, 270, 320

McClintock, J. E., Li, F. K., Canizares, C. R., & Grindlay, J. E., 1980, ApJ, 235, L81

Mereghetti, S., 1999, in The Neutron Star - Black Hole Connection, astro-ph/9911252

Mereghetti, S., & Stella, L., 1995, ApJ, 442, L17

Mészáros, P., 1992, High-energy radiation from magnetized neutron stars, (Chicago: University of Chicago Press)

Mészáros, P., & Nagel, W., 1985a, ApJ, 298, 147

Mészáros, P., & Nagel, W., 1985b, ApJ, 299, 138

Middleditch, J., Mason, K. O., Nelson, J. E., & White, N. E., 1981, ApJ, 244, 1001

Mihara, T., 1995, *Ph.D. thesis*, University of Tokyo

Mihara, T., Makishima, K., & Nagase, F., 1998, Advances in Space Research, 22, 987

Mihara, T., Makishima, K., Ohashi, T., Sakao, T., & Tashiro, M., 1990, Nature, 346, 250

Mihara, T., Ohashi, T., Makishma, K., Nagase, F., Kitamoto, S., & Koyama, K., 1991, PASJ, 43, 501

Murakami, T., Ikegami, T., Inour, H., & Makishima, K., 1987, PASJ, 39, 253

Mushotzky, R. F., Roberts, D. H., Baity, W. A., & Peterson, L. E., 1997, ApJ, 211, L129

Nagase, F., 1989, PASJ, 41, 1

Nagase, F., Corbet, R. H. D., Day, C. S. R., Inoue, H., Takeshima, T., Yoshida, K., & Mihara, T., 1992, ApJ, 396, 147

Nagase, F., Dotani, T., Tanaka, Y., Makishima, K., Mihara, T., Sakao, T., Tsunemi, H., Kitamoto, S., Tamura, K., Yoshida, A., & Nakamura, H., et al., 1991, ApJ, 375, L49

Nagase, F., Hayakawa, S., Sato, N., Masai, K., & Inoue, H., 1986, PASJ, 38, 547

Narayan, R., & Ostriker, J. P., 1990, ApJ, 352, 222

Nelson, R. W., Bildsten, L., Chakrabarty, D., Finger, M. H., Koh, D. T., Prince, T. A., Rubin, B. C., Scott, D. M., Vaughan, B. A., & Wilson, R. B., et al., 1997, ApJ, 488, L117

Nelson, R. W., Wang, J. C. L., Salpeter, E. E., & Wasserman, I., 1995, ApJ, 438, L99

Nugent, J. J., Jensen, K. A., Nousek, J. A., Garmire, G. P., Mason, K. O., Walter, F. M., Bowyer, C. S., Stern, R. A., & Riegler, G. R., et al., 1983, ApJS, 51, 1

Ohashi, T., Inoue, H., Koyama, K., Makino, F., Matsuoka, M., Suzuki, K., Tanaka, Y., Hayakawa, S., Tsunemi, H., & Yamashita, K., et al., 1984, PASJ, 36, 699

Oppenheimer, J. R., & Volkoff, G. M., 1939, Phys.Rev, 55, 374

Orlandini, M., Dal Fiume, D., Frontera, F., Cusumano, G., Del Sordo, S., Giarrusso, S., Piraino, S., Segreto, A., Guainazzi, M., & Piro, L., et al., 1998, A&A, 332, 121

Orlandini, M., Dal Fiume, D., Frontera, F., Del Sordo, S., Piraino, S., Santangelo, A., Segreto, A., Oosterbroek, T., & Parmar, A. N., et al., 1998, ApJ, 500, L163

Ostriker, E. C., & Shu, F. H., 1995, ApJ, 447, 813

Owens, A., Oosterbroek, T., & Parmar, A. N., 1997, A&A, 324, L9

Pacini, F., 1967, Nature, 216, 567

Pakull, M., van Amerongen, S., Bakker, R., & van Paradijs, J., 1983, A&A, 122, 79

Pelling, M. R., Rothschild, R. E., MacDonald, D. R., Hertel, R., & Nishiie, E., 1991, SPIE Proceedings, 1549, 134

Piraino, S., Santangelo, A., Segreto, A., Giarrusso, S., Cusumano, G., Del Sordo, S., Robba, N. R., Dal Fiume, D., Orlandini, M., Oosterbroek, T., & Parmar, A. N., et al., 2000, A&A, 357, 501

Pravdo, S. H., Day, C. S. R., Angelini, L., Harmon, B. A., Yoshida, A., & Saraswat, P., 1995, ApJ, 454, 872

Pringle, J. E., 1996, MNRAS, 281, 357

Pringle, J. E., & Rees, M. J., 1972, A&A, 21, 1

Rappaport, S., & Joss, P. C., 1977, Nature, 266, 683

Rappaport, S. A., & Joss, P. C., 1983, in Accretion Driven Stellar X-ray Sources, (Cambridge/New York: Cambridge University Press), 1

Ravenhall, D. G., & Pethick, C. J., 1994, ApJ, 424, 846

Reig, P., & Coe, M. J., 1999, MNRAS, 302, 700

Remillard, R., Levine, A., Takeshima, T., Corbet, R. H. D., Marshall, F. E., Swank, J. H., & Chakrabarty, D., 1998, IAU Circular, 6826, 2

Reynolds, A. P., Bell, S. A., & Hilditch, R. W., 1992, MNRAS, 256, 631

Reynolds, A. P., & Parmar, A. N., 1995, A&A, 297, 747

Rickard, J. J., 1974, ApJ, 189, L113

Robba, N. R., Burderi, L., Wynn, G. A., Warwick, R. S., & Murakami, T., 1996, ApJ, 472, 341

Robba, N. R., Di Salvo, T., Burderi, L., Barbera, A. L., & Cusumano, G., 1999, in The Fifth Compton Symposium, ed. M. L. McConnell, J. M. Ryan, Vol. 366, (New York: American Institute of Physics Press), 213

Robba, N. R., & Warwick, R. S., 1989, ApJ, 346, 469

Roberts, M. S. E., Michelson, P. F., Leahy, D. A., Hall, T. A., Finley, J. P., Cominsky, L. R., & Srinivasen, R., 2001, astro-ph/0103140, ApJ in press

Rose, L. A., Marshall, F. E., Holt, S. S., Boldt, E. A., Rothschild, R. E., Serlemitsos, P. J., Pravdo, S. H., & Kaluzienski, L. J., 1979, ApJ, 231, 919

Rothschild, R., Boldt, E., Holt, S., Serlemitsos, P., Garmire, G., Agrawal, P., Riegler, G., Bowyer, S., & Lampton, M., et al., 1979, Space Science Instrumentation, 4, 269

Rothschild, R. E., Blanco, P. R., Gruber, D. E., Heindl, W. A., MacDonald, D. R., Marsden, D. C., Pelling, M. R., Wayne, L. R., & Hink, P. L., et al., 1998, ApJ, 496, 538

Rots, A. H., Jahoda, K., Macomb, D. J., Kawai, N., Saito, Y., Kaspi, V. M., Lyne, A. G., Manchester, R. N., Backer, D. C., Somer, A. L., Marsden, D., & Rothschild, R. E., et al., 1998, ApJ, 501, 749

Rubin, B. C., Finger, M. H., Scott, D. M., & Wilson, R. B., 1997, ApJ, 488, 413

Rubin, B. C., Finger, M. H., Wilson, R. B., Fishman, G. J., Meegan, C. A., Paciesas, W. S., Prince, T., Chiu, J., & Chakrabarty, D., et al., 1994, in The Evolution of X-ray Binaries, ed. S. Holt, C. S. Day, (New York: American Institute of Physics Press), 455

Rybicki, G. B., & Lightman, A. P., 1979, Radiative processes in astrophysics, (New York: Wiley-Interscience)

Sadakane, K., Hirata, R., Jugaku, J., Kondo, Y., Matsuoka, M., Tanaka, Y., & Hammerschlag-Hensberge, G., 1985, ApJ, 288, 284

Santangelo, A., Del Sordo, S., Segreto, A., Dal Fiume, D., Orlandini, M., & Piraino, S., 1998, A&A, 340, L55

Santangelo, A., Segreto, A., Giarrusso, S., Dal Fiume, D., Orlandini, M., Parmar, A. N., Oosterbroek, T., Bulik, T., Mihara, T., Campana, S., Israel, G. L., & Stella, L., et al., 1999, ApJ, 523, L85

Santangelo, A., Segreto, A., Orlandini, M., Parmar, A. N., Oosterbroek, T., & Campana, S., 2002, submitted to ApJ Letters

Sato, N., Nagase, F., Kawai, N., Kelley, R. L., Rappaport, S., & White, N. E., 1986, ApJ, 304, 241

Savonije, J., 1983, in Accretion Driven Stellar X-ray Sources, (Cambridge/New York: Cambridge University Press), 343

Schandl, S., & Meyer, F., 1994, A&A, 289, 149

Schlegel, E. M., Serlemitsos, P. J., Jahoda, K., Marshall, F., Petre, R., Boldt, E., Mushotzky, R., Swank, J., Szymkowiak, A., Smale, A., & Weaver, K., et al., 1993, ApJ, 407, 744

Schreier, E., Levinson, R., Gursky, H., Kellogg, E., Tananbaum, H., & Giacconi, R., 1972, ApJ, 172, L79

Schwartz, D. A., Griffiths, R. E., Bowyer, S., Thorstensen, J. R., & Charles, P. A., 1980, AJ, 85, 549

Scott, D. M., & Leahy, D. A., 1999, ApJ, 510, 974

Scott, D. M., Leahy, D. A., & Wilson, R. B., 2000, ApJ, 539, 392

Serlemitsos, P. J., Becker, R. H., Boldt, E. A., Holt, S. S., Pravdo, S. H., Rothschild, R. E., & Swank, J. H., 1976, in X-ray Binaries, ed. W. H. G. Lewin, J. van Paradijs, E. P. J. van den Heuvel, (Cambridge/New York: Cambridge University Press), 67

Shakura, N. I., Ketsaris, N. A., Prokhorov, M. E., & Postnov, K. A., 1998, MNRAS, 300, 992

Shakura, N. I., Prokhorov, M. E., Postnov, K. A., & Ketsaris, N. A., 1999, A&A, 348, 917

Shakura, N. I., & Sunyaev, R. A., 1973, A&A, 24, 337

Shapiro, S. L., & Lightman, A. P., 1976, ApJ, 204, 555

Shapiro, S. L., & Teukolsky, S. A., 1983, Black holes, white dwarfs, and neutron stars: The physics of compact objects, (New York: Wiley-Interscience)

Shinoda, K., Kii, T., Mitsuda, K., Nagase, F., Tanaka, Y., Makishima, K., & Shibazaki, N., 1990, PASJ, 42, L27

Smith, D. A., & Takeshima, T., 1998, IAU Circular, 7014, 1

Soong, Y., Gruber, D. E., Peterson, L. E., & Rothschild, R. E., 1990, ApJ, 348, 641

Soong, Y., Gruber, D. E., Peterson, L. E., & Rothschild, R. E., 1990, ApJ, 348, 634

Staelin, D. H., & Reifenstei, E. C., 1968, Science, 162, 1481

Stelzer, B., Wilms, J., Staubert, R., Gruber, D. E., & Rothschild, R., 1999, A&A, 342, 736

Sunyaev, R. A., & Titarchuk, L. G., 1980, A&A, 86, 121

Takeshima, T., & Chakrabarty, D., 1998, IAU Circular, 7016, 1

Takeshima, T., Corbet, R. H. D., Marshall, F. E., Swank, J., & Chakrabarty, D., 1998, IAU Circular, 6826, 2

Tamura, K., Tsunemi, H., Kitamoto, S., Hayashida, K., & Nagase, F., 1992, ApJ, 389, 676

Tanaka, Y., 1986, in IAU Colloq. 89: Radiation Hydrodynamics in Stars and Compact Objects, ed. D. Mihalas, K. H. Winkler, (New York: Springer), 198

Tananbaum, H., Gursky, H., Kellogg, E. M., Levinson, R., Schreier, E., & Giacconi, R., 1972, ApJ, 174, L143

Tawara, Y., Yamauchi, S., Awaki, H., Kii, T., Koyama, K., & Nagase, F., 1989, PASJ, 41, 473

Taylor, J. H., Manchester, R. N., & Lyne, A. G., 1993, ApJS, 88, 529

Telting, J. H., Waters, L. B. F. M., Roche, P., Boogert, A. C. A., Clark, J. S., de Martino, D., & Persi, P., 1998, MNRAS, 296, 785

Thompson, C., & Duncan, R. C., 1995, MNRAS, 275, 255

Thompson, C., & Duncan, R. C., 1996, ApJ, 473, 322

Tjemkes, S. A., van Paradijs, J., & Zuiderwijk, E. J., 1986, A&A, 154, 77

Trümper, J., Pietsch, W., Reppin, C., Voges, W., Staubert, R., & Kendziorra, E., 1978, ApJ, 219, L105

Tsuruta, S., & Cameron, A. G. W., 1965, Nature, 211, 356

Turner, M. J. L., Thomas, H. D., Patchett, B. E., Reading, D. H., Makishima, K., Ohashi, T., Dotani, T., Hayashida, K., Inoue, H., Kondo, H., Koyama, K., Mitsusa, K., Ogawara, Y., Takano, S., Awaki, H., Tawara, Y., & Nakamura, N., et al., 1989, PASJ, 41, 345

Unger, S. J., Roche, P., Negueruela, I., Ringwald, F. A., Lloyd, C., & Coe, M. J., 1998, A&A, 336, 960

Valinia, A., & Marshall, F. E., 1998, ApJ, 505, 134

van den Heuvel, E. P. J., 1991, in NATO ASIC Proc. 344: Neutron Stars, ed. J. Ventura, D. Pines, (Dordrecht: Kluwer), 171

van den Heuvel, E. P. J., & Rappaport, S. A., (eds.) 1992, X-ray binaries and recycled pulsars, (Dordrecht: Kluwer)

van Kerkwijk, M. H., van Oijen, J. G. J., & van den Heuvel, E. P. J., 1989, A&A, 209, 173

van Kerkwijk, M. H., van Paradijs, J., Zuiderwijk, E. J., Hammerschlag-Hensberge, G., Kaper, L., & Sterken, C., 1995, A&A, 303, 483

van Paradijs, J., Taam, R. E., & van den Heuvel, E. P. J., 1995, A&A, 299, L41

Ventura, J., 1979, Phys.Rev.D, 19, 1684

Voges, W., Aschenbach, B., Boller, T., Bräuninger, H., Briel, U., Burkert, W., Dennerl, K., Englhauser, J., Gruber, R., Haberl, F., Hartner, G., Hasinger, G., Kürster, M., Pfeffermann, E., Pietsch, W., Predehl, P., Rosso, C., Schmitt, J. H. M. M., Trümper, J., & Zimmermann, H. U., et al., 1999, A&A, 349, 389

Voges, W., Aschenbach, B., Boller, T., Brauninger, H., Briel, U., Burkert, W., Dennerl, K., Englhauser, J., Gruber, R., Haberl, F., Hartner, G., Hasinger, G., Pfeffermann, E., Pietsch, W., Predehl, P., Schmitt, J., Trümper, J., & Zimmermann, U., et al., 2000, IAU Circular, 7432, 3

Voges, W., Pietsch, W., Reppin, C., Trümper, J., Kendziorra, E., & Staubert, R., 1982, ApJ, 263, 803

Wang, Y.-M., 1981, Space Science Reviews, 30, 341

Wang, Y.-M., 1981, A&A, 102, 36

Wang, Y.-M., 1996, ApJ, 465, L111

Wang, Y.-M., & Robnik, M., 1982, A&A, 107, 222

Warwick, R. S., Marshall, N., Fraser, G. W., Watson, M. G., Lawrence, A., Page,

C. G., Pounds, K. A., Ricketts, M. J., Sims, M. R., & Smith, A., et al., 1981, MNRAS, 197, 865

Weth, C., 2001, astro-ph/0101044, submitted to ApJL

Wheaton, W. A., Doty, J. P., Primini, F. A., Cooke, B. A., Dobson, C. A., Goldman, A., Hecht, M., Howe, S. K., Hoffman, J. A., & Scheepmaker, A., et al., 1979, Nature, 282, 240

Wheeler, J. A., 1966, ARA&A, 4, 393

White, N. E., Mason, K. O., Huckle, H. E., Charles, P. A., & Sanford, P. W., 1976, ApJ, 209, L119

White, N. E., Mason, K. O., & Sanford, P. W., 1977, Nature, 267, 229

White, N. E., Mason, K. O., Sanford, P. W., & Murdin, P., 1976, MNRAS, 176, 201

White, N. E., & Swank, J. H., 1984, ApJ, 287, 856

White, N. E., Swank, J. H., & Holt, S. S., 1983, ApJ, 270, 711

White, N. E., Swank, J. H., Holt, S. S., & Parmar, A. N., 1982, ApJ, 263, 277

Wijnands, R., & van der Klis, M., 1998, Nature, 394, 344

Wilms, J., Nowak, M. A., Dove, J. B., Fender, R. P., & di Matteo, T., 1999, ApJ, 522, 460

Wilson, C. A., Finger, M. H., Wilson, R. B., & Scott, D. M., 1998, IAU Circular, 7014, 2

Wilson, C. A., Zhang, S. N., Finger, M. H., Wilson, R. B., Scott, M., Koh, T., Chakrabarty, D., Vaughan, B., & Prince, T. A., et al., 1995, IAU Circular, 6238, 1

Wilson, R. B., Harmon, B. A., & Finger, M. H., 1999, IAU Circular, 7116, 1

Woltjer, L., 1964, ApJ, 140, 1309

Wood, K. S., Meekins, J. F., Yentis, D. J., Smathers, H. W., McNutt, D. P., Bleach, R. D., Friedman, H., Byram, E. T., Chubb, T. A., & Meidav, M., et al., 1984, ApJS, 56, 507

Worrall, D. M., Knight, F. K., Nolan, P. L., Rothschild, R. E., Levine, A. M., Primini, F. A., & Lewin, W. H. G., 1981, ApJ, 247, L31

Zel'dovich, Y. A., & Shakura, N. I., 1969, Soviet Astronomy, 13, 175